# Advances in hybrid plasmonics : from passive to active functions

Xuan Zhou

Thèse
de doctorat
de l'UTT

Xuan ZHOU

# Advances in Hybrid Plasmonics: From Passive to Active Functions

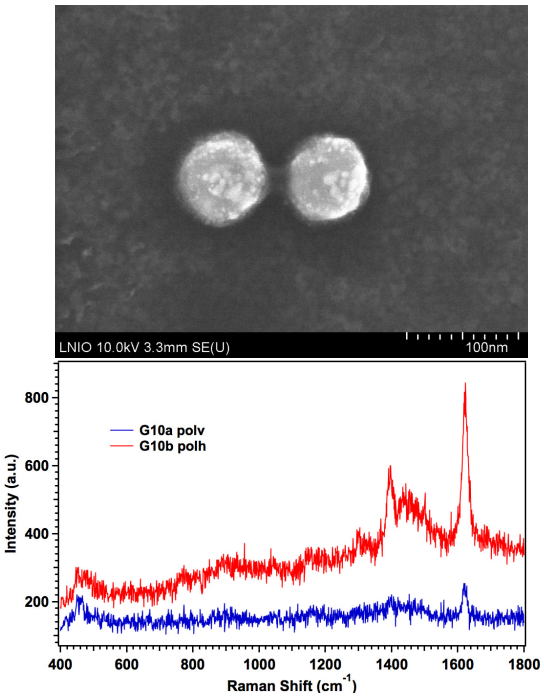


**Spécialité :**
Optique et Nanotechnologies

2013TROY0015

Année 2013

utt
université de technologie
Troyes

# THESE

*pour l'obtention du grade de*

## DOCTEUR de l'UNIVERSITE DE TECHNOLOGIE DE TROYES

**Spécialité : OPTIQUE ET NANOTECHNOLOGIES**

*présentée et soutenue par*

**Xuan ZHOU**

*le 18 juillet 2013*

# Advances in Hybrid Plasmonics: From Passive to Active Functions

## JURY

| | | |
|---|---|---|
| M. N. FELIDJ | PROFESSEUR DES UNIVERSITES | Président |
| M. R. BACHELOT | PROFESSEUR DES UNIVERSITES | Directeur de thèse |
| Mme C. FIORINI | CHERCHEUR - HDR | Examinateur |
| M. S. GRESILLON | MAITRE DE CONFERENCES - HDR | Rapporteur |
| M. P. LECLERE | CHERCHEUR QUALIFIE FNRS | Rapporteur |
| M. J. PLAIN | PROFESSEUR DES UNIVERSITES | Examinateur |

## Personnalité invitée

| | |
|---|---|
| M. D. GOSZTOLA | RESEARCHER |

# Acknowledgements

This PhD work is accomplished with the support of numerous people from inside and outside LNIO.

First of all, I would like to give my very grateful thanks to Prof. Renaud Bachelot, my advisor, for all his advices, encouragement and care ever since I started my thesis under his supervision. He is an extraordinary supervisor that is meticulous in science and with plenty of ideas. His patient, amiable, optimistic, and humorous characteristics and qualities have provided me a very pleasant environment for research. It is my great honor to work with him to start my research life.

I would like to thank Dr. Claire Deeb, who, as well, gave me many recommendations and supports throughout my work. I accepted from her lot of good habits during my first contact with scientific research. She is always ready to lend me a hand in both research and daily life. In my eyes, she is not only an advisor, but also a very close friend who shares my happiness and depression.

Our collaborators, Dr. Alexandre Bouhelier and Dr. Sylvie Marguet, as well as my colleagues Julien Proust, Thomas Lerond, Serguei Kochtcheev, and Jérémie Béal, have provided some samples or nanoparticles for this dissertation. Thanks for their help in fabricating these beautiful samples, which allow us to achieve reliable quantitative measurements.

The numerical simulations and theoretical calculations involved in this PhD work were performed by our collaborators Dr. Prashant K. Jain, Dr. Stephen K. Gray, Dr. Ryan Miller, Dr. Milo Russell, Dr. Gérard Colas des Francs, and my colleague Dr. Rémi Vincent. Thanks should be given to them for the calculated results and fruitful discussions.

I would like to thank our partners Dr. Gary P. Wiederrecht, Dr. David J. Gosztola, Dr. Shengye Jin, Prof. Nordin Félidj, and Dr. Johan Grand for all the questions, comments, and ideas, as well as the warm hospitalities during my visits. I would also like to thank Dr. Olivier Soppera, Dr. Fabrice Charra, and Dr. Céline Fiorini for their suggestions and discussions.

Thanks should be given to Prof. Jérôme Plain, who participated in almost all our discussions, for giving very helpful ideas, comments and suggestions. Prof. Pierre-Michel Adam, Dr. Safi Jradi, Dr. Anne-Laure Baudrion-Béal, Dr. David Gérard, Dr. Rodolphe Jaffiol, and Prof. Alexandre Vial have proposed many valuable suggestions and comments on my work.

I would like to give many thanks to Régis Deturche for training me on the scanning electron microscope, and Dr. Irène Izquierdo for the information on Raman spectrometer.

Thanks should also be given to Huan, Jérémie, Julie, Kun, Lama, Mohamed, Silvère, Wei, Zohreh, as well as guys from LNIO whose names have been mentioned above, for sharing with me a very pleasant and memorable time in this lab. It is wonderful to have them as my colleagues.

Just before going to the financial supports, I would like to thank my family for standing with me during these years.

Last but not least, I would like to give my acknowledgements to China Scholarship Council for funding. This is the prerequisite for my coming to France for this Thesis. Research works in this dissertation were supported by the Partner University Fund (PUF) and the project of Hybrid Anisotropic Plasmon-Photonics for Light Emission (HAPPLE) funded by Agence Nationale de la Recherche (ANR). I would like also to thank the platform Nano'mat as well as the Center for Nanoscale Materials of Argonne National Laboratory (under Contract No. DE-AC02-06CH11357).

# Table of Contents

# Nomenclature

| | |
|---|---|
| AFM | Atomic force microscopy |
| BSE | Backscattered electron |
| CCD | Charge coupled device |
| CTAB | Cethltrimethylammonium |
| DDA | Discrete dipole approximation |
| EY | Eosin Y (2',4',5',7'-tetrabromo-fluorescien disodium salt ) |
| EBL | Electron beam lithography |
| EELS | Electron-energy-loss spectroscopy |
| FDTD | Finite-difference time-domain |
| FRET | Förster resonance energy transfer |
| HOMO | Highest occupied molecular orbital |
| IPA | Isopropanol |
| ISC | Inter-system crossing |
| ITO | Indium-tin-oxide |
| IVR | Intra-molecular vibrational redistribution |
| LSPR | Localized surface plasmon resonance |
| LUMO | Lowest unoccupied molecular orbital |
| MB | Methylene blue |
| MDEA | Methyldiethanolamine |
| MIBK | Methyl isobutyl ketone |

| | |
|---|---|
| MNP | Metal nanoparticle |
| NA | Numerical aperture |
| NE | Nano-emitter |
| NPGS | Nanometer pattern generation system |
| PEEM | Photo-emission electron microscopy |
| PETIA | Pentaerythritol Triacrylate |
| PMMA | Polymethyl Methacrylate |
| QD | Quantum dot |
| RH6G | Rhodamine 6G |
| ROC | Radius of curvature |
| SE | Secondary electron |
| SEM | Scanning electron microscopy |
| SERS | Surface enhanced Raman spectroscopy |
| SERRS | Surface-enhanced resonance Raman spectroscopy |
| SNOM | Scanning near-field optical microscopy |
| SPM | Scanning probe microscopy |
| TERS | Tip-enhanced Raman spectroscopy |

# Introduction

Near-field optics deals with optical behaviors such as absorption, scattering and emission in a sub-wavelength distance of an element. The metal nanostructure is one of the favorite materials for near-field studies and applications because they support surface plasmons, which are known as collective charge oscillations at the metal/dielectric interface. This oscillating evanescent wave produces a very localized enhancement on the optical field, which leads to some significantly modified phenomena such as emission and scattering. Benefiting from this augmentation of the local field, surface plasmons have been a hotspot that opened new doors in many different domains, for instance, solar cell, data storage, fluorescence, Raman spectroscopy, cancer diagnostics and treatment, etc. None of the above applications, however, can be realized on bare metal nanostructures. In other words, the combination of metals with other materials such as quantum emitters, biomolecules, and inorganic elements are required. This is a general idea of hybrid plasmonics.

Other than the utilizations listed above, hybrid plasmonics has significantly contributed to fundamental studies on the energy transfer between metal nanoparticle (MNP) and molecule. The traditional hybrids are constructed from a homogeneous layer of dye molecules as a shell and MNPs as a core. As a nano-emitter, however, this configuration stops the selection of specific emission mode with incident light.

Driven by the purpose of developing an anisotropic hybrid light-emitting nanosystem, this PhD work focused on a photopolymer/metal hybrid nanostructure that introduced the anisotropic distribution of dye. It should be emphasized that he fabrication of this nanosystem is a near-field imaging process with a much more improved resolution (sub 5nm) as compared to the conventional techniques (20-100nm). Triggered by the surface plasmon enhancement, the photopolymerization is well-controlled in the vicinity of MNPs imprinting its near-field. This technique provides not only high-resolution images through “near-field photography”, but also quantitative measurements of the near-field of MNPs. Polymerized with dipolar plasmon mode, the obtained hybrid light-emitting nanostructure is inhomogeneous with controllable emission modes by alternating the incident polarization.

The first chapter of this dissertation will describe the hybrid plasmonics of MNPs by evoking its basic properties as well as recent developments. The surface plasmon supported by the MNP is a key factor of hybrid plasmonic structures and therefore becomes the very first point of our discussions. It is tunable by the variation of such properties as size, shape, nature, and environment of the nanoparticle. The energy loss of surface plasmons results from finite size effects including radiative damping, non-radiative damping, as well as dynamic depolarization. Being enhanced

by surface plasmons, the local optical electromagnetic field of a MNP is able to modify the fluorescence and Raman scattering features of dye molecules that are close to the particle. Hybrid plasmonic nanostructures provides convenient method to study the interactions between dye molecules and MNPs. We will introduce briefly in the end of this chapter the hybrid nanostructure that will be discussed throughout this dissertation. As will be presented in detail, it serves as a technique for the near-field characterization and production of a nano-emitter with selectable emission modes.

In chapter two, we will introduce all the experimental procedures and techniques in this PhD work. The detailed procedures of hybridization will be presented, including both optical configurations and photochemical procedures. Chemical synthesized gold colloids and electron-beam lithographic gold nanoparticles are utilized to support surface plasmons. We will go through the detailed procedures for fabricating samples for the coming chapters. Besides, the characterizing methods in this dissertation will be introduced. For passive hybrid plasmonics (i.e., in the context of near-field characterization), topographic imaging techniques such as atomic force microscope and scanning electron microscope will be utilized. In the case of active hybrid plasmonics (i.e. nano-emitters), our hybrid structure is characterized with optical methods as surface enhanced Raman scattering and fluorescence. In each of the techniques, some of the images or spectra will be shown as examples.

Chapter three deals with the quantitative investigation of the near-field on many different types of particles. The field distribution of E-beam lithographic gold nanorods as well as colloidal gold nanospheres and nanocubes will be studied in this chapter. With gold nanospheres, the size-dependent near-field distribution will be quantified. We will optimize the diameter of the sphere to obtain a maximum dipole volume. Then the off-resonance photopolymerization on differently oriented nanorods will confirm the high resolution of this technique by imaging local electromagnetic field with a low enhancement factor and strong surface confinement. Finally, nanocubes with different orientations related to the exciting field will serve as plasmon sources. In this study, the dose of incident energy will be varied to excite corners and ridges of the nanocubes. Based on the polymer thickness for different doses, we can reproduce the single exponential decay of the surface plasmon. This distinguishes our technique from other methods.

Chapter four presents the optical features of the hybrid nanostructures. Polymerized with dipolar mode plasmon, the metal/polymer hybrid nano-emitter being sensitive to the incident light. We will show the different response of fluorescence intensity to different incident polarization on gold nanosphere/photopolymer hybrid nano-emitters (i.e., different emission modes). To our knowledge, this is the first report of anisotropic nano-emitter based on the anisotropy of gain medium. Besides, surface enhanced Raman spectroscopy will be utilized for the optical characterization of hybrids of gold dimer/photopolymer. As a reference, polarization-dependent SERS signal on hybrid structure based on a monomer of gold nanodisk will be presented.

This thesis will end up with concluding remarks and perspectives. In the part of appendix, a very brief description can be found concerning some theoretical calculation and numerical simulation methods in this thesis.

# CHAPTER 1

# Molecular Plasmonics: Toward Hybrid Plasmonics

Hybrid plasmonics provides effective methods for both fundamental studies and applications of the surface plasmon, which is the collective charge oscillation of electrons on the metal surface while it interacts with an incident light. Generally, the hybrid plasmonic structure is a subwavelength combined configuration of metal and other materials, in which the metal supports surface plasmons. Other materials, according to different requests, could be semiconductors,[1-2] organic dyes,[3-5] inorganic elements,[6-7] biomolecules,[8] or even more complex structures like combinations of several different materials.[9-10] These functional structures are designed to profit from the excited field for its unique characteristics.

This chapter is intended to sketch out an outline of fundamental studies and development related to the hybrid plasmonics of MNPs. We will start with some related principles of surface plasmons such as radiative and non-radiative damping, the phase retardation, and the characterization. Then we will turn our attention to the surface enhanced fluorescence and Raman scattering, which are two of the main techniques for the analyses and uses of surface plasmons. It will end by a brief overview of some hybrid plasmonic structures, including the one that would be studied in this dissertation. These reminders, together with the state of the art, will allow us to analyze and evaluate the obtained results in chapters 2-4.

## 1.1 Surface plasmons

Conductive electrons are distributed on the surface of metal. At the metal/dielectric interface, the positive charge is only inside the metal, leaving the electron density extends a non-negligible distance into the dielectric. When interact with an incident optical electromagnetic field, these electrons oscillate, under the restoring force from the positively charged nuclei, as a collective group back and forth across the interface. This collective oscillation of electrons is defined as surface plamons. It is associated to both surface wave and particle.

In the context of nanoparticles, it is termed as localized surface plasmons. At certain incident frequency, MNPs interact the most efficiently with the incident light, resulting in a maximum light extinction. This is defined as the localized surface plasmon resonance (LSPR) of the nanoparticle. The LSPR depends on the size,

shape, and nature of the nanoparticle as well as the medium that surrounds it. Typically, particle size is variable in a large scale and shapes of the nano-objects can be also very different. Noble metals, especially gold and silver, are much more popular than other materials. Although silver structures present better behaviors on the surface plasmon excitation, their relatively high reactivity, especially with oxygen, should not be underestimated. In this dissertation, all types of studied nanoparticles are gold particles because of their high chemical and thermal stabilities as well as a controllable near-field behavior in the visible.

Series of studies on the near-field based on different shapes of MNP have been reported. Stories started with the nanosphere for its extremely symmetrical geometry. The early work can be dated back to 1908, done by Gustav Mie[11] on solving the Maxwell's equations for the scattering of electromagnetic wave by spheres. Mie theory gives exact solutions to scattering problems and it can be applied on the ellipsoidal MNPs as well. Nowadays, Mie theory is still attracting much attention for its applications and extensions.[12-13] However, it is not universally applicable because in most cases, nanoparticles are not that regularly shaped. Thus, numerical techniques such as finite difference time domain (FDTD),[14] discrete dipole approximation (DDA),[15] multiple multipole,[16] and the T-matrix[17] were developed for the near-field modeling of nanoparticles of any shape (triangles, stars, etc.). The quasistatic approximation is also commonly used. Usually it can give good results but is not as complete as the Mie theory to obtain physical insights from the results.[18]

### 1.1.1 Quasistatic approximation

While considering a metallic sphere whose dimension is much smaller than the incident wavelength, the spatial dependence of the incident far-field is negligible however time dependence should still be considered. In other words, the metal sphere is iso-phase (all the electrons vibrate in phase) while the electromagnetic nature of the field is still taken into account. The potential at any point in the incident field can be described by Laplace equation

$$\nabla^2\varphi = 0 \tag{1.1}$$

Solving the equation under boundary conditions in spherical coordinates $(r, \theta, \phi)$ for a sphere, the two solutions obtained are the potentials outside $\varphi_{out}$ and inside $\varphi_{in}$ the sphere:

$$\begin{cases} \varphi_{out} = -E_0 r\cos\theta + \frac{\varepsilon_m-\varepsilon_d}{\varepsilon_m+2\varepsilon_d}\frac{E_0R^3\cos\theta}{r^2} \\ \varphi_{in} = -\frac{3\varepsilon_d}{\varepsilon_m+2\varepsilon_d}E_0 r\cos\theta \end{cases} \tag{1.2}$$

where $E_0$ is the incident electric field, $r$ represents the distance from the center of the metal sphere, $R$ is the radius of the metal sphere, $\varepsilon_m = \varepsilon_r + i\varepsilon_i$ is the dielectric function of metal, and $\varepsilon_d$ is the dielectric constant of the medium.

Consequently, the near-field amplitude $E_{nf}$, which is in this case the electric field inside the sphere, can be expressed as

$$E_{nf} = -\nabla\varphi_{in} = \frac{3\varepsilon_d}{\varepsilon_m+2\varepsilon_d}E_0 \tag{1.3}$$

The polarizability $\alpha$ of the metal sphere is

$$\alpha = R^3\,\frac{\varepsilon_m-\varepsilon_d}{\varepsilon_m+2\varepsilon_d} = R^3\xi \tag{1.4}$$

where $\xi = \frac{\varepsilon_m-\varepsilon_d}{\varepsilon_m+2\varepsilon_d} = \frac{\alpha}{R^3}$. Then equation 1.3 can be written as

$$E_{nf} = |1-\xi|E_0 \tag{1.5}$$

The field intensity enhancement factor $F_{nf}$ is consequently given by

$$F_{nf} = \frac{|E_{nf}|^2}{|E_0|^2} = |1-\xi|^2 \tag{1.6}$$

Physically speaking, it is clear from equations 1.4 and 1.5 that the generated near-field amplitude is described by the permittivity of the dielectric medium, the dielectric function and the size of metallic particle. The near-field amplitude reaches its maximum when $\varepsilon_r \approx -2\varepsilon_d$, which is known as the resonance condition of the MNP.

Quasistatic approximation is suitable for modeling the field distribution on a small metal sphere.[18] However, it is limited because it ignores some realistic effects such as radiative and non-radiative damping of the oscillating field. Another significant effect is the dynamic depolarization that is caused by phase retardation. These effects are responsible for the loss of energy of the oscillating wave. It is the size of MNP that determines which effect is playing the dominant role.

### 1.1.2 Surface plasmon damping: finite-size effects

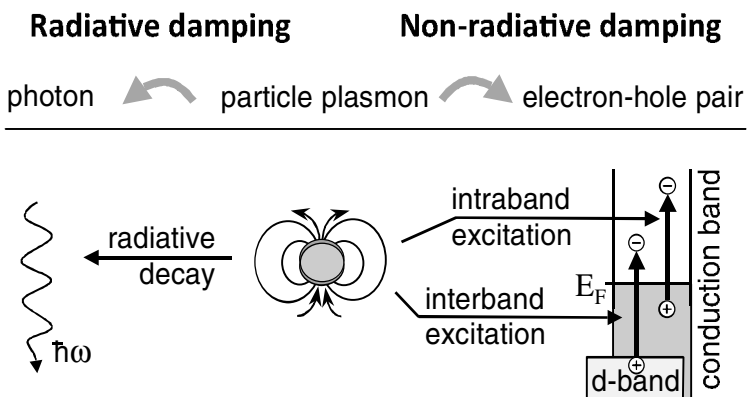


*Figure 1.1: Scheme representing the radiative and non-radiative damping of surface plasmons of noble metal nanoparticles.*[19]

As stated above, the surface plasmons of MNPs decay via mainly three mechanisms: radiative and non-radiative damping, and dynamic depolarization. The schematic description of the first two processes is shown in Figure1.1.[19] We will discuss them one by one in the following.

❖ **Radiative damping**

Radiative damping is the main decay mechanism for nanoparticles with large diameters.[20-21] It results from the transformation of particle plasmon into photons, i.e. light scattering. The radiative damping causes an additional radiation field $E_{rad}$,[22]

$$E_{rad} = \left(\frac{k^2}{R} + i\frac{2}{3}k^3\right)\mu' \tag{1.7}$$

Where $k = \frac{\omega}{c}$ is the wave vector of the incident light, $\mu'$ is the induced dipole moment on the nanoparticle:

$$\mu' = \alpha(E_0 + E_{rad}) = \alpha' E_0 \tag{1.8}$$

$\alpha'$ is the modified effective polarizability. We can deduce from equations 1.7 and 1.8 that

$$\frac{1}{\alpha'} = \frac{1}{\alpha} - \frac{k^2}{R} - i\frac{2}{3}k^3 \tag{1.9}$$

Consequently, the field intensity enhancement is written as

$$F'_{nf} = |1 - \xi'|^2 \tag{1.10}$$

where $\xi'$ is the modified coefficient

$$\xi' = \frac{\alpha'}{R^3} = \frac{\xi}{1 - k^2R^2\xi - i\frac{2}{3}k^3R^3\xi} \tag{1.11}$$

According to equation 1.11, for large particles (where $kR << 1$ is not satisfied) the influence of its size cannot be ignored. The modified coefficient increases as the radius of nanoparticle rises. As a consequence, according to equation 1.10, the near-field enhancement decreases.

❖ **Non-radiative damping**

The non-radiative damping of surface plasmons results from the plasmonic electron-hole pair formations via either intraband excitation in the conduction band or the interband excitation between other band and the conduction band[19] (see Figure 1.1). It constitutes the light absorption of MNPs and generally results in phonon excitation and heat generation. When the surface/volume ratio of a MNP is not negligible, i.e. small nanoparticles, non-radiative damping is dominant.[19,23]

As the particle diameter reduces to a value that is even smaller than the electron mean-free path in bulk metal, which is 20nm in the case of gold,[23] the electron scattering of the metal surface contributes considerably to the energy loss. The total non-radiative damping rate $\gamma$ is consequently a function of both interband damping rate $\gamma_{bulk}$ and the rate for electron scattering from the metal surface:[23-24]

$$\gamma = \gamma_{bulk} + \frac{A v_f}{R} \tag{1.12}$$

where $v_f$ is the Fermi velocity and $A$ is a proportionality factor that depends on the geometry. The non-radiative damping influences the near-field enhancement of a nanoparticle via the dielectric function of the metal given by the Drude model[11]

$$\varepsilon_m(\omega) = \varepsilon_\infty - \frac{\omega_p^2}{\omega^2 + i\omega\gamma} \tag{1.13}$$

$\varepsilon_\infty$ is the high-frequency limit of the dielectric constant, $\omega$ the frequency of incident light, and $\omega_p$ the plasma oscillation frequency of free electrons, i.e. bulk plasma frequency, written as

$$\omega_p = \sqrt{\frac{ne^2}{m_e \varepsilon_0}} \tag{1.14}$$

where $e$ is the electron charge, $n$ the free electron density, and $m_e$ the effective mass of free electrons.

❖ **Dynamic depolarization**

The excited oscillating field has always phase retardation with respect to the incident field. The expression of depolarization field generated by the polarized matter was given by Meier in 1983:[25]

$$\boldsymbol{E}_{dep} = -\frac{4\pi}{3}\left(1 - k^2R^2 - i\frac{2}{3}k^3R^3\right)\boldsymbol{P} \tag{1.15}$$

with the polarization $\boldsymbol{P}$, which is assumed to be homogeneous over the spherical volume, calculated by $4\pi\boldsymbol{P} = (\varepsilon_m - 1)(\boldsymbol{E}_0 + \boldsymbol{E}_{dep})$.[25] It can be finally deduced as

$$\boldsymbol{P} = \frac{3}{4\pi}\frac{\varepsilon_m - 1}{(\varepsilon_m + 2) - (\varepsilon_m - 1)k^2R^2 - i\frac{2}{3}(\varepsilon_m - 1)k^3R^3}\boldsymbol{E}_0 \tag{1.16}$$

In the case of small nanoparticles ($kR \ll 1$), the component $k^3R^3$ of the denominator is negligible. In the resonance condition, the real part of the denominator equals 0, resulting in

$$\boldsymbol{P}_{res} = \frac{3}{4\pi}\frac{\varepsilon_{m,res} - 1}{i\varepsilon_i(1 - k^2R^2)}\boldsymbol{E}_0 \tag{1.17}$$

As the radius of the MNP increases, the damping in the medium decreases.

For the nanoparticles with larger dimensions, the component of $k^3R^3$ is no longer negligible. The polarization under resonance condition is written as

$$\boldsymbol{P}_{res} = \frac{3}{4\pi}\frac{\varepsilon_{m,res}-1}{i\varepsilon_i(1-k^2R^2)-i\frac{2}{3}(\varepsilon_r-1)k^3R^3}\boldsymbol{E_0} \tag{1.18}$$

with the real part of the denominator equals to 0:

$$\varepsilon_r(1-k^2R^2)+2+k^2R^2+\tfrac{2}{3}\varepsilon_i k^3R^3 = 0 \tag{1.19}$$

As the radius of MNP increases, $\varepsilon_r$ has to go more in the negative to satisfy equation 1.19. This results in the redshift of plasmon resonance,[25-26] which indicates more energy loss. In other words, the damping increases.

According to the discussion above, the depolarization leads to a non-linear variation with the augmentation of the particle size. This has been confirmed via theoretical calculations performed by one of our collaborators, P. K. Jain. The three finite-size effects that have been introduced above will result all together in the size dependence of the near-field enhancement in the vicinity of MNPs. The maximum field enhancement is found with nanoparticles of 50nm size. The corresponding calculated data and experimental evidence will be discussed in details in Chapter 3.

### 1.1.3 Arbitrary shaped nanostructures

Metallic nanostructures with more complicated structure attract as well much attention for some peculiar effects, the lightning-rod effect[27] for example. Plenty of simulated and experimental results have been reported. Shapes most commonly used are nanorods,[28] cubes,[29-30] pyramids,[31-32] and shells.[33-34] Interactions between two nanoparticles of a dimer would produce an even higher field enhancement, especially within the gap. Coupling of the two nanoparticles increases as the gap size reduces. Many studies have been performed on dimers of disks and rods.[35-36] Greater enhancements from the coupling between two triangles[37] and cubes[38-39] are always expected for an additional field enhancement due to lightning-rod effect at the corners.

Gold nanoparticles of different shapes were used for this dissertation. The near-field distribution of colloidal nanocubes, spheres, electron-beam lithographic nanorods and dimers of nanodisks will be discussed in Chapters 3 and 4.

### 1.1.4 Experimental techniques for near-field characterization

Numerical techniques provide a clear way for us to understand the behaviors of nanoparticles, not limited by their shape, size, nature, or the environment. However, they are always treating the ideal case with many assumptions. For example, a sphere in simulations is usually one with perfect surface. In reality, however, such a

sphere does not exist. The calculated results for the maximum of field enhancement right on the surface of a nanoparticle are generally higher than that of the experimental results. Fine structures of nanoparticles are always producing a modification to their near-field distributions.

Therefore, experimental techniques are necessarily developed to analyze the near-field of a nanoparticle. The most commonly used one is scanning near-field optical microscope (SNOM) operating in either aperture or apertureless mode. The latter is to collect light scattered by the sample while it is coupling to a sharp SPM probe[40] or a single MNP antenna[41-42] scanning in its very vicinity. The aperture mode, by either detecting or exciting with an aperture probe at the end of an optical fiber, was more popular until recently.[43-44] SNOM breaks the diffraction-limit of far-field microscopy by collecting evanescent near-field signal of the metallic samples. The best resolution achieved is 20nm to 100nm.[42-45]

Electron-energy-loss spectroscopy (EELS) and Photoemission electron microscopy (PEEM) are two recent techniques with higher resolution and sensitivity by taking the advantage of electrons. EELS[46] analyses the variations of energy of electrons that interact with the sample, while PEEM[47] is based on the transformation of a photon into electrons. Although they are able to produce “electron-based optical images” with resolutions about 20nm or even better, the mapping of near-field distribution and its quantitative measurement still remain difficult. Furthermore, they require expensive technology involving vacuum electron acceleration and electronic optics.

Over the past decade, new techniques were developed in LNIO for near-field characterization with an ultra high resolution. One of them relies on the use of co-polymer (PMMA-DR1) that move under near-field illumination, resulting in an optically induced topography that can be characterized by AFM.[48] The other is to use free-radical photopolymerization that is triggered only by the near-field enhancement to imprint the spatial distribution of the surface plasmon.[49-51] Both techniques are able to offer images of near-field with high qualities but only the latter has shown to be able to provide an accurate quantitative measurement and reproduce the evanescent decay of the near-field.[50]

The approach of nanoscale photopolymerization is used in this dissertation for all the near-field characterizations. Detailed procedures and approach will be introduced in Chapter 2 and examples of different shapes of nanoparticles will be in Chapter 3 and Chapter 4. One additional advantage for using this technique is that the dye molecule, which is a component of the polymerizable formulation, can be trapped in the generated polymer nanostructure. This provides dye-doped metal/polymer hybrid structures, with which surface plasmon enhanced anisotropic nano-emitters can be developed in Chapter 4.

## 1.2 Fluorescence modified by MNP

Fluorescence is the relaxation of a fluorescent substance from the excited state (usually S1) to the ground state, accompanied with the emission of photons. The energy of the emitted photons is typically smaller than that of the photons absorbed by the molecules to get to the excited state. This results in the redshift of emission spectra with respect to the absorption of the molecule. For different fluorescent substances, the energies of emitted photons are different.

### 1.2.1 Fluorescence in free space

A fluorophore molecule in the ground state $|g\rangle$ that absorbs photons with certain energy can be excited to the excited state $|e\rangle$. The excitation rate is given by the Fermi's golden rule:[52]

$$\gamma_{ex} = \frac{2\pi}{\hbar}|\langle e|\boldsymbol{E}(\boldsymbol{r},\omega)\cdot\boldsymbol{p}|g\rangle|^2\rho_e \tag{1.20}$$

where $\boldsymbol{p}$ is the transition dipole moment, $\rho_e$ is the density of the excited states, $\boldsymbol{r}$ describes the location of the molecule, and $\boldsymbol{E}(\boldsymbol{r},\omega)$ is the local electric field. In free space, the local field equals to the incident electric field $\boldsymbol{E}_0(\boldsymbol{r},\omega)$. This leads to an excitation rate denoted by $\gamma_{ex}^0$. From equation 1.20, for a given molecule, the excitation rate depends on the electric field intensity as well as the orientation of molecular dipole with respect to the electric field.

The energy of the molecule in the excited state can be dissipated *via* two mechanisms: radiative decay and non-radiative decay. For a fluorescence substance, we usually expect its radiative decay rate to be as large as possible. Let us point out that the decay rate is related to a probability of event (Einstein coefficient). Quantum yield (or quantum efficiency) is a measure related to the ratio of radiative decay rate to the total decay rate. In free space, the quantum yield of a molecule (intrinsic quantum yield) is given by:

$$q = \frac{\gamma_{rad}^0}{\gamma_{tot}^0} = \frac{\gamma_{rad}^0}{\gamma_{rad}^0+\gamma_{nr}^0} \tag{1.21}$$

with $\gamma_{rad}^0$ the intrinsic radiative rate, $\gamma_{nr}^0$ the intrinsic non-radiative rate, and $\gamma_{tot}^0 = \gamma_{rad}^0 + \gamma_{nr}^0$ the total rate. Therefore, the emission rate $\gamma_{em}^0$ of the molecule is given by

$$\gamma_{em}^0 = \gamma_{ex}^0 q = \gamma_{ex}^0 \frac{\gamma_{rad}^0}{\gamma_{rad}^0+\gamma_{nr}^0} \tag{1.22}$$

Fluorescence lifetime is another important measure of the fluorophore. It is defined as the average time that molecules stay in the excited state before emitting photons to get to the ground state. Lifetime is related to the total decay rate:

$$\tau = \frac{1}{\gamma_{tot}} \tag{1.23}$$

Typically, the lifetime of organic fluorescent molecule is in the nanosecond scale and the excitation time scale is in picosecond. The emission intensity at time $t$ is expressed as

$$I = I_0 e^{-t/\tau} \tag{1.24}$$

where $I_0$ is the maximum fluorescence intensity during excitation. This is a transient phenomenon after a very short excitation.

This is the description of the entire excitation-emission process of a molecule in free space. The problem with most of the isolated fluorescent substances is that, the emission is usually quite weak due to low quantum yield, especially in the case of organic dye molecules. When placed near a metallic nanostructure, the fluorescence is significantly modified.

### 1.2.2 Fluorescence with MNP in presence

Numerous studies have been performed on how a MNP modifies the emission of a dye molecule. Briefly, in presence of a MNP, the emission of fluorophore can be either quenched or enhanced. Fluorescence intensity varies as a function of the excitation rate and the quantum efficiency. Many factors such as molecular dipole orientation, distance between the dye molecule and nanoparticle, embedding medium, wavelength of incident light, particle size, and collection efficiency of the optical setup can contribute to the modifications.

In 2002 Dulkeith and coworkers[54] published a drastic decrease of the lifetime of lissamine molecules placed at 1nm distance from the surface of gold nanospheres with different radius from 1nm to 30nm. All the molecule-nanoparticle configurations showed fluorescence quenching.

Halas and coworkers presented in 2009[55] a quantum yield of IR800 enhanced from 7% as isolated molecules to 86% in presence of a gold nanoshell, while 74% near a gold nanorod. However, It should be noticed that these huge enhancements were obtained with spacers of at least 5nm thick between *IR800* molecules and nanoparticles.

Novotny and coworkers reported in 2006[41] a study on the influence of separation distance between molecule and nanoparticle on fluorescence modification. Figure 1.2 presents both their experimental and theoretical results illustrating that the separation distance influences fluorescence intensity. By considering a single *nile blue* molecule-single gold nanosphere configuration, they detected a maximum fluorescence enhancement at 5nm away from a nanoparticle of 80nm in diameter. When the separation distance reduced below 5nm, the molecules were quenched.

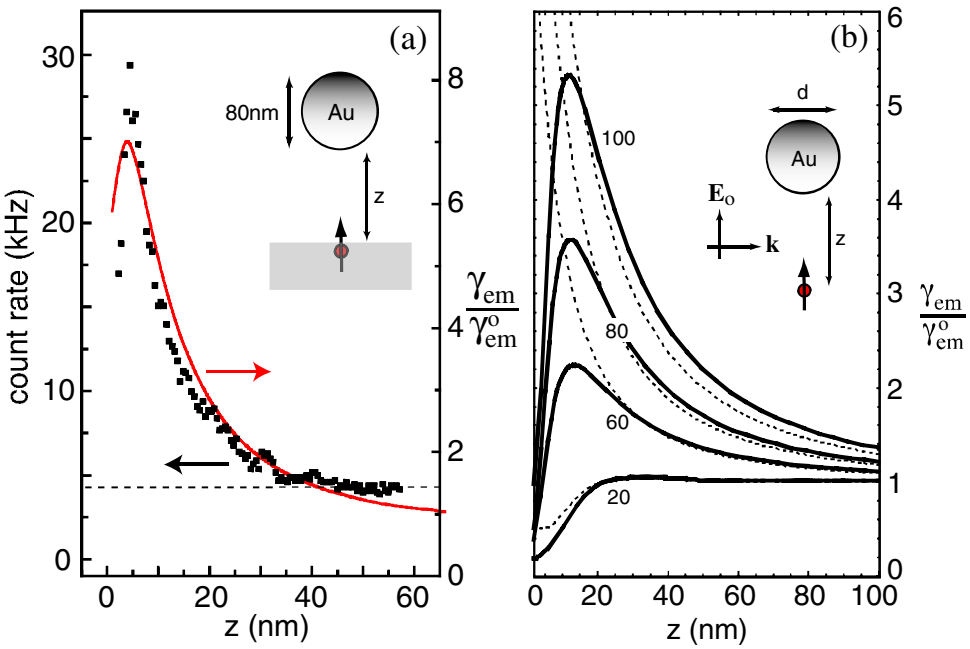


*Figure 1.2: Fluorescence of nile blue molecule modified by a gold nanosphere. (a) Experimentally measured free-space-normalized emission rate as a function of distance z between a molecule and the Au surface. The molecule is oriented along the polarization. Diameter of the gold nanoparticle is 80nm. (b) Theoretical calculated emission rates for different diameters of Au nanoparticle.*[41]

Hartling and coworkers did in 2007[56] a theoretical calculation on the emission based on different molecular dipole orientation, particle size, distance to the nanoparticle, and embedding medium. It turns out that the maximum fluorescence enhancement appears when the molecular dipole is perpendicular to the nanoparticle surface and parallel to the local electric field polarization. Enhancement occurs only when the molecular dipole has a component along the polarization of the local electric field, and has a large enough molecule/particle separation distance. All other particle-molecule configurations lead to nothing but quenching. His calculations also indicated that the emission could be modified by varying the surrounding medium or the excitation wavelength.

All the phenomena listed above were describing the fluorescence modification. However, what is its inner mechanism?

The essential factor to consider is the emission rate, which is modified as

$$\gamma_{em} = \gamma_{ex} Q \tag{1.25}$$

with $\gamma_{ex}$ the modified excitation rate and $Q$ the modified quantum yield. For a given dye molecule that is moved from free space to the vicinity of a MNP, the modification to excitation rate can be written as

$$\frac{\gamma_{ex}}{\gamma_{ex}^o} = \left| \frac{\boldsymbol{E}(\boldsymbol{r}) \cdot \hat{\boldsymbol{p}}}{\boldsymbol{E}_o(\boldsymbol{r}) \cdot \hat{\boldsymbol{p}}} \right|^2 \tag{1.26}$$

where $\hat{\boldsymbol{p}}$ is a unit vector pointing in the direction of the molecular dipole. Clearly, the modification to the excitation rate concerns both the local field intensity and the molecular dipole orientation with respect to the local electric field. The local electric field can be enhanced considerably by the surface plasmon supported on a MNP, which, as introduced in section 1.1, depends on the incident wavelength, embedding medium, the size of nanoparticle, etc. This leads to the surface plasmon enhanced excitation.

As to the dye molecule itself, the local electric field at its position depends on its distance from the surface of the nanoaparticle (defined by $\boldsymbol{r}$). In addition, the molecular dipole orientation contributes to $|\boldsymbol{E}(\boldsymbol{r})\cdot\hat{\boldsymbol{p}}|$. A minimum value of 0 will be obtained when the dipole is perpendicular to the polarization of local electric field. This would finally lead to quenching.

Now let us consider the quantum yield in equation 1.22. Other than the modified radiative decay rate of the molecule itself, one more effect has to be considered: the energy transfer from the molecule to the nanoparticle contributes to the excitation of surface plasmons. As a consequence, the modified quantum yield can be written as[59]

$$Q = \frac{\gamma_{rad}}{\gamma_{rad}+\gamma_{nr}} = \frac{\gamma_{rad}/\gamma_{rad}^{0}}{\gamma_{rad}/\gamma_{rad}^{0}+\gamma_{nr}^{ET}/\gamma_{rad}^{0}+(1-q)/q} \tag{1.27}$$

where $\gamma_{nr} = \gamma_{nr}^{0} + \gamma_{nr}^{ET}$ is the modified non-radiative decay rate of the molecule, $\gamma_{nr}^{ET}$ is the energy transfer rate from molecule to nanoparticle, and $\gamma_{rad}$ is the modified radiative rate. Experimentally, this variation is rather difficult to distinguish from that of the energy transfer.[60] Some theoretical calculations, however, are able to provide the profile of this modification.

The lifetime of the molecule will be modified as well by the MNPs:

$$\tau = \frac{1}{\gamma_{rad}+\gamma_{nr}^{0}+\gamma_{nr}^{ET}} \tag{1.28}$$

Lifetime measurement is able to provide a general description on the molecule-particle separation distance. The lifetime of molecules that are bond to the nanoparticle $\tau_B$ and that are far from the particle $\tau_F$ are different. The emission intensity follows consequently a double-exponential decay:[61]

$$I(t) = \alpha_F e^{-t/\tau_F} + \alpha_B e^{-t/\tau_B} \tag{1.29}$$

where $\alpha_F$ and $\alpha_B$ are the coefficients related to concentrations $[F]$ and $[B]$ by

$$\frac{\alpha_F}{\alpha_B} = \frac{\varepsilon_F}{\varepsilon_B}\frac{Q_B\tau_F}{Q_F\tau_B}\frac{[F]}{[B]} \tag{1.30}$$

$\varepsilon_F$ and $\varepsilon_B$ are the extinction coefficient at excitation wavelength, $Q_F$ and $Q_B$ are the quantum yield of the molecule in free space and that in presence of MNPs, respectively.

When the molecule is in the vicinity of MNPs, the non-radiative rate increases due to energy transfer. As the separation distance between molecules and nanoparticle decreases, the energy transfer augments and the radiative rate decreases correspondingly, which may lead to the quenching of the dye molecule.

### 1.2.3 Photo-bleaching

Photo-bleaching is a well-known shortcoming of fluorescence. Under strong resonance excitation, most of the dyes pass through an inter-system crossing procedure to transit from the singlet state to the triplet state.[58,62] It has been shown that molecules in the triplet state exhibit relatively high chemical reactivity, especially in the oxygen environment.[62-63] This effect causes the destruction of the molecule and therefore leads to the photo-bleaching of the dye that stops emitting.

Figure 1.3[58] is the simplified Jablonski energy diagram showing the main transition procedures of electrons, including excitation (abs), intra-molecular vibrational redistribution (IVR), fluorescence, inter-system crossing (ISC), phosphorescence and photo-bleaching.

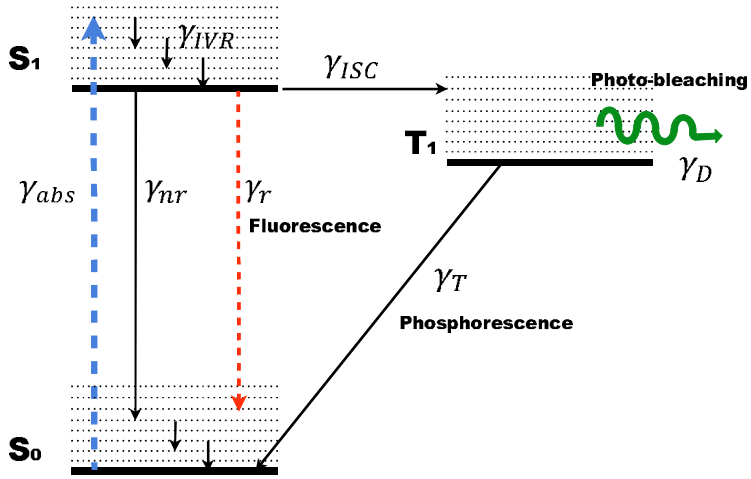


*Figure 1.3: Jablonski energy diagram of a two-level system with a triplet state.*[58] *Dashed lines refer to radiative transitions, while solid lines indicate non-radiative transitions. IVR: intra-molecular vibrational redistribution. ISC: inter-system crossing.*

The absorption rate of dye molecules is expressed as[58]

$$\gamma_{abs} = \sigma_{abs} \frac{S}{\hbar\omega} \tag{1.31}$$

where $\sigma_{abs}$ is the absorption cross section of the dye molecule, $\hbar\omega$ is the energy of photons of incident light, and $S$ is the incident power density in free space. It is proportional to the intensity of the incident electric field.

The photo-bleaching process can be divided into two steps: i) excitation of molecules to the triplet state and ii) destruction of molecules due to chemical reactions. Therefore, the probability of photo-bleaching $\phi_{bl}$ is written as[58]

$$\phi_{bl} = p_{ISC} p_D = \frac{\gamma_{ISC}}{\gamma_{tot}} \frac{\gamma_D}{\gamma_T} \tag{1.32}$$

where $p_{ISC}$ and $p_D$ are the probabilities of inter-system crossing and that of being destructed, respectively, for a molecule. $\gamma_{ISC}$ is the transition rate from singlet state to triplet state. $\gamma_D$ is the destruction rate, $\gamma_T$ is the decay rate from triplet state to ground state (i.e. phosphorescence). Consequently, the expression of photo-bleaching rate[58] can be deduced from equations 1.31 and 1.32:

$$\gamma_{bl} = \phi_{bl} \gamma_{abs} = \phi_{bl} \sigma_{abs} \frac{S}{\hbar\omega} \tag{1.33}$$

According to equation 1.33, the bleaching rate is proportional to the incident power. In the presence of a MNP, $S$ is enhanced by the near-field. Thus, the bleaching rate of molecule will be multiplied by a factor as well.

In this dissertation, as will be discussed in chapter 4, we need to compare the fluorescence intensities obtained by adopting two different incident polarizations on our anisotropic dye-doped-polymer/MNP hybrid configuration. The different fluorescence intensities come from dye molecules in the tiny polymer lobes. Thus, it would make the measurement and extremely difficult if the photo-bleaching rate of the molecule is too high. Besides, photo-bleaching could be reduced from its generating mechanism. That means to protect the dye molecules from oxygen. Either using a droplet of immersion oil or keeping the sample in a vacuum chamber would lower the photo-bleaching rate. Finally, low temperature is able to augment the quantum yield of the EY molecule from 2 to over 100 times depending on the embedding medium.[61,64]

The use of quantum dots might be a reasonable solution for their relatively high optical stability and well-known much higher quantum yield. However in our study, at least until now, quantum dots suffers probably from two points. The first one concerns their size. The dimensions of quantum dots are generally about 2 to 8nm, which is quite large for our hybrid system. Further, they form aggregates in a micrometer scale in our polymerizable solution. These two limits have to be overcome before adopting quantum dots in our hybrid structure.

## 1.3 Surface Enhanced Raman Spectroscopy

Although solving the problem of photo-bleaching is still debatable, it is a fact that SERS is able to overcome the problem of quenching of molecules from its generation mechanism. As a result, we will turn our attention to the Raman scattering in Chapter 4, Section 4.2.

### 1.3.1 Raman Scattering

Unlike Rayleigh scattering, Raman scattering is an inelastic scattering leading to energy transfer between incident photons and molecules. This energy transfer results in the electron transition between vibrational states as well as the emission of a photon whose energy differs from the incident photon. It is an instantaneous effect without the direct absorption of photons and with only radiative procedures involved. In other words it involves the "virtual" energy levels (Figure 1.4) that corresponds to the intermediate quantum state of the molecule related to the "absorption" and subsequent emission of photons.

The energy of the scattered photon $E_s$ can be either lower (Stokes process) or higher (anti-Stokes process) than that of the incident photon $E_i$, corresponding to the transition from ground state to the excited vibrational state or the inverse. As to the latter, the molecule has to be on the excited vibrational state before the entire process. Raman shift is the essential measure in this technique, written as

$$\Delta\bar{\nu}_R = \frac{1}{\lambda_i} - \frac{1}{\lambda_s} \tag{1.34}$$

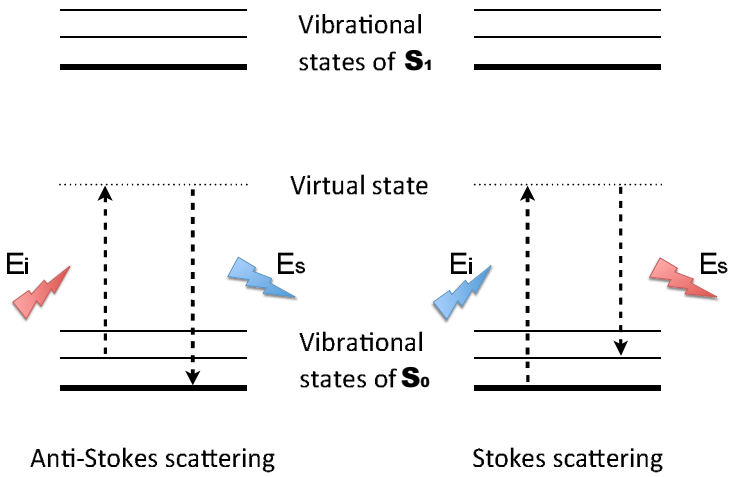


*Figure 1.4: Energy diagram of two cases in Raman scattering: the anti-Stokes scattering and Stokes scattering.*

where $\lambda_i$ and $\lambda_s$ are the wavelengths of incident light and scattered light, respectively. Equation 1.34 can be easily deduced from the expression of electron energy $E_{i,s} = hc/\lambda_{i,s}$. Evidently, Raman shift indicates the light energy that is lost or gained during the interaction with the molecule. It is the energy that this molecule takes or releases for the electron transition between its vibrational states. And this corresponds to a unique chemical bond, like a fingerprint, of the target molecule.

Since no direct absorption is involved, Raman spectroscopy can be collected principally from any molecule and with any incident wavelength. Besides, the Raman peaks, which are highly correlated with the chemical components, allow an extraordinarily high specificity. Therefore, Raman spectroscopy should be an

extremely widespread technique in analyzing and sensing. However, this was not the case due to low signal yield until the 1970s when SERS was discovered.

### 1.3.2 SERS

In the very beginning of its detection, the enormous enhancement of Raman scattering near silver electrode was thought due to large number of target molecules (pyridines).[65] Three years later, in 1977, researchers found that surface enhancement effect was playing the crucial role.[66-67] Since then, much attention has been gathered, on both fundamental studies and the applications of SERS.

SERS is not limited to metal surface. It has been applied also on many other types of substrate such as metallic nanowires,[68-69] periodic structures,[70-71] and all shapes of nanoparticles like spheres,[72] rods,[73-74] cubes,[75] triangles.[76] Many effects based on surface plasmons such as hotspots generation and plasmon resonance were adopted to increase the enhancement. Placing target molecules in the gap of a dimer is a good example.[77-79] One notable instrumentation improvement is the tip-enhanced Raman spectroscopy (TERS),[80-81] which profits from the controllable hotspot created at the end of an SPM probe close to the surface. Studies indicate that by matching the excitation wavelength of SERS with the resonance of the target molecule, one can obtain an enhancement factor that is even higher.[82-83] This technique is known as surface enhanced resonance Raman spectroscopy (SERRS).

One of the most impressive recent activities in SERS is the single molecule detection. It was first achieved by Kneipp[84] and Nie[85] by using an extremely low concentration of target molecules. Single molecule SERS makes possible the precisely controlled studies with many different parameters, which can hardly be achieved by bulk measurements. Examples of parameters include incident wavelength, incident polarization, particle size, and molecular orientation.[85]

The magnitude of enhancement of Raman scattering can easily reach $10^6$-$10^9$,[86-87] sometimes as high as $10^{14}$-$10^{15}$.[85] In this dissertation we will focus on the MNP based SERS. It is generally believed that this huge enhancement arises from two mechanisms: the electromagnetic enhancement and the chemical enhancement. The former is accepted as the key factor.[88-90] While the latter, as many studies reported, contributes roughly to 2 orders of magnitudes on the enhancement factor.[89]

❖ **Electromagnetic enhancement**

There are mainly two effects involved in the electromagnetic enhancement: the local field enhancement and the Raman field enhancement. The local field enhancement has been discussed in section 1.1 and the field intensity enhancement factor $F_{nf}$ in equation 1.6. It is related to the surface plasmons of MNPs and has nothing to do with the intrinsic properties of molecules.

As to the molecule, the power of Raman scattering is modified as well due to the breakdown of the molecular symmetry when a MNP is nearby.[91] When

considering a single molecule, the molecular dipole orientation with respect to the local field is playing a role on whether the generated Raman field (i.e. scattered field) is quenched or enhanced.[58] The modification of the local Raman field intensity is given by[92-93]

$$M_{loc}(\boldsymbol{r},\omega_R) = \frac{|\boldsymbol{E}_{loc}(\boldsymbol{r},\omega_R)|^2}{|\boldsymbol{E}_0(\omega)|^2} \tag{1.35}$$

where $E_{loc}(\omega_R)$ represents the local Raman field, $\boldsymbol{r}$ describes the location of the molecule, and $\omega_R$ is the scattered frequency. In most of the cases the Raman shift is small enough to make the approximation $\omega_R \approx \omega$ reasonable. Therefore, the single molecule enhancement factor $F_{SM}$ can be approximated to[93]

$$F_{SM} \approx M_{loc}(\boldsymbol{r},\omega)\cdot F_{nf}(\boldsymbol{r},\omega) \approx \frac{|\boldsymbol{E}_{loc}(\boldsymbol{r},\omega)|^4}{|\boldsymbol{E}_0(\omega)|^4} \tag{1.36}$$

This is known as the $|E|^4$-approximation. Now consider the configuration of a nanosphere with radius $R$ and a molecule at distance $d$ from the sphere surface. From equation 1.2, the local electric field outside the nanosphere can be deduced as

$$E_{loc} = -\nabla\varphi_{out} = E_0 - \frac{2\alpha E_0}{(R+d)^3} \tag{1.37}$$

Clearly from equations 1.36 and 1.37, the local electric field decreases as $1/(R+d)^3$ and therefore the SERS enhancement factor decreases as $1/(R+d)^{12}$. In contrast to the fluorescence quenching at short distance from the nanoparticle, the maximum SERS enhancement appears right at the particle surface, where $d = 0$.

One can easily deduce from equations 1.22, 1.25 and 1.26 that, the fluorescence enhancement factor is a function of the square of the intensity enhancement of electric field amplitude. Suppose that the fluorescence enhancement of a dye molecule is $10^3$ in the vicinity of a MNP. Then for the same nanoparticle-molecule configuration, SERS enhancement factor can reach $10^6$. This order of magnitude can be even higher because of no quenching effect arisen from small molecule-particle distance. In this case, the fluorescence signal appears to be much lower than the SERS signal.

❖ **Chemical enhancement**

With a small metal-molecule separation distance (within 2nm), the chemical effect may cause an enhancement of 10-$10^3$ to the Raman scattering,[89,90,94] which is not much in comparison with the electromagnetic enhancement, but constitutes a non negligible contribution additional to $F_{SM}$.

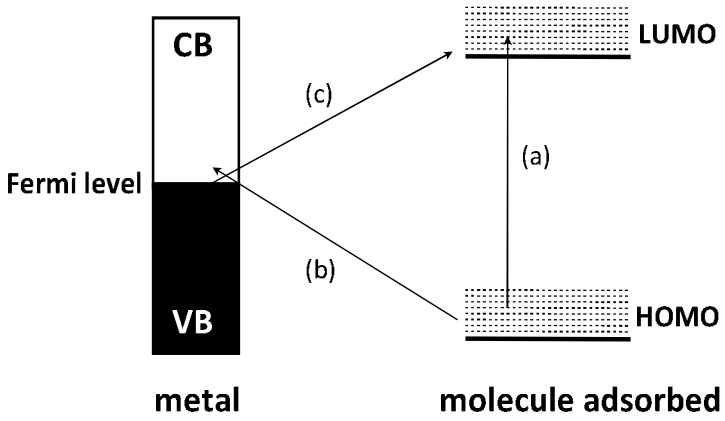


*Figure 1.5: Scheme for the charge transfer mechanism. Path (a) is the transition happening when it is in resonance with the laser, while path (b) + (c) is the transition that profits from the metal.*[58]

The most commonly accepted explanation for chemical enhancement is based on the charge transfer[95-96] (see figure 1.5). Electrons at the highest occupied molecular orbital (HOMO) can transit first to the conducting band of metal and then to the lowest unoccupied molecular orbital (LUMO). In this way, the resonance of molecule at half of the energy gap between HOMO and LUMO can make the charge transfer happen. A higher chemical enhancement comes thus from a larger energy gap.[58]

Although almost all molecules can be used as Raman labels, dye molecules are proved to work more efficiently for their higher SERS signals. In chapter 4 of this dissertation, gold dimers with different gap sizes will be used for the hotspot within the gap. We used methylene blue molecules for mainly three reasons. First, it is a photosensitizer that can form the radical to trigger the photopolymerization leading to hybrid metal/polymer nano-object. Second, MB molecules are known to easily adsorb onto Au[97] and therefore emit less fluorescent signal as SERS background. Third, the absorption of MB molecules, which is in red, is very close to the LSPR of the dimer. By applying a red incident laser, we can take advantage of the plasmon field in getting a larger enhancement to the Raman signal.

## 1.4 Different approaches to hybridization

Considering so many benefits that the MNP may produce, the main issue that arises now is how to combine it with the quantum emitter. Many previous studies are performed by simply coating a homogeneous layer of molecules on the entire sample[5,98-99] and possibly with a spacer layer of certain thickness if necessary.[100] This is a convenient method with good results obtained for both fluorescence and SERS studies. Nevertheless, molecules far from the nanoparticles cause problems. Although they are not enhanced by the plasmon field, yet the signal from a large number of molecules on the background cannot be ignored. Furthermore, for some specific applications such as nano-emitters, dye molecules are usually not expected

to be everywhere. Consequently, hybridization, which allows creating the MNP/molecule configuration, has become a popular tool in these studies. In particular, single hybrid nano-objects can ultimately be addressed.

One of the most commonly adopted techniques is to use DNA chains as highly specified linkers to attach the dye molecules onto MNPs. It provides an extremely accurate and controllable hybrid configuration, and thus has contributed much in the studies of fluorescence quenching and enhancement regime as a spacer.[101-102] Besides, other biomolecules such as human serum albumin[33,55] and antibodies[103] are utilized as both linkers and spacers in the hybrid system. The biological procedures, however, have shortcomings like high requirements for the surroundings, complex biochemical treatments, and relatively high costs. Besides, their contributions to the signal, especially in SERS studies when these biomolecules can serve as SERS labels,[104-105] might needlessly cause some troubles.

Noginov et al. reported in 2009[106] an Au/silica/dye core-shell nanoparticle utilized as a nanolaser. Dye-molecule embedded silica shell was coated on a single metallic nanostructure. This structure was claimed to cause less surface plasmon loss than a regular spacer. Lei Zhao and coworkers studied on FRET process between two molecules based on the configuration of Au/Ag nanocrystal coated with dye-doped silica shell.[60]

Other than metal/dye molecule configuration, hybrid plasmonic nanostructure include metal/dielectric medium combination as well. Studies focused mostly on the core (metal)-shell (dielectric) structure,[107-108] whose LSPR was tunable in a very large scale. Hui Wang and collaborators fabricated an Au/$Fe_2O_3$ core-shell nanorice that combined the advantages of both nanorod and nanoshell.[109] This structure was able to provide larger near-field enhancement and higher LSPR sensitivity in comparison with other metal/dielectric hybrids.

Despite all the advantages that each configuration might possess, in the domain of nano-emitters, the isotropic configurations of these hybrid nanostructures prevent the selection of specific emission modes with the incident light. We aim at developing a new generation of light-emitting hybrid nanostructure whose emission properties (decay, intensity, color, emission pattern, etc.) can be controlled via the illumination conditions (polarization state, wave vector, etc.). In this dissertation, the polarization dependence of fluorescence intensity and SERS intensities has been observed. This type of light-emitting hybrid nanostructure is superior in the following aspects:

- The polymer structure imprints the surface plasmon of the MNP. Thus, the fabrication of the hybrid system by itself is a near-field characterization procedure. This technique has an ultra high resolution of sub 5nm, in comparison with 20-100nm for SNOM.
- The geometry of metal/polymer hybrid is highly variable. An anisotropic hybrid structure can be easily fabricated. The shape and size of the polymer structure

are controllable just by adjusting the incident polarization and wavelength. Besides, this technique works with any structure that supports surface plasmons.

- The hybrid structure serves as the anisotropic nano-emitter. Dye molecules in the chemical composition of polymerizable formulation will be trapped inside the polymer nanostructure during the photochemical process. This provides a natural label for the fluorescence or SERS measurements.

The fabrication of this metal/polymer hybrid system and other related details will be introduced in Chapter 2. Further, Chapter 3 and 4 involve detailed discussions on how our metal/polymer hybrid nanostructures work as near-field imaging tools and as anisotropic nano-emitters.

## 1.5 Summary

In this chapter, we have had theoretical discussions on the behaviors of surface plasmons of MNPs including, in particular, the radiative damping, non-ratiative damping, and depolarization. As the particle size increases, the radiative decay plays a more and more important role on the energy loss while non-radiative becomes less and less important. The phase retardation, however, is a tricky factor since it helps in increasing the enhancement for small sized nanoparticles while in decreasing it in the case of larger sizes. These factors lead to a relatively complex behavior of the field enhancement that will be studied in Chapter 3 (Section 3.1).

Based on the plasmon enhancement, the fluorescence and Raman scattering of a dipolar molecule is modified by a MNP close by. In the case of fluorescence, the emission intensity is influenced by the modifications to excitation rate and quantum yield of the molecule. Those factors depend on local electric field, molecular orientation and separation distance between molecule and nanoparticle. In comparison, small molecule-particle separation distance does not raise any problem in SERS. The maximum Raman intensity can be obtained when the molecule is right on the MNP.

Hybrid plasmonics offers a good opportunity for researchers to better understand the energy transfer between the molecule and the MNP. Besides, it has many different applications. Until now, many different isotropic hybrid plasmonic configurations have been studied but the anisotropic hybrid plasmonics remains rarely reported. In the following chapters, the fabrication and application of our anisotropic metal/polymer hybrid systems will be discussed. Both the passive hybrid plasmonic nanostructures (applied to near-field imprinting) and the active hybrid plasmonic nano-objects (used as anisotropic nano-emitters) will be studied.

# CHAPTER 2

# Experimental Procedures

The classic procedures for a study on the metal/polymer hybrid plasmonic structure is to characterize the bare initial nanoparticles, run the hybridization process, and characterize the hybridized sample. Characterizations on the same sample for both steps (before and after the hybridization) allow us to highlight the polymer structure that has been created during the process, which imprints the near-field of the MNP.

The obtained structure is in priori a passive hybrid plasmonic structure. By saying “active hybrid plasmonics” in this work, we mean that there is a yield of photons, due to either emission or scattering, from the hybrid nanostructure. These features depend on both the properties of the hybrid structure and the incident light. They can be activated or modified under different conditions.

This chapter presents in detail all the experimental procedures that are involved, starting with our main approach in both optical and photochemical standpoints. It is then followed by the optical configuration for hybridization, preparation of samples of nanoparticles, fabrication and characterization of both passive and active hybrid plasmonic nanostructures.

## 2.1 Main approach to fabricate the metal/polymer hybrid nanostructure

Briefly, the fabrication of the anisotropic hybrid system is based on the photopolymerization that is triggered only by the plasmon-enhanced local optical electromagnetic field in the vicinity of MNPs. During the process, a homemade photopolymerizable solution is required. Details of the chemical components and related reactions will be presented in section 2.2. There is a threshold dose for polymerization. In other words, polymer is created only when the local dose of the optical field is above the threshold.

The process is described in Figure 2.1. The MNP (Figure 2.1 (a)) on a glass substrate is coated with a drop of the photopolymerizable solution (Figure 2.1 (b)). In order to obtain an anisotropic hybrid structure, a linearly polarized incident laser is applied to excite the dipolar (or an higher order) mode surface plasmon of MNP (Figure 2.1 (c)). It should be stressed that the dose of the incident light must be below the threshold. Otherwise the polymerization will be driven by the far field to generate a polymer layer that covers the entire exposed region. The excited surface

plasmon causes a great enhancement on the local optical electromagnetic field. As a consequence, the dose of the local field exceeds the threshold and triggers the photopolymerization.

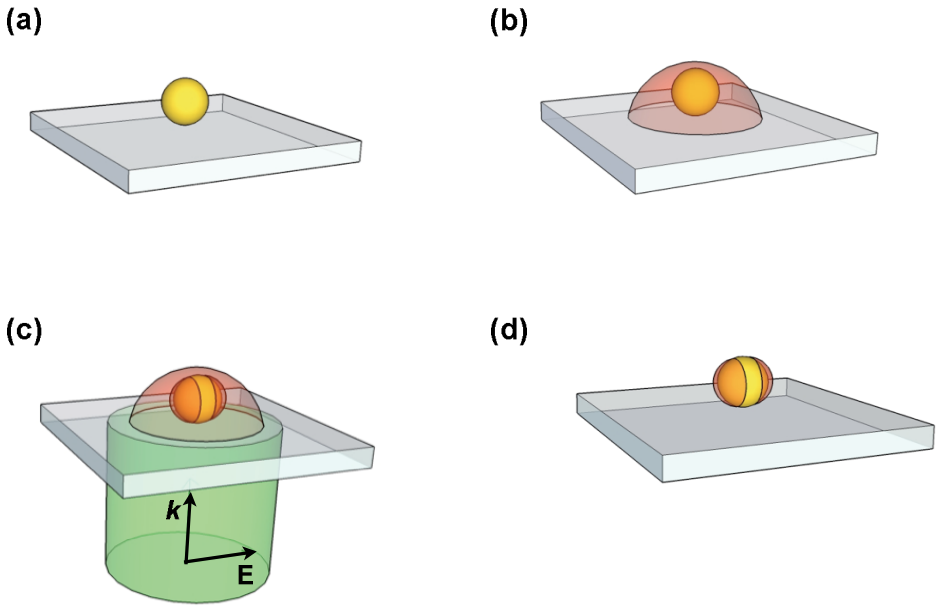


*Figure 2.1: Scheme showing the main metal/polymer hybridization procedures. (a) MNP on a glass substrate; (b) a drop of photopolymerizable solution is deposited on the sample; (c) irradiation with linearly polarized laser; and (d) the metal/polymer hybrid system obtained after rinsing.*

After polymerization, the sample is rinsed to remove all the non-polymerized part of the solution (Figure 2.1 (d)). Generally, ethanol and isopropanol (IPA) are used as the solvent for rinsing. The sample is kept immersed in ethanol for 10 minutes, then in isopropanol for 5 minutes. Last, it is dried very gently with air.

When collecting the fluorescence signal from the obtained hybrid system, we noticed a non-negligible fluorescence from the background (see Chapter 4 for details), i.e. on the same substrate where no nanoparticle exists. This indicates that the dye molecules on the substrate are not perfectly cleaned by the rinsing process. To get the sample better cleaned, some other solvents like acetone and chloroform were tried. The quality of the sample surface has been improved, but still not perfect. The rinsing procedure remains to be a challenge for further studies on the active hybrid plasmonic nanostructures. This point will be highlighted in Chapter 4.

## 2.2 Chemical components and photochemical reactions

Photopolymerization is the light-driven process that consists in making react monomer molecules together to form three-dimensional networks or polymer chains.

Most of the reactions rely on radicals to initiate the polymerization procedure. Usually, the polymerization extends to a long distance because radicals are distributed everywhere. In our approach, the homemade photopolymerizable solution does not contain radicals because it is able to create radicals when absorbing visible photons. The photochemical reactions are restricted in a localized area. It leads to a relatively controllable polymerization in nanometer scale by monitoring the local optical field of the nanoparticle.

### 2.2.1 Chemical components

The free-radical photopolymerizable solution was developed over 2 decades by our collaborators from Département de Photochimie Générale in Mulhouse.[110-112] Three components are necessary for the basic formulation: a multifunctional acrylate monomer, a co-synergist amine and a photosensitizer. Previous studies[51,111] on the photopolymer demonstrated the optimized formulation is 96%wt pentaerythritol triacrylate (PETIA) as the monomer, 4%wt methyldiethanolamine (MDEA) the amine, and 0.5%wt Eosin Y (EY) the photosensitizer. In Figure 2.2, panels (a) to (c) show the molecular formulas of the chemical components of the formulation. The solution is prepared by mixing the components with a stirring magnet. Typically the solution is stable for 3-4 weeks ever after it has been prepared.

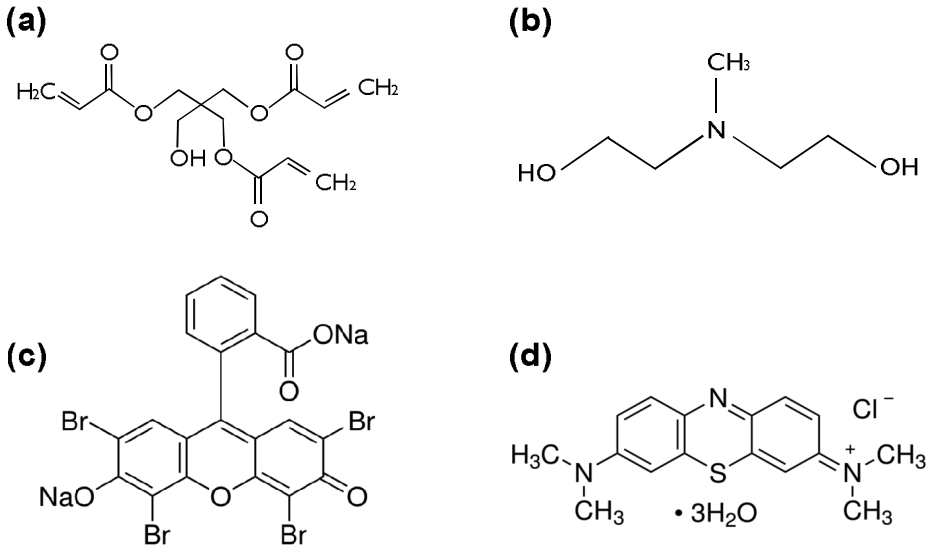


*Figure 2.2: Molecular formulae of the chemical components of the photopolymerizable formulation: (a) PETIA, (b) MDEA, (C) EY, and (d) Methylene blue (MB). Note that either EY or MB was used (not both of them at the same time).*

EY can be replaced by other organic dyes such as Rhodamine, Fluorescein, and Methylene Blue (MB) according to different requirements on the absorption of the polymerizable solution. This dissertation concerns EY and MB (Figure 2.2 d) to match the LSPR of different samples.

The absorption spectra of EY (Figure 2.3 a) and MB (Figure 2.3 b) solved in PETIA were collected with a *CARY 100* UV-visible spectrometer. As illustrated by the figure, the absorption band of EY molecule is in the [450 - 550] nm range, with a maximum absorption at 530nm. It is in agreement with the LSPRs of colloidal gold nanospheres that we used. In comparison, MB is more sensitive in red. It absorbs from 550nm to 700nm, with a 660nm maximum. Therefore MB-based formulation is suitable for LSPR in the red. Dimers of gold nanodisks with diameter of about 100nm are good examples.

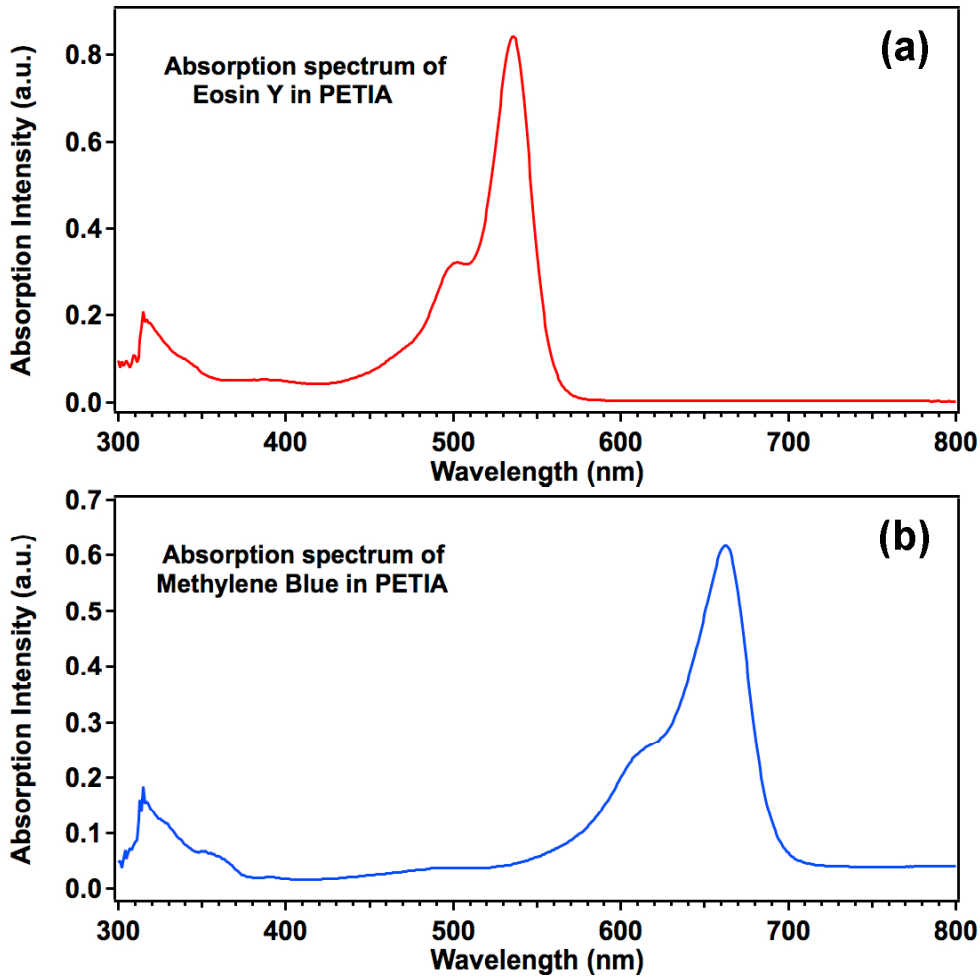


*Figure 2.3: Absorption spectrum of (a) EY and (b) MB in PETIA.*

### 2.2.2 The photochemical reaction

Figure 2.4 shows the reactions during the photopolymerization procedure. The dye molecule is excited from ground state ($\mathbf{S_0}$) to the singlet state ($\mathbf{S_1}$) after the absorption of photons. It then transits *via* intersystem crossing to the triplet state ($\mathbf{T_1}$). The co-synergist amine contributes, in the photoreduction of the triplet state dye, to produce radicals that initiate the polymerization procedure. The reaction ends up with a 3D network. Other than the main pathway, some side reactions, such as the deactivation of the dye molecule in triplet state and the peroxidation of the radical by

oxygen, are inevitable during the procedure. These reactions lead to an inhibition period, which results in the existence of the threshold dose.

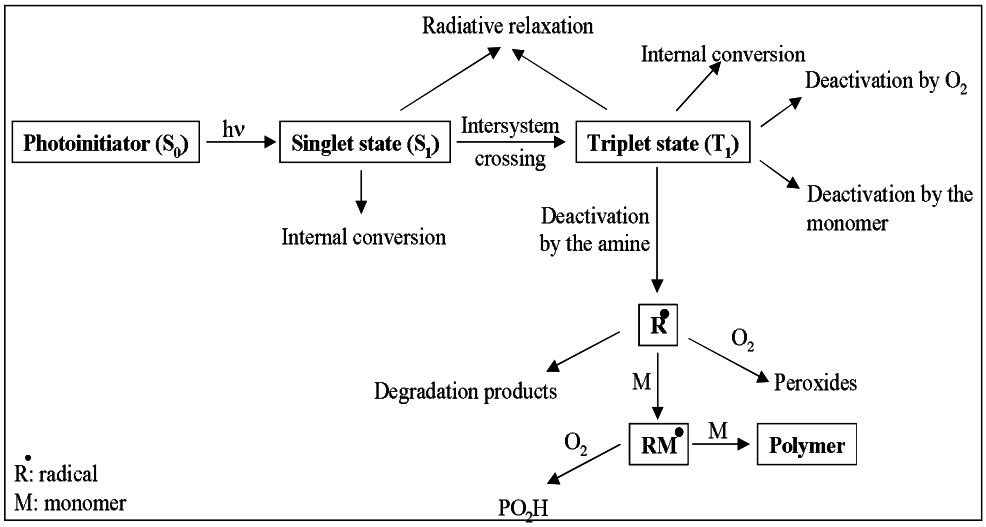


*Figure 2.4: Reaction diagram of the photopolymerization.*[112]

Accordingly, before going through the hybridization procedures on the sample, we have to determine the threshold of the solution. This process involves only photopolymerization on the glass substrate with a normal incident laser. By adjusting the incident power and the exposure time, we are able to find a threshold dose, beyond which a polymer layer is fabricated, while below which no polymer can be obtained. Even for the same formulation, the threshold varies with such factors as incident wavelength and diffusion of oxygen. Only the wavelength is controllable in our experiment.

The wavelength of the incident laser is necessarily chosen to be in the absorption band of the dye molecule. The exact value to use depends on the LSPR of the MNPs as well. In most cases, especially when the fluorescence or Raman response is expected from the nanostructures, the incident wavelength is selected to match the LSPR in order to create polymer structures that are as large as possible. This would allow more dye molecules to be trapped inside the polymer.

The diffusion of oxygen, as figure 2.4 illustrates, is largely responsible for the inhibiting reactions. In experiment, the polymerization threshold augments as time goes by. This is principally due to the increasing amount of oxygen that results in a 3-4 weeks' "lifetime" of the photopolymerizable solution. Therefore, it is necessary to check the threshold dose under the exact wavelength each time right before performing the hybridization on nanoparticles.

Once the threshold dose of the photopolymerizable solution is determined, we need to choose an incident dose. Theoretically talking, it can be any value that is below the threshold. Practically, we used a dose between 5% and 75% of the threshold to get a polymer structure, while avoiding far-field-triggered polymerization.

Either the exposure time or the power can be varied to adjust the incident dose. Previous studies done by C. Deeb et al.[51] (Figure 2.5) indicate that even with the same value of incident dose, the size of the polymer nanostructure can be different. It turns out that the obtained polymer size is larger if the power is adjusted while the exposure time is kept constant. Consequently, in our experiments, the power is adjusted for a proper incident dose.

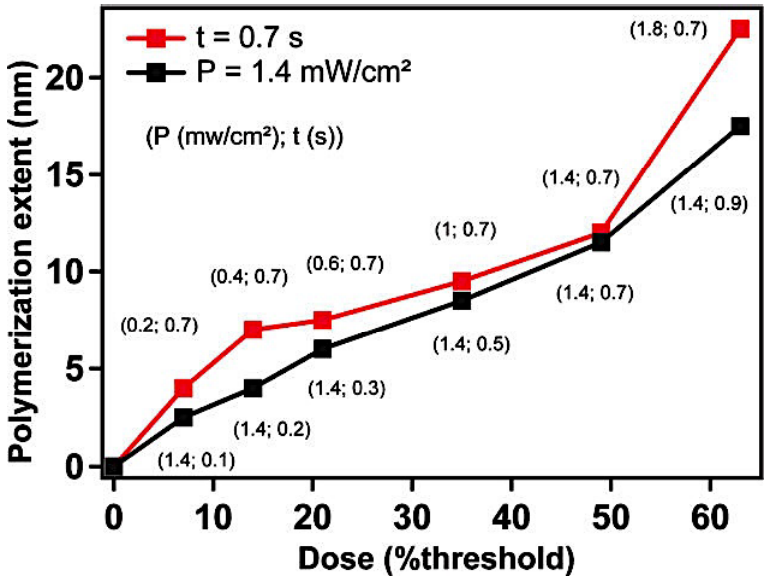


*Figure 2.5: Polymer thickness near Ag nanoparticles as a function of threshold-normalized-incident dose with both power and time varied. Polymerizable solution with EY as the sensitizer under a λ = 514nm incident laser.*[51]

## 2.3 Optical configuration

The optical path of the incident beam used for photopolymerization is sketched in Figure 2.6. The light comes from an Ar:Kr laser source and passes through a spatial filter made up of two lenses and a pinhole in between. The pinhole is placed at the focal plane (Fourier space) of the first lens. It blocks the multiple-order peaks of the laser beam to let pass only the central maximum with a clean Gaussian profile. The light is then re-collimated by the second lens. Afterwards, it is reflected by a mirror onto the sample. Above the sample stage is installed a power-meter to read the incident power.

The lens-pinhole-lens spatial filter in this configuration can be replaced by a single-mode optical fiber, in which incident beam is launched. It can behave as a spatial filter to output a pure Gaussian beam. Besides, according to some specific requirements, the laser can be coupled into an inversed microscope to fabricate some standing polymer tips, or to induce the far-field excitation to hybridize the nanoparticles distributed in a very small region.

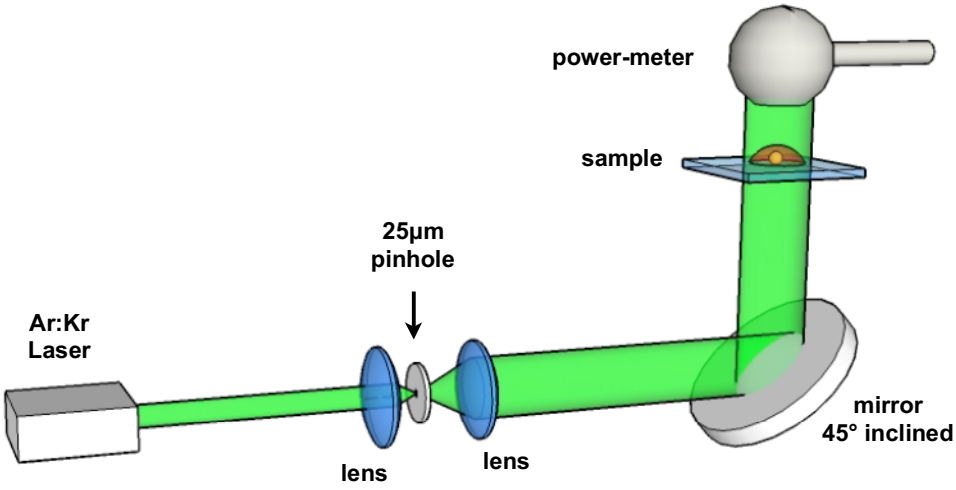


*Figure 2.6: Scheme of the optical configuration for photopolymerization.*

## 2.4 Sample preparation

Basically, two types of nanoparticles are involved in Chapter 3 and 4: the electron-beam-lithographic nanoparticles made by a top-down approach (EBL + lift off) and the chemically synthesized colloids. By using top-down approach, it is possible to fabricate nanoparticles with controlled shapes and of different materials; while chemical synthesis allows for particles with highly pure crystal structures. Of course, preparation procedures of the sample are different for these two types of MNPs.

### *2.4.1 Top-down approach*

Electron beam lithography (EBL) is a widespread technique for manufacturing the samples of nanoparticles. The main idea of this method is to use polymethyl methacrylate (PMMA) as a mask, on which the scanning electron beam writes the designed patterns. PMMA chains breakdown in the irradiated regions and are easily removed to leave holes on the PMMA layer, which are subsequently filled by evaporated metals. After removing the PMMA mask, only metals in the holes are left on the substrate, which imprints the designed patterns.

EBL samples used in this dissertation were fabricated on two different types of substrates: normal glass and indium-tin-oxide (ITO) coated glass. The corresponding EBL procedures on these two kinds of substrates differ slightly from each other (Figure 2.7).

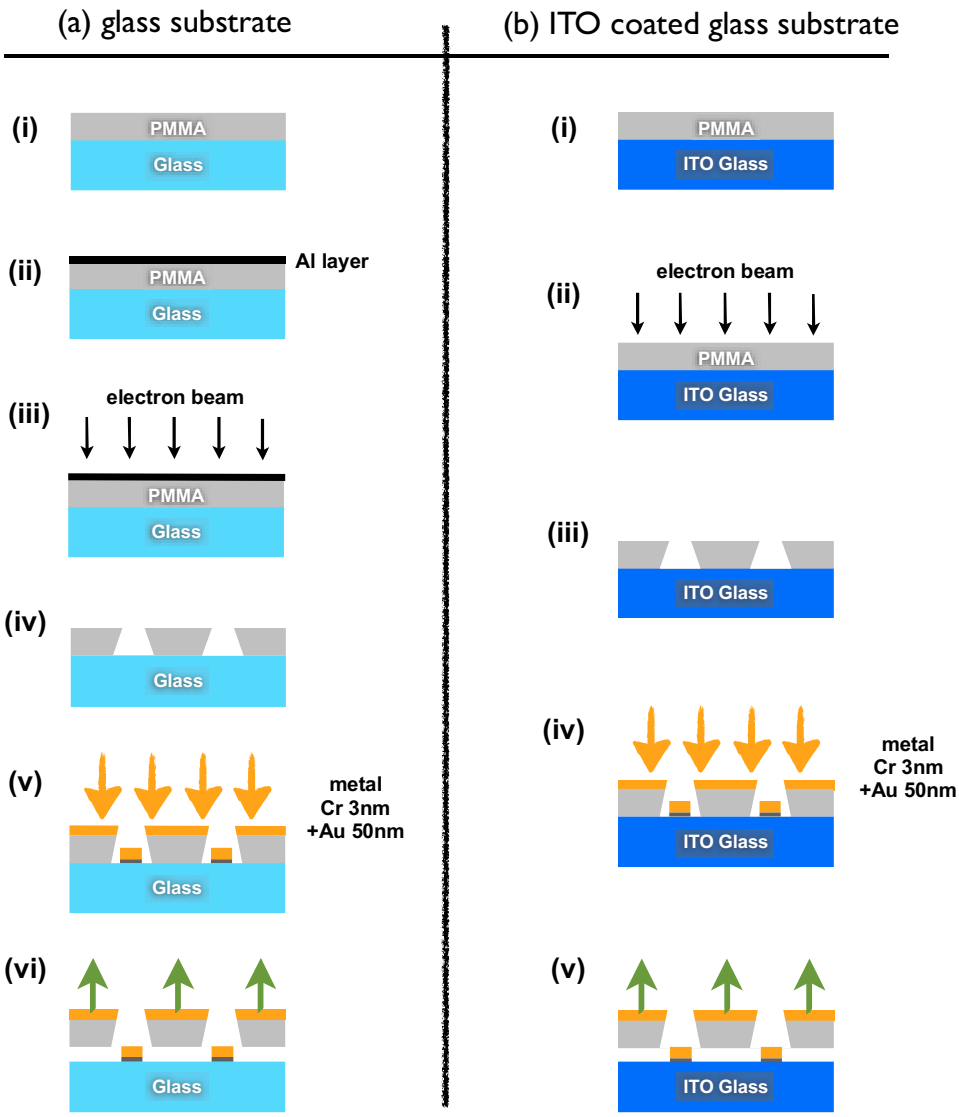


*Figure 2.7: Scheme of electron beam lithography procedures on (a) bare glass substrate and (b) ITO coated glass substrate.*

❖ **Normal glass substrate**

***Substrate cleaning***

The glass substrates utilized in this dissertation are 170µm-thick coverslips. They have to be cleaned before use. The entire cleaning procedure is done in ultrasound. The substrates are sonicated at 45°C in *decon 90* solution (2%-5% of concentration in distilled water) for 5-10min. It is followed by rinsing with distilled water for 5min. This rinsing process is repeated for 3 times to remove the decon 90. After that, they are kept immersed in acetone and then isopropanol, for 5min in each solvent. Last, the substrates are dried with air.

***Spin-coating of PMMA (Figure 2.7a i)***

The supplied PMMA is already solved at a concentration of 30g/L in methyl isobutyl ketone (MIBK). A PMMA layer of 150nm thickness is needed for our nanoparticles of 50nm in height (a ratio of 3 to 1). It requires the spin-coating parameters of 4000rpm/sec in acceleration, 3000rpm in speed and 30 sec in time.

Due to the viscosity of PMMA/MIBK solution and the centrifugal force during spin-coating, the PMMA layer is not ideally flat. It would raise a problem of the fluctuation of focus during lithography. Thus, a heating procedure was adopted to prevent this from happening. By heating the substrate, the solvent MIBK evaporates, leaving the PMMA, which become soft with higher mobility, to take its place to diminish the defects in the polymer layer. It also helps dissipating the stress in the film. Putting the substrate either in an oven at 160°C for 3hrs or on a hot plate at 170°C for 15min has led to good results. In experiment, however, we noticed that processing the heating procedure with the hot plate sometimes results in cracks of the PMMA layer in micrometer scale. Consequently, the oven is strongly recommended.

***Evaporation of Al layer (Figure 2.7a ii)***

To avoid charging of the sample during the e-beam lithography, a thin layer of aluminum is required to conduct the electrons. It is coated on the PMMA layer *via* thermal evaporation with a 10nm thickness. The evaporator *PLASSYS* is used for all the evaporating events in EBL. The substrate is then ready for the lithography.

***Electron beam exposure (Figure 2.7a iii)***

Two scanning electron microscopes (SEM) are available for EBL in Nano'mat: *HITACHI S-3500* and *RAITH E-LINE*. For the former, patterns of the nanoparticles are designed by the software Design CAD. The irradiation is controlled by nanometer pattern generation system (NPGS). A high tension of 30kV and a current intensity of 10pA are used. As to the E-LINE system, the tension of 10kV and current intensity of 150pA should be set for EBL.

***Sample development (Figure 2.7a iv)***

Afterwards, the sample is developed to remove the PMMA chains that have been broken-down by e-beam, i.e., those in the designed patterns. The aluminum layer is solved by KOH solution for 1min until the aluminum layer is completely solved. The residual of KOH on the substrate is cleaned by distilled water. Then the sample is immersed in MIBK:IPA (1:3) solution for 1 min to solve the deconstructed polymer. Last, it is rinsed with IPA for 20sec and dried with air.

***Evaporation of Cr + Au (Figure 2.7a v)***

After the development, the sample is ready for the evaporation of metals. Since gold is not easy to adhere tightly on the glass, a 3nm-thick adhesive layer of Cr or $TiO_2$ is needed.

***Lift-off (Figure 2.7a vi)***

After the evaporation of metals, the sample is immersed in acetone for about 12hrs to dissolve the PMMA film. Afterward, it is rinsed with IPA. Since PMMA residuals on the substrate have been observed sometimes after the lift-off, the sample is immersed in toluene for 2-5min just before final rinsing with IPA.

❖ **ITO coated substrate**

The steps are slightly modified in the case of ITO coated substrate. The aluminum film is no more necessary because the ITO layer is conductive. It can be used for EBL just after coating a PMMA film. Besides, the ITO layer needs to be activated before using.

As a consequence, the top-to-down process on ITO coated substrate starts by activating the ITO layer by placing the substrate on a hot plate at 400°C for 5-8min until the yellow color is completely faded. Then it goes through the procedures of cleaning the substrate, spin-coating a layer of PMMA, heating the PMMA coated substrate, and irradiating with electron beam. The development of sample includes only 1min in MIBK/IPA and 20sec in IPA. Afterwards, 3nm Cr and 50nm Au are evaporated. The process ends up with the lift-off same as that in the case of normal glass substrate.

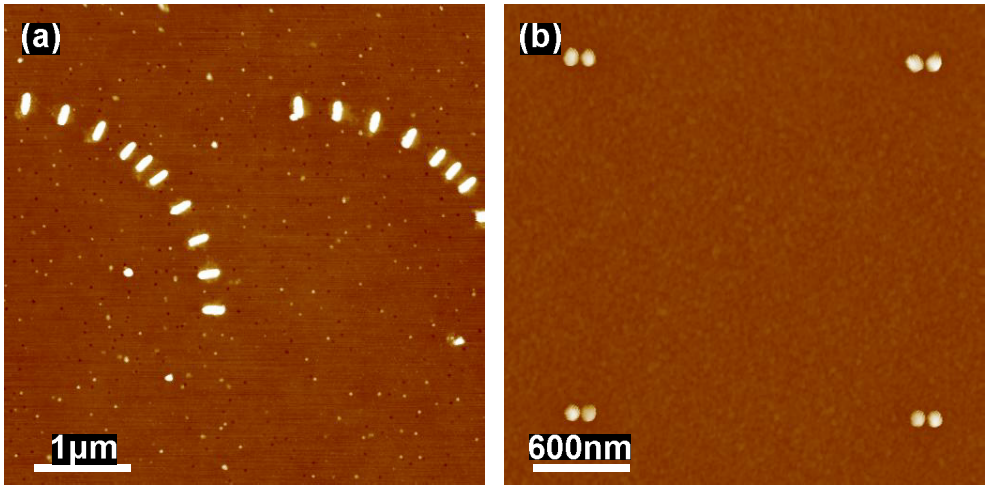


*Figure 2.8: AFM image of electron-beam lithographic gold (a) nanorods on normal glass slide fabricated by A. Bouhelier and (b) dimers of nanodisks on 3nm ITO coated substrate done by S. Kochtcheev.*

Figure 2.8 gives two examples of gold nanostructures fabricated by EBL. The gold nanorods (Figure 2.8a) are made on normal glass, while the dimers of gold nanodisks (Figure 2.8b) lay on an ITO coated substrate. Undoubtedly, EBL is a powerful tool for manufacturing arbitrary shaped nanoparticles. However, a very particle surface or a very sharp corner is very difficult to obtain. Subsequently, some chemical methods were developed for synthesizing the colloids.

### 2.4.2 Samples of chemically synthesized colloids

Compared with EBL nanoparticles, chemically synthesized colloids are usually better in shape. Two types of colloids are involved in this dissertation: gold nanospheres and gold nanocubes. Though both kinds of particles were fabricated *via* the seed-mediated method, the procedures to follow are completely different.

❖ **Gold nanospheres**

***Synthesis of the colloidal solution***

The colloids of gold nanospheres were fabricated by T. Lerond and J. Proust from LNIO utilizing seed-mediated growth method.[113] Seed solution of 12nm gold nanospheres should be prepared in the very beginning. The $HAuCl_4 \bullet 3H_2O$ solution (100ml, 0.25mM) is heated to boil while stirring. Then 3ml of 1% aqueous sodium citrate is added into the solution, followed by a series of color change until it appears to be wine red. The solution is then kept boiling and stirring for 30min. After cooling to room temperature, distilled water is added to compensate the water that was evaporated during boiling. The final volume of the seed solution is 100ml.

To obtain solutions of gold nanospheres in different diameters, ascorbic acid (100ml, 0.4mM) is added slowly (10ml/min) into a 150ml water-diluted solution that consists of the 12nm seed solution (0.25mM in Au) and $HAuCl_4 \bullet 3H_2O$ (10mM). The required volumes of those two solutions rely on the diameter of gold nanospheres.[113]

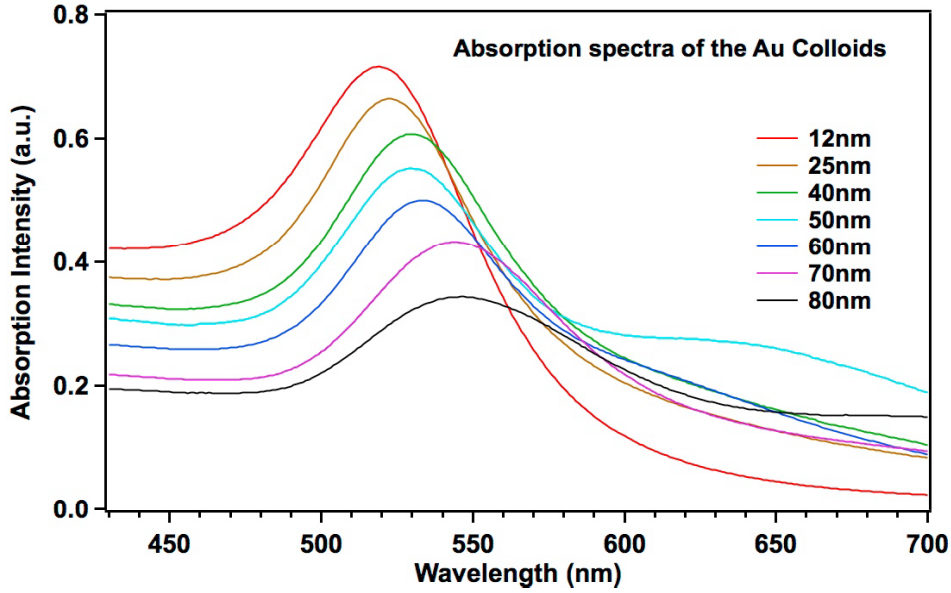


*Figure 2.9: Absorption spectra of the gold colloids in distilled water.*

The absorption spectra, shown in Figure 2.9, were taken from the result solution of gold nanospheres. Note that the diameters written in the legend are the mean values of particle size in each solution. The exact size of a unique nanosphere

(Chapter 3, section 3.1) is demonstrated from the AFM image: it corresponds to the measured height of the nanosphere.

***Fabrication of landmarks by EBL***

Since the colloids are randomly distributed on the substrate, landmarks are fabricated through top-to-down process to help recognizing the regions. Gold is used as the metal for evaporation. This is an extremely helpful method, especially when fluorescent signals have to be collected from a certain well-characterized hybrid nanostructure (Chapter 4, section 4.1).

***Cleaning substrate***

In order to firmly attach the gold nanospheres onto glass substrates, functionalization of the glass is needed. Generally, amino-silane is used. The functionalization starts with the cleaning and activation of the substrate using either piranha solution or UV-ozone.

Piranha is prepared by gently adding $H_2O_2$ into $H_2SO_4$ (98%), with a volume ratio of 1: 2 ($H_2O_2$: $H_2SO_4$). The substrate is put in piranha for 2hrs. It is then rinsed properly with distilled water and dried by spin-coating with parameters of 6000rpm/sec (acceleration), 6000rpm (speed) and 30sec (time).

UV-ozone is another cleaning method. To make it proper for functionalization, the substrate is sonicated in distilled water for 15min and dried with air. Afterwards, the substrate is exposed under UV-ozone for 30min.

Typically, we prefer piranha to UV-ozone because it is believed to better clean the glass. However, when the substrate has been labeled with the gold landmarks, using piranha solution is risky because it can remove the landmarks.

***Functionalization of the substrate***

Functionalization is performed in a glove box under Ar condition. The cleaned substrate is immersed into 50ml anhydrous toluene. Then, 450µl of the aminosilane is added drop-by-drop into the toluene. It is kept in the solution for 24hrs away from light, usually by covering the container with aluminum foil. Afterwards, the substrate is rinsed with toluene and isopropanol, and then dried with air. Now the substrate is ready for use.

***Adhesion of gold nanospheres***

The colloidal gold nanospheres are dip-coated on the functionalized substrate. Figure 2.10 is an example of colloidal gold nanospheres of 50nm in diameter. The substrate was immersed for 30min in the colloidal solution with a concentration of gold nanoparticles of $1.7\times10^{13}$ $L^{-1}$. After dip-coating, the sample is rinsed with distilled water.

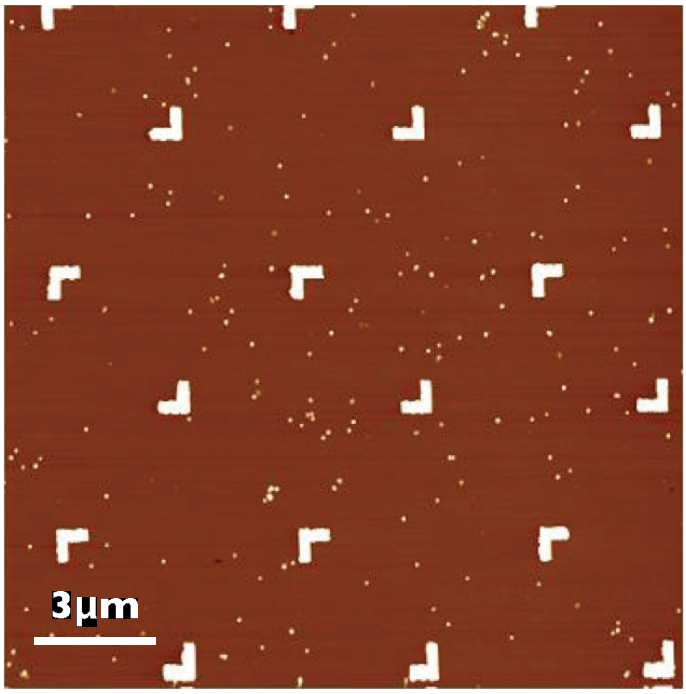


*Figure 2.10: AFM image of EBL landmarked sample of gold colloidal nanospheres. Each region marks an area of 3µm×3µm.*

❖ **Gold nanocubes**

***Synthesis of gold nanocubes***

The gold nanocubes were fabricated by S. Marguet from CEA Saclay. The synthesis of cubes follows the seed-mediated method.[114-115] It starts with the preparation of seed solution by adding ice-cold solution of $NaBH_4$ (0.42ml, 10mM) into aqueous solution of $HAuCl_4$ (92ml, 10mM) and cetyltrimethylammonium (CTAB) (0.4ml, 10mM). Then the growth solution is obtained by successively adding the solutions of CTAB (9ml, 22mM), $HAuCl_4$ (0.25ml, 10mM), and ascorbic acid (3ml, 38mM). Finally, the 20ml water diluted seed solution is added into the growth solution. It is remarkable that the seed solution should be kept at 25°C for 2hrs, and the result solution have to be kept overnight at 25°C before using.

***Depositing gold nanocubes on ITO coated glass substrate***

The preparation process of gold nanocubes was developed on ITO coated glass. First of all, the ITO layer has to be activated by heating the substrate on a hot plate at 400°C for 5-8min with the ITO layer facing up. Then it is sonicated for 5 min in each of the three: acetone, ethanol, and distilled water. After being exposed under UV-ozone for 15min, the substrate is deposited immediately with 1µl of the CTAB diluted gold nanocube solution (60 times dilution). Once the droplet of the colloids is dry, the substrate is heated at 50-100°C for 3-5 min. Finally, it is rinsed with ethanol and dried with air. Figure 2.11 shows a 2µm × 2µm AFM image of a sample of gold nanocubes. It should be noted that due to AFM resolution, the cube orientation could

not be easily deduced from the AFM image. We will come back to this point in section 2.5.3.

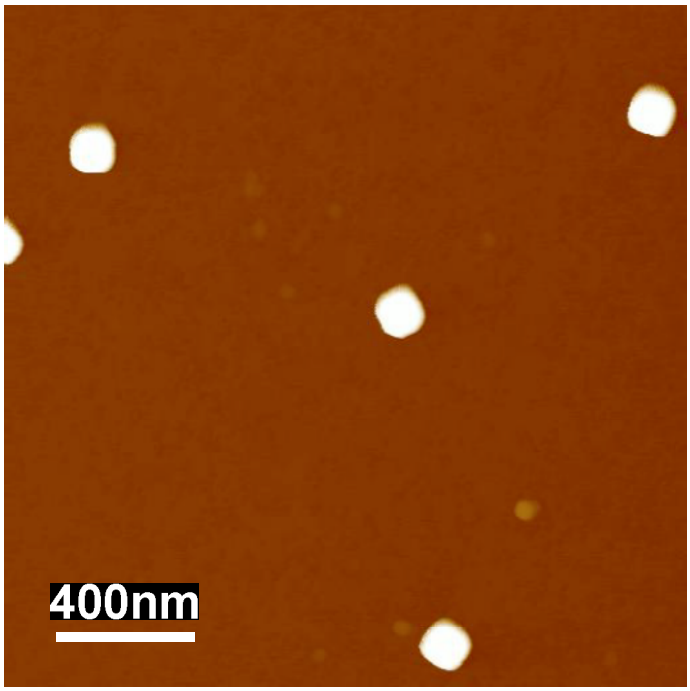


*Figure 2.11: AFM image of colloidal gold nanocubes on ITO coated glass.*

## 2.5 Techniques for characterization

The characterization techniques can be divided in this dissertation into two categories: the methods for passive hybrid plasmonic structures and those for active ones. AFM is the most important tool in the first case, while optical methods of fluorescence spectroscopy and Raman spectroscopy are used for active structures. Alternatively, the SEM is occasionally chosen to characterize the passive hybrid plasmonic structures.

### *2.5.1 AFM and the differential imaging*

All the samples that will be discussed in the coming chapters have been characterized with the AFM of *VEECO BIOSCOPE II*. With the tip oscillating at a certain frequency above the sample to produce a point-by-point image, tapping mode was adopted throughout the studies. Contact mode might have our polymer structures damaged by keeping scratching the sample surface with the probe.

The tapping mode AFM provides meanwhile a phase image in addition to the normal 3D topographic image. It provides information on the phase lag of the cantilever oscillation during the scan. The phase image highlights the edges and is not influenced by a large difference in height while scanning. Figure 2.12 is an example of AFM topographic and phase images on a gold nanocube. Evidently, the phase image in panel (b) offers a clearer signature of the metal nanostructures with

sharper corners and edges. We rely on the phase image to measure more accurately the orientations angles of cubes, rods, and triangles.

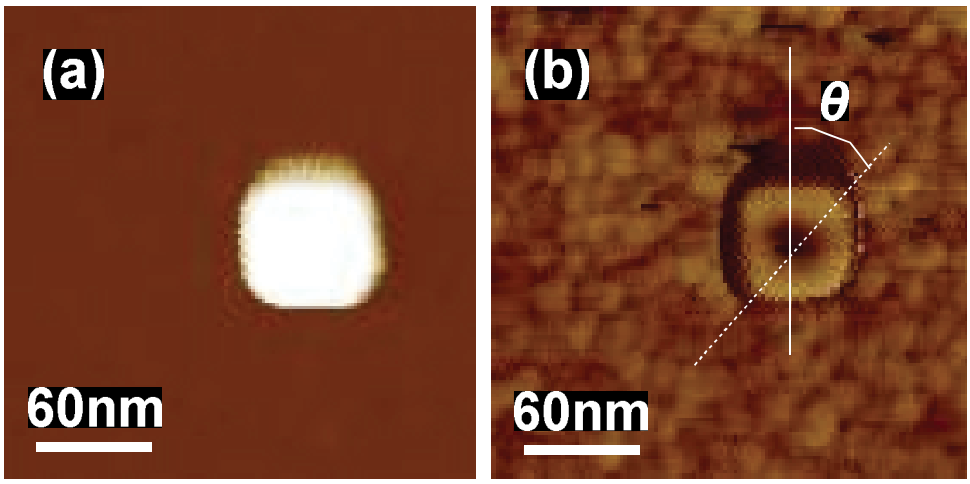


*Figure 2.12: AFM (a) topographic image and (b) phase image of a gold nanocube. The white lines in panel (b) illustrate the measurement of the orientation of diagonal of the nanocube.*

Merely collecting an AFM image of the sample is not our final goal. As has been introduced in Chapter 1, the passive hybrid plasmonic structure that we fabricated is dedicated to characterize the near-field of the metal, which has already been imprinted by the polymer part. Therefore, the task is transformed into the acute characterization of the integrated polymer nanostructure. AFM images have to be collected for the same particle before and after the hybridization. The difference between these two images describes the created polymer, i.e., the near-field. The differential image is adopted to highlight this feature. It is the result image of a pixel-to-pixel calculation of the two images, to be more precise, the one taken before the hybridization subtracted from that after it.

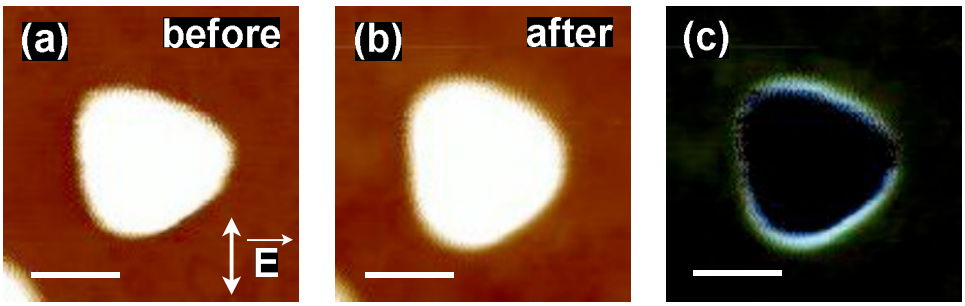


*Figure 2.13: Hybridization-based Near-field characterization: AFM image (a) before and (b) after the photopolymerization. (c) The differential image highlighting the polymer structure that imprints the near-field of the gold nanotriangle. Scale bars represent 60nm. Polarization of incident laser for hybridization is shown in panel (a).*

Figure 2.13 is an example of the characterization performed on a gold nanotriangle. Let us notice that the integrated polymer presents an anisotropic geometry. We will come back to this point in Chapter 3.

Differential AFM images will be used throughout this thesis as one of the most important characterizing techniques. The AFM provides us extraordinary clear and detailed signature of the hybrid structures and allows the quantitative study on the near-field distribution.

It should be noted that the AFM tip has its own radius of curvature (ROC, approximately 7nm in our case), which contributes to the measured values of particle sizes. Generally, the ROC does not influence our results because its contribution to the measured value can be canceled out in the differential AFM images. That is also the reason why the ROC of the tip does not limit the resolution (sub 5nm, Chapter 3) of our method for near-field characterization.

This technique works almost perfectly with unique particles. Yet when scanning on sharp corners or dimers with very small gaps, the AFM tip would raise some troubles. Some other techniques are needed to compensate for this deficiency.

### 2.5.2 SEM: SE and BSE image

It is from recently that we have started using scanning electron microscope (SEM) to characterize our hybrid nanostructures. The *RAITH E-LINE* system offers us a pathway to collect simultaneously both the secondary electron (SE) image and the backscattered electron (BSE) image. Secondary electrons cannot go deep into the sample surface. They are reflected by both the polymer and metal of our hybrid structure. The backscattered electrons, however, have higher energy to pass through the polymer. Subsequently, these two types of electrons provide another method for characterizing our metal/polymer hybrid structures (Figure 2.14).

Both images (SE and BSE) in Figure 2.14 were captured simultaneously under a relatively low voltage of 10kV. The SE image in the left panel shows both polymer and metal of the hybrid system via different contrasts. Thus, only an image taken after the polymerization procedures would be sufficient for the characterization of the hybrid structure. Generally, it is a convenient method with fast imaging process.

However, every technique has its own shortcomings. Electrons with high energy would destroy the dye molecules that are trapped in the polymer structure. Moreover, the electron beam deposits a layer of carbon on the particle that has been characterized. Definitely this method is not suitable for the active hybrid plasmonic system that is expected to emit light after the characterization. Besides, a conductive surface is necessary to take the SEM image. That means either the hybrid nanostructure is fabricated on an ITO substrate or the entire sample is coated with a metal layer. The latter solution loses the contrast on metal and polymer while the former is not always suitable for the preparation of any sample.

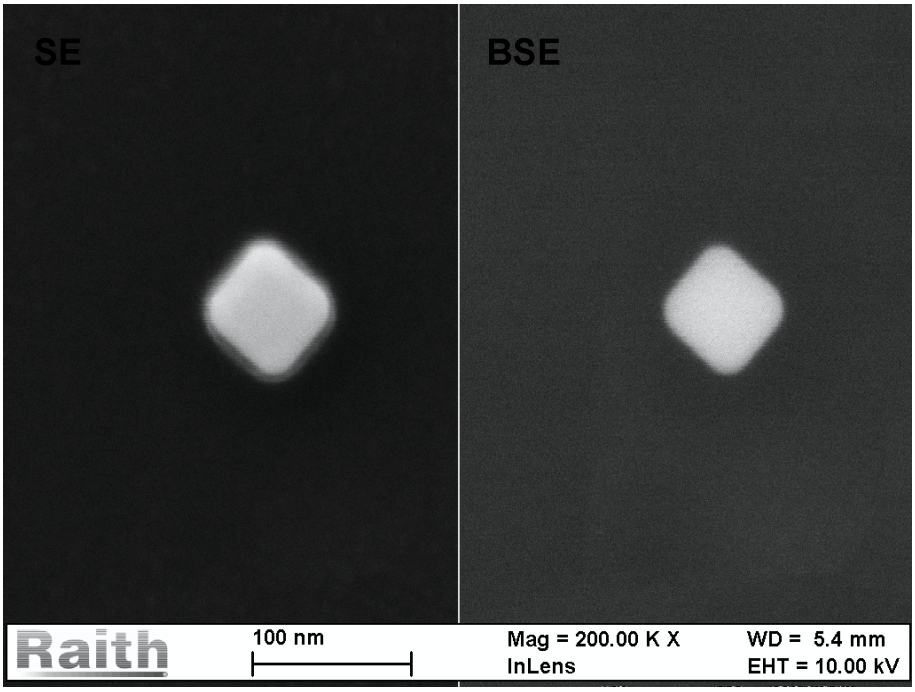


*Figure 2.14: SEM images of a gold nanocube/polymer hybrid system. SE image in the left panel is characterizing the polymer and metal with different contrasts. BSE image in the right panel characterizes the gold nanocube.*

### 2.5.3 Dark-field image and scattering spectra

The UV-visible absorption spectra mentioned in section 2.4.2 (Figure 2.9) are used as a reference for LSPR of gold nanoparticles in solution. Nevertheless, if the LSPR of one single nanoparticle is needed, the UV-visible spectrometer is no longer helpful. The dark-field scattering spectroscopy is a powerful tool for characterizing the LSPR of a given nanoparticle.

A dark-field condenser with a numerical aperture (NA) of 0.9 is installed above the sample stage of an inversed microscope. The scattered light is collected by an objective of 40X/0.6NA. Then the signal is focused by a tube lens ($f = 180mm$) into the slit of *ANDOR* spectrometer. Signals are collected by a CCD of *iDus.*

As a matter of fact, by using the camera of the spectrometer with this optical configuration, it is impossible to recognize a unique nanoparticle whose diameter is below 100nm, especially in the case of colloids. Definitely the system has to be improved. The solution is to add a lens between the output of microscope and the spectrometer in order to have the image amplified. A convex lens with a focal length of 25.4mm is installed and the slit of spectrometer is placed at the second image plane. With this improvement, as is shown in Figure 2.15 (a), colloidal nanoparticles of 70nm can be clearly recognized. Figure 2.15 (b) is the scattering spectrum of one single hybrid structure of polymer/gold nanoparticle.

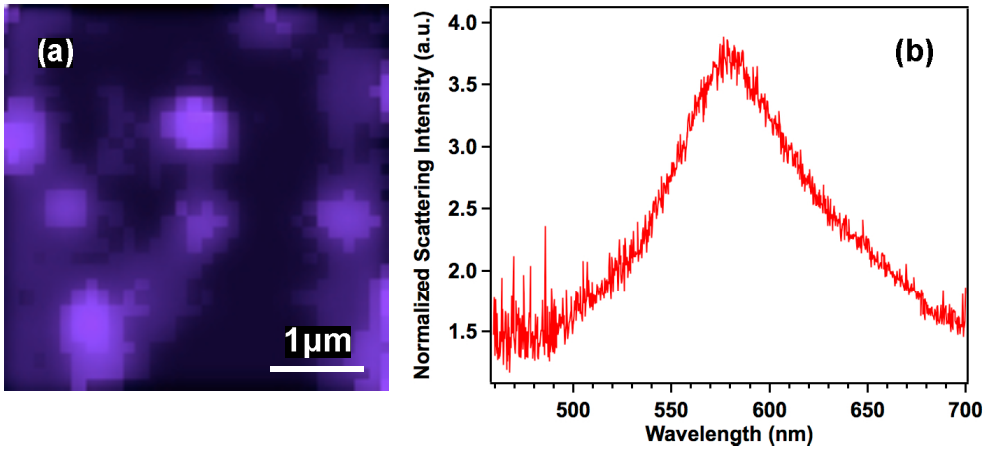


*Figure 2.15: (a) Dark field image on a sample of gold colloids of 70nm diameter. Each dot corresponds to an isolated gold nanoparticle. (b) Scattering spectrum from a unique hybrid system of gold nanosphere/polymer.*

By using the multi-track mode of the spectrometer, the signal can be collected from only 1 pixel, corresponding roughly to a detecting region of about 100nm×100nm on the sample. However, a nanoparticle of 60nm actually takes up several pixels on the CCD due to the system resolution that still needs to be improved. Thus, the signal from a region of 500nm×500nm is always collected to make sure the target particle is encompassed.

### 2.5.4 Fluorescence spectroscopy

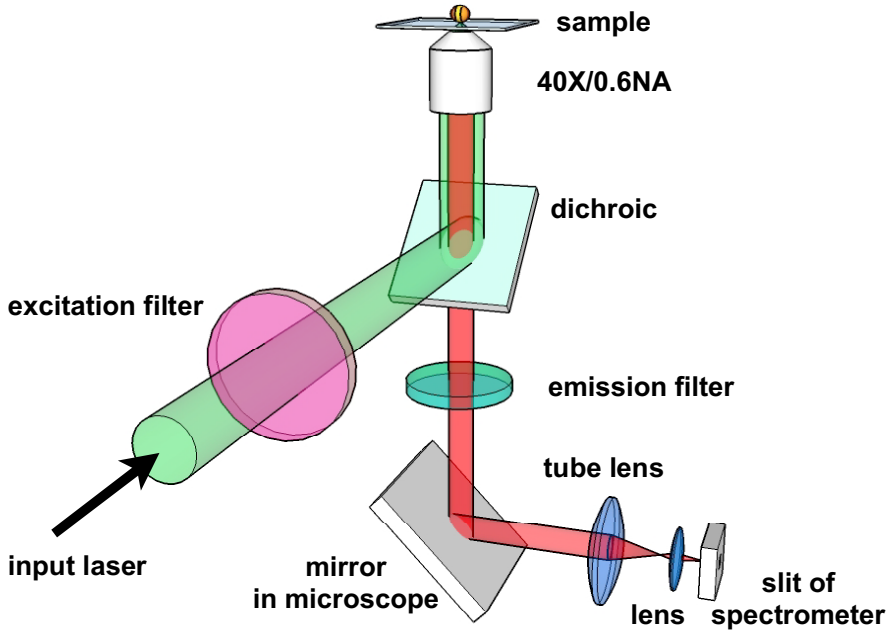


*Figure 2.16: Scheme of our optical configuration of fluorescence spectroscopy.*

Our system of fluorescence spectroscopy is based on an inversed microscope. As Figure 2.16 illustrates, the laser beam is launched into the microscope. It is

reflected by a dichroic beam-splitter up to an objective of 40×/0.6NA to irradiate the sample. The objective is used for both excitation and collection. The dichroic mirror is transparent to the fluorescence signal. After being purified by an emission filter, the signal is induced into the slit of the spectrometer that is placed at the second image plane. The lens between the tube lens and the spectrometer is right the one added to amplify the image.

According to our experiment, the EY or MB molecules are still able to emit light after the hybridization procedures. These molecules can be therefore utilized directly as labels for optical detecting techniques, which are fluorescence and SERS in this thesis. Figure 2.17 is the AFM image (panel (a)) of standing polymer tips with EY the photosensitizer, and the fluorescence signal (panel (b)) of EY collected from a polymer tip of about 1μm in height and 1μm in diameter (polymer tips on the bottom of the AFM image in panel (a)). The excitation wavelength was 514nm and a 514nm high-pass emission filter was used. The fluorescence signal of EY in polymer is peaked at 555nm.

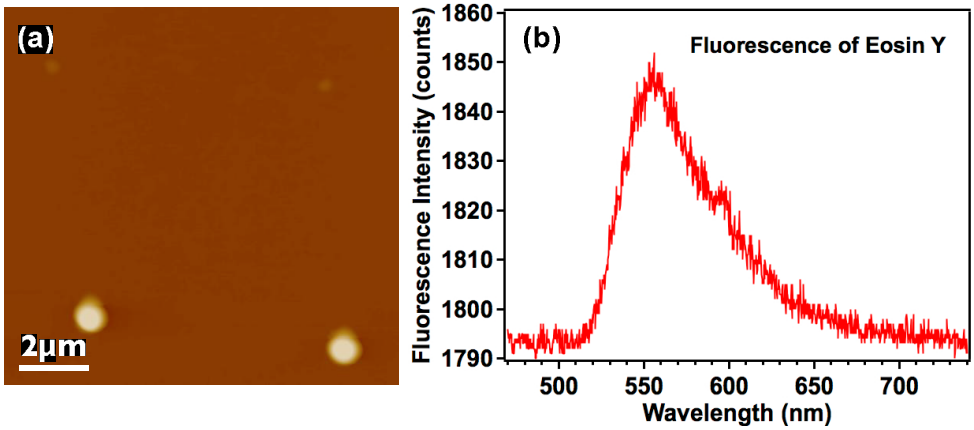


*Figure 2.17: (a) AFM image of polymer tips fabricated with a focalized laser. (b) Emission of EY from a polymer tip of 1μm in diameter and 1μm in height.*

In the situation of a single hybrid system, we have to rely on the real-time dark-field scattering image to recognize and to align the hybrid structure with the incident laser spot. The fluorescent spectra are necessarily collected from the hybrids with different incident polarizations, for the nanostructure is an anisotropic light emitter. (See section 4.1 for detailed experiments of the fluorescence on a unique polymer/gold nanosphere hybrid system.)

### 2.5.5 Raman spectroscopy

SERS is another optical characterization method for our anisotropic nano-emitter. Two commercial Raman spectroscopes were used in this dissertation. A preliminary study on the SERS of MB molecules near gold nanodisks was performed in Université Paris Diderot with a *LabRAM* confocal Raman microscope. The study on the sample of polymer/gold dimers in Chapter 4 section 4.2 was done in CNM, Argonne National Laboratory with a *RENISHAW INVIA* confocal Raman microscope.

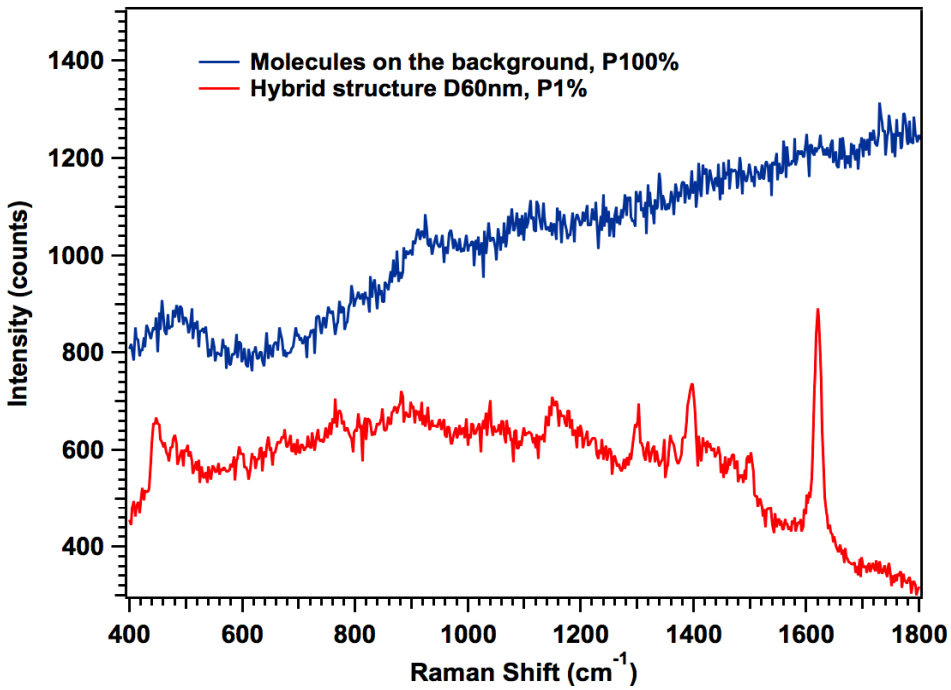


*Figure 2.18: Raman scattering spectra of MB from a hybrid structure made of a gold nanodisk of 60nm in diameter (red), and the molecules on the background (blue). Note that the incident power of the red curve is 100 times smaller than that of the blue.*

Figure 2.18 shows the result of a preliminary study that illustrates the enhancement to Raman signal of MB molecules on gold nanodisk. The incident wavelength is 633nm. As has been stated in section 2.1, the rinsing procedure after photopolymerization is not yet perfect. Some dye molecules remain on the glass substrate. This is a limiting point that, however, provides a convenient approach to the acquisition of signals from the molecules that are not modified by any MNP. Considering the same order of magnitude of molecule numbers in both cases, it is reasonable to use the spectra that are taken from the substrate but away from the particle as the references.

The spectrum in blue color in Figure 2.18 was collected from molecules on the background as a reference. The one in red was collected form the polymer/gold nanodisk hybrid structure. A surface enhancement on the Raman signal can be clearly seen. We can recognize the Raman modes at 448cm$^{-1}$ that corresponds to the (C-N-C) band, 765, 882, and 1039 cm$^{-1}$ that associate with the (C-H) band, 1139 cm$^{-1}$ that correlates to (C-N), 1303 and 1396 that are related to (C-H); and 1620cm$^{-1}$ that assigning (C-C) ring.[116-117] It should be noted that the power applied on background molecules was 100 times higher than that on the hybrid system. As a result of strong plasmon enhancement, we can recognize a fluorescence signal of MB from the baseline of the SERS spectra on the hybrid nanostructure.

## 2.6 Summary

To sum up, this chapter contains the fundamental principles of our technique, including detailed procedures and configurations to fabricate and characterize our hybrid structure.

From some viewpoint, our approach consists in playing with the local dose of the optical electromagnetic field to prevent or trigger the photopolymerization. Due to many side reactions, the homemade free-radical photopolymerizable solution is characterized by a threshold dose. With an incident dose below the threshold, the far-field polymerization is avoided. In the surface-plasmon-enhanced region adjacent to a MNP, the local dose can exceed the threshold to locally initiate polymerization. The photopolymer that is created imprints the near-field of the particle. The obtained hybrid structure characterizes the near-field and meanwhile serves as an anisotropic nano-emitter.

The most sophisticated characterization tool for the passive hybrid plasmonic structure is based on differential AFM images to highlight the integrated polymer nanoparts. Besides, the second electron SEM image is able to provide a difference in the contrasts of metal and polymer of the hybrid nanostructure. Both techniques have their own assets and limits. As far as the active hybrid structures are concerned, specific tools such as the fluorescence spectroscopy and the Raman spectroscopy are adopted to collect optical signals. The anisotropy of the gold/polymer hybrid structure is expected to lead to a new generation of polarization-sensitive nano-emitters.

# CHAPTER 3

# Passive Hybrid Plasmonics

The fabrication of our metal/polymer hybrid nanostructure, as has been pointed out in previous chapters, is used to imprint the near-field distribution in the vicinity of MNPs. Compared with traditional techniques, it has a higher resolution and allows quantitative measurements of the near-field. This chapter exhibits some results of the quantitative characterization of the near-field distribution on three different types of gold nanoparticles: colloidal spheres, colloidal cubes and rods fabricated by EBL. Detailed synthesis and preparation processes of each sample have been presented in Chapter 2, section 2.4. We will start with the gold nanospheres for a size-dependent study. Then gold nano-rods with different orientations were polymerized under off-resonance excitation condition. This study proves that our technique is sensitive enough in characterizing very weak near-field. Finally, the surface plasmon distributions were characterized for differently oriented gold nanocubes.

## 3.1 Size-dependent near-field distribution of gold nanospheres[1]

There has been extensive work on identifying nanoparticle geometries (sharp tips, nanoparticle junctions, etc) that exhibit the strongest possible field enhancements.[22,109,118-119] Surprisingly, the size tunability of near-fields is not understood in as much detail, despite a few works on this topic of plasmon resonance and field damping.[25,120-121] In this section, we are going to investigate the near-field distribution and amplitude on gold nanospheres of different diameters from 12nm to 85nm.

The colloids of gold nanospheres of diameters of 12nm, 25nm, 40nm, 50nm, 60nm, 70nm and 80nm were fabricated *via* a seed-mediated growth method reported for the first time by C. J. Murphy and coworkers.[113] Particles used in this study were prepared by my colleagues J. Proust and T. Lerond. The gold colloids were dip-coated on an aminosilane-functionalized glass substrate. Detailed process for the sample preparation has been introduced in section 2.4. The dark-field scattering spectra in Figure 3.1 are from different nanospheres with diameters of 40nm, 50nm, 60nm, and 80nm. Each of the spectra was collected from a unique nanoparticle on the functionalized glass substrate. As the particle size goes larger, the scattering

---

[1] *C. Deeb, X. Zhou, J. Plain, G. Wiederrecht, R. Bachelot, M. Russell, and P. K. Jain. Size dependence of plasmonic near-field measured via single nanoparticle photoimaging.* ***J. Phys. Chem. C****. 2013, 117, 10669-10676.*

peak redshifts and the full-width at half maximum (FWHM) increases. These indicate that the LSPR redshifts and the quality factor of the gold nanosphere decrease as diameter increases.

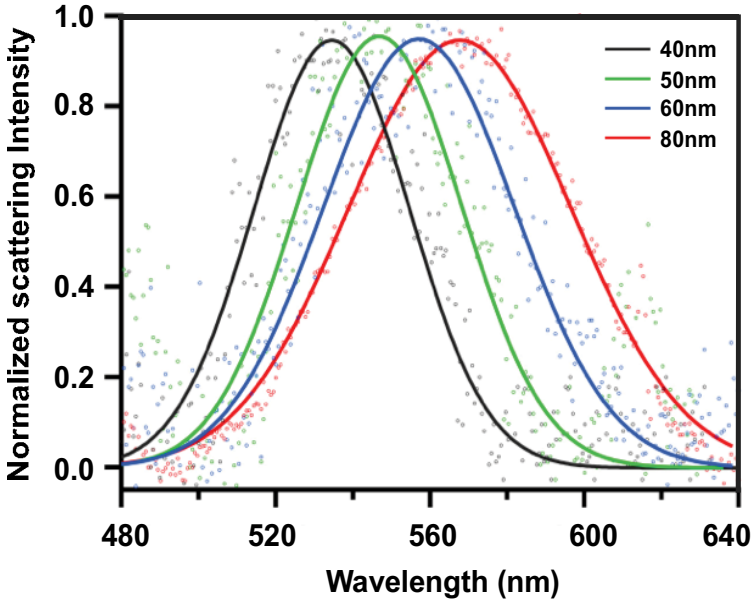


*Figure 3.1: Normalized dark-field scattering spectra indicating the LSPR of unique gold nanospheres with different diameters on the glass substrate.*

### 3.1.1 Near-field imprinting

After being characterized by AFM, the sample was coated by a drop of photopolymerizable solution. The photopolymerizable formulation in this study was 96%wt PETIA + 4%wt MDEA + 0.5%wt EY. The laser with a wavelength of $\lambda = 532$nm and a dose of 75% of the threshold ($D_0 = 0.75D_{th}$) was adopted for a normal incident irradiation for photopolymerization. After the rinsing procedures of the sample, AFM characterization was performed again on each nanoparticle that was scanned before the polymerization.

Figure 3.2 shows nanoparticles of 70nm in diameter. It should be pointed out that the diameter of each nanosphere was measured relying on its height to avoid the contribution of the radius of curvature of the AFM probe to the measured particle size. Only the particles that were most approximate to perfect spheres were selected for the measurement. For example, NP2 in Figure 3.2 was studied while NP1 was not. Both nanoparticles are elongated along the polarization whose direction is shown by $\vec{E}_0$ in panel (b). The elongation of NP1 is larger than NP2. By comparing these two nanoparticles, we can see an influence of fine structures on the near-field of the nanoparticle.

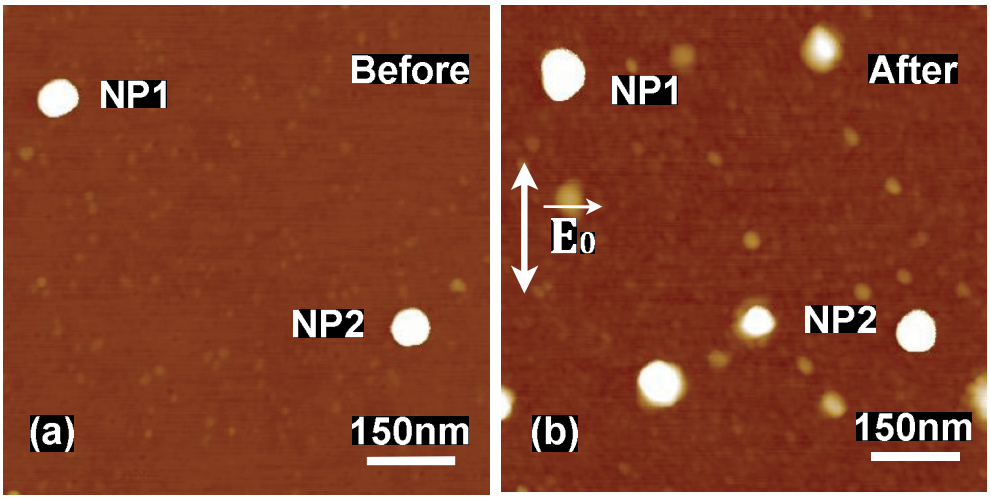


*Figure 3.2: AFM images of the same region (a) before and (b) after photopolymerization on the sample of gold nanospheres with diameters of 70nm. $E_0$ in panel (b) represents the direction of the incident laser for photopolymerization.*

Some nanostructures other than the two MNPs can be found in Figure 3.2 (b), the image taken after polymerization. These structures are the residuals of photopolymerizable solution that were not perfectly cleaned by the solvents during rinsing process. They are responsible for the fluorescence signal on the background with an ineligible intensity. Details regarding this point can be found in Chapter 4, section 4.1.

Differential AFM images (see section 2.5.1) are shown in Figure 3.3. The four panels correspond to polymer/gold nanosphere hybrid structures with diameters of 40nm, 50nm, 60nm, and 70nm, respectively. The differential image characterizes the near-field distribution by highlighting the polymer structures that are fabricated. From Figure 3.3 (b), a maximum polymer size was obtained from the nanosphere with a diameter of 50nm. Polymer structures were oriented along the incident polarization due to the charge distribution at the metal/polymer interface. Detailed discussions on this point will be in section 3.2. The photopolymerizable solution can adhere on the surface of gold nanoparticles and is possible to induce a tiny polymer elongation perpendicular to the incident polarization.

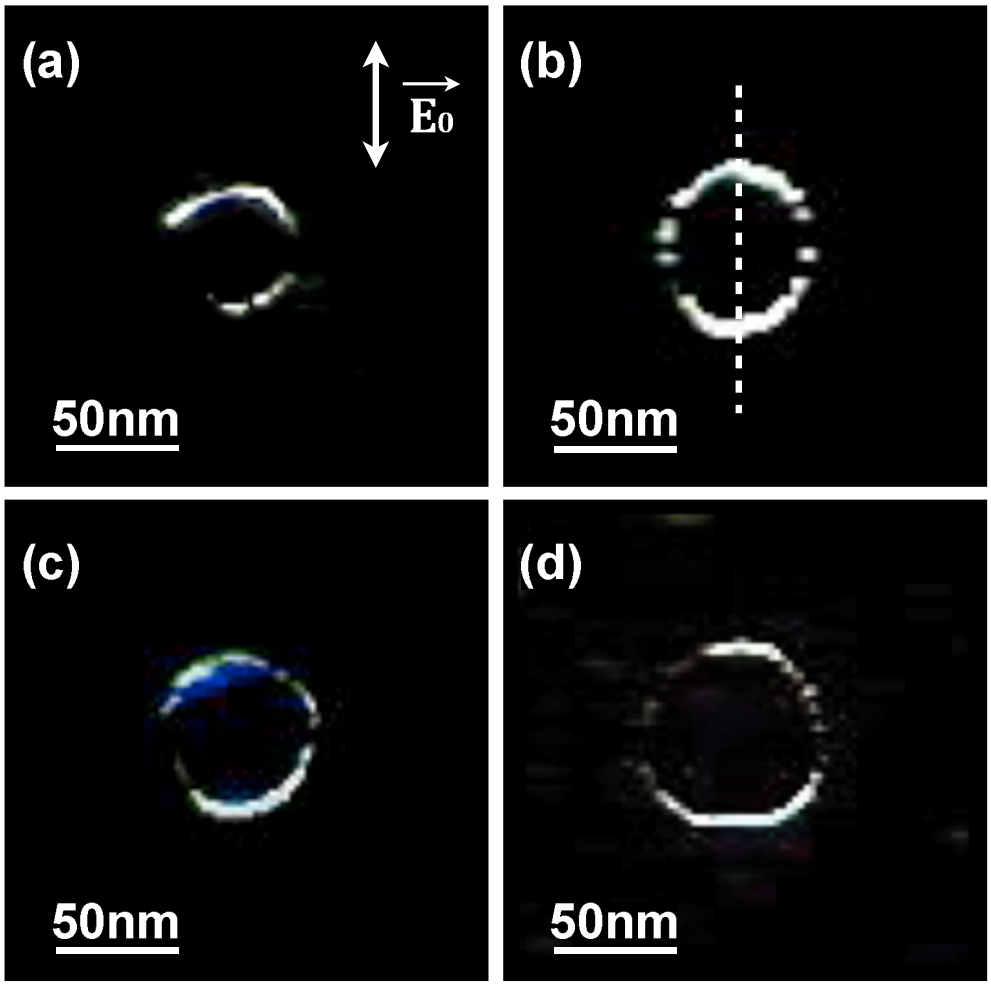


*Figure 3.3: Differential AFM images of gold nanospheres with diameters of (a) 40nm, (b) 50nm, (c) 60nm, and (d) 70nm. A maximum polymer size appears in panel (b), the nanosphere of 50nm in diameter.*

### 3.1.2 Near-field measurement

The polymer thickness (or polymer extent), which represents the distance from the particle surface to the point whose field intensity enhancement decreases to 1/0.75 along the polarization direction, can be utilized as a measure of the near-field intensity. The exact values of the polymer thickness were measured via cross-section profiles of the hybrid systems along incident polarization direction. The dashed line in Figure 3.3(b) is an example for the cross-section. The profiles in Figure 3.4 are corresponding to the four particles in Figure 3.3, from 40nm to 70nm in diameter. The two peaks in each cross-section profile illustrate the two polymer lobes fabricated during the photopolymerization.

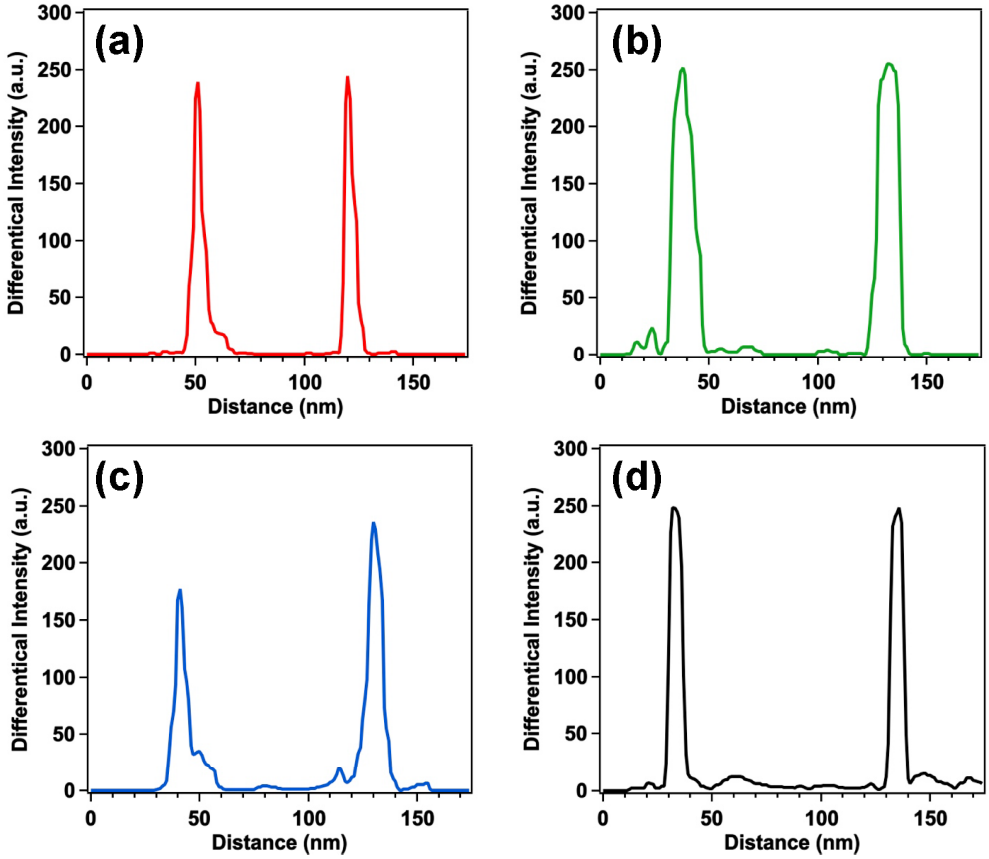


*Figure 3.4: Cross section profiles along the incident polarization of gold nanospheres with diameters of (a) 40nm, (b) 50nm, (c) 60nm, and (d) 70nm.*

From Figure 3.4, the polymer extension increases significantly as the diameter of the nanosphere augments from 40nm to 50nm. At the diameter of 50nm, the obtained polymer thickness reaches a maximum of 20nm. It then decreases as the diameter rises to 60nm and 70nm. This variation of the polymer thickness demonstrates the tendency of near-field intensity as the diameter of gold nanoparticle increases. Since fine structure of the nanoparticles has a non-negligible influence on the near-field distribution, it is reasonable to perform the measurement on several different particles and note the average polymer thickness for each diameter.

### 3.1.3 Size-dependence of near-field enhancement

In addition to the four particles above, nanospheres with other different diameters from 12 to 85nm were studied. For each of the particle sizes, the polymer elongation was measured on 3 or 4 different nanoparticles (i.e. 6 or 8 polymer lobes). The average thickness of a polymer lobe is plotted in Figure 3.5 as a function of the diameter of gold nanosphere. Error bars in this figure represent the standard experimental deviations of the polymer sizes.

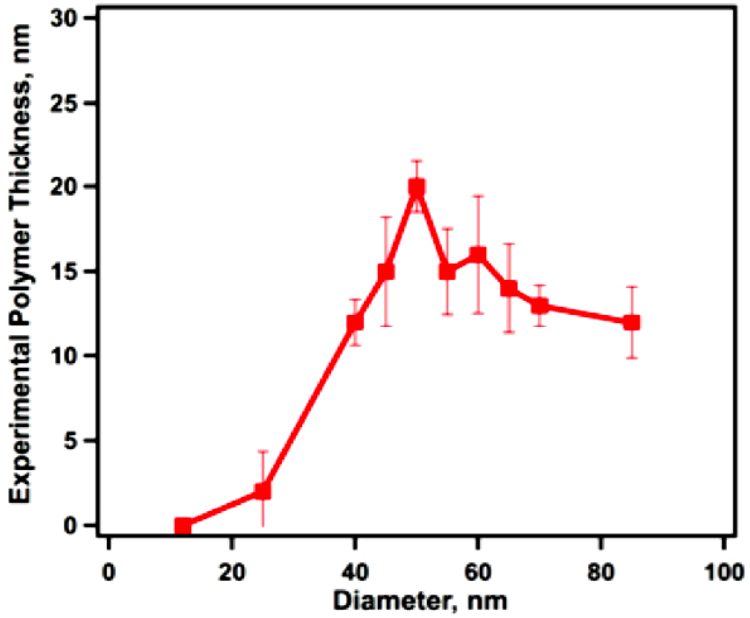


*Figure 3.5: Measured polymer thickness as a function of the diameter of gold nanoparticles. Error bars represent the standard experimental deviations. A maximum polymer extent was measured at the diameter of 50nm.*

The experimental data illustrates clearly that the measured polymer extent increases from 0 to a maximum of 20nm as the diameter of particle grows from 12 to 50nm. It decreases then as the diameter keeps increasing from 50nm to 85nm. To better understand the mechanisms behind the experimentally measured data, theoretical calculations and DDA simulations were performed.

### 3.1.4 Theoretical calculations and DDA simulations

The theoretical work was achieved by P. K. Jain from University of Illinois Urbana-Champaign. Field intensity enhancement was calculated as a function of diameter of gold nanospheres. The particles are embedded in a surrounding medium whose refractive index was $n_d = 1.48$, corresponding to the photopolymerizable solution ($n = 1.48$) and the glass substrate ($n = 1.5$).

❖ **Finite-size effects**

We presented in Chapter 1 section 1.1 about some finite-size effects that cause the damping of surface plasmons involving the radiative and non-radiative damping, as well as the phase retardation. Figure 3.6 compares the calculated results of the field intensity enhancement factor by including (panel (a)) and excluding (panel (b)) all these three effects.

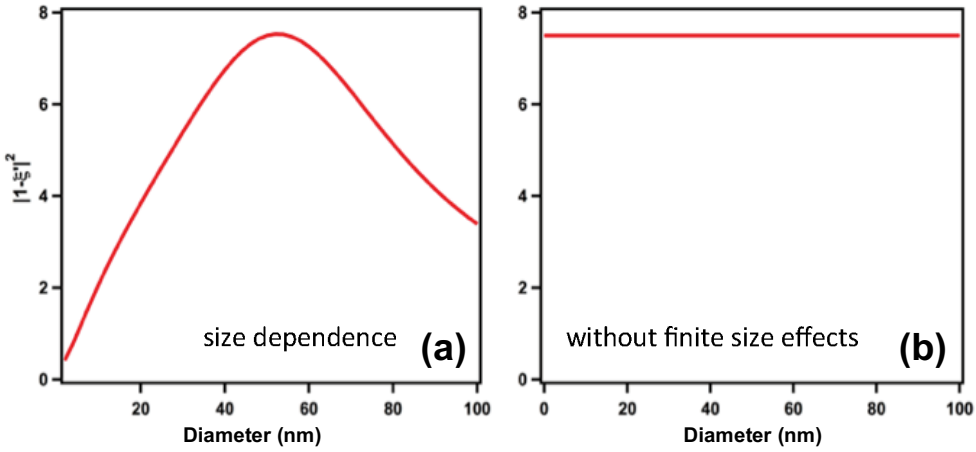


*Figure 3.6: Calculated enhancement factor of the near-field intensity ($|1-\xi'|^2$) as a function of the spherical diameter. (a) The size-dependence of field intensity enhancement factor resulted from the finite-size effects: radiative damping, non-radiative damping, and phase retardation. (b) The enhancement factor without considering the finite-size effects. The calculation was performed for Au nanospheres embedded in a typical medium ($n_d = 1.485$) under the incident light with a wavelength of $\lambda = 535nm$.*

Figure 3.6 (a) shows the calculated enhancement factor of the field intensity by putting the finite-size effects into consideration. A maximum field enhancement was obtained around 52nm. Figure 3.6 (b) is the result based on equations 1.4, 1.5 and 1.6 excluding all the finite-size effects. According to these equations, the enhancement factor relies only on the dielectric function of the metal and the permittivity of the surrounding medium, which are constant values in this study. In other words, enhancement factor is independent from the size of the nanoparticle. Undoubtedly, the finite-size effects are of great significance to the enhancement of near-field. In addition to Figure 3.6 (a), Figure 3.7 illustrates the influence of each of the three effects on the enhancement factor.

Non-radiative damping is important for small particles but is negligible for big ones. The enhancement on the field intensity was calculated for different diameters on the basis of equations 1.6, 1.12, and 1.13. Figure 3.7 (a) is the calculated enhancement factor by considering the non-radiative damping alone. The bulk dielectric function from Johnson and Christy[122] was used, with correction for surface scattering, unless otherwise stated. Note $\omega_p = 1.36 \times 10^{16}$ rad·s$^{-1}$ and $\gamma_{bulk} = 1.1 \times 10^{14}$ s$^{-1}$. As the diameter increases, the calculated non-radiative damping reduces rapidly, resulting in an augmentation of the enhancement factor.

In contrast, radiative damping of the surface plasmon increases non-linearly as the particle size grows. Relying on equations 1.10 and 1.11, the intensity enhancement factor was calculated in Figure 3.7 (b). Radiative damping is negligible for small nanoparticles but not for bigger ones. This leads the enhancement factor to be at a maximum value at small diameters and decrease as the particle size increases.

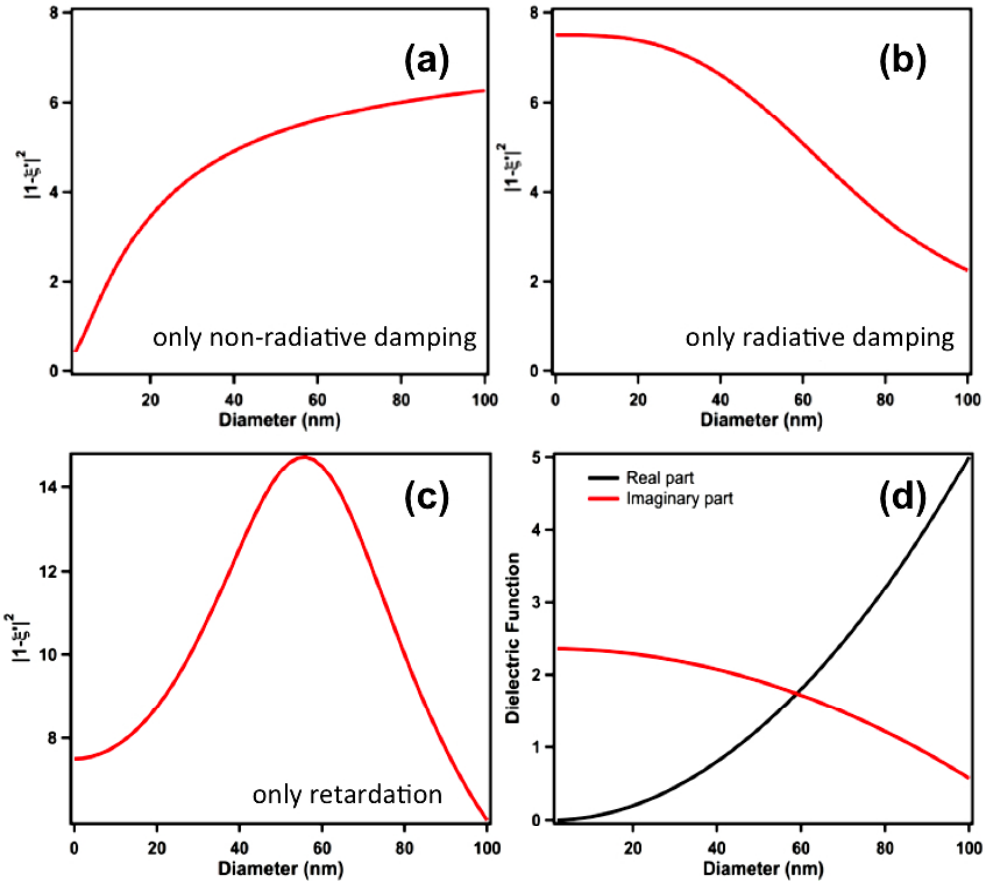


*Figure 3.7: The size-dependence of the field intensity enhancement factor under the influence of each of the three size-finite effects: (a) non-radiative damping, (b) radiative damping, and (c) phase retardation. (d) illustrates the real and imaginary part of the dielectric function given by $3\varepsilon_d k^2R^2 + i\varepsilon_i(1 - k^2R^2)$. The bulk dielectric function from Johnson and Christy was used with correction for surface scattering.*

As to the phase retardation, according to the discussions in section 1.1, we know that it reduces the damping at small sizes but augments the damping at large sizes as the diameter of nanoparticle increases. This results in a trend of the enhancement factor shown in Figure 3.7 (c). The optimized diameter, according to the calculated result, is about 50nm. To better understand this behavior, equation 1.11 is written under resonant conditions as

$$\xi' = \frac{-3\varepsilon_d + i\varepsilon_i}{3\varepsilon_d k^2R^2 + i\varepsilon_i - i\varepsilon_i k^2R^2 + i\varepsilon_d 2k^3R^3 + \varepsilon_i \frac{2}{3}k^3R^3} \tag{3.1}$$

In this experiment, the factor of $k^3R^3$ ($\ll 1$) is negligible when the radius of the particle is smaller than 50nm. When the magnitude of equation 3.1 is at its minimum (i.e., maximum denominator), the induced dipole moment and field enhancement reach a maximum. The denominator of equation 3.1 can be written as

$$3\varepsilon_d k^2R^2 + i\varepsilon_i(1 - k^2R^2) \tag{3.2}$$

We say that expression 3.2 defines a “phase retardation factor”. Both real part and imaginary part of this of this factor were plotted as a function of particle diameter (Figure 3.7 (d)). The intersection of these two curves corresponds to a maximum enhancement factor at 58nm diameter in Figure 3.7 (c). Because of the retardation, the imaginary part of this dielectric function, which constitutes non-radiative losses, reduces with the increasing particle size; while the real part, which constitutes the far-field scattering, increases as particle size augments. For small particles where the non-radiative losses dominate, the decreasing imaginary part results in an increasing enhancement factor of field intensity. As to larger particles where the far-field scattering dominates, the increasing real part leads to a reduction as the particle size rises.

Under the influences of finite-size effects, the enhancement factor of near-field intensity displays a non-linear trend shown in Figure 3.6 (a). To make a comparison between experimental and theoretical data, the calculation was performed on the size of one polymer lobe (i.e. polymer thickness) for each of the diameters of nanospheres.

❖ **Polymer extent**

The polymer thickness is the maximum polymer extent of a hybrid particle. In other worlds, it measures, along the long axis of the hybrid structure, the distance between the particle surface and the frontier of the created polymer structure. Since an incident dose of $D_0 = 75\%D_{th}$ was utilized for the irradiation, a minimum enhancement factor of $F_{nf} = 1/0.75 = 4/3$ was required to initiate the photopolymerization. Therefore, the calculated polymer thickness is the maximum distance between the particle surface and the iso-intensity surface where the enhancement factor equals to $4/3$. This DDA simulation was performed for each diameter and the resulted polymer thicknesses were plotted in Figure 3.8.

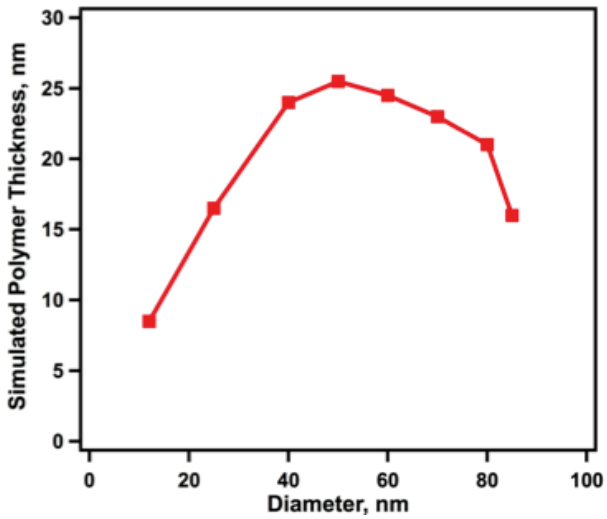


*Figure 3.8: DDA simulated polymer thickness as a function of the diameter of gold nanospheres. A maximum is found at 50nm diameter.*

The simulated polymer thickness increases as the diameter of nanoparticle augments from 12nm to 50nm. It decreases beyond 50nm. This trend is similar to our experimental results in Figure 3.5. Besides, the simulated polymer thicknesses are in the same range of the measured values. It should be stressed that this behavior results from mainly two factors, including the LSPR of nanoparticles and the finite-size effects.

❖ **Surface enhancement factor**

It is remarkable that the polymer thickness reflects the field on the particle surface as well as the distance decay of the near-field away from the nanoparticle. As the diameter increases, the near-field penetrates a longer distance from the surface of the nanoparticle. Besides, the enhancement factor at the particle surface varies also with the particle dimension. However, these two factors cannot be separated by the experimental measurement because neither of them can be measured directly. Therefore, we did a theoretical simulation for the enhancement factor on the surface of gold nanospheres with different diameters. The results are shown in Figure 3.9.

According to the simulated data, the enhancement factor on the surface of the nanoparticle exhibits size-dependence. It is very similar to the trend of polymer thickness. The maximum enhancement factor appears at the diameter of 40nm, which is smaller than the 50nm in the case of the polymer extent.

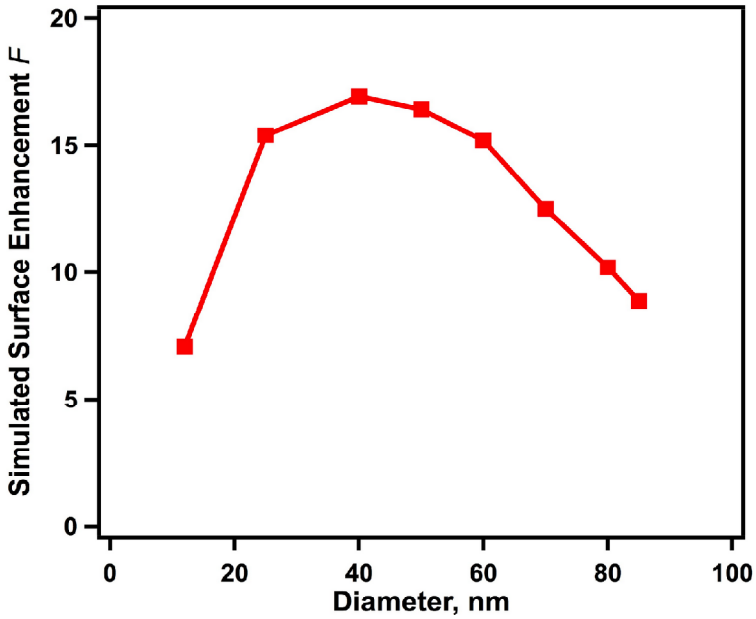


*Figure 3.9: Enhancement factor of the near-field intensity at the particle surface as a function of the diameter of gold nanospheres. A maximum enhancement factor appears at the diameter of 40nm.*

Both experimental measured results and simulated data display a size-dependence of the surface plasmon supported by gold nanospheres. This trend

reflects the finite-size effect in the electrodynamics of the nanoparticles. As captured by our model, the non-radiative dissipation dominates in small nanoparticles, whereas the radiative damping dominates in larger particles. The phase retardation of the surface plasmon helps reducing the non-radiative damping but meanwhile increasing the radiative damping. As a result, the measured data agrees with the theoretical calculated result on an optimum diameter of the nanosphere at 50nm. Nanoparticles larger than the optimum 50-nm size provide smaller field enhancement due to radiative decay and electromagnetic retardation, both of which contribute significantly to damping at larger sizes. As to particles with a diameter smaller than 50nm, their plasmonic fields are relatively weaker due to increased surface scattering of electrons at small sizes. Intermediate size nanoparticles profit from a surprising but beneficial role of electromagnetic retardation. All these effects give rise to the size-dependent trend of near-field enhancement.

## 3.2 Off-resonance excitation of gold nanorods[2]

Photopolymerization in section 3.1 was performed with an incident laser whose wavelength was near the resonances of gold nanoparticles. Significant (compared with particle sizes) polymer thicknesses were obtained because of the on-resonance plasmon excitation. Most of the reported studies on the surface plasmon were carried with an incident wavelength on the resonance of the MNP. The off-resonance case, however, is seldom studied apart from the lightning-rod effect.[126-127] It is due to the weak excited oscillating field that is extremely hard to characterize. In this section, we will report on the spatial distribution of surface charges of the gold nanorods that were excited off-resonance.

The sample of gold nanorods was fabricated by A. Bouhelier from Laboratoire Interdisciplinaire Carnot de Bourgogne, Université de Bourgogne. Figure 3.10 is the SEM image that zooms in one of the numerous regions on a glass substrate. The insert image of a unique nanorod gives the definition of the particle orientation $\theta$, which is the angle of the major axis of the nanorod with respect to the y-axis. A single region contains 11 gold nanorods with different orientations from $\theta = 0° \; to \; 90°$. The major and minor axes of the rods are 235nm and 85nm, respectively. The thickness of the nanorod is 28nm.

[2] *C. Deeb, X. Zhou, D. Gérard, A. Bouhelier, P. K. Jain, J. Plain, O. Soppera, P. Royer, and R. Bachelot. Off-resonant optical excitation of gold nanorods: nanoscale imprint of polarization surface charge distribution.* ***J. Phys. Chem. Lett.*** *2011, 2, 7-11.*

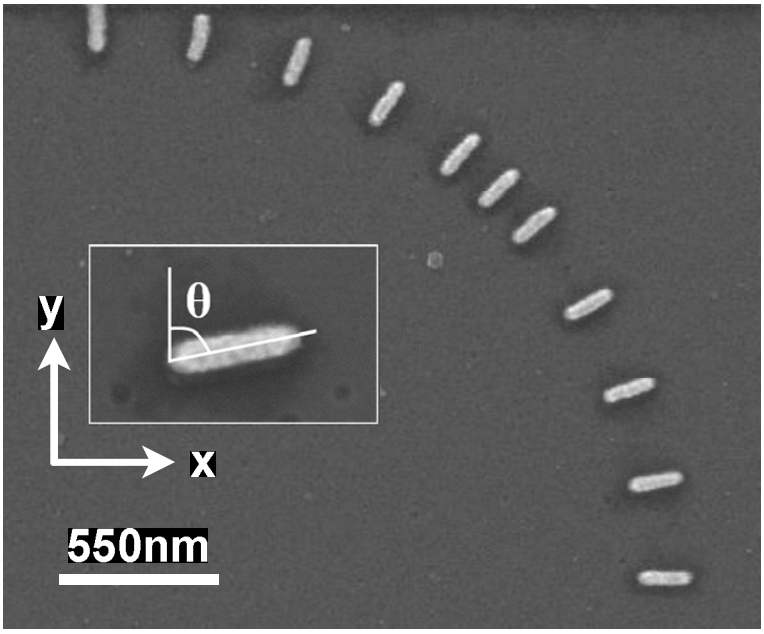


*Figure 3.10: SEM image of the differently oriented ($\theta = 0° \; to \; 90°$) gold nanorods. The insert image gives the definition of the orientation $\theta$ of nanorod: the angle between the major axis and the vertical direction.*

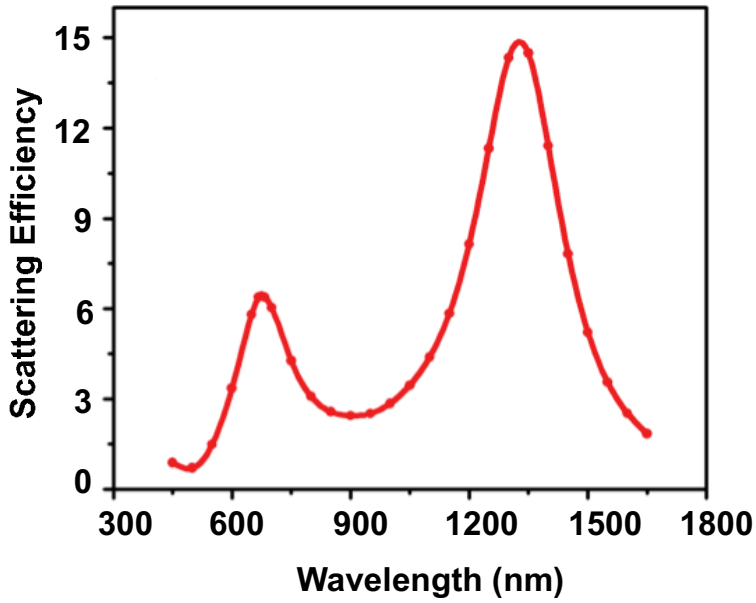


*Figure 3.11: DDA calculated far-field scattering spectrum on a unique gold nanorod that is embedded in a medium of refractive index $n = 1.485$. The two peaks at 662nm and 1313nm correspond to the dipolar LSPR of minor and major axis of the gold nanorod, respectively. Calculation was performed by P. K. Jain.*

The far-field scattering spectrum of a unique gold nanorod was calculated by DDA, as shown in Figure 3.11. This calculation was performed by P. K. Jain. The refractive index of the embedded medium was 1.485, which corresponds to the glass substrate ($n = 1.5$) and the photopolymerizable solution ($n = 1.48$). The dielectric function of gold was described by the experimental data for bulk from Johnson and

Christy without any additional size correction. The spectrum in Figure 3.11 illustrates two peaks at 662nm and 1313nm, corresponding to the dipolar LSPRs of major and minor axes, respectively.

### 3.2.1 Near-field imaging

The differently oriented gold nanorods were first characterized by AFM. Afterwards, the photopolymerization procedure was performed on the sample. We used in this study the photopolymerizable formulation with EY as the photosensitizer. The incident laser with a wavelength of $\lambda = 532nm$ was adopted in this study and the incident dose was $D_0 = 65\%D_{th}$. Polarization of the incident light was chosen to be along the y-axis in Figure 3.10. After exposure, the sample was rinsed with ethanol and isopropanol. Finally the AFM characterization was carried out on the particles that were scanned before photopolymerization.

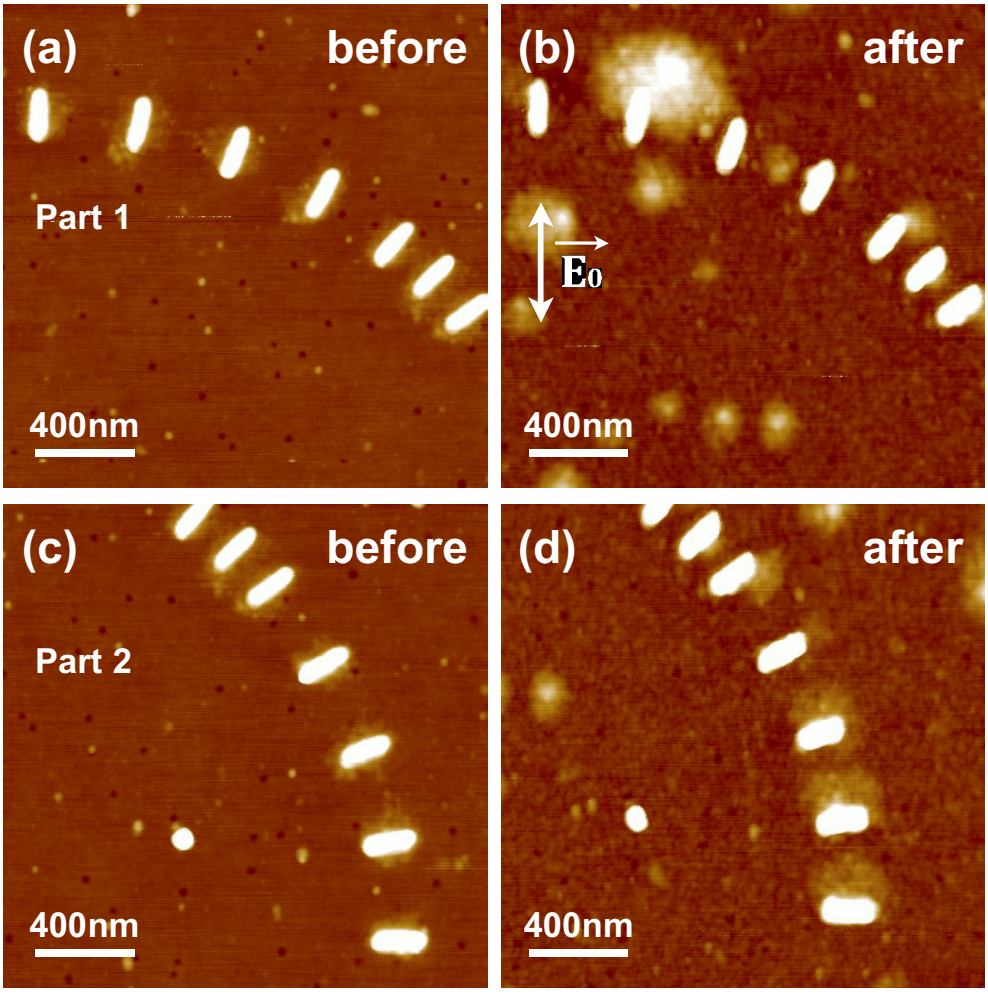


*Figure 3.12: AFM characterization on a region (a, c) before and (b, d) after polymerization. The 11 differently oriented gold nanorods were separated into two parts while scanning in order to guarantee a high quality of AFM image.*

AFM images of a given region before and after photopolymerization process are shown in Figure 3.12. To guarantee a high quality of the image, large AFM scan size should be avoided. Thus, panel (a) illustrates the obtained AFM image of "part 1" of one region of the gold nanorods. Panel (b) is the corresponding image after polymerization. Panels (c) and (d) are the AFM images on the second part of this region before and after the polymerization procedures, respectively. The direction of the electric field in panel (b) labels the incident polarization.

By comparing these images, we can guess a polymer extent along the incident polarization for each of the nanorods. It is clearer in the case of inclined nanorods. Differential AFM images were performed on three typical rods with different orientations of $\theta = 0°$, $22.5°$, and $90°$. The results are shown in Figure 3.13. Panels ($a_1$), ($b_1$) and ($c_1$) are the AFM images before photopolymerization of the three particles: $\theta = 0°$, $22.5°$, and $90°$, respectively. The corresponding AFM images after polymerization are in panels ($a_2$), ($b_2$), and ($c_2$). The last column, involving panels ($a_3$), ($b_3$), and ($c_3$), shows the differential image of each nanorod that highlights the photopolymer nanostructure.

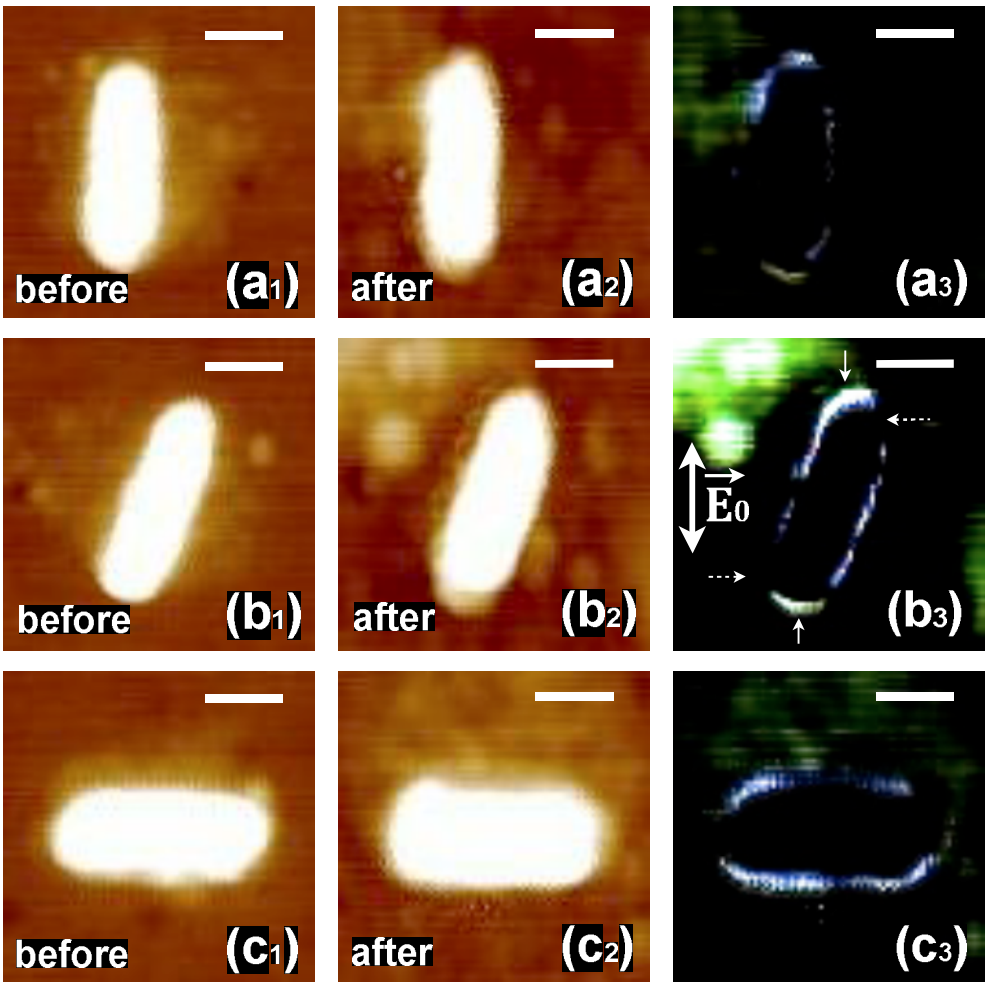


*Figure 3.13: Characterization of the near-field distribution on three differently oriented nanorod: three lines illustrating three different orientations of (a) $\theta = 0°$ (b) $\theta = 22.5°$ and (c) $\theta = 90°$. The three colums correspond to (1) before and (2) after the photopolymerization*

*process, as well as (3) differential AFM image, respectively. The scale bars in all the panels represent 90nm.*

The polymer structure in our approach indicates the plasmon enhancement that allows the energy of local field exceed the threshold of photopolymerization. Therefore, the differential AFM image displays the spatial distribution of free polarization charges excited on the surface of gold nanorods under the incident polarized laser.

For the nanorod whose long axis is along the incident polarization direction (panel ($a_3$) $\theta = 0°$), a maximum polymer elongation appears at both ends. On the two sides of the nanorod, there is a minimum polymer thickness. In the case of the rod whose orientation is $\theta = 90°$ (panel ($c_3$)), the maximum polymer extent appears at the two sides, while no polymer was created at the extremity. The inclined nanorod (panel ($a_3$) $\theta = 22.5°$) exhibits a largest polymer structure at the two points indicated by the solid arrows, while no polymer structure was fabricated at the two points where the two dashed arrows suggest.

We can infer from Figure 3.13 that when the surface normal unit vector $\boldsymbol{n}$ is parallel to the polarization of the incident laser, the maximum photopolymer structure is obtained. In contrast, if the surface normal unit vector is parallel to the incident polarization, no polymer structure is created.

We propose an interpretation to this behavior based on the boundary conditions. The electric field that propagates from metal to dielectric satisfies the Gauss's low (source-free):

$$\boldsymbol{\nabla} \cdot \boldsymbol{D} = 0 \tag{3.3}$$

with the electric displace field $\boldsymbol{D}$ defined as

$$\boldsymbol{D} = \varepsilon_0 \boldsymbol{E} + \boldsymbol{P} \tag{3.4}$$

$\boldsymbol{P} = \chi \varepsilon_0 \boldsymbol{E_0}$ is the polarization density, $\chi$ is the metal electric susceptibility and $\boldsymbol{E_0}$ is the incident electric field. We can deduce from equations 3.3 and 3.4 a relationship between the electric field and the polarization at the metal/dielectric interface:

$$\varepsilon_0 E_{m,n} - \varepsilon_0 E_{d,n} = P_{d,n} - P_{m,n} \tag{3.5}$$

In equation 3.5, the subscript $m$ stands for metal, $d$ for dielectric, and $n$ for the normal factor. The polarization density causes surface polarization charges at the interface[128]

$$\boldsymbol{\nabla} \cdot \boldsymbol{P} = -\rho_{pol} \tag{3.6}$$

where $\rho_{pol}$ is the polarization charge density. Therefore, equation 3.5 can be rewritten as

$$E_{m,n} - E_{d,n} = \frac{\rho_{pol}}{\varepsilon_0} = \chi \boldsymbol{n} \cdot \boldsymbol{E_0} \tag{3.7}$$

Then let us turn our attention back to the differential AFM images of the three nanorods in Figure 3.13. For any given point on the surface of the nanoparticle, when $\boldsymbol{n} \parallel \boldsymbol{E_0}$, according to equation 3.7, the maximum value of surface charge density can be obtained. This finally leads to optical field enhancement and a maximum polymer extent. In contrast, when $\boldsymbol{n} \perp \boldsymbol{E_0}$, the surface charge density equals to 0, which prevent the solution from getting photopolymerized. Therefore, no polymer structure can be obtained.

### 3.2.2 Quantitative near-field measurement

The variations on the dimensions of major and minor axes were measured. For a given nanorod with an orientation of $\theta$, the length of the major axis is measured as shown by the double-arrow in Figure 3.14 (a). In comparison, the dimension of minor axis is measured as Figure 3.14 (b) illustrates. The thickness of the photopolymer was obtained by simply subtracting the value obtained before polymerization from that after the process. The polymer extents along major and minor axes of the nanorod are denoted by $l_M$ and $l_m$, respectively.

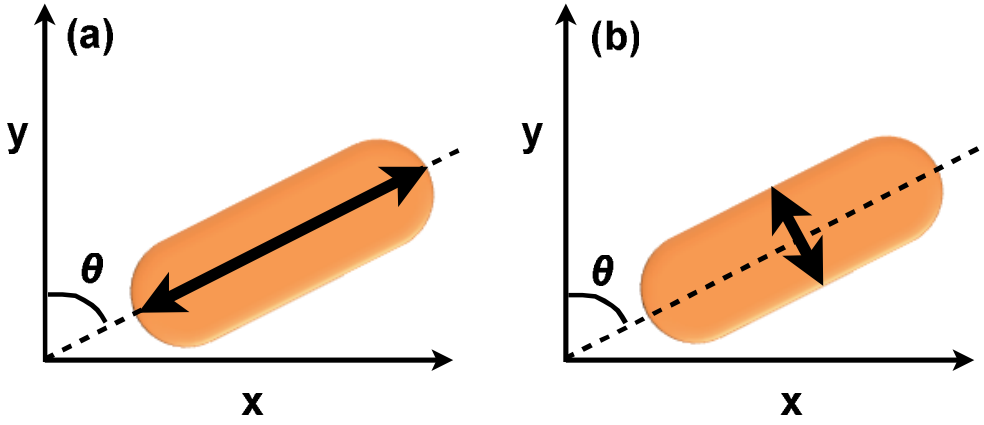


*Figure 3.14: Schemes demonstrating the measurement of (a) major and (b) minor axes of a nanorod, respectively. Polymer elongation along the major axis is noted as $l_M$, while that along the minor axis is noted as $l_m$.*

We collected the AFM images from 4 different regions and the polymer thicknesses of all the 44 nanoparticles were measured. For both major and minor axes at each particle orientation, the average value of the elongations is plotted in Figure 3.15. Error bars denote the standard experimental deviations.

In the case of major axis (Figure 3.15 (a)), the maximum polymer thickness is at $\theta = 0°$, namely, a nanorod whose major axis is aligned with the incident polarization. The polymer size decreases as the particle inclines from the polarization

direction with an increasing $\theta$. Finally, it reduces to 0, i.e. no polymer, in the case of the horizontally oriented nanorod ($\theta = 90°$).

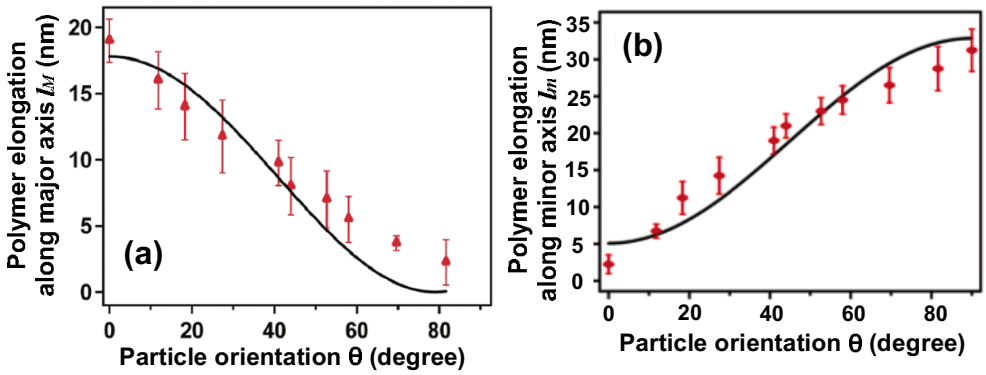


*Figure 3.15: Polymer elongation along (a) major and (b) minor axes of the gold nanorod with an increasing orientation from $\theta = 0°$ to $\theta = 90°$. For each $\theta$, the polymer elongations on four nanorods were averaged and plotted in the figure in red dots. These experimental data are fitted by the black curves: (a) $l_M = l_0(1 + \chi^2 cos^2\theta + 2\chi cos\theta)$, where $\chi = -5.2 \pm 0.1$; (b) $l_m = l_0(1 + \chi^2 sin^2\theta + 2\chi sin\theta) + l_1$, where $\chi = -5.8 \pm 0.3$ and $l_1 = 8.3nm$. $l_0 = \alpha I_0$ was set at 1nm, representing the minimum polymer elongation that can be measured.*

The minor axis displays an opposite trend to the major axis, shown in Figure 3.15 (b). In other words, the polymer elongation along minor axis is at its minimum when the nanorod is oriented along the polarization ($\theta = 0°$). It reaches a maximum value of 32nm as $\theta$ augments to $90°$

Note that in comparison with the maximum polymer elongation along major axis (18nm), the one for minor axis is larger (32nm). We can find an interpretation from the scattering spectrum of the nanorod in Figure 3.12. Although the rods were irradiated off the plasmon resonance, the mode that was closer (minor axis) to the incident wavelength 532nm was excited more efficiently than the other (major axis).

Once the local dose is above the threshold, photopolymerization is initiated. Polymer elongation $l$ is roughly proportional to the local electric field intensity at the surface of the nanoparticle $I_{surf}$

$$l = \alpha I_{surf} \tag{3.8}$$

where $\alpha$ is a coefficient that corresponds to the photo-physical properties of the polymer. At the surface of the nanoparticle, the local electric field is the sum of the incident field and the excited oscillating field. In the situation of quasi-static approximation, the phase difference between the incident field and the induced dipole field is ignorable. Therefore, the field intensity at the particle surface can be expressed as

$$I_{surf} = (\boldsymbol{E_0} + \chi \boldsymbol{n} \cdot \boldsymbol{E_0})^2 \tag{3.9}$$

The field intensity at two ends and two sides of the nanorod, which result in the polymer elongations along minor and major axis, respectively, are written as

$$I_{surf}^{M} = I_0(1 + \chi^2 \cos^2\theta + 2\chi \cos\theta) \tag{3.10}$$

$$I_{surf}^{m} = I_0(1 + \chi^2 \sin^2\theta + 2\chi \sin\theta) \tag{3.11}$$

As a consequence, from equations 3.8, 3.10, and 3.11, the polymer elongation for both axes can be deduced as

$$l_M = l_0(1 + \chi^2 \cos^2\theta + 2\chi \cos\theta) \tag{3.12}$$

$$l_m = l_0(1 + \chi^2 \sin^2\theta + 2\chi \sin\theta) \tag{3.13}$$

with $l_0 = \alpha I_0$ set to be 1nm, representing the minimum elongation that can be detected using AFM. These two equations were utilized to fit the experimental data in Figure 3.15, with an offset $l_1$ in addition to the expression for minor axis. In other words, data in panel (b) was fitted by

$$l_m = l_0(1 + \chi^2 \sin^2\theta + 2\chi \sin\theta) + l_1 \tag{3.14}$$

The black curves in Figure 3.15 illustrate the fitting results. For the major axis, we got an electric susceptibility of $\chi = -5.2 \pm 0.1$ for gold. In the case of minor axis, $\chi = -5.8 \pm 0.3$ and $l_1 = 8.3nm$ were obtained. This offset may result from the greater interface of gold/polymerizable solution along minor axis (rod sides) as compared to that along the major axis (rod ends). It increases the possibility for the formulation to attach on the surface of the nanoparticle and resist rinsing process, even without photo-exposure.

It is remarkable that the average value of our experimentally obtained electric susceptibilities equals to $\chi = -5.5$. We can deduce that the real part of the dielectric function of gold at 530nm is $\varepsilon_r = \chi + 1 = -4.5$, which matches perfectly with the reported value from literature for bulk.[129-130] In our case the measured $\chi$ is local surface susceptibility.

### 3.2.3 FDTD simulations

To confirm our results obtained from the experiments, 3D-FDTD simulations were performed on a single gold nanorod. The numerical simulations were done by P. K. Jain. Our model for the computing has a dimension of 88nm in width and 238nm in length, with a radius of 44nm for the semi-circular end-caps. The embedding medium adopted for the simulation has a refractive index of $n = 1.485$ as the real part and $k = 5.13\times10^{-3}$ the imaginary part. Figure 3.16 shows the FDTD simulated near-field distributions on the three gold nanorods shown in Figure 3.13.

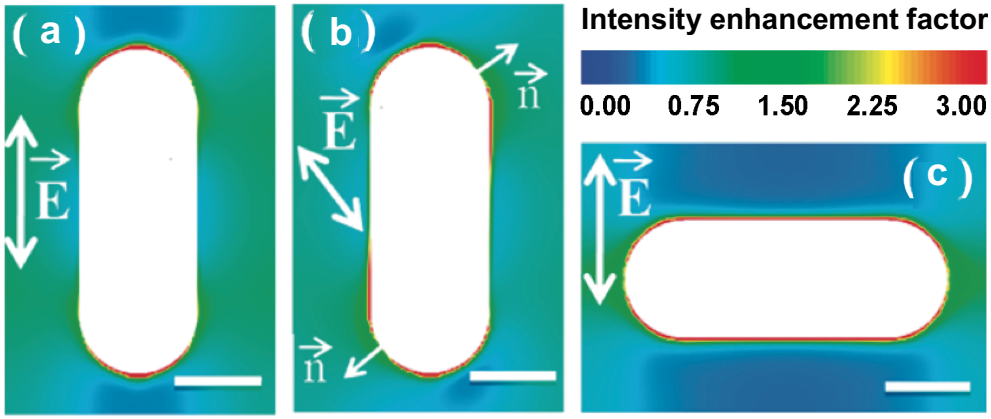


*Figure 3.16: 3D-FDTD simulated near-field distribution of the three gold nanorods in Figure 3.13, whose particle orientations are (a) $\theta = 0°$ (b) $\theta = 22.5°$ and (c) $\theta = 90°$ with respect to the polarization of incident light. The nanorods were embedded in the medium with refractive index of $n = 1.485$. To initiate the polymerization, a minimum enhancement factor of $F = 1/0.65 \approx 1.53$ is required. Error bars represent a length of 90nm.*

In the case of the nanorod that aligned with the polarization, shown in Figure 3.16 (a), the surface charges concentrate mainly at the ends of the rod. It is in great agreement with our experimental result. When the particle is tilted to $\theta = 90°$, which is the case of Figure 3.16 (c), the surface charges are distributed on the two sides of the nanorod. For the particle in Figure 3.16 (b) with an orientation of $\theta = 22.5°$, no surface charges are excited at the points where the white arrows point out. At these two points, the surface normal unit vector is perpendicular to the incident polarization, which leads to the absence of photopolymer.

The calculated near-field enhancement in Figure 3.16 is in great agreement with the experimental photopolymer distribution for the corresponding particle in Figure 3.13. It is noteworthy that the maximum intensity enhancement factor at the surface of the gold nanorod is about 3, which is much lower compared with the on-resonance situation in section 3.1. Such a low enhancement factor in this study comes from the off-resonance excitation of the gold nanorod.

Generally, the off-resonance excitation creates very tiny plasmonic field that is strongly confined at the surface and is extremely difficult to measure. Our technique of the photopolymerization triggered by surface plasmon provides a resolution high enough for both imaging and quantitative measurement of the near-field. The polymer distribution indicates the localized electromagnetic field enhancement associated with the surface charge densities supported by the nanorods. With this technique, the signature of the spatial distribution of the surface charges can be visualized. Finally, it is interesting to notice that in experiment (Figure 3.13), the integrated polymer is not as well-shaped as the simulated result (Figure 3.16). This is due to the fine structure at the surface of the nanoparticle.

## 3.3 Side and corner excitation of gold nanocubes[3]

Metallic nanocubes have attracted much attention because of the complex geometry that comes from different orientation of the corners and the edges. These hot spots provide huge enhancement on such optical phenomena as fluorescence, SERS,[30,75,123] and optical nonlinearities.[124] Most of these studies were performed in the far-field, yet little is known about near-field properties of the nanocubes. Although many theoretical calculations were performed,[30,125] direct experimental measurements on the near-field distribution were rarely reported before our work.

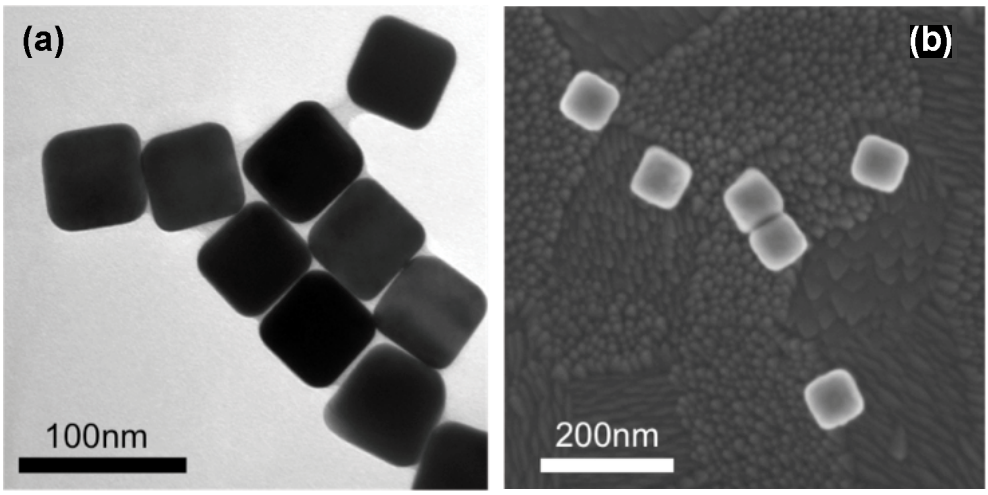


*Figure 3.17: (a) TEM image of gold nanocubes on carbon-coated copper grids and (b) SEM image of the nanocubes on ITO-coated glass substrate.*

The colloids of gold nanocubes were synthesized by S. Marguet from Laboratoire Francis Perrin, CEA Saclay. The edge length of the nanocube is 60±3nm. TEM and SEM images in Figure 3.17 were taken on carbon-coated copper grids and ITO-coated glass substrate, respectively. The size and ROC of the nanocubes are in high level of homogeneity. In our study, the particles were deposited on ITO-coated glass substrates. The thickness of the ITO layer was 3nm.

Figure 3.18 illustrates both experimental extinction spectrum (in red) and the calculated spectrum (in blue) of the gold nanocubes. Calculations in this section were performed by S. K. Gray and R. Miller from Argonne National Laboratory. The experimental spectrum that was collected from the aqueous solution of the nanocubes exhibits a peak at 562nm, which agrees with the theoretical calculated result of 570nm from a unique particle in water.

[3] *C. Deeb, X. Zhou, R. Miller, S. K. Gray, S. Marguet, J. Plain, G. P. Wiederrecht, and R. Bachelot. Mapping the electromagnetic near-field enhancements of gold nanocubes.* ***J. Phys. Chem. C*** *2012, 116, 24734-24740.*

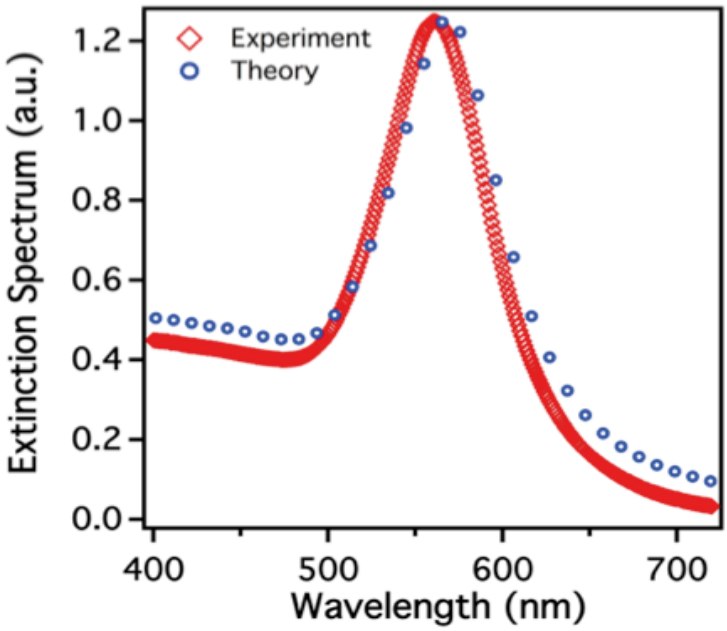


*Figure 3.18: Experimental (in red) and theoretical (in blue) extinction spectra of the gold nanocube in water. The peak at 562nm of the experimental spectrum is in high agreement with the one at 570nm for the calculated spectrum (by S. K. Gray and R. Miller, ANL).*

### 3.3.1 Imprinting of the near-field

After being characterized by AFM (Figure 3.19(a)), the laser exposure was carried out for nanoscale photopolymerization. The polymerizable solution used in this study was the one with EY as the photosensitizer. We utilized an incident wavelength of $\lambda_0 = 532\,\text{nm}$, which is in the absorption band of the nanocubes. Different incident doses, from 5% to 75% with a step of 10% of the threshold dose, were adopted on 8 samples that have been fabricated simultaneously following exactly the procedures introduced in Chapter 2, section 2.4.2. After rinsing procedures, the AFM characterization was carried out again (Figure 3.19(b)) on the nanocubes that were scanned before polymerization.

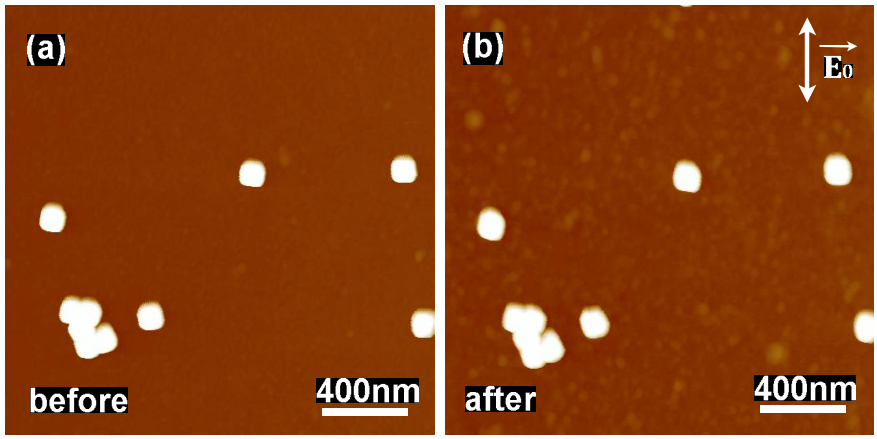


*Figure 3.19: AFM image of the same region (a) before and (b) after the photopolymerization. The incident dose for this sample was $D_0 = 65\%D_{th}$.*

For an individual gold nanocube, the image calculation was performed by subtracting the AFM image taken before polymerization from that of after polymerization. The result, which is called differential AFM image, highlights the near-field. Figure 3.20 shows the differential AFM images of two nanocubes. In panel (a), the diagonal of he nanocube is approximately along the polarization direction of incident laser. We obtained a maximum polymer elongation at the top and bottom corners. At the left and right corners of the cube, no polymer was created. Two edges of nanocube in panel (b) are aligned with the polarization direction. As a result, at the top and bottom side of the cube, maximum polymer elongations are obtained. At the left and right sides of this nanocube, the obtained polymer size is at minimum.

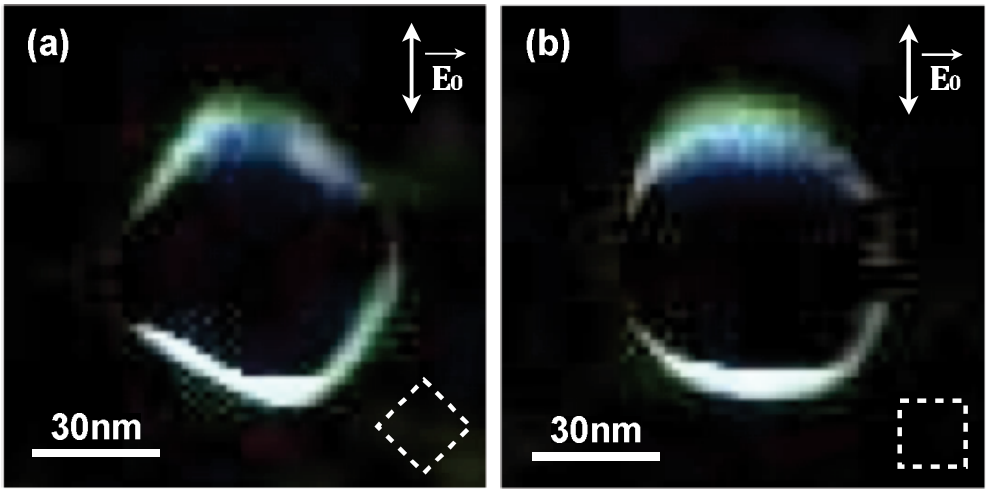


*Figure 3.20: Differential AFM images of two nanoparticles with different orientations. Electron field in both panels represents the incident polarization.*

Based on the differential images, we can draw an inference that for any given point on the surface of nanocubes, when the surface normal unit vector $\boldsymbol{n}$ is parallel to the polarization direction, a maximum polymer extent can be achieved. In contrast, if the surface normal unit vector at that point is perpendicular to the polarization direction, the minimum polymer elongation (or no polymer) is obtained. These results are in good accordance with what has been discussed in previous sections.

### 3.3.2 Quantitative measurement of the near-field with different orientations of nanocubes

As stated above, we used different incident doses for the photopolymerization. Since the colloids of gold nanocubes were randomly oriented, we were allowed to study the polymer elongation at the edges and corners as a function of the particle orientation. To make further discussions more convenient, we give here two definitions of angles (Figure 3.21):

- **Side orientation**, denoted by $\theta_s$ in Figure 3.21 (a), is the angle of surface normal unit vector on the edge of the cube with respect to the polarization direction. The

**side elongation** was measured along the dashed line shown in panel (a). At $\theta_s = 0$ the incident field is perpendicular to the edge.

- **Corner orientation**, denoted by $\theta_c$ in Figure 3.21 (b), is the angle between the direction of the diagonal of the nanocube and the incident polarization. The **corner elongation** was measured along the dashed line shown in panel (b). At $\theta_c = 0$ the incident field is oriented along the diagonal.

The quantitative measurement on the nanocube will demonstrate the plasmon excitation at side and corner. With the polarization kept constant, these two definitions provide an information about the orientation of any given cube and lead to a maximum plasmon field excitation at $\theta = 0$ ($\theta = \theta_s$ for side and $\theta = \theta_c$ for corner).

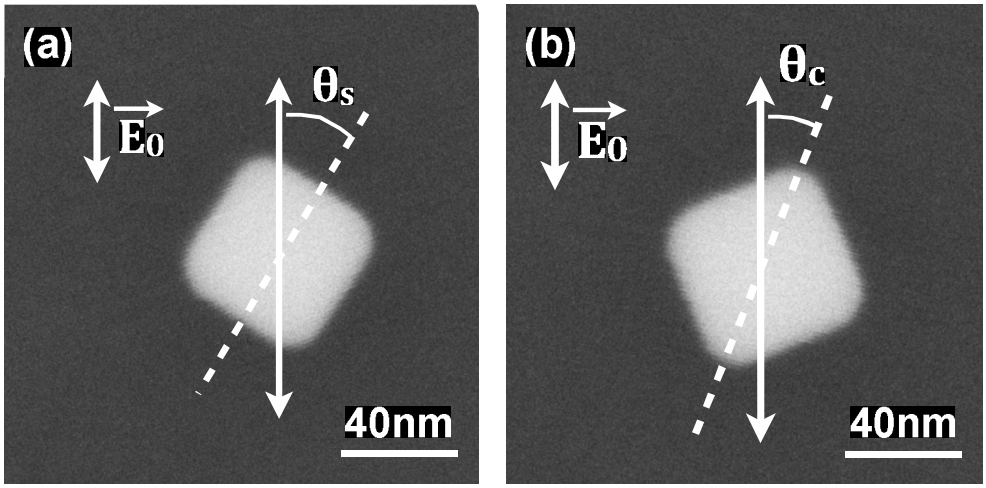


*Figure 3.21: Definitions of (a) side orientation $\theta_s$ and (b) corner orientation $\theta_c$ of gold nanocubes. Double arrows represent the polarization direction. The side and corner elongations were measured along the dashed lines as illustrated in panel (a) and (b), respectively.*

The side elongation (in blue) and corner elongation (in red) of differently oriented nanoparticles under different incident doses were measured and plotted in Figure 3.22. The incident doses from 75% to 5% of the threshold dose were utilized. For each incident dose, about 10 to 15 gold nanocubes were studied. Error bars in this figure represent the lateral resolution of the AFM measurement (±1nm). For the bottom axes of each panel in this figure, $\theta = \theta_s$ for the side elongation and $\theta = \theta_c$ for the corner elongation.

According to Figure 3.22, the side elongation of the gold nanocubes decreases as the side orientation $\theta_s$ varies from 0° to 90°, which correspond to the edge of the nanocube with a surface normal unit vector changing from along the polarization to the direction that is perpendicular to the polarization. At $\theta_s = 90°$, the side elongations are approximately 0. The corner elongation has a similar trend as the side elongation. It decreases as the diagonal of the cube tilts away from the polarization direction (from $\theta_c = 0°$ to $\theta_c = 90°$).

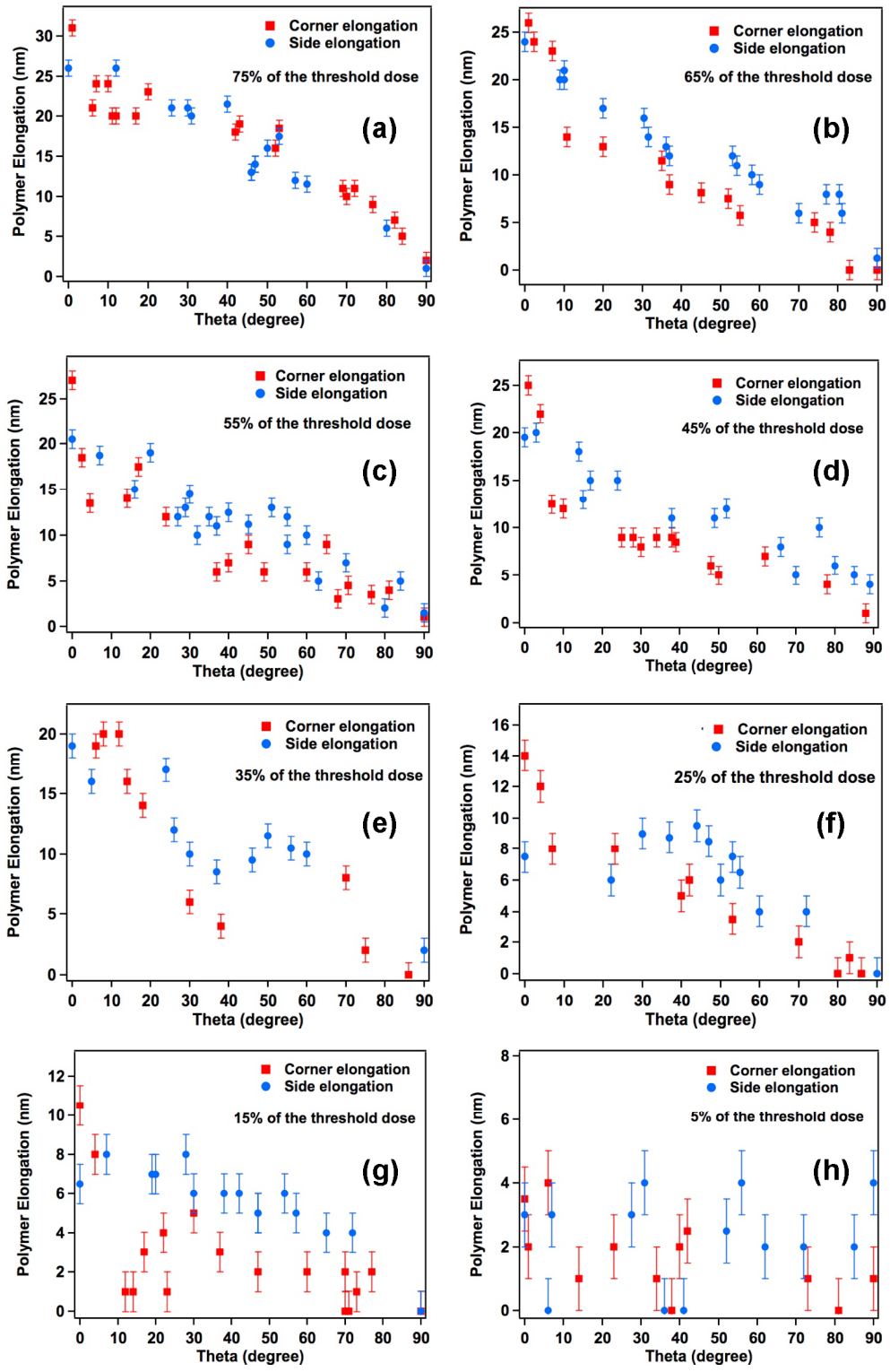


*Figure 3.22: Experimentally measured polymer elongations at corners and sides of the gold nanocubes under different incident doses of exposure. The incident doses utilized were (a) 75%, (b) 65%, (c) 55%, (d) 45%, (e) 35%, (f) 25%, (g) 15%, and (h) 5% of the threshold dose for photopolymerization. $\theta = \theta_s$ for the side elongation, while $\theta = \theta_c$ in the case of corner elongation. The error bars illustrate the uncertainty of the AFM measurement.*

By comparing the side elongation and the corner elongation under a given incident dose, we can see from the figure that the corner is more sensitive to $\theta$ at small angles. Whenever the diagonal of the nanocube tilts only a little bit away from the polarization direction, the corner elongation has a drastic decrease (approximately 50% drop within 10°). In contrast, the side elongation decreases slower at small $\theta_s$. Besides, the corner elongation at small angles is larger than the side elongation. These two effects comes from the presence of a strong charge density near the end points which lead to a larger near-field enhancement at the corner, namely, tip-effect or lightening-rod effect. It is reported to induce very high local field enhancement and has been applied in tip-enhanced optical microscopy.[131] Since the cubes in this experiment have rounded-off corners instead of very sharp ones, the charge density at cube corner is only slightly higher as compared to the cube side.

The trends described above are independent from the incident dose. However, for any given orientation of the nanocube (other than $\theta = 90°$), the polymer extent decreases as the incident dose reduces. Let us take $\theta = 0°$ as an example. The maximum polymer elongation, for both corner and side, was measured at $D_0 = 75\%D_{th}$ (Figure 3.22 (a)); while a minimum polymer elongation was obtained at $D_0 = 5\%D_{th}$ (Figure 3.22 (h)).

It is remarkable that in panel (h), where the incident dose was $5\%D_{th}$, both side and corner elongations fluctuate in a very low level instead of exhibiting an orientation-independence of polymer elongation. This is because that the tiny polymer thickness is very close to the lateral resolution of the AFM measurement (1nm as illustrated by the error bars).

Discussions above are about some general rules in the local field distribution. However, there are always some exceptions in experiment. For instance, the slight augmentation of side elongation from 40° to 50° in panel (e), the smaller side elongation at 0° and 20° compared to larger orientations (30°-50°) in panel (f), the drop of corner elongation to the minimum at roughly 15° in panel (g), etc. These exclusions result probably from the defects on the cube surface, which may induce a variation on the plasmon distribution.

### 3.3.3 Incident dose-dependent polymer elongation

The above results of the polymer elongations can be understood by considering the local dose $D_{loc}$, which decreases exponentially from the particle surface to larger distances:[50]

$$D_{loc} = F_{max} D_0 e^{-\alpha y} \tag{3.15}$$

where $F_{max}$ is the maximum (on the particle surface) enhancement factor of near-field intensity, $\alpha$ is the decay constant of the field intensity, with $\alpha^{-1}$ represents the decay length of the near-field intensity, and $y$ is the distance of the considering point

from the surface of the nanoparticle in Y-axis (shown in Figure 3.23 (a) in the case of a nanocube oriented at $\theta_c = 0°$). To create the nano-scale photopolymer in the vicinity of MNPs, the local dose has to exceed the threshold, i.e., $D_{loc} \geq D_{th}$. Thus, we can obtain from equation 3.15 a condition for polymerization occurs:

$$e^{-\alpha y} \geq \frac{D_{th}}{F_{max} D_0} \tag{3.16}$$

At the frontier of the polymer structure, which is exactly the point whose distance to the particle surface equals the measured polymer elongation, $y$ reaches its maximum value. $y_{max}$ can be deduced from equation 3.16:

$$y_{max} = \alpha^{-1} ln\left(F_{max} \frac{D_0}{D_{th}}\right) \tag{3.17}$$

With $f = D_0/D_{th}$ defined as normalized dose, equation 3.17 can be written as

$$y_{max} = \alpha^{-1} ln(F_{max} f) \tag{3.18}$$

In other words, $y_{max}$ is nothing but the measured polymer elongation. Equation 3.18 shows that the $f$ dependence of $y_{max}$ is of logarithmic nature, which is the signature of the evanescent intensity described in relation 3.18. In the situation of $\theta_c = 0°$, i.e., diagonal of the nanocube is along the incident polarization, the polymer extent at the corners of nanocubes reaches its maximum. At this particle orientation, the experimentally measured corner elongation is plotted in Figure 3.23 (b) as a function of the normalized dose.

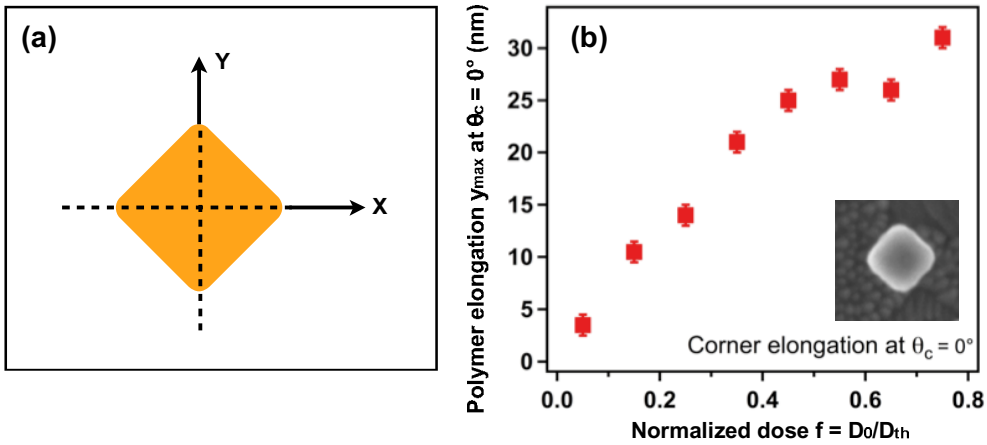


*Figure 3.23: (a) Scheme of a gold nanocube with an orientation of $\theta_c = 0°$. Incident polarization for photopolymerization is along Y-axis. (b) Corner elongation as a function of the normalized dose at $\theta_c = 0°$*

With an incident dose of $D_0 = 5\% D_{th}$, the polymer nanostructure created at the corner of the gold nanocube has a maximum thickness of 4nm. This thickness increases non-linearly as an increasing dose. In equation 3.18, $F_{max}$ and $\alpha^{-1}$ are independent from the incident dose. Therefore, $y_{max}$ increases logarithmically as an

increasing normalized dose $f$. This trend can be read as well from Figure 3.23 (b). In the following we are going to quantify $F_{max}$ and $\alpha^{-1}$ based on precise analysis of the data.

### 3.3.4 Reproducing the evanescent decay of surface plasmons

Based on our technique, the evanescent decay of the surface plasmon can be reproduced. Let us take $\theta_c = 0°$ as an example. Under the incident dose of $D_0 = 5\%D_{th}$, the near-field enhancement factor $F_{nf}$ has to reach a minimum value of $1/0.05 = 20$ to initiate the photopolymerization. It is right the in case of the frontier of the polymer structure, which is the point that is 4nm-away from the corner of the gold nanocube. It is plotted in Figure 3.24 as the first point from left: at the distance of 4nm away from particle surface, the enhancement factor of the near-field intensity is 20. In this way, the enhancement factors for other distances from the surface of the nanocube are plotted as well in Figure 3.24. Each dot corresponds to an incident dose adopted in this study. The enhancement factor exhibits a single exponential decay as the increasing distance from the surface of the nanocube.

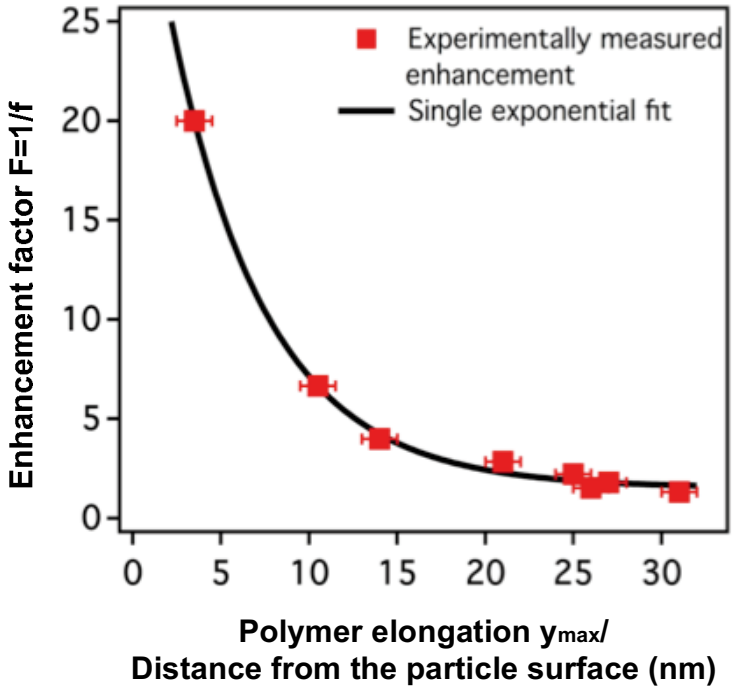


*Figure 3.24: Reproducing the evanescent decay of the surface plasmon: the exponential decay of the intensity enhancement factor as a function of distance from the surface of gold nanocubes. The experimental data are represented in red squares and are fitted with the single exponential decay.*

At the frontier of the polymer structure where the local dose equals to the threshold for photopolymerization, the enhancement factor $F$ is expressed as

$$F = \frac{D_{th}}{D_0} = \frac{1}{f} \tag{3.19}$$

Therefore, it is not difficult to deduce from equation 3.16 and 3.19 that

$$F = F_{max} e^{-\alpha y_{max}} \tag{3.20}$$

Equation 3.20 was used to fit the experimentally measured data expressed in red squares in Figure 3.24. Fitting parameters of $F_{max} = 35$ and $\alpha^{-1} = 5nm$ can be obtained. This indicates an enhancement factor of 35 on the particle surface at the cube corner and a 5-nm spatial extension of the near-field intensity. The decay length $\alpha^{-1} = 5nm$ can be considered as the size of the plasmonic nanosources.

### 3.3.5 Numerical simulations

Other than the experimental measurement, the distribution of the near-field was simulated by DDA for two differently oriented gold nanocubes that correspond to those in Figure 3.20. The simulations were carried out by S. K. Gray and R. Miller. The model for simulation is shown in Figure 3.25. Considering the fine structure of the nanocubes in experiment, the model for calculation did not have sharp corners as an ideal cube. Instead, the corners were modified by spheres with a radius of 12nm.

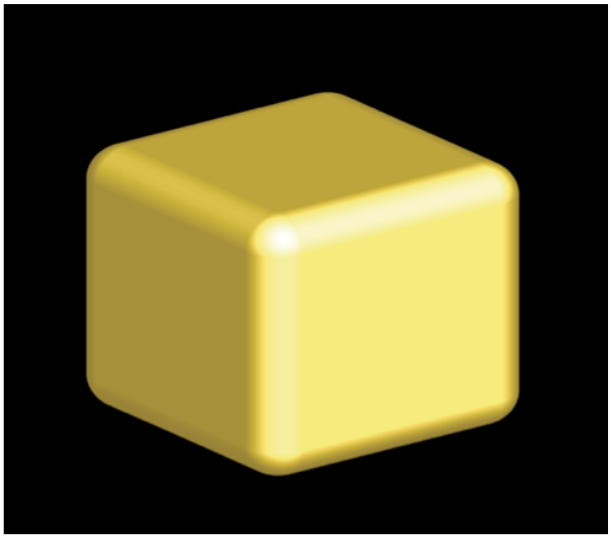

*Figure 3.25: Model of the gold nanocube for calculations. Corners of the nanocube are modified by small spheres of 12nm in radius.*

The refractive index of photopolymerizable solution is in the range of 1.48-1.52. The refractive indexes of ITO and glass substrate are 1.8 and 1.5, respectively. Since the ITO layer coated on the glass is only 3nm in thickness, it seemes reasonable for us to perform the DDA simulation on gold nanocubes embedded in a homogeneous medium with a refractive index of 1.5.

❖ **Field distribution**

Figure 3.26 demonstrates the spatial distribution of simulated field intensity enhancement factor of the differently oriented nanocubes. In this figure, we drew in white color the frontier of the polymer structure fabricated in the vicinity of gold nanocubes. Before this iso-intensity line, polymer structures can be created. However, beyond the line, no polymer can be obtained. The incident dose utilized for the calculation was $D_0 = 25\%D_{th}$. For the nanocube whose diagonal is parallel to the incident polarization (i.e., corner excitation), the simulated result is matching perfectly with the differential AFM image in Figure 3.27(a). A maximum field enhancement can be found at the top and bottom corners of the nanocube. At the left and right corner of the cube, the field enhancement is at its minimum.

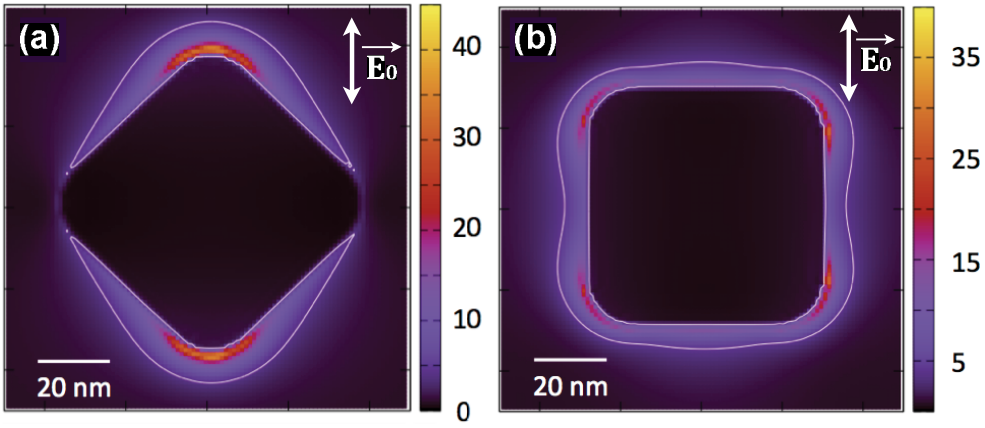


*Figure 3.26: Top views of DDA calculated distribution of the near-field intensity enhancement factor* $F_{nf} = |\boldsymbol{E}_{nf}|^2/|\boldsymbol{E}_0|^2$ *with (a) corner and (b) side excitation of the gold nanocube with different orientations. The white contour lines in both panels represent an enhancement factor of* $F_{nf} = 4$*, which is the frontier of polymer structure with an incident dose of* $D_0 = 25\%D_{th}$.

It is noteworthy that the nanocube in panel (a) is exactly the same as that has been studied experimentally in Figure 3.23 and 3.24. Based on the DDA calculation, we obtained at the top and bottom corners of the nanocube a maximum enhancement factor of the near-field intensity of 45. It decays rapidly with a decay length of 2.7nm. Compared with our experimentally deduced values of $F_{max} = 35$ and $\alpha^{-1} = 5nm$, the calculated maximum field intensity enhancement factor is higher ($F_{max} = 45$) but decreases faster ($\alpha^{-1} = 2.7nm$). It is more likely that our experimental values reflect a spatial average near a given point. Thus, we averaged the simulated values within a sphere of 2nm in radius and obtained a maximum intensity enhancement of $F_{max} = 30$ and a decay length of $\alpha^{-1} = 3.6nm$. These results are much more in agreement with the experiment. Consequently, our nanoscale photopolymerization technique resolves field variations with a remarkable 2nm resolution.

In the case of side excitation of the nanocube (Figure 3.26 (b)), at the points where the surface normal unit vector is parallel to the polarization (i.e. top and bottom sides), the field intensity enhancement is much lower than that in panel (a)

(the top and bottom corners). Besides, the side elongation along the polarization direction is also smaller than the corner elongation shown in panel (a). There is one difference between the theoretical calculation and experimental measurement of side elongation at $\theta_s = 90°$. It is clear from Figure 3.26 (b) that on the left and right sides, polymer thickness is not 0 by calculation. It may due to the propagation of surface plasmon along these two sides. In experiment, however, the existance of irregular defects on the cube surface prevents the propagation of plasmon wave.

❖ **Polymer extent as a function of the cube orientation**

Both corner and side elongations were calculated under the incident dose of $D_0 = 25\%D_{th}$. The theoretical calculated polymer thicknesses as a function of the cube orientation are shown in Figure 3.27, to be compared with Figure 3.22 (f). Evidently, according to this figure, the calculated corner elongation is larger than the side elongation at small angles. Both of them are in the range of 10nm, which matches the experimental measurement. Furthermore, the corner elongation, although not showing a drastic at small angles, decreases faster than the side elongation.

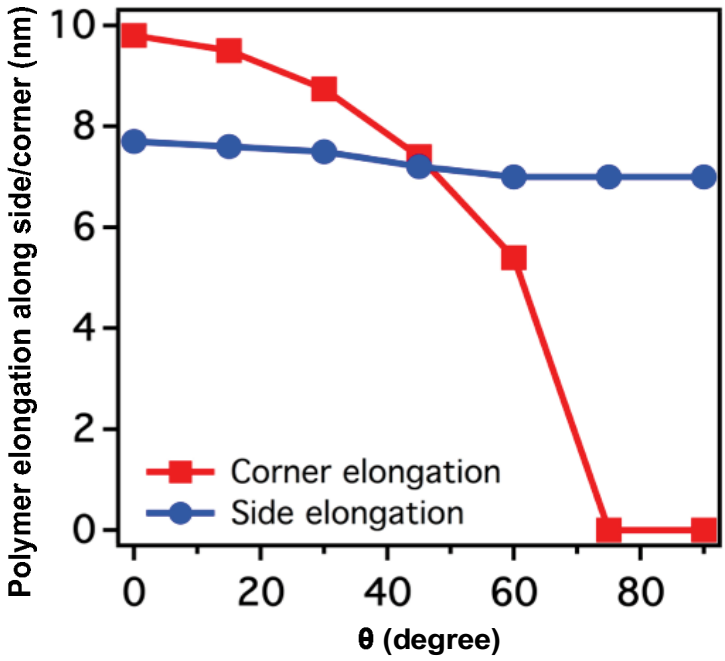


*Figure 3.27: Orientation-dependent corner (red square) and side (blue circle) elongations under an incident dose of $D_0 = 25\%D_{th}$. $\theta = \theta_c$ for corner elongation, while $\theta = \theta_s$ in the case of side elongation.*

However, there exist as well some disagreements between the simulated and the experimental data. The calculated corner elongation does not show a fast decrease at small angles of orientation as the experimental result. Moreover, The calculated side elongation decreases much slower than the experimental one. These differences could result form many aspects. In experiment, the near-field distribution of nanocubes is very sensitive to the fine structure.

## 3.4 Conclusions

The near-field of three different types of gold nanoparticles have been investigated in this chapter. Our method of near-field imaging and quantitative measurements is based on nanoscale photopolymerization. In other words, it is the polymerization triggered only by the local optical electromagnetic field that is enhanced by the surface plasmon supported by MNPs. The created polymer imprints the distribution of the surface plasmon and associated spatial distribution of surface charges on the metal surface. From the experiments, this technique turns out to have an ultra-high resolution of sub 5nm.

Gold nanospheres with diameters from 12 to 80nm were studied. Due to the finite-size effect that has been discussed in Chapter 1, the plasmonic near-field displays non-linear size-dependence with an optimum diameter of 50nm. For particles smaller than 50nm in diameter, the field intensity enhancement augments with the increasing size of the nanoparticle due to the decreasing non-radiative dissipation as well as the phase retardation. In contrast, for larger particles whose diameter is above 50nm, the field enhancement reduces with the increasing of particle size because of a stronger far-field scattering and the retardation. As a consequence, the non-linear trend with a maximum polymer extent at 50-nm diameter was observed via our experimental measurements.

In addition to the near-resonance excitation of the gold nanospheres, a study was carried on the gold nanorods whose surface plasmons were excited off-resonance. A maximum enhancement factor of 3 was achieved, which is much lower than the previous near-resonance excitation. The distribution of this very tiny plasmonic near-field and associated charge density was visualized and measured by our technique on differently oriented nanorods.

Apart from the nanosphere and the nanorod, a more complex structure of nanocube was studied for its interesting effects at the hotspots. With different cube orientations, the variations of the near-field at both corner and side of the gold nanocubes were measured. A maximum enhancement factor of 35 was obtained at the corner of the cube whose diagonal is aligned with the incident polarization during polymerization. For small angles, the plasmon-enhanced field intensity at the corner is higher than that at the side of the nanocube. More importantly, this value decreases much faster compared with the side as the orientation angle increases. Also, based on this technique, we reproduced and quantified the evanescent decay of the surface plasmon at the corner of nanocubes.

As can be seen from the differential AFM image for all the nanoparticles studied, the distribution of surface charges obeys the boundary conditions at metal/dielectric interface. This makes the oscillating field intensity at any point on the particle surface to be proportional to $\boldsymbol{n} \cdot \boldsymbol{E_0}$. As a consequence, maximum polymer extents were observed from points where $\boldsymbol{n} \parallel \boldsymbol{E_0}$, while no polymer can be created whenever $\boldsymbol{n} \perp \boldsymbol{E_0}$ is satisfied.

From the studies in this chapter, our method of surface plasmon based nanoscale photopolymerization has become a quite sophisticated tool with high resolution to characterize the near-field. In the case of dipolar excitation, the obtained metal/polymer hybrids are anisotropic. With some sensitizer dye molecules imprisoned by the polymer, these hybrid structures could be utilized as surface plasmon enhanced light-emitters that are sensitive to the incident polarization. Unlike the reported nano-emitters, this hybrid nanostructure emit light anisotropically due to its geometry. The coming chapter deals with surface enhanced fluorescence and Raman scattering based on this hybrid system.

# CHAPTER 4

# Active Hybrid Plasmonics

By providing us convincing high-resolution images as well as the quantitative information on surface plasmons, the hybrid structure of MNP/ polymer has already served as an effective and sophisticated tool for near-field characterizations. Meanwhile, the indispensable component of photosensitizer dye allows the hybrid nanostructure to act as a nano-emitter (NE).

In the reported configurations of hybrid NEs, organic fluorophores or QDs were combined homogeneously to the MNP.[60,101-102,106] It is undeniable that these structures have contributed significantly to the fundamental studies on the interactions between metal and dye/QD interactions. However, the isotropic nature of these hybrid nanostructures prevents the incident light from selecting any specific emission mode (i.e., switch on/off plasmon enhanced emission). Wang and coworkers reported in 2009[132] a polarization dependent plasmon-enhanced fluorescence on a gold nanorod/dye doped silica core/shell hybrid nanostructure. The dyes were distributed homogeneously in the isotropic silica shell. The polarization dependence was resulted from the excitation of different plasmon modes of the gold nanorod, namely, the long axis and short axis modes. In other words, the distribution of dye molecules constituting the gain medium did not contribute to the anisotropic effect.

This chapter presents how the incident light (polarization) can control the optical properties of our NE. Both fluorescence and SERS analysis were performed. We are going to start with a symmetric metallic nano-object (gold nanosphere) to verify *via* fluorescence spectroscopy the inhomogeneous nature of our light-emitting hybrid nanostructure. Afterwards, a SERS study of the hybrid system based on dimers of gold nanodisks will be presented. Note that both studies were carried out on individual hybrid NEs.

## 4.1 Polarization-dependent fluorescence on a gold nanosphere-based hybrid nano-emitter[4]

In our case, the fluorescence is polarization dependent because the concentration of dye molecules is higher inside than outside the dipolar nano-

[4] *X. Zhou, C. Deeb, R. Vincent, T. Lerond, P.-M. Adam, J. Plain, G. P. Wiederrecht, F. Charra, C. Fiorini, G. Colas des Francs, O. Soppera, and R. Bachelot. Polarization-dependent fluorescence from an anisotropic gold/polymer hybrid anisotropic nano-emitter. Accepted by* ***Appl. Phys. Lett.*** *Dec. 2013.*

polymer structures. The gold nanosphere was selected in our study for its geometric homogeneity, which makes it the best candidate to avoid the anisotropic contribution of MNP to the surface plasmon enhanced fluorescence. To recognize a certain nanoparticle from numerous randomly distributed colloids, Au landmarks were fabricated on the glass substrate by EBL. The functionalized substrate was dip-coated into the aqueous solution ($4.8\times10^{12}\ L^{-1}$) of 70-nm diameter gold nanospheres for 1.5hrs. The scattering spectrum on gold nanosphere with the same size can be found in Chapter 2, section 2.5.3. Figure 4.1 is an AFM image of a $5.5\mu m\times5.5\mu m$ region of the sample. The distance between any two nanoparticles in this selected region is larger than 1μm. Under this condition, we are confident that the fluorescence signal is collected from a unique NE.

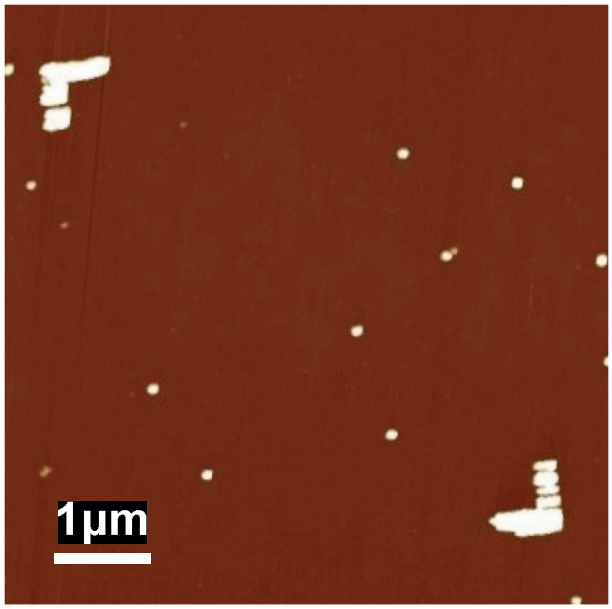


*Figure 4.1 : AFM image on a 5.5μm ×5.5μm region of the sample of 70-nm diameter gold nanospheres.*

For the hybridization, the photopolymerizable formulation with EY (0.5%wt) as the sensitizer dye was adopted. The $\lambda_0 = 532nm$ laser with an incident dose of $D_0 = 70\%D_{th}$ were chosen for the exposure. The obtained light-emitting hybrid nanostructure was characterized both topographically with differential AFM image and optically with fluorescence spectroscopy.

### 4.1.1 Topographic characterization of the NE

In Figure 4.2, panel (a) shows the typical differential AFM image of a unique gold/polymer hybrid nanostructure. $\boldsymbol{E_0}$, along the Y-axis, represents the polarization direction of the incident laser for photopolymerization. The incident laser was propagating along Z-axis (perpendicular to the XOY plane). Panel (b) illustrates its cross-section profile along the long axis of the hybrid structure (dashed line in panel (a)). The two peaks correspond to the two integrated polymer lobes whose average

thickness is 15nm (full width of the peaks). Some residuals can be clearly recognized on the background.

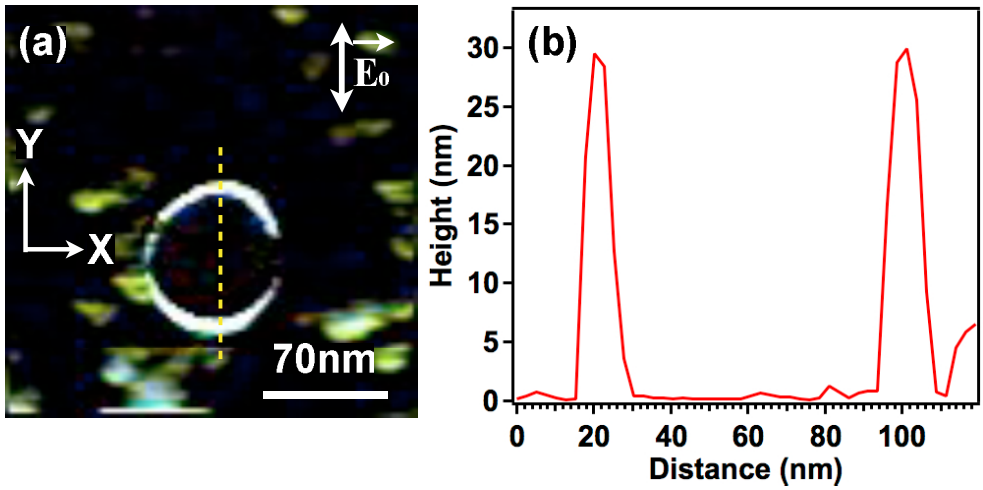


*Figure 4.2: (a) Differential AFM image of a unique nanoparticle. (b) Profile of the cross-section along the dashed line in panel (a). The average polymer thickness is 15nm.*

### 4.1.2 *Optical characterization of the NE: polarization dependent plasmon-enhanced fluorescence*

During the photopolymerization, not all the molecules of photosensitizer dye in the volumes of photopolymer structures were excited to the triplet state to help forming radicals. This has been proved by the detection of EY emission signal in Figure 2.17 in Chapter 2 from a polymer tip. Thanks to the unbleached dye molecules that survive from photopolymerization, the hybrid structure can behave as a nano-emitter whose optical properties can be characterized by fluorescence microscopy. The absorption and emission spectra of EY molecules in polymer can be found in Chapter 2.

Fluorescence signals from EY were collected from an isolated well-characterized Au/polymer hybrid structure whose profile is shown in Figure 4.2. An inverse microscope with an objective of $40\times/0.6NA$ was utilized for both excitation and collection. A $\lambda_{ex} = 514nm$ laser of $15\,\mu W/\mu m^2$ in power at the focus of the objective was utilized for excitation. The emission signal was purified by a [530-570] nm band-pass emission filter and was focused at the output of microscope into a spectrometer, with which we can choose to detect the signal from an individual NE. The selection of different emission filters leads to a different shape of emission spectra of EY in Figure 4.3 (530-570nm band-pass filter) as compared to Figure 2.17 (514nm high-pass filter). However, for both figures, the maximum emission was found at $\lambda_{em} = 555nm$.

In this study, dye molecules at four types of positions were considered (Figure see Figure 4.3 (a) and (b)): 1) on the background (BG) far from the nanostructure (i.e. far-field emitters); 2) outside the polymer but close to the nanoparticle; 3) inside the

polymer and can be enhanced by applying either X or Y incident polarization; and 4) inside the polymer and can be activated by the near-field only with Y polarization. The concentration of molecules at positions 3 and 4 is higher than positions 1 and 2.

We used two different incident polarizations to excite different emission modes, short axis and long axis modes, of our NE. In order to make further discussions easier, here we give two definitions of the fluorescence spectra (see also Figure 4.3):

- **Sx**: fluorescence signal excited with an incident polarization **perpendicular** to the long axis of the hybrid MNP/polymer structure. Fluorescence of molecules at positions 2 and 3 are enhanced by the near-field.
- **Sy**: fluorescence signal excited with an incident polarization **Parallel** to the long axis of the hybrid MNP/polymer structure. Fluorescence of molecules at positions 3 and 4 are enhanced by the near-field.

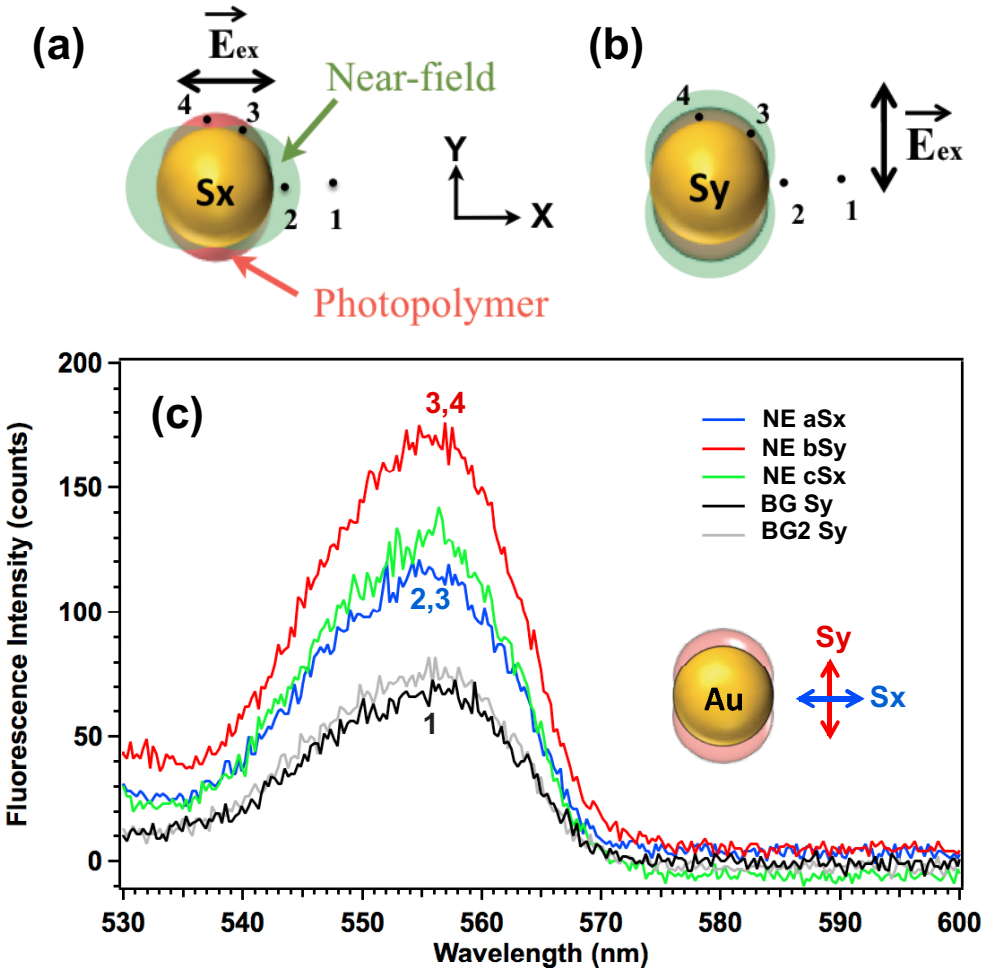


*Figure 4.3: Scheme of the definitions (a)Sx and (b)Sy. (c) Fluorescence spectra of EY molecules from the individual NE whose profile was shown in Figure 4.2. Spectra were collected following a chronological order of a-b-c, corresponding to incident polarizations of y-x-y. The spectra on the background, BG in black and BG2 in grey, were collected from two different points on the substrate without the presence of any gold nanoparticle.*

Figure 4.3 (c) illustrates the fluorescence spectra of EY molecules from an individual NE excited under both incident polarizations as well as the signal on the background. The acquisition of each spectrum took 15sec. Signals were collected following a chronological order of a-b-c shown in the legend. In other words, we started with an incident polarization perpendicular to the polymer lobes (aSx in blue), for which the emission of the trapped EY molecules are not enhanced by the surface plasmon supported by the nanoparticle. Then an incident polarization along the polymer lobes (bSy in red) was adopted to excite these molecules by near-field. To reproduce the result, the polarization was rotated back to collect the Sx (cSx in green). In order to avoid any difference in fluorescence intensity that arises from the polarization sensitivity of the optical system, we oriented the sample by 90° to excite different modes of the NE instead of really rotating the polarization of the incident light.

Figure 4.3 provides 3 important pieces of information about the hybrid NE:

First, the background signals (BG and BG2), which were collected from two different points on the substrate over 2-μm away from the NE, are not equal to 0. Although a slight difference exists between BG and BG2, intensities of both spectra are much lower than that on the NE. Thus, it is fair enough to believe that fluorescence signal on the background is quite stable as the detecting region varies. Emission signals on the background indicate that some EY molecules remain on the substrate after rinsing process. Residuals of the photopolymer can be even recognized in the differential AFM image (Figure 4.2 (a)). The cleaning of the substrate is definitely one of the main issues for future studies.

Second, Sx on the NE is higher than the BG. This difference describes the modification to the emission of EY molecules by a gold nanoparticle. The experimental measurement indicates an enhancement of the fluorescence from an average of 68 to 115 counts. With the presence of MNP, according to equations 1.25, 1.26 and 1.27, the emission rate is modified by i) surface plasmon-enhanced local optical electromagnetic field, ii) the radiative rate of the dye, and iii) the energy transfer from dye molecules to the nanoparticle. The enhancement involves the modifications to both excitation rate and quantum yield, which will be calculated in section 4.1.2.

Third, we obtained from the NE a higher Sy (170 counts) than Sx (115 counts). Seen from this figure, the cSx is slightly higher in intensity than aSx. This indicates a fluctuation of signal. Although instability exists, the two Sx spectra are in another level compared with the Sy. Two effects are primarily responsible for this difference of emission intensity: i) a higher concentration of EY molecules (approximately 4 molecules per $10\times10\times10nm^3$ volume) are excited by the near-field when collecting Sy as compared to Sx and ii) the near-field of nanosphere contributes to the enhancement of the emission signal of EY molecules that are trapped in polymer lobes. The anisotropy of our hybrid NE can be described by the ratio of BG-corrected fluorescence intensities $(\mathrm{Sy}-\mathrm{BG})/(\mathrm{Sx}-\mathrm{BG})\approx 2.2$. This ratio results from the larger

number of molecules that is excited by the near-field when the incident polarization is overlapping with the dye-doped polymer.

It is remarkable that the refractive index of the surrounding medium is responsible for the fluorescence intensity via modifications to the quantum yield of the dye. Theoretical calculations of Härtling et al.[56] confirmed a lower $\gamma_{em}/\gamma_{em}^{0}$ in a dielectric medium (immersion oil) of higher refractive index. As has been discussed above, the signal of BG is an evidence for the existence of EY molecules outside the polymer lobes. These molecules are covered by the residuals of the organic products (e.g. PETIA) instead of exposing directly in air. Based on this assumption, all the molecules of EY are considered as in a photopolymer environment.

In order to highlight the anisotropy of the NE, we subtracted the spectrum aSx from bSy. The resulted differential spectrum is shown (in red) in Figure 4.4 (a). The differential spectrum on the BG is also plotted (in black) in this figure as a reference. The fluorescence of EY on the substrate without the presence of gold nanoparticle shows no polarization dependence. In comparison, the NE exhibits a positive differential result. This indicates a higher fluorescence signal when the near-field is exciting the long axis than the short axis of the NE.

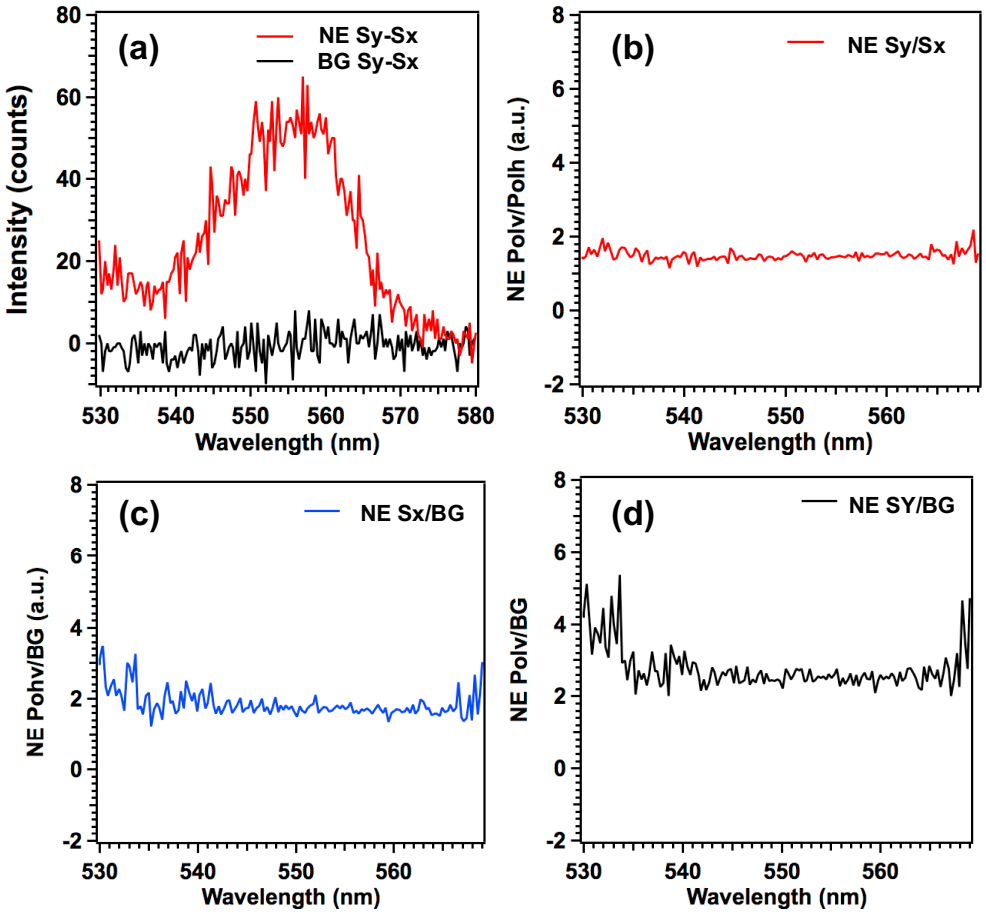


*Figure 4.4: (a) Differential fluorescence spectra of Sy-Sx on both NE and BG. The BG exhibits no polarization dependence, while the NE displays a higher Sy than Sx. (b) NE Sy/Sx illustrating the ratio of fluorescence intensities of the long-axis mode to the short-axis mode of*

*NE. (c) NE Sx/BG representing the normalized emission rate, i.e., the enhancement factor of the emission rate caused by the presence of the gold nanoparticle. (d) NE Sy/BG, the BG-normalized long axis mode emission.*

To get the exact enhancement factor of the fluorescence intensity, we plotted the ratio of the spectra Sy to Sx for the NE (Figure 4.4 (b)), the ratio of Sx on NE to BG (Figure 4.4 (c)), and the ratio of Sy on NE to BG (Figure 4.4 (d)). The rotation of near-field is controlled by varying the incident polarization. At some polarizations, the near-field overlaps with the presence of the gain medium. It is not the situation for other incident polarizations. This leads to a variation of emission intensity as polarization changes. According to panel (b), the fluorescence signal excited by an incident polarization along the long axis is 1.5 times higher than that along the short axis. This, as has been discussed above, is primarily due to the excitation of larger number of molecules by the near-field (because the near-field overlaps with the gain medium). The ratio of Sx/BG in panel (c) indicates an enhancement factor of 1.7 due to the presence of gold nanoparticle. Panel (d) illustrates the BG-normalized emission of the NE with its long axis excited by the surface plasmon. The ratio of 2.5 is a result of both nanoparticle-enhanced emission rate as well as the anisotropic EY distribution (more molecules along the long axis of NE).

For an individual molecule, as it has been discussed in Chapter 1 Section 1.2, distance and dipole orientation play a crucial role on its emission rate. At a given particle-molecule separation distance, a molecule is excited most efficiently when its molecular dipole is oriented along the local electric field. The emission of molecules is quenched at small separation distance but enhanced at larger distance. It is worth noticing that our experiments allow the measurements on neither molecular orientation nor separation distance for dye molecules. The measured enhancement factors were averaged from numerous EY molecules with different orientations and distances to the surface of the gold nanoparticle. To have a general impression about the modified fluorescence, we performed some calculations based on Mie theory for the emission. Throughout the calculations, an averaged molecular orientation was adopted.

### 4.1.3 Mie calculations

Our hybrid nano-emitter has a complex configuration with different concentrations of dye molecules surround the MNP. For the moment, we are not able to do a calculation on its anisotropy. We calculated the normalized emission rate on an individual molecule based on Mie theory. In other words, it is a calculation on the emission rate of a single molecule when moving it from position 1 to position 2 in Figure 4.3 (a). The emission from an individual molecule near an antenna, according to previous discussions in Chapter 1, is determined by excitation rate $\gamma_{em}$, modified quantum yield $Q$, as well as the emission diagram. Both components depend on the molecular dipole moment $\boldsymbol{p}$. So the emission rate can be thus written as

$$\gamma_{em}(\boldsymbol{p}) = \gamma_{ex}(\boldsymbol{p})\, Q(\boldsymbol{p}) \tag{4.1}$$

with $Q$ the modified quantum yield given in equation 1.27 and the excitation rate $\gamma_{ex}(\boldsymbol{p})$ influenced by both dipole moment and the local electric field by $\gamma_{ex}(\boldsymbol{p}) \propto |\boldsymbol{E}_{loc} \cdot \boldsymbol{p}|^2$.

The electric field distribution is calculated on the basis of Mie theory on solving Helmholtz equation in a divergence-less field. This method provides exact solutions (expansions) of the local field in vector spherical harmonics and Mie coefficients. The local field is expressed as the sum of incident and scattered field, whose exact solutions can be obtained respectively. More details about this calculation method will be presented in appendix. Theoretical calculations in this study were performed by R. Vincent form LNIO, UTT. Figure 4.5 presents the field intensity enhancement factor near a gold nanosphere with a diameter of $d = 70nm$ in air (panel (a), $n = 1$) and in the photopolymer (panel (b), $n = 1.48$). The direction of the local electric field is presented by the white arrows.

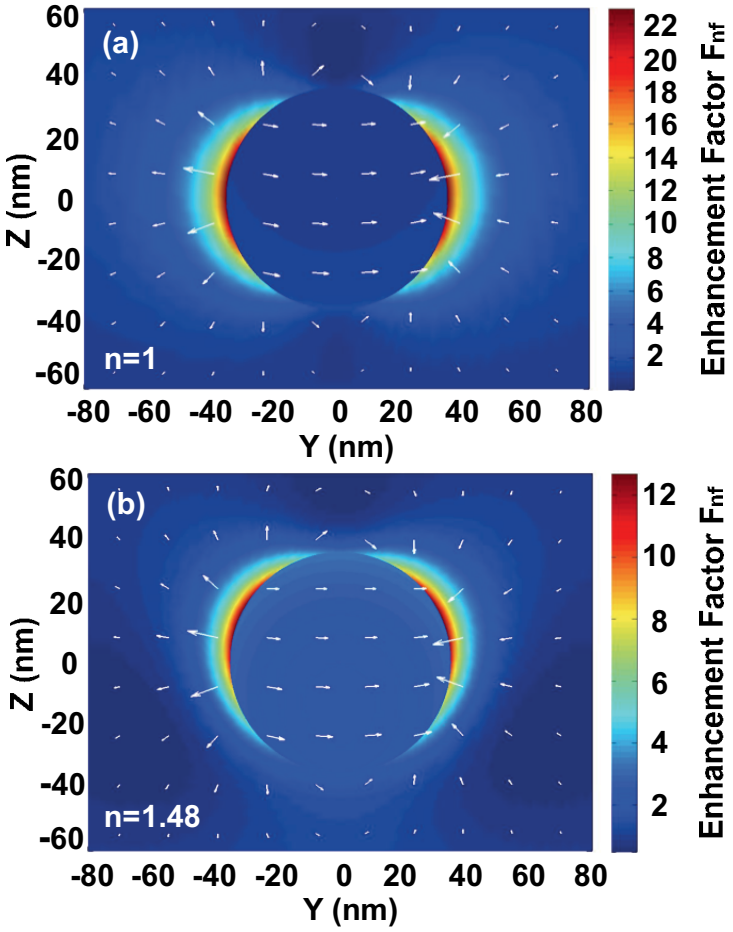


*Figure 4.5: Calculated electric field distribution of a $d = 70nm$ gold nanosphere (a) in free space and (b) in a typical medium of $n = 1.48$, corresponding to the photopolymer. The wave vector of the laser ($\lambda_{ex} = 514nm$) is along the Z-axis from bottom and the polarization is along the Y-axis. The white arrows represent the direction of local electric field.*

In air, the radius of gold nanospheres is much smaller than the excitation wavelength ($r \ll \lambda_{ex}$). The resulted dipolar field reaches a maximum field intensity

enhancement factor of 22 on the nanoparticle surface. In polymer, the effective wavelength is $\lambda'_{ex} \approx 347nm$ due to a higher refractive index of $n = 1.48$. Under this effect, the size of gold nanosphere still satisfies, however weakens, the condition of $r \ll \lambda'_{ex}$. This leads to a very slight excitation of plasmon modes of higher order, which finally results in the inclination of highest field by a polar angle away from the Y-axis (see panel (b)). A maximum field intensity enhancement factor of 12 was obtained in polymer. It is worth noticing that the inclination of dipoles happens in YOZ plane. Our differential AFM image, however, characterized the NE in XOY plane, in which this inclination cannot be observed.

As has been presented above, the molecular dipole orientation, which influences both excitation rate and quantum yield, is not yet controllable in our system. Therefore, the emission rate in this calculation was averaged by three molecular orientations along X, Y and Z-axes, respectively (one component perpendicular and two others parallel to the particle surface)[133-134]

$$\langle \gamma_{em} \rangle = \frac{1}{3}\left[\gamma_{em}(\boldsymbol{p}_x) + \gamma_{em}(\boldsymbol{p}_y) + \gamma_{em}(\boldsymbol{p}_z)\right] \tag{4.2}$$

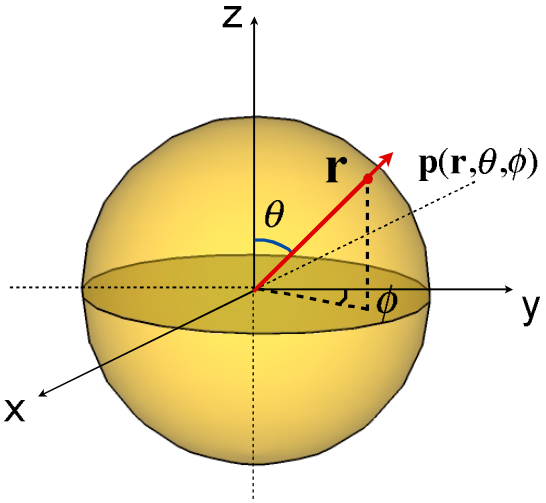


*Figure 4.6: Scheme of spherical coordinates $(\boldsymbol{r}, \theta, \phi)$.*

In spherical coordinates $(\boldsymbol{r}, \theta, \phi)$, shown in Figure 4.6, the emission rate of dye molecules modified by MNPs can be written as

$$\langle \gamma_{em} \rangle = \frac{1}{3}\left[\gamma_{ex}(\boldsymbol{p}_r)Q(\boldsymbol{p}_r) + \gamma_{ex}(\boldsymbol{p}_\theta)Q(\boldsymbol{p}_\theta) + \gamma_{ex}(\boldsymbol{p}_\phi)Q(\boldsymbol{p}_\phi)\right] \tag{4.3}$$

where $\boldsymbol{p}_r$, $\boldsymbol{p}_\theta$, and $\boldsymbol{p}_\phi$ are the components of molecular dipole moment. In equation 4.3, $Q(\boldsymbol{p}_r)$ is the quantum yield of the molecule whose orientation is perpendicular to the particle surface, while $Q(\boldsymbol{p}_\theta) = Q(\boldsymbol{p}_\phi)$ are associated to the molecules parallel to the surface of nanoparticle. Therefore, this equation can be simplified as

$$\langle \gamma_{em} \rangle = \frac{1}{3}\left[\gamma_{ex}(\boldsymbol{p}_r)Q(\boldsymbol{p}_\perp) + Q(\boldsymbol{p}_\parallel)\left(\gamma_{ex}(\boldsymbol{p}_\theta) + \gamma_{ex}(\boldsymbol{p}_\phi)\right)\right] \tag{4.4}$$

where $\boldsymbol{p}_{\parallel}$ and $\boldsymbol{p}_{\perp}$ represent the molecular dipole parallel and perpendicular, respectively, to the surface of the MNP. Excitation rate is influenced by local field *via* $\gamma_{ex}(\boldsymbol{p}_i) \propto |\boldsymbol{E}_{loc} \cdot \boldsymbol{p}_i|^2$ for each component $i = r, \theta, \phi$ at any given point outside the nanosphere.

In free space, $\boldsymbol{E}_{loc} = \boldsymbol{E}_0$. And $\gamma_{rad} = \gamma_{rad}^0$ leads to $Q(\boldsymbol{p}) = q$ (equation 1.27). Consequently, the dipole orientation-averaged emission rate of dye molecules without the presence of MNP can be written as

$$\langle \gamma_{em}^0 \rangle = q\gamma_{ex}^0(\boldsymbol{p}_r) \tag{4.5}$$

With $\boldsymbol{E}_0$ along Y-axis, the excitation rate satisfies $\gamma_{ex}^0(\boldsymbol{p}_r) \propto |E_0|^2$.

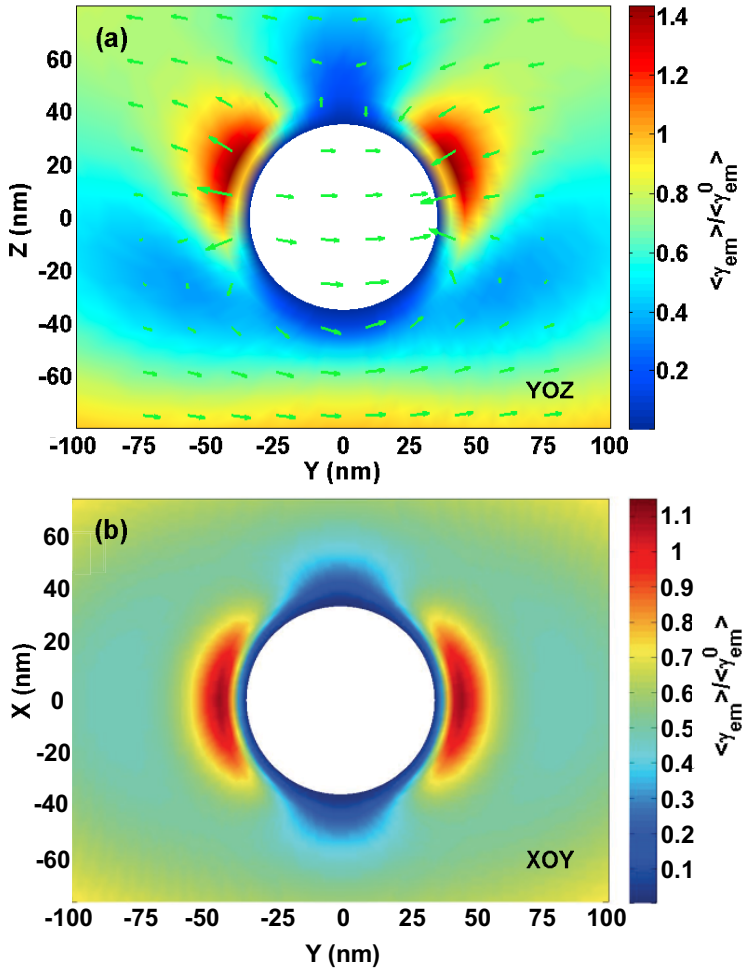


*Figure 4.7: Average normalized emission rate $\langle \gamma_{em} \rangle / \langle \gamma_{em}^0 \rangle$ of EY molecules in a medium of $n = 1.48$ with an excitation laser of $\lambda_{ex} = 514nm$, view in (a) YOZ plane and (b) XOY plane (across the center of the sphere). The incident light propagates along Z-axis with a polarization in Y-axis. The green arrows represent the direction of the local electric field.*

According to Figure 4.7 (a), within a shell surrounding the gold nanoparticle, the normalized emission rate, or say, the enhancement factor of the emission rate, is below 1. This is a sign of quenching effect of the dye molecules. A maximum

enhancement factor of 1.45 can be reached along the tilted emission rate poles, which results from the inclination of the maximum local electric field as has been illustrated in Figure 4.5 (b). The emission rate distribution (Figure 4.7 (a)) around a nanosphere differs from the field distribution (Figure 4.5 (b)) due to the modified quantum yield. In the XOY plane that is across the center of gold nanosphere, shown in Figure 4.7 (b), we obtained a maximum normalized emission rate of 1.1. Along the X-axis, which is perpendicular to the polarization direction, molecules are quenched. When a NE is excited along its short axis, this quenching effect prevents EY molecules in the lobes from the contributing to fluorescence signal due to near-field excitation. The far field (incident light), however, is exciting the polymer lobes.

Evidently, for molecules in the planes parallel to XOY, the maximum normalized emission rate can be varying. Figure 4.4 (c), which presents the nanoparticle-modified fluorescence that is normalized by the BG (i.e., free space), is comparable to the calculated results. In experiment, we obtained a normalized emission rate of 1.7, which is in the same order of magnitude and is even higher than the calculated maximum value of 1.45. The mismatching between theory and experiment comes mainly from i) the complex anisotropy of the gain medium, which is not included in the model and ii) the larger concentration of near-field excited EY molecules at position 3 (Figure 4.3 (a)) than that on the background (position 2). All these factors confirm, though indirectly, the anisotropy of our hybrid NE.

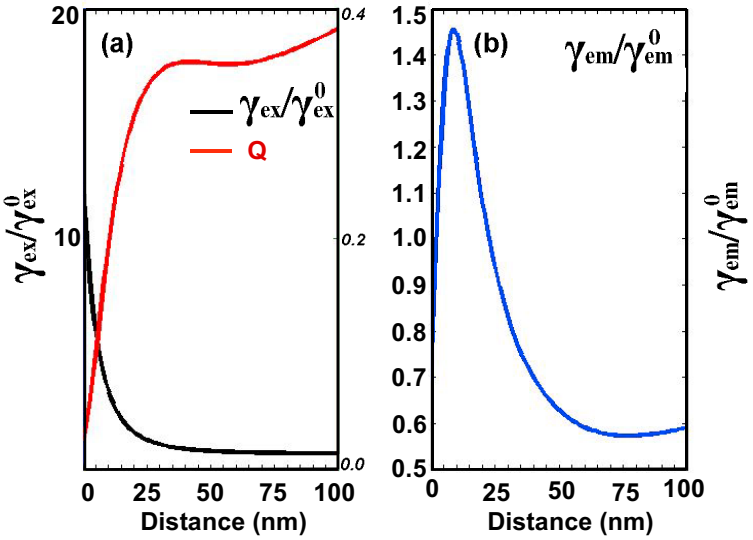


*Figure 4.8: (a) Normalized excitation rate (in black) and quantum yield (in red) in photopolymer as a function of gold nanoparticle-molecule separation distance. (b) The resulted normalized emission rate of Eosin Y molecule in medium ($n = 1.48$). The calculations were performed for a molecule that is oriented perpendicular to the nanoparticle, under an excitation wavelength of $\lambda_{ex} = 514nm$ and emission wavelength of $\lambda_{em} = 555nm$.*

Figure 4.8 demonstrates the normalized excitation rate, quantum yield, and the normalized emission rate as a function of the particle-molecule separation distance. The calculation was performed on a dipole that is perpendicular to the particle surface. The excitation rate, after averaging the molecular dipole orientation, is now

proportional to the local field intensity $|\boldsymbol{E}_{loc}|^2$. Thus, the normalized excitation rate, shown in black curve in Figure 4.8 (a) is equal to the enhancement factor of the electric field intensity (Figure 4.5 (b)). It reaches a maximum enhancement factor of 10 on the particle surface, and exhibits an exponential decay as the molecule separates from the nanoparticle. Nevertheless, the normalized emission rate is low for a molecule close to the particle (panel (b)) because of the high energy transfer rate $\gamma_{nr}^{ET}$ that leads to the quenching effect (low quantum yield shown in red curve in panel (a)).

Along the maximum emission poles in Figure 4.7 (b), we calculated the normalized emission rate in Figure 4.8 (b) for a dipole that perpendicular to the surface of the sphere. The molecules are quenched within a separation distance of 3nm. As the molecule departing from the particle surface, a maximum emission rate enhancement factor of 1.45 appears at a separation distance of 9nm. It is in the same order of magnitude but is slightly smaller than our experimental results (Sx/BG=1.7 shown in Figure 4.4 (c)).

This small difference between theory and experiment can be interpreted as the contribution of the higher concentration of EY molecules that is excited by the far-field (incident field). As the signal of BG indicates, the rinsing process of photopolymerization is not perfect and some EY molecules are likely to remain on the substrate. We assume that these residual molecules distribute homogeneously and oriented randomly on the substrate. When the incident polarization of excitation light is oriented along the short axis of NE, the number of molecules excited by the near-field is similar to that excited by the incident field on BG. However, fluorescence signals are resulted not only from the near-field, but also from the incident field that is exciting all the region of exposure. In experiment, this incident field (no matter what the polarization is excited more molecules on NE than on BG due to a higher concentration of EY molecules in the polymer structure; in calculation, this higher molecule concentration was not taken into account. Consequently, the difference between the experimental Sx/BG and the calculated normalized emission rate indicates, through incident far-field excitation of EY, the anisotropy of our hybrid nano-emitter.

Based on the surface plasmon-enhanced fluorescence characterization, it turns out that our hybrid NE is giving different fluorescence intensities by applying different incident polarizations. However, currently the anisotropic fluorescence cannot be repeated on all NEs and further studies will be carried out to optimize the hybrid system from several aspects. First of all, rinsing procedure, which is not yet effective enough to clean the outside polymer structures, has to be improved to diminish the BG signal. Second, QD-doped polymerizable solution will be adopted to overcome the photo-bleaching effect. Third, the emission of the NE should be improved. According to the calculations, within a 15nm-thick polymer lobe, the average enhancement factor of the emission rate is below 1. Theoretically, the emission of NE can be improved by overcoming the quenching effect via controlling the molecular dipole orientation and the particle-molecule separation distance.

Practically, the optimization of the separation distance can be realized by fabricating a spacer (eg. silicon shell) outside the nanoparticle. However, it is still unknown if the EY molecule undergoes a re-orientation process in photopolymer (or polymerizable solution) under a polarized incident light. Adjusting and detecting molecular orientation remains to be a challenge. Besides, some other optical characterizing techniques can be used to overcome the shortcomings of fluorescence. SERS is used in the coming section because the fluorescence-quenching for small nanoparticle-dye molecule distance is not expected to influence the Raman intensities.

## 4.2 SERS on unique hybrid structure of Au dimer/ MB-doped photopolymer[5]

As an alternative to fluorescence spectroscopy, SERS can also characterize the optical features of our hybrid nano-emitter. In this study, we utilized dimers of gold nanodisks. With a varying gap between the two monomers of nanodisk, the LSPR of the dimer can be significantly changed. The dimer is, in natural, an anisotropic structure that provides higher electromagnetic enhancement in the gap along the inter-particle axis.

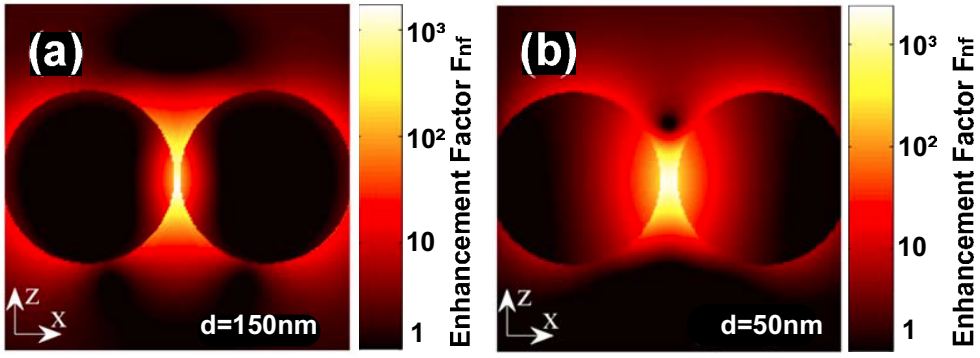


*Figure 4.9: Calculated field intensity enhancement distribution on silver dimers of (a) $d = 150nm$ (b) and $d = 50nm$.[135] The gap is $g = 5nm$ for both dimers. The incident wavelengths for the two dimers are 533nm and 469nm, respectively. The incident light propagates along Z-axis and is polarized along X-axis.*

Figure 4.9 shows some calculated field distributions on silver dimers of nanospheres with a gap of $g = 5nm$ and a diameter of (a) $d = 150nm$ and (b) $d = 50nm$.[135] The incident wavelengths for the two dimers are 533nm and 469nm, respectively. In both cases, the enhancement factor in the gap can reach as high as $10^3$. This huge field enhancement in the gap of two coupling nanoparticles can cause a high SERS signal. By hybridizing along this long axis of the dimer, dye molecules distribute more likely in the gap due to the photopolymer. As a consequence, the optical anisotropy of the hybrid nanostructure is expected to be amplified because

[5] *X. Zhou, C. Deeb, S. Kostcheev, G. Wiederrecht, D. Gosztola, J. Grand, N. Félidj, P.-M. Adam, O. Soppera and R. Bachelot. Paper under preparation. 2013*

active species are present mainly in the gap whose electromagnetic excitation is strongly polarization dependent.

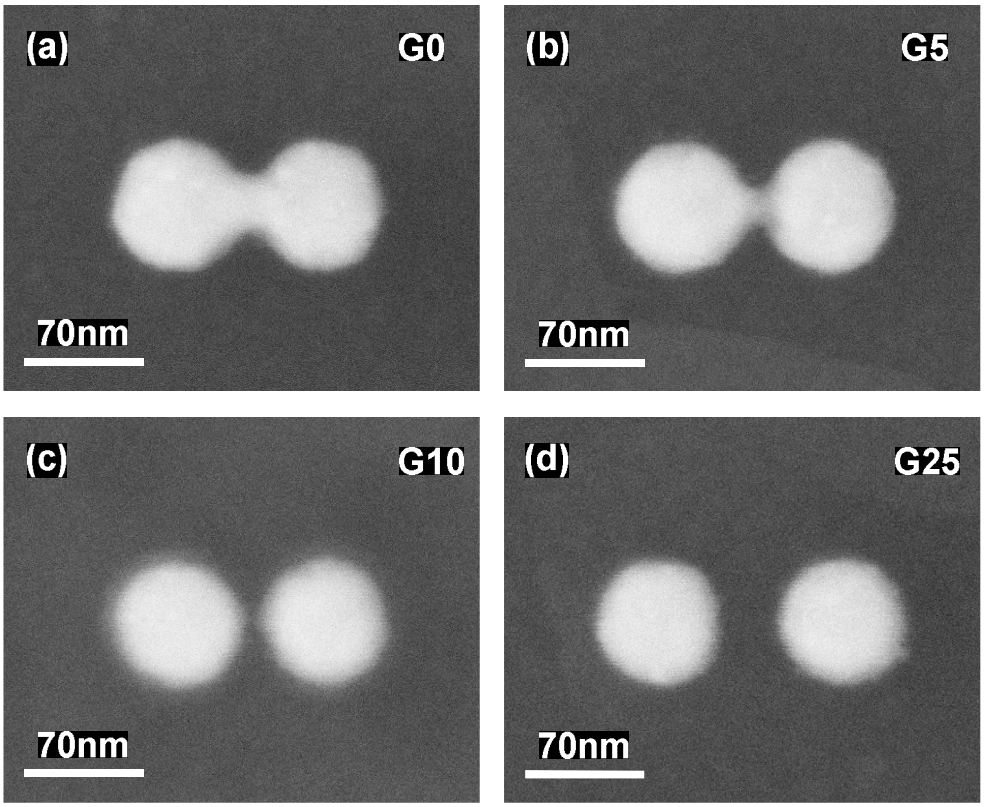


*Figure 4.10: SEM image of the dimers of gold nanodisks with gaps of (a) $g = 0$, (b) $g = 5nm$, (c) $g = 10nm$, and (d) $g = 25nm$. Note that the two nanoparticles of the $g = 5nm$ dimer are connected.*

The gold dimers were fabricated by EBL on an ITO coated glass substrate. Each of the nanodisks is 50nm in height and 70nm in diameter. The gap size is varying from 0 to 55nm with a step of 5nm. Figure 4.10 shows some of the dimers with different gap sizes. The photopolymerizable formulation with 0.5%wt MB as the photosensitizer was chosen in the SERS study because MB molecules are easily adsorbed on gold and thus produce less fluorescence as the background of SERS signals. The hybridization was achieved by a $\lambda_0 = 647nm$ laser with an incident dose of $D_0 = 65\%D_{th}$. This wavelength was used because it is close to the maximum absorption of MB and allows for a resonance Raman effect. The incident polarization was along the long axis of the dimer.

### 4.2.1 Topographic feature of the hybrid structure

The nanostructure was characterized with AFM before and after the hybridization to obtain a differential image that highlights the polymer structure. In Figure 4.11, panels (a) and (c) exhibit the differential AFM images of two typical gold dimers with gap sizes of 25nm and 45nm, respectively. Panels (b) and (d) are the corresponding cross-section profiles along the long axis of these two dimers. As can

be seen from this figure, when the two particles are close to each other ($g = 25nm$ in panel (a)), the gap of the dimer is filled with photopolymer due to the field enhancement in the gap. The interaction between two monomers in a small gap causes field re-distribution that focuses most of the energy in the gap. This leads to a small polymer height at both ends of the long axis of the 25nm-gap dimer. In the case of a larger gap ($g = 45nm$ in panel (c)), the polymer has similar contributions because no coupling exists between the two monomers.

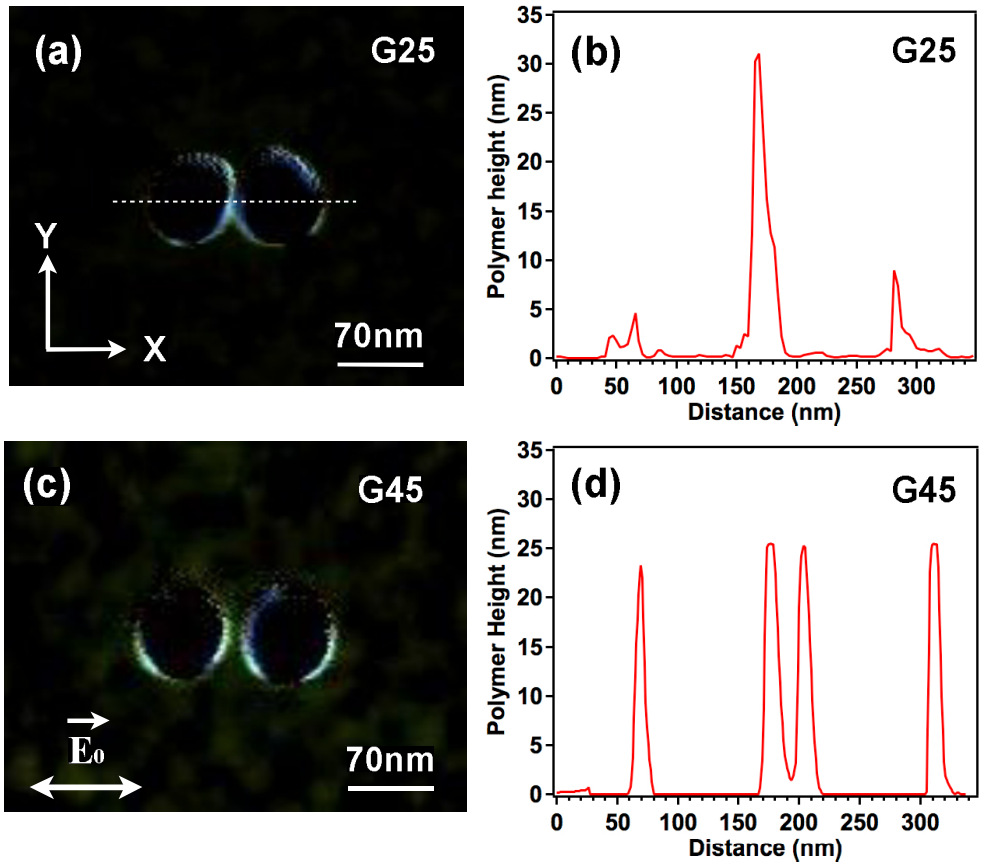


*Figure 4.11: Profiles of two typical dimers with different gaps. (a) The differential AFM image and (b) the cross-section profile of a hybrid nanostructure based on gold dimer with a gap of $g = 25nm$. Panels (c) and (d) are the differential AFM image and the cross-section profile, respectively, of a $g = 45nm$ gold dimer/MB-doped polymer.*

Other than differential AFM images, SEM images were also utilized for the topographic characterization of the hybrid nanosystem. Secondary electrons, as has been presented in Chapter 2, produce a different contrast on polymer and on gold. As Figure 4.12 illustrates, polymer structure can be recognized in the 20nm-gap of this gold dimer.

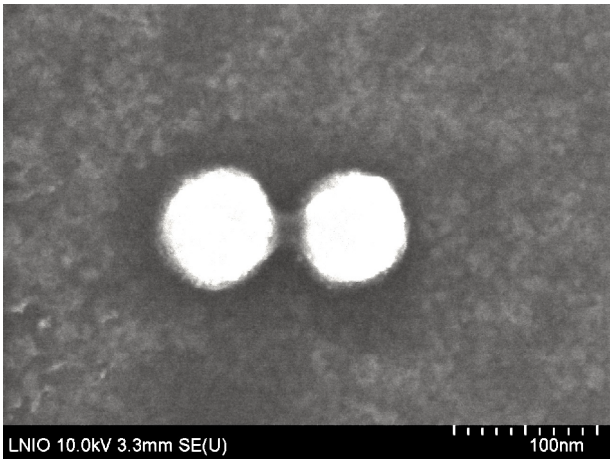


*Figure 4.12: SEM image of a hybrid nanostructure $g = 20nm$. This image was collected with a secondary electron detector. Gold nanodisks and the photopolymer shown in different contrasts.*

### 4.2.2 LSPR of the hybridized nano-dimers

Before going to the SERS spectra of the dimers, let us focus our attention onto the LSPR of the hybridized nano-dimers (i.e., dimers after photopolymerization). The positions of LSPR will help us in the following discussions on the SERS signals.

Figure 4.13 shows some of the dark-field scattering spectra that were collected on individual dimers with incident polarizations along the long axis (panel (a)) and the short axis (panel (b)). These dimers have similar LSPR along the short axis at approximately 625nm. Along the long axis, the LSPR of the dimer decreases as the gap size increases from 10nm to 30nm. It stays constantly beyond starting from $g = 30nm$ as the gap keeps increasing. This suggests the disappearance of plasmon coupling between the two nanodisks of the dimer starting from a spacing of $g = 30nm$. Note that the incident light, which is peaked at 665nm, has shown a small influence on all the scattering spectra detected.

There are two other spectra along the long axis of the dimer that worth noticing: the $g = 0nm$ in red and the $g = 5nm$ in gray. The first one exhibits two plasmon modes. One of them is blue-shifted with respect to the LSPR of all other dimers, and the other is in NIR (it is read as 665nm in this figure because the incident light for these spectra was in visible and the NIR mode cannot be excited). Many studies have been performed on the dimers of two separating, touching, and overlapping particles. These studies illustrate a red-shift LSPR when the spacing of the two monomers reduces but larger than 0. Starting from $g = 0$[136] (some claims that it is from $g = 0.5nm$[137]) appears a blue-shifted mode that is associated to the transverse charge oscillations between the two particles.[137-138] It shifts in blue as the two particles overlap more.[136] For the $g = 5nm$ dimer in our study, the peak appears at 625nm. This LSPR suggests that the two particles start connecting with each other. Technologically, 5nm gap is rarely obtained by EBL (Figure 4.10(b)). We could

neither obtain an image of this dimer that is showing a clear gap because 5nm is beyond the resolution of both AFM and SEM.

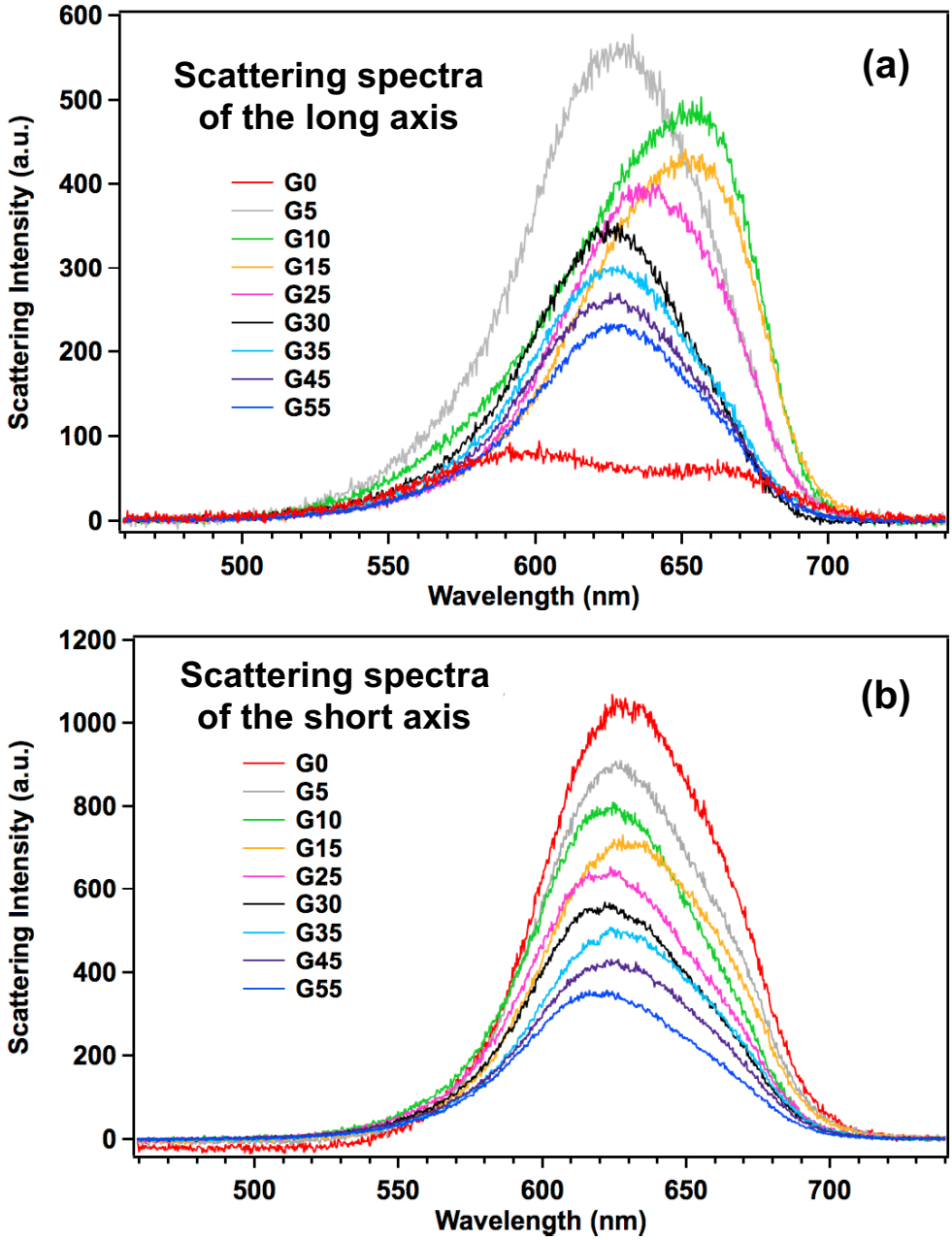


*Figure 4.13: Scattering spectra on the dimers after polymerization with the incident polarization along (a) long axis and (b) short axis of the dimer. Each of the spectra was collected from a unique dimer.*

### 4.2.3 SERS signals on gold dimer/MB-doped polymer hybrid nanostructures

SERS spectra on the hybrid nanostructure of dimers were collected at the Center for Nanoscale Materials in Argonne National Laboratory during my visit there with a *RENISHAW INVIA* confocal Raman spectrometer. A laser at $\lambda_{ex} = 633nm$ with

an incident power of 9.4μW has been used for this study. This incident wavelength is in the absorption band of the MB molecules (Figure 2.3 in Chapter 2), but is more in blue compared to the maximum MB absorption peak at 660nm. For each of the dimers, SERS spectra under two different incident polarizations (along X and Y axes, respectively) were collected.

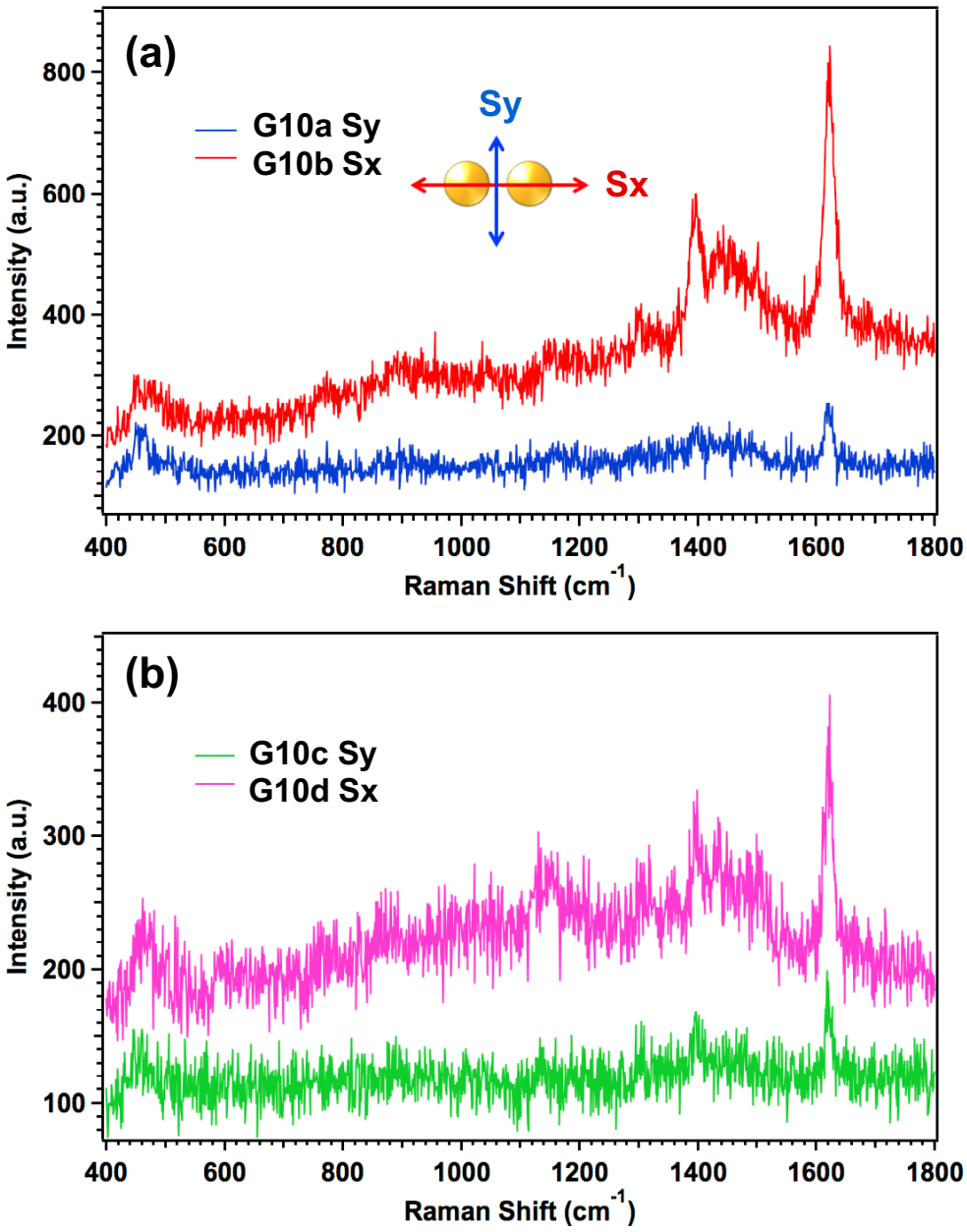


*Figure 4.14: SERS spectra on a gold dimer with a gap of $g = 10nm$. The signals were collected in a chronological order of a-b-c-d, corresponding to the spectra with incident polarizations of y-x-y-x. Panel (a) exhibits clearly a higher Sx than Sy, and panel (b) reproduces this result on the same dimer.*

Figure 4.14 is an example of SERS spectra on a dimer with a gap of $g = 10nm$. An acquisition time of 30sec was applied to collect each spectrum. As illustrated in the legend of panel (a), we define

- **Sx** as the Spectrum collected with an incident polarization along the **long axis** of the dimer.
- **Sy** as the SERS spectrum collected with an incident polarization along the **short axis** of the dimer;

SERS signals were collected following a chronological order of a-b-c-d. In other words, the spectrum with incident polarization perpendicular to the long axis was taken first (aSy), and then the one along the long axis was collected (bSx). This procedure was repeated by cSy and dSx in Figure 4.14 (b) in order to confirm the result. The mode of 1620cm$^{-1}$, which always displays a highest peak intensity among all the modes appeared, will be used as a measure for the SERS intensity throughout the coming discussions. This mode corresponds to the stretching C-C ring of the MB molecule.[116-117] We will present in section 4.2.4 a control study on thermally polymerized PETIA, which indicates that the monomer does not contribute to this Raman mode. Since the incident laser is near the maximum absorption of MB, we are actually in the situation of resonant Raman scattering.

We can draw the following important conclusions from Figure 4.14:

First, for the spectra with same incident polarizations (aSy and cSy, bSx and dSx), the Raman peak intensity is decreasing as time goes by. The "peak intensity" refers to the intensity of the Raman peak that has been corrected from the baseline. Typically, since the Raman scattering does not involve real absorption of photons, photo-bleaching of dye molecules is not expected. When the excitation wavelength matches the absorption of the dye, however, photo-bleaching exists. It has been confirmed by Etchegoin and coworkers in 2002[139] through the sudden breakdown of a pure exponential decay of resonant-SERS intensity of RH6G molecules at intermediate and low concentrations. Similar phenomenon was observed in our stability test of the setup, which will be discussed in section 4.2.4. In this study, the excitation wavelength, although did not match the maximum absorption of MB, yet still lies in the absorption band of it. Therefore, this decrease in the Raman peak intensity is believed to result from photo-bleaching of MB molecules.

Second, the peak intensity at 1620cm$^{-1}$ decreases more rapidly in the case of Sx than Sy. The MB-doped photopolymer was created along the long axis (particularly in the gap) of the dimer. When the incident polarization is along the short axis, these molecules are excited only by the incident far field because near-field light confinement in the gap does not occur at this wavelength. In comparison, with an incident polarization along the long axis, the MB molecules trapped in the polymer are excited by both near-field and the incident far field. With this field enhancement, molecules are bleached faster in the case of Sx due to the higher local power.

Third, the obtained intensity of mode 1620cm$^{-1}$ is higher for Sx than Sy. The baseline-corrected peak intensity of $g = 10nm$ dimer increased to 4.6 times higher from 101 (Sy) to 460 (Sx). It is worth noticing that the scattering spectra (Figure 4.13) of this dimer indicate that compared to that along the long axis, the LSPR of the short

axis is closer to the 633nm-excitation wavelength. In order to avoid the troubles that might result from photo-bleaching for interpreting the higher peak intensity in Sx, we collected the SERS signal Sy before Sx. In the case of a homogeneous nano-object, it is reasonable to expect a lower intensity when the polarization is rotated by 90° for Sx, (the second SERS spectra). While in our situation of a dimer, Sx is able to correct the photo-bleaching and exceed Sy by a considerable higher peak intensity. This anisotropy results mainly from two effects. The first one is the coupling between the two particles of the dimer that produces a high near-field enhancement in the gap with incident polarization along the long axis. The second one is the larger number of MB molecules trapped in the photopolymer, which distributes only along the long axis, than outside the polymer. This polymer is confined where light is enhanced during photopolymerization process.

It is worth wondering how much the anisotropic distribution of MB molecule contributes to the anisotropic SERS signal. Definitely, a single nanodisk is needed to collect SERS spectra under different incident polarizations. The $g = 55nm$ gold dimer was chosen because the separation distance between the two nanodisks are large enough to avoid the plasmon coupling. Besides, an additional control study was carried out on a sample of monomers of nanodisks (see section 4.2.4 for details).

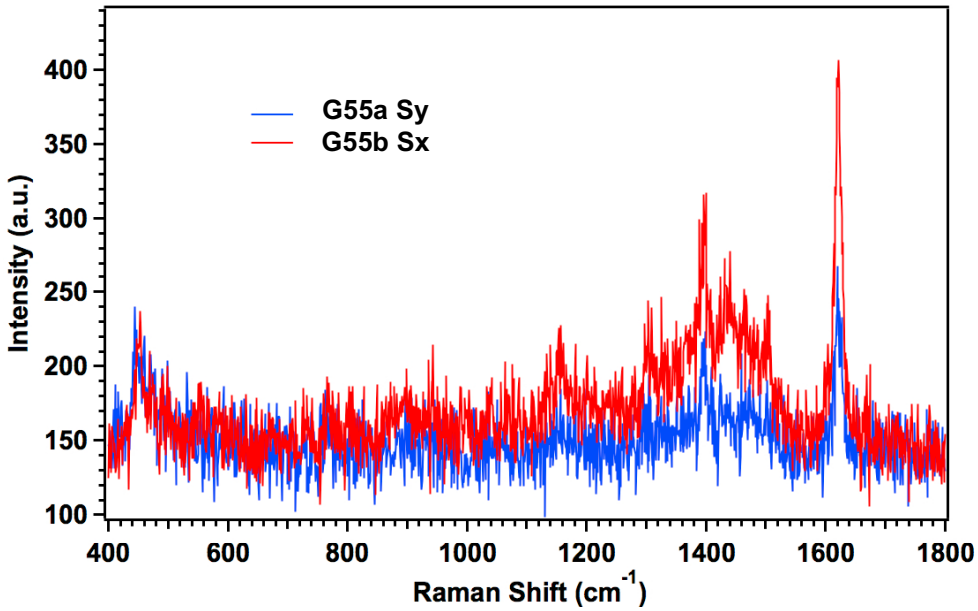


*Figure 4.15: SERS spectra on a hybridized nano-dimer of $g = 55nm$. A higher Sx than Sy was obtained at this gap size (no coupling exists between the two nanoparticles).*

Figure 4.15 shows the SERS spectra on the $g = 55nm$ gold dimer with both incident polarizations. As previously, Sx was collected after Sy to circumvent the influence of photo-bleaching. The Raman peak intensity at 1620cm$^{-1}$ increased to two times higher from 124 for Sy to 254 for Sx (baseline corrected values). As has been discussed above, the LSPR of the long axis does not shift any more beyond $g = 30nm$. In other words, plasmon coupling between the two particles disappears for a gap larger than 30nm in our study. Thus, the $g = 55nm$ dimer can be treated as

two isolated monomers. Therefore, the polarization-dependent Raman peak intensity on this dimer results only from the inhomogeneous distribution of MB, confined along the "h" direction by photopolymerization.

In order to complete the study of dimers with 10nm and 55nm gaps, the polarization-dependent SERS study has been performed on all other dimers with different gaps. The baseline-corrected intensity of the mode at 1620cm$^{-1}$ is plotted in Figure 4.16 for Sy (blue dot) and Sx (red square).

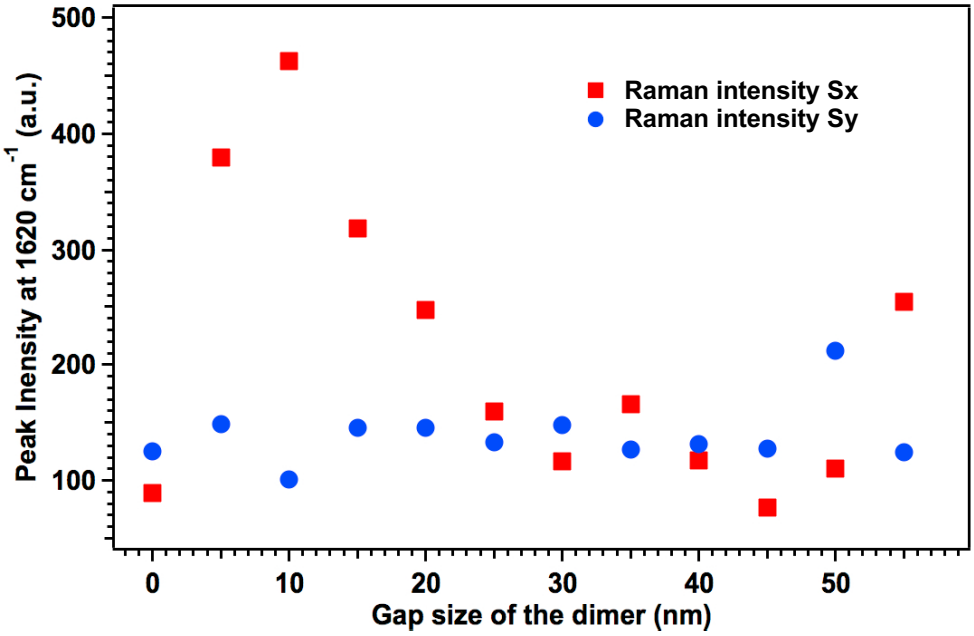


*Figure 4.16: Baseline corrected Raman peak intensity at 1620cm$^{-1}$ for both Sy (blue dot) and Sx (red square). Sx reaches its maximum at $g = 10nm$ but fluctuates at large gaps. The peak intensity of Sy is flat around 140 in comparison with the varying Sx.*

As is demonstrated in this Figure 4.16, a flat Raman peak intensity for Sy was obtained, while Sx varies as the gap size changes. In the case of $g = 0$, when no gap (and therefore no molecule) exists between the two nanodisks, Sx is in the same level as Sy. It augments to maximum as the gap increases to 10nm. With a gap size beyond 10nm, Sx decreases progressively to the same level as Sy. The different trends of Sy and Sx result from the inhomogeneity of the hybrid structure, involving both anisotropic distribution of MB and the electromagnetic enhancement of gold dimers. For some of the dimers, particularly those with larger gaps ($g = 30$ to $g = 45$nm), Sx fluctuates in the same level as Sy. This oscillation could result from the fine structure of the gold dimers as well as some residuals of the polymerizable solution that happen to be near the nanoparticle.

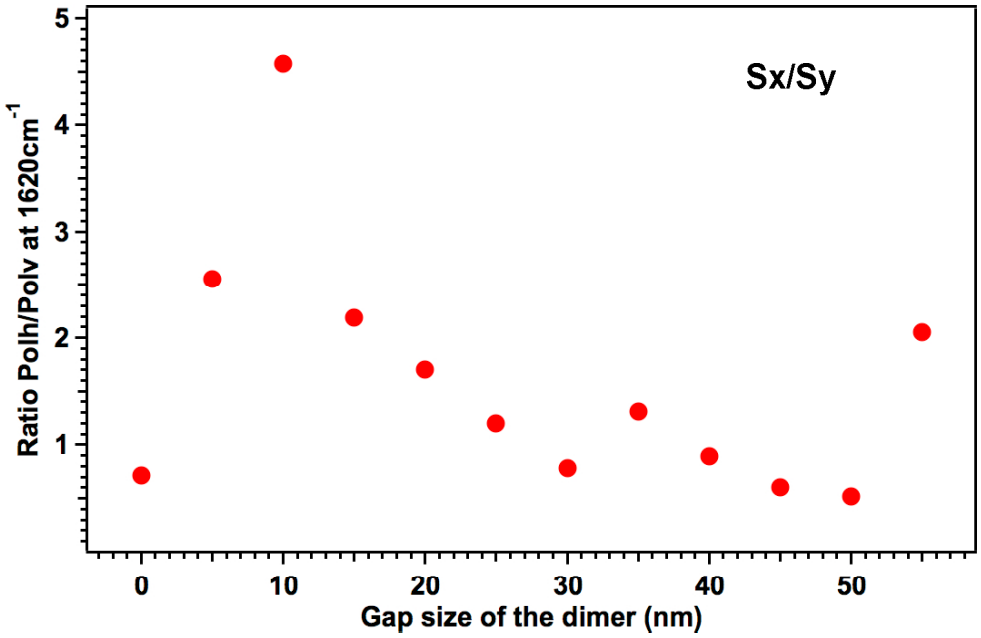


*Figure 4.17: Ratio of the SERS intensity Sx/Sy at 1620cm$^{-1}$ on the hybridized nano-dimers as a function of gap size.*

To see the signal enhancement of the long axis plasmon mode (Sx) as compared to the short axis plasmon mode (Sy), we plot the ratio (Sx/Sy) of peak intensity at 1620cm$^{-1}$ in Figure 4.17. The ratio of the Raman peak intensities of the mode at 1620cm$^{-1}$ displays a similar trend as Sx in Figure 4.16. The $g = 55nm$ dimer shows a ratio Sx/Sy of 2.05. Since no plasmon coupling exists in this size of gap according to Figure 4.13 (a), this ratio results from the larger number of MB molecules that are excited by near-field along the long axis than along the short axis.

In comparison, the ratio of Sx/Sy reaches a maximum of 4.6 at $g = 10nm$. The polymer expansion in small gaps (Figure 4.11 (b)) is restricted by the gap size; even a high electromagnetic enhancement plasmon coupling can be obtained. In contrast, polymer expansion in large gaps ($g > 30nm$) is greater (Figure 4.11 (d)). This smaller number of molecules in the small gap contributes an enhancement factor of less than 2.05 (in the case of $g = 55nm$). As a consequence, electromagnetic enhancement is responsible for the other part, which is greater than $4.6/2.05 = 2.24$. This is just a very coarse estimation without considering the field redistribution in small gaps (Figure 4.11 (b)). To learn more details about the contributions of the molecular confinement as well as the electromagnetic field enhancement, simulations of field distribution around the dimers will be required. This work, which is not presented in this dissertation, will be done in our future study.

Of course, the fluctuation of the SERS signal has made the polarization dependence on 55nm-gap dimer seems to be less convincing. To confirm that the anisotropy of polymer distribution does contribute to this polarization dependent SERS response, we have performed some control experiments on many different

samples including monomers of gold nanodisks. Details can be found in the coming section.

### 4.2.4 SERS Control studies

Despite many interesting results obtained from previous discussions on the hybridized nano-dimer, some important points still need to be clarified. For example, what does the Raman spectrum of MB look like without gold nanoparticles? Did PETIA contribute to the SERS spectra? Is the Raman setup stable? Etc. To answer these questions, we carried out a series of supplementary studies as the control experiment for the polarization-dependent SERS signal on the hybrid nano-dimers.

❖ **Stability test: time evolution of the Raman peak intensity**

In SERS, it is well known that the intensities of the Raman modes fluctuate in some range. In order to make sure that the polarization-dependent SERS response is convincing, we have to know the amplitude of the fluctuation. Thus, a test has been performed on the stability of SERS signals as a function of time on a hybridized nano-dimer.

With an incident polarization kept along the long axis of the dimer, 5 SERS spectra were collected continuously. The acquisition of each spectrum took 50sec. We name each of the acquisition procedure as a "cycle", as the bottom axis of Figure 4.18 indicates. For each spectrum, the Raman peak intensity at 1620cm$^{-1}$ was measured. The obtained values were plotted in Figure 4.18.

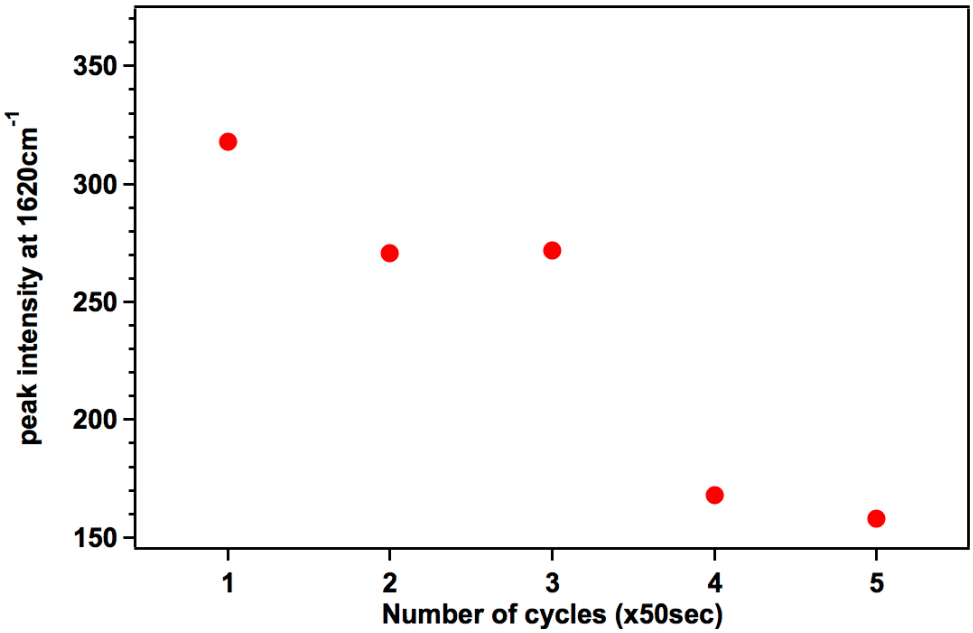


*Figure 4.18: Stability test on a hybrid nanostructure of gold dimer/MB-doped polymer. This test was done in ANL with the RENISHAW INVIA Raman spectrometer.*

The stability test shows clearly the existence of photo-bleaching of MB molecules in our study. The peak intensity displays an overall decreasing trend. To be more precise, a sudden jump can be found from the third to the fourth spectrum. It makes the peak intensity follow an exponential decay from the first to the third spectrum, while another exponential-like decay from the third to the fifth. The reproducibility of this sudden jump by another Raman spectrometer (Figure 4.19) convinced that it does not result from system fluctuation.

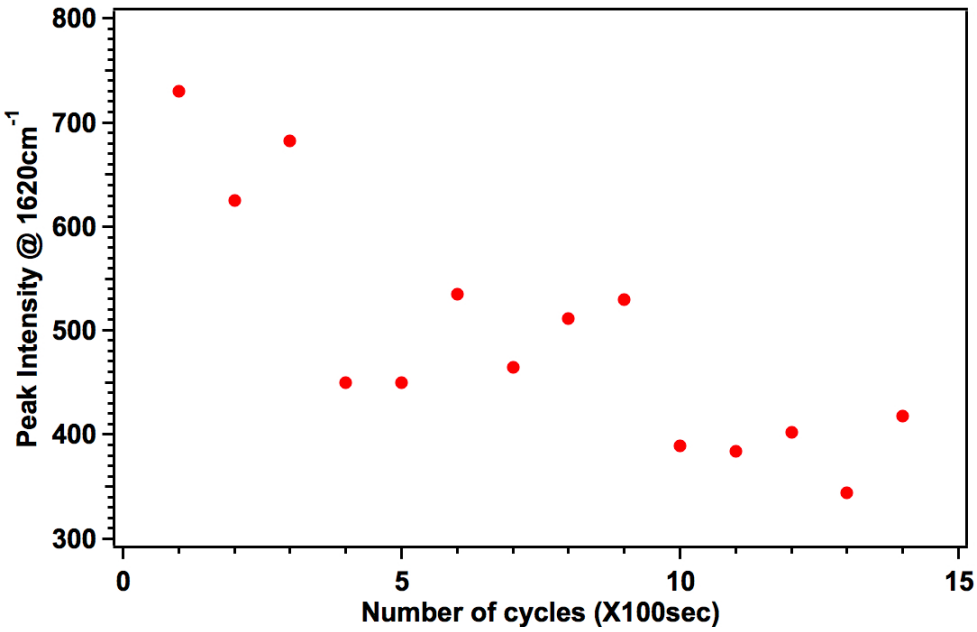


*Figure 4.19: Stability test on a hybrid monomer of gold nanodisk/MB-doped polymer. This test was done with the LABRAMAN spectrometer in LNIO.*

Figure 4.19 shows the time evolution of the 1620cm$^{-1}$ mode intensity from a hybrid monomer of gold nanodisk/MB-doped polymer. Sudden drops of the signal can be observed at third/fourth and ninth/tenth spectrum although the peak intensity is fluctuating in each step and sometimes has an augmentation of up to 90 unites. The fluctuations of SERS intensity, including augmentations and small decreases, could be due to the instability of the setup and of the active hybrid spices. For instance, the incident power of the laser could be fluctuate in a small range; the sample stage could be slightly moved due to vibrations or noise; the dye molecules could be more likely to escape from light; etc. The huge sudden jumps, as has been mentioned above, were also reported at low concentrations of RH6G molecules by Etchegoin and coworkers in 2002.[139] They correspond to the breakdown of the pure exponential decay and are the evidence for single molecule photo-bleaching.

❖ **Raman scattering reference spectra**

As a reference to the polarization-dependent SERS response of the nano-dimer, Raman scattering spectra on four other samples were collected: MB doped standing polymer tip, thermally polymerized PETIA film, glass substrate, and

hybridized monomers of nanodisks. The first three spectra can be found in Figure 4.20, and we will come back to the nanodisks later.

Instead of exciting some Raman modes, we obtained only the fluorescence signal of MB molecules from the micrometer-scaled polymer tip (Figure 4.20 in red). Without the presence of metallic structures, the Raman peaks can be hardly distinguished from the baseline of fluorescence. From the spectrum on PETIA film (in blue), we can see some Raman modes. The one at 1631.7cm$^{-1}$ is worth noticing because it is very close to the mode at 1620cm$^{-1}$ of the MB molecules. Seen from the spectra in section 4.2.3, fortunately, it was not much enhanced to influence the 1620cm$^{-1}$ mode of MB. Other modes of PETIA in the region of [400-1800] cm$^{-1}$ were neither seen. The scattering signal of the glass substrate (in gray) is responsible to the baseline of the spectrum of PETIA layer as well as the detected signal on the standing polymer tips. Based on these spectra, it is convincing that the SERS peaks in previous discussions were from the MB molecules.

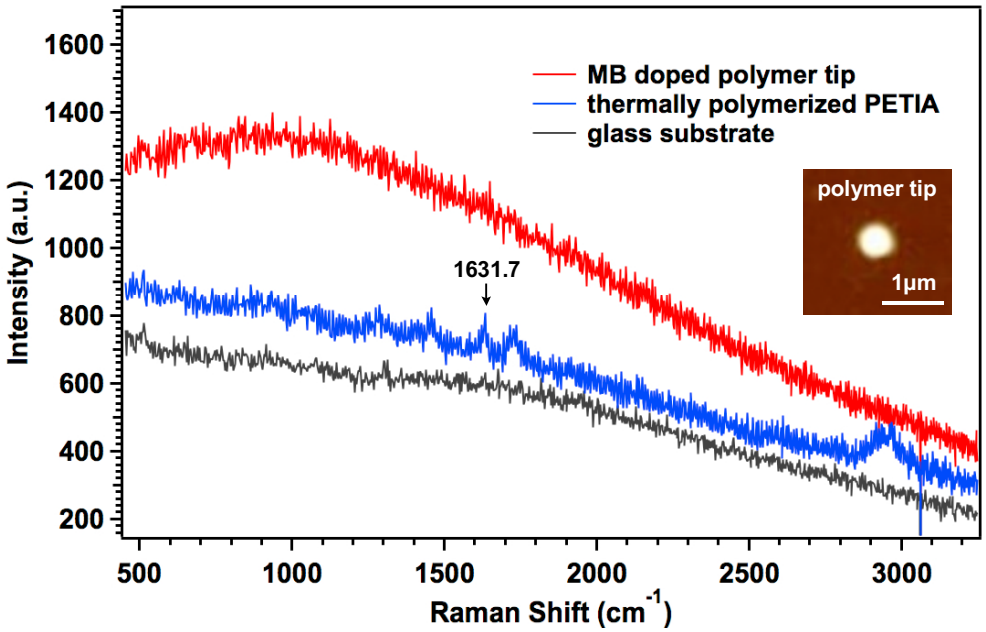


*Figure 4.20: Raman scattering spectra collected from a glass substrate (in black), a film of thermally polymerized PETIA (in blue), and a MB-doped standing polymer tip (in red). The AFM image of the polymer tip is inserted on the right. The Raman peak at 1631.7cm$^{-1}$ on PETIA film is the peak that is closest to the 1620cm$^{-1}$ mode of MB molecule.*

### ❖ SERS on the hybrid nanostructure of gold nanodisk/MB-doped polymer

In addition to the dimer with a 55nm gap, we collected the SERS spectrum (Figure 4.21) from the hybrid nanostructure of gold nanodisk /polymer as a reference. Considering the resolution of the Raman setup, these monomers were fabricated in a diameter of 180nm. As always, the spectrum Sy (in blue) were collected firstly with an incident polarization along the long axis (i.e., parallel to polymer lobes). Then the sample was rotated by 90° for Sx (in red), in which case the polarization is perpendicular to the polymer lobes.

From Figure 4.21, we can still see a difference between the intensity of 1620cm$^{-1}$ mode between Sy and Sx on the gold nanodisk, although it is not as obvious as in the case of $g = 55nm$ dimer. Other than the difference in the number of gold nanoparticles, another key factor is that the LSPR of a 180-nm diameter gold nanodisk is in the infrared, which is away from the 633nm excitation laser. The off-resonance excitation leads to a lower near-field enhancement factor and therefore is responsible for the smaller difference between Sy and Sx. In that case the difference is clearly due to an anisotropy of molecular spatial distribution.

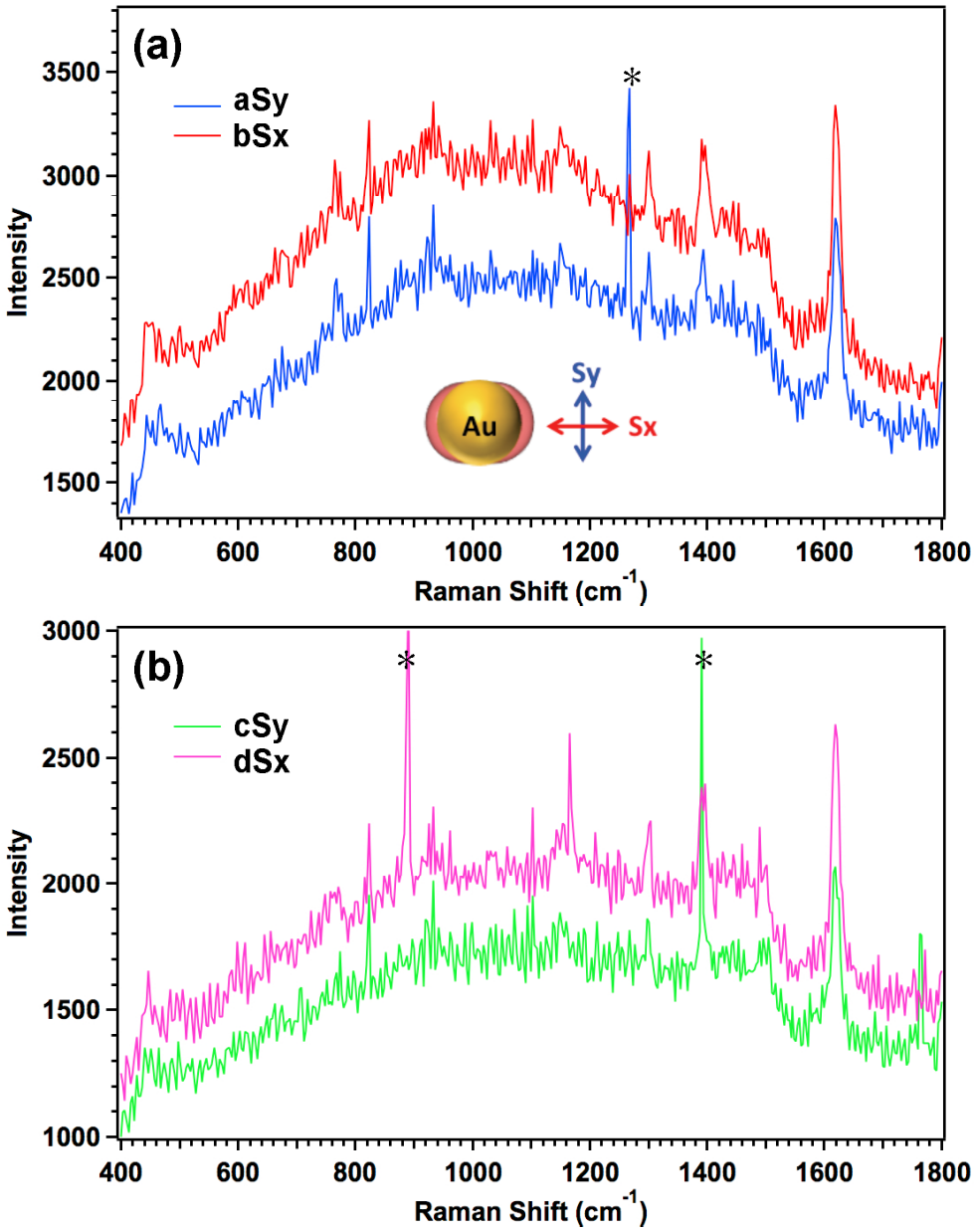


*Figure 4.21: SERS on an individual gold nanodisk/MB-doped photopolymer. The Raman signals were collected in a chronological order of a-b-c-d with an acquisition time of 100sec for each spectrum. The incident polarization of Sx is along the polymer lobes. The peaks marked with stars are cosmic rays.*

In both panels of Figure 4.21, we can see clearly the fluorescence of the MB molecules as the baseline, which interestingly, displays as well polarization dependence. However, we did not obtain the fluorescence signal that contributes to the baseline on the sample of dimers because those SERS spectra were collected 5 months after the hybridization. In comparison, the sample of gold nanodisk was prepared one week before collecting the SERS signals. The fluorescence of dye molecules are known to decrease as time goes by, while the SERS, which does not involve the direct absorption of photons, is still reliable.

The acquisition of SERS signals Sy and Sx was repeated for three times on this individual hybrid nanostructure. As is shown in Figure 4.22, the baseline-corrected Raman peak intensity at 1620cm$^{-1}$ always presents a polarization-dependence.

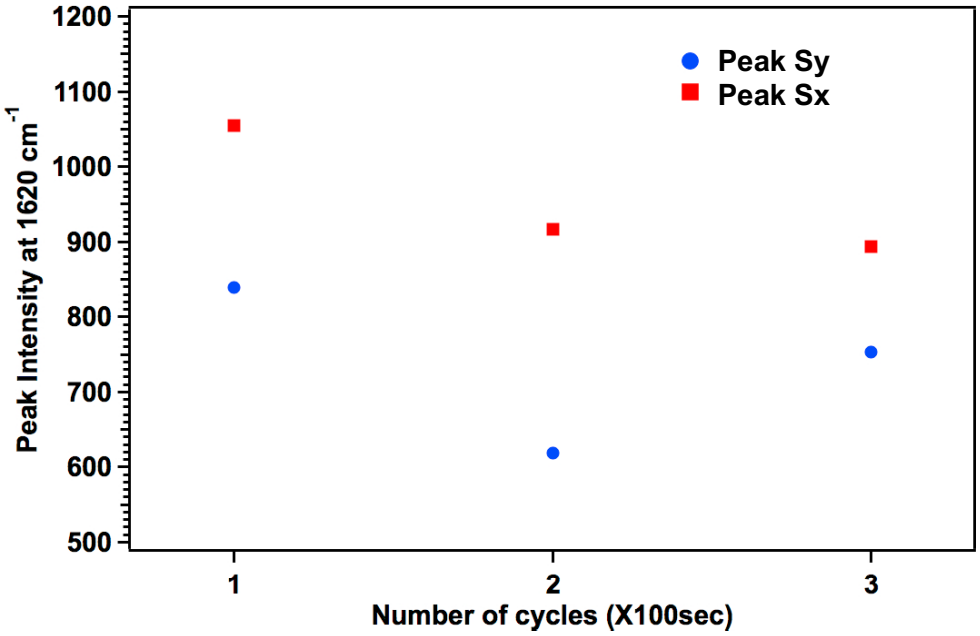


*Figure 4.22: Baseline corrected Raman peak intensity at 1620cm$^{-1}$ for both Sy (blue dot) and Sx (red square) on the hybrid monomer of gold nanodisk/MB-doped photopolymer.*

The intensity of mode 1620cm$^{-1}$ of Sx exceeds Sy in cycles 1, 2, and 3 by 216, 298, and 140 units, respectively. Considering the time evolution of Raman peak intensity in Figure 4.19, which exhibited a maximum augmentation of 90 units due to fluctuation, the higher Sx is somehow reliable in this experiment. It should be notified that the result of higher Sx than Sy is not always reproducible on any other hybrid nanostructure due to i) low off-resonance surface plasmon enhancement factor, ii) random distribution of MB molecules, and iii) photo-bleaching of MB molecules.

## 4.3 Conclusions

We have presented in this chapter the polarization dependence of our light-emitting hybrid nanostructures based on nanospheres and dimers. The hybrid nano-

emitters were characterized by plasmon-enhanced fluorescence and SERS with two different polarizations of the incident light: perpendicular and parallel to the axis of polymer nanostructures.

The fluorescence intensity of the gold nanosphere-based nano-emitter is higher with an incident laser polarized along the long axis than along the short axis. In comparison, the molecules that are far from the nanoparticles exhibit no polarization-dependence. This study highlights, by using a spherical gold nanoparticle, the anisotropic optical feature of our hybrid NE. We performed also the theoretical calculations on the enhancement factor of the emission rate (i.e., normalized emission rate) in polymer. Thanks to the large concentration of dye molecules in the photopolymer nanostructures, the fluorescence intensity of the long-axis emission mode overcomes the problems arisen from photo-bleaching and quenching effects, and finally exceeds the short-axis emission mode.

The SERS study on the hybridized gold nano-dimers shows in general a higher intensity with an incident polarization along the long axis than the short axis. Unlike the nanosphere, the gold dimer is an inhomogeneous structure by itself. Therefore, the ratio of SERS intensities of the NE excited along the long axis to that along the short axis (Sx/Sy) resulted from both electromagnetic field enhancement and the anisotropic dye distribution, especially in the case of the dimers with small gaps when there is a plasmon coupling between the two nanoparticles. As a result, Sy/Sx changes as an increasing gap. A maximum ratio of 4.6 was obtained on a dimer of 10nm-gap. Besides, the single molecule photo-bleaching of MB molecules was confirmed in our study.

Although some preliminary results were obtained for the first time from anisotropic hybrid nano-emitters, further studies are still needed to improve their performances. For instance, optimization of the rinsing process, addition of the spacer (in the fluorescence case), using of doped photopolymer, and control of the molecular orientation. Besides, more excitation polarizations other than the long axis and short axis can be introduced to launch an intensity-polarization study. Furthermore, other techniques that characterize the emitters, such as lifetime measurement, should be used as well. In general, there is still a long way to go for our anisotropic nano-emitter.

# Conclusions

We presented a hybrid plasmonic metal/polymer whose fabrication is based on nano-photopolymerization. The method turns out to be an efficient tool for near-field characterization. The approach has been used in this thesis for quantitative studies on several nano-structures and has led as well to anisotropic nano-emitters.

The fabrication of this hybrid nanostructure is based on the nano-photopolymerization that is triggered by very local enhancement of the optical electromagnetic field due to surface plasmon supported by MNPs. By imprinting the surface plasmon distribution with the fabricated polymer nanopart, this metal/polymer hybrid nanostructure is able to provide us the detailed profile of the near-field of an individual nanoparticle. The thickness of polymer structure leads to a measure of the plasmon decay depth.

The passive hybrid plasmonics approach contributes to the quantitative characterization of the near-field. We have studied in this dissertation the size-dependent effect of surface plasmon of gold nanospheres with an optimized particle diameter at 50nm. This results from the contribution of finite-size effects: i) radiative damping that constitutes the far-field scattering of large particles, ii) non-radiative damping that is responsible for the absorption of small particles, and iii) dynamic depolarization that helps decreasing the energy loss at small diameters (<50nm) but increasing it at large sizes (>50nm). Additionally, we successfully imaged and measured the field of differently oriented gold nanorods that are excited out of the LSPR modes. It is a direct observation of free charges spatial distribution related to the boundary conditions of electromagnetic field. This experiment demonstrated a sub 5nm ultra high resolution of our near-field measuring technique. Finally, study on the gold nanocubes of different orientations relative to incident field direction has allowed us to describe the near-field at both cube ridges and corners. It has also shown the possibility for reproducing the single exponential decay of the plasmon wave. This study also allowed for the measurement of enhancement factor and decay length of the near-field.

Benefiting from the dye molecules that are trapped in the polymer structure, we studied the hybrid plasmonics as active nano-emitters. The most attracting feature of the hybrid nano-emitters is its inhomogeneous optical properties that result from the dipolar distribution of dye-doped photopolymer instead of MNPs. In other words, the gain medium is spatially anisotropic. This has been proved by the detection of polarization-dependent fluorescence signals on the gold nanosphere/photopolymer hybrid nanostructure. Larger fluorescence intensity was detected with an incident polarization parallel to dipolar photopolymer structures compared to the perpendicular case. Similar polarization dependent result was achieved by SERS on

the dimers of gold nanodisks that were hybridized along the gaps. Both electromagnetic enhancement and the number of dye molecules in the gap contributed to this result. The electromagnetic enhancement was reflected by the varying SERS intensity with a polarization along the gap.

Although the nano-photopolymerization has become a sophisticated tool for surface plasmon characterization and hybrid nano-emitter fabrication, there is still a long way to go for our metal/photopolymer hybrid nanostructures, especially in the domain of active hybrid plasmonics. Currently, we can have to repeat the polarization dependent emission on some of the nano-emitters. In other words, the anisotropic optical response to the incident polarization is not 100% reproducible from one hybrid system to another. Following points are likely to be responsible to this problem: i) the random distribution of dye molecules, ii) the orientation of molecular dipole, iii) the signal from molecules outside the polymer, and iv) the photo-bleaching of dye molecules.

Therefore, in our further studies, one of the most urgent needs is to improve the development process to remove the residual layer of the photopolymerizable solution. Oxygen plasma could be considered as a possible solution to this problem. Meanwhile, the photopolymer can be doped with quantum dots that are more photo-stabilized than organic dyes. Moreover, spacers could be adopted to reduce or avoid quenching of the fluorophores. Silicon shell covering a MNP is a good choice as has been already utilized in many reported works. Furthermore, molecular orientation is another parameter that should be controlled. This subject, however, could be a significant challenge for future studies.

# FRENCH SUMMARY

## NOUVELLES AVANCÉES EN NANOPLASMONIQUE HYBRIDE : INTÉGRATION DE FONCTIONS PASSIVE ET ACTIVES

## 5.1 Introduction

La plasmonique hybride fournit des méthodes efficaces pour les études fondamentales et les applications des plasmons de surface. Généralement, la structure plasmonique hybride est une configuration sub-longueur d'onde qui se compose de métal et d'autres matériaux. Le métal fonctionne comme une source de plasmons et les autres matériaux comme des structures fonctionnelles. Ces structures fonctionnelles, qui peuvent être semi-conducteurs,[1-2] biomolécules,[8] colorants,[3-5] et matériaux inorganiques,[6-7] sont dessinées à se coupler au champ plasmonique pour permettre de nouvelles propriétés et fonctionnalités.

Cette thèse présente une structure hybride polymère/nanoparticule métallique qui est fabriquée par photopolymérisation initiée par le plasmon de surface localisé. Le photopolymère caractérise le champ proche de la nanoparticule avec une haute résolution. Dans le cas du mode plasmon dipolaire, les structures de photopolymère sont distribuées de façon inhhomogène dans le voisinage de la particule métallique. Avec des molécules de colorant piégées dans le polymère, la nanostructure hybride fonctionne également comme une nano-émetteur (NE) anisotrope. Deux applications de cette structure hybride sont présentées : caractérisation du champ proche (plasmonique passive hybride) nano émetteur anisotrope (plasmonique active hybride).

La technique souvent utilisée pour caractériser le plasmon de surface est le microscope optique en champ proche (SNOM). Le SNOM franchit la limite de diffraction des microscopies en champ lointain en détectant le signal du champ proche. La meilleure résolution est entre 20nm et 100nm.[42-45] En outre, la spectroscopie électronique à perte d'énergie (EELS)[46] et la microscopie électronique de photo-émission (PEEM)[47] sont deux techniques récentes avec une résolution et une sensibilité plus hautes en tirant avantage de l'utilisation des électrons. Ces deux techniques permettent une résolution d'environ 20nm. Cependant, les images sont obtenues à base d'électrons. Il manque une technique de résolution plus haute qui fournit directement l'information du champ optique très localisé à la surface des nanoparticules.

Par ailleurs, les NEs hybrides dans les études publiées sont fabriquées le plus souvent par dépôt d'une couche homogène de molécules de colorant[5, 98-99]. Il s'agit

d'une méthode pratique avec des bons résultats de fluorescence et de diffusion Raman exaltée de surface (SERS). Les molécules biologiques, par exemple les chaînes d'ADN[101-102] et les anticorps,[103] sont utilisées comme liens entre colorants et nanoparticules métalliques. C'est une méthode à haute spécificité et contrôlabilité mais avec aussi des problèmes biomoléculaires associés : par exemple, les traitements biochimiques complexes et les contributions aux signaux (en particulier dans les études SERS où ces molécules biologiques peuvent se comporter comme les étiquettes SERS[104-105]). La configuration *core-shell* Au/silice/colorant a été rapportée par Noginov en 2009[106] dans le cadre du développement d'un nano-laser. Toutes ces configurations isotropes de nanostructures hybrides empêchent de sélectionner les modes d'émission.

Une structure hybride de nanoparticule métallique/photopolymère a été développée au LNIO[49-51]. La fabrication de cette nouvelle nanostructure est basée sur une approche de photopolymérisation à l'échelle nanométrique. Cette technique ne fournit pas seulement l'image de la distribution du champ, mais permet aussi des mesures quantitatives des plasmons de surface avec une résolution sub-5nm. A l'aide du mode plasmon dipolaire, une distribution anisotrope de matériau organique est intégrée dans le voisinage de la nanoparticule métallique. Avec une haute concentration de molécules de colorant dans le polymère, l'intensité des signaux de fluorescence et Raman du NE hybride sont sensibles à la polarisation incidente. Les principaux principes et méthodes sont présentés ci-dessous.

## 5.2 Principes

Quatre types de nanoparticules d'or sont utilisés pour générer des plasmons de surface localisés : des nanosphères, des nanocubes, des nanorods et des dimères de nanocylindres. Les sphères et les cubes sont colloïdaux alors que les rods et les dimères sont fabriqués par EBL (lithographie éléctronique)

### *5.2.1 Photopolymérisation*

Pour fabriquer des structures hybrides, nous avons utilisé une solution photopolymérisable constituée d'un monomère PETIA (96%wt), de méthyldiéthanolamine MDEA (4%wt), et d'un colorant (0.5%wt) d'Eosin-Y (EY) ou de Bleu Méthylène (MB) . Le spectre d'absorption d'EY dans PETIA est entre 450nm et 550nm avec un maximum à 530nm. Pour MB, il se trouve dans la région de [550-700] nm et le maximal d'absorption se trouve à 660nm. Les processus de la photopolymerization sont très sensibles à la présence d'oxygène jouant le rôle d'inhibiteur. En outre, la relaxation radiative et la conversion interne provoquent aussi une perte d'énergie. Il y a donc un seuil d'énergie pour la polymérisation. Notre approche de nano photo polymérisation plasmonique consiste à utiliser une dose incidente inférieure à cette dose seuil et à contrôler les plasmons de surface de la nanoparticule métallique de façon à ce que la dose locale dépasse le seuil par résonance plasmon. Les différentes étapes sont montrées dans la Figure 5.1

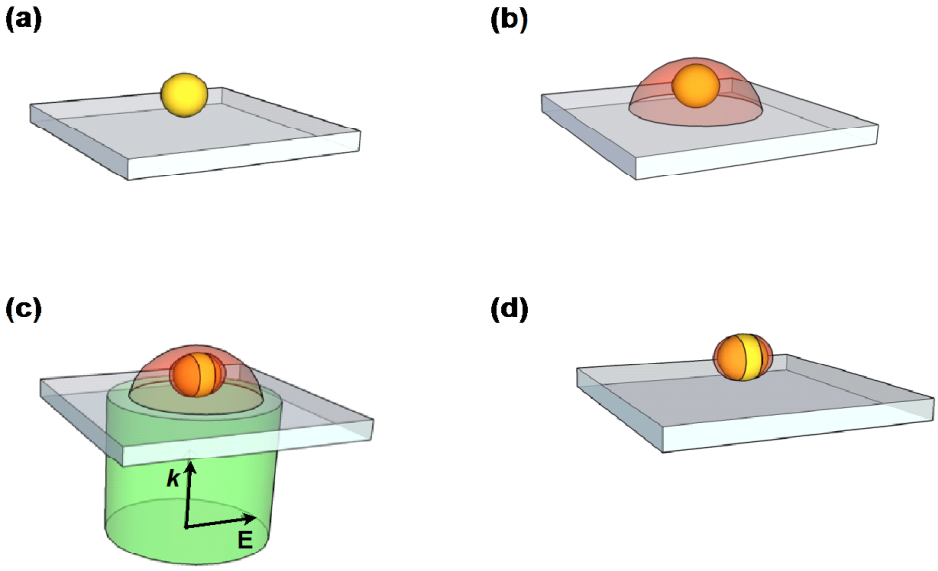


*Figure 5.1: Processus de photopolymérisation. (a) Nanoparticule d'or sur lame de verre. (b) Dépot d'une goutte de la solution photopolymérisable sur la particule. (c) L'échantillon est irradié par un laser incident normal et polarisé linéairement (dose incidente < dose seuil) (d) Après rinçage, on obtient une nanostructure hybride.*

On dépose une goutte de la solution photopolymérisable sur les nanoparticules intégrées sur un substrat de verre (Figures 5.1 (a,b)). L'échantillon est irradié par un laser incident polarisé linéairement (Figure 5.1 (c)). Les longueurs d'onde 532nm et 647nm sont choisies pour photo polymériser en utilisant les solutions de EY et de MB, respectivement. La dose incidente est en dessous (5%-75%) du seuil pour empêcher la polymérisation du champ lointain. Le plasmon de surface qui est supporté par les nanoparticules augmente le champ local pour dépasser le seuil de photo polymérisation. Les nanostructures de photopolymère sont crées uniquement à certains endroits où la dose locale est au-dessus du seuil. Dans le cas particulier d'une excitation dipolaire, on obtient une nanostructure hybride anisotrope constituée de deux lobes (Figure 5.1 (d)). Cette structure est révélée par un rinçage avec l'éthanol pendant 10 min et l'isopropanol pendant 5 min.

### 5.2.2 Caractérisation topographique

Si l'on caractérise la même particule avant et après la procédure de photopolymérisation, la différence entre ces deux images permet de mettre en évidence le polymère intégré localement. Ainsi, une image différentielle « avant – après » permet d'imager le matériau photo polymérisé qui peut être vu comme une image du champ proche de cette nanoparticule. La Figure 2 est un exemple dans le cas d'un nanotriangle d'or. La direction de polarisation incidente est marquée en panneau (a). Notons que la distribution du champ proche n'est pas homogène autour de la particule.

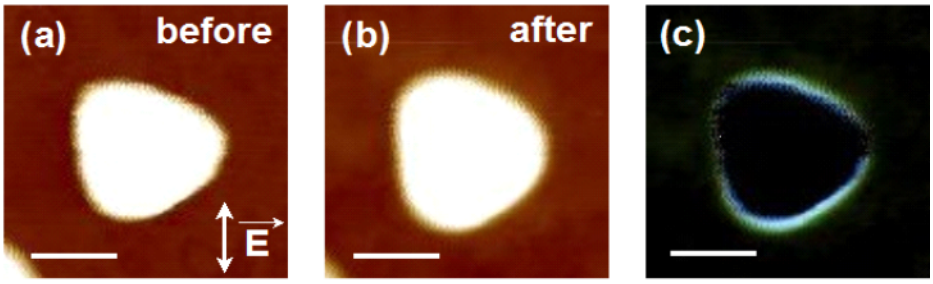


*Figure 5.2: Images AFM d'un nanotriangle d'or (a) avant et (b) après la photopolymérisation. (c) Image différentielle « avant – après » montant le champ proche de cette nanoparticule. La polarisation incident est en verticale comme marqué en panneau (a). Les barres d'échelle représentent une distance de 60nm.*

A partir des images différentielles qui soulignent la distribution spatiale du plasmon de surface, la caractérisation AFM permet de mesurer quantitativement le champ proche avec une résolution extrême (sous 5nm). C'est cette approche que nous utilisons pour toutes les études dans cette thèse. Dans le cas du plasmon hybride actives (NEs), les caractérisations optiques sont nécessaires.

### 5.2.3 Caractérisations optiques

Deux types de NEs anisotropiques sont concernés dans cette thèse : nanosphères or/photopolymère dopé par EY nanodimère d'or/photopolymère dopé par MB. On utilise la spectroscopie fluorescence pour EY et SERS pour MB. Dans ces deux cas, la polarisation du laser incident est contrôlée pour mettre en évidence l'anisotropie optique.

❖ **Fluorescence**

Le schéma de la configuration optique de la spectroscopie de fluorescence est montré sur la Figure 5.3 (a). Un microscope inversé (*Veeco Bioscope II*) est adopté dans cette thèse pour exciter et aussi collecter le signal fluorescent d'EY. La longueur d'onde d'excitation est $\lambda = 514\text{nm}$. En utilisant un condenseur *dark-field*, on a réussi à voire et collecter le signal d'une particule individuelle. Le signal de fluorescence est purifié par un filtre d'émission et focalisé dans un spectroscope (*Andor iDus*). La Figure 5.3 (b) montre le spectre fluorescent d'EY dans une pointe polymère fabriquée par un laser focalisé. Le diamètre et la hauteur de cette pointe sont environ 1μm. Le maximum de l'intensité fluorescent se trouve à 555nm.

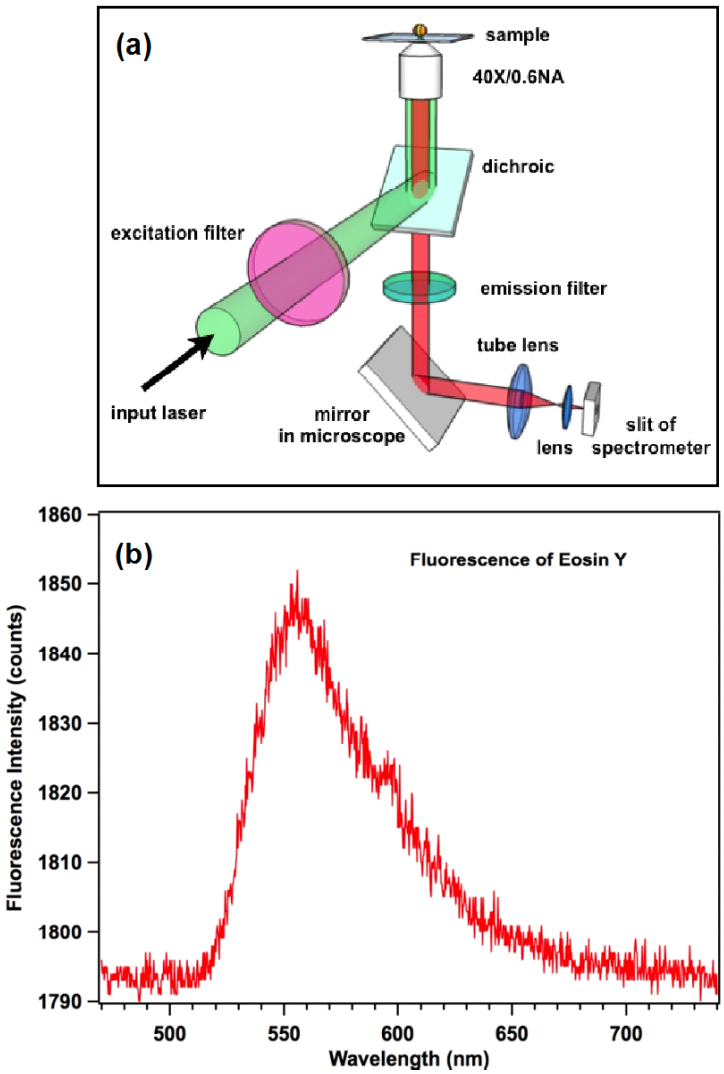


*Figure 5.3: (a) Schéma illustrant la configuration optique pour détecter le signal fluorescence. (b) Spectre de fluorescence d'EY dans une pointe polymère de 1μm de diamètre et de 1 μm de hauteur.*

### ❖ SERS

Les molécules de MB adsorbent très facilement sur la surface d'or résultant en une fluorescence faible mais un signal SERS renforcé. La Figure 5.4 représente en bleu un spectre de Raman des molécules MB loin de la nanoparticule, et en rouge un signal SERS des molécules au voisinage d'un nanodisque de 60nm en diamètre. On peut voire clairement sur le spectre SERS une augmentation des modes 1620cm$^{-1}$, 1397cm$^{-1}$, et 1303cm$^{-1}$. Dans la section 5.4, on va discuter uniquement du mode à 1620cm$^{-1}$ qui est le plus haut en intensité.

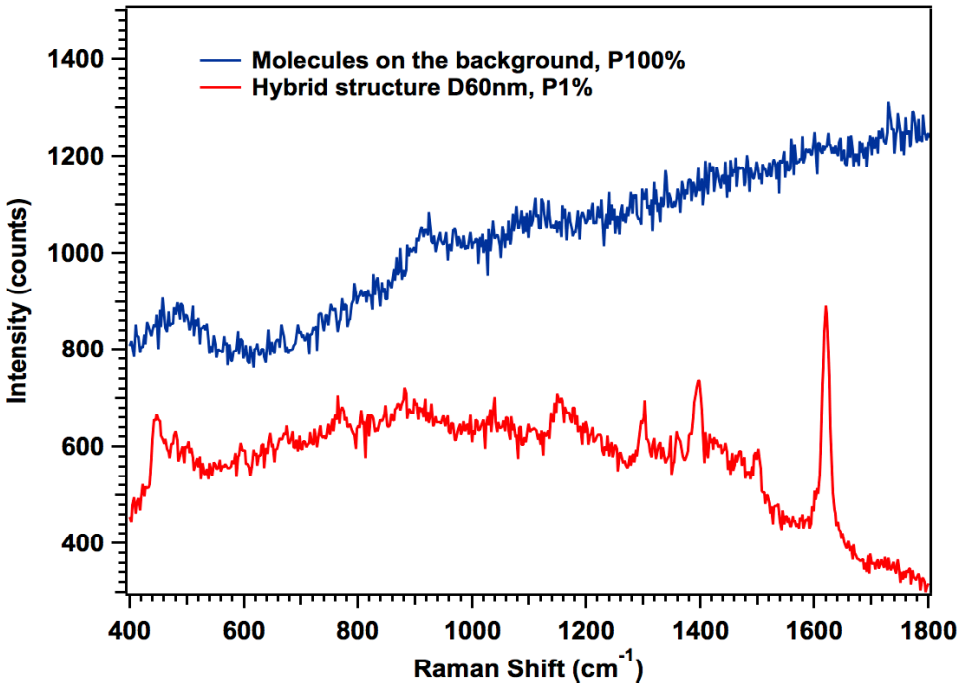


*Figure 5.4: Spectres Raman des molécules MB au voisinage d'un nanocylindre d'or de 60nm au diamètre (en rouge), et loin de la nanoparticule (en bleu). Notez que l'énergie incidente du spectre en bleu est 100 fois plus forte que celle en rouge.*

## 5.3 Plasmonique passive hybride: caractérisation du champ proche avec une résolution sub-5nm

Nous présentons dans cette section l'application de la structure hybride polymère/métal comme un outil puissant de caractérisation du champ proche optique. En utilisant des particules d'or (nanosphère, nanorod et nanocube), nous observons une dépendance en taille, une excitation hors-résonance, et une influence de la polarisation incidente.

### *5.3.1 Nanosphère d'or : distribution du champ proche optique influencée par la taille de nanoparticule*

Les solutions colloïdales de nanosphère d'or, avec un diamètre variant de 12nm à 80nm, ont été fabriquées par J. Proust et T. Lerond (LNIO) dans une méthode de croissance des grains[113]. Les spectres d'absorption des colloïdales sont montrés dans la Figure 5.5. Pour adhérer les nanoparticules, la lame de verre a fonctionnalisée par amino-silane. Chacun des échantillons a été préparé en immergeant le substrat dans une solution colloïdale.

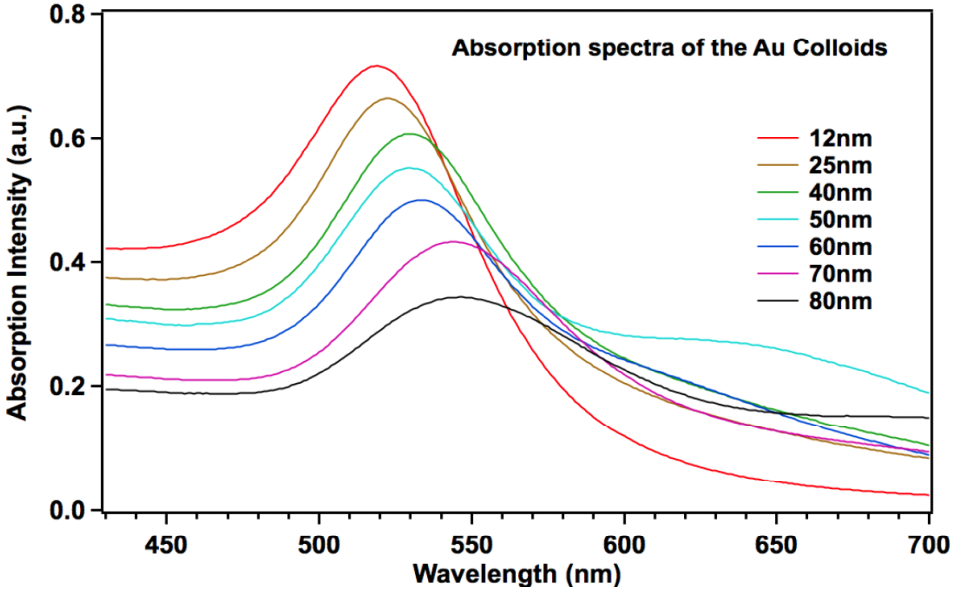


*Figure 5.5: Spectres d'absorption des colloïdes de nanosphères d'or.*

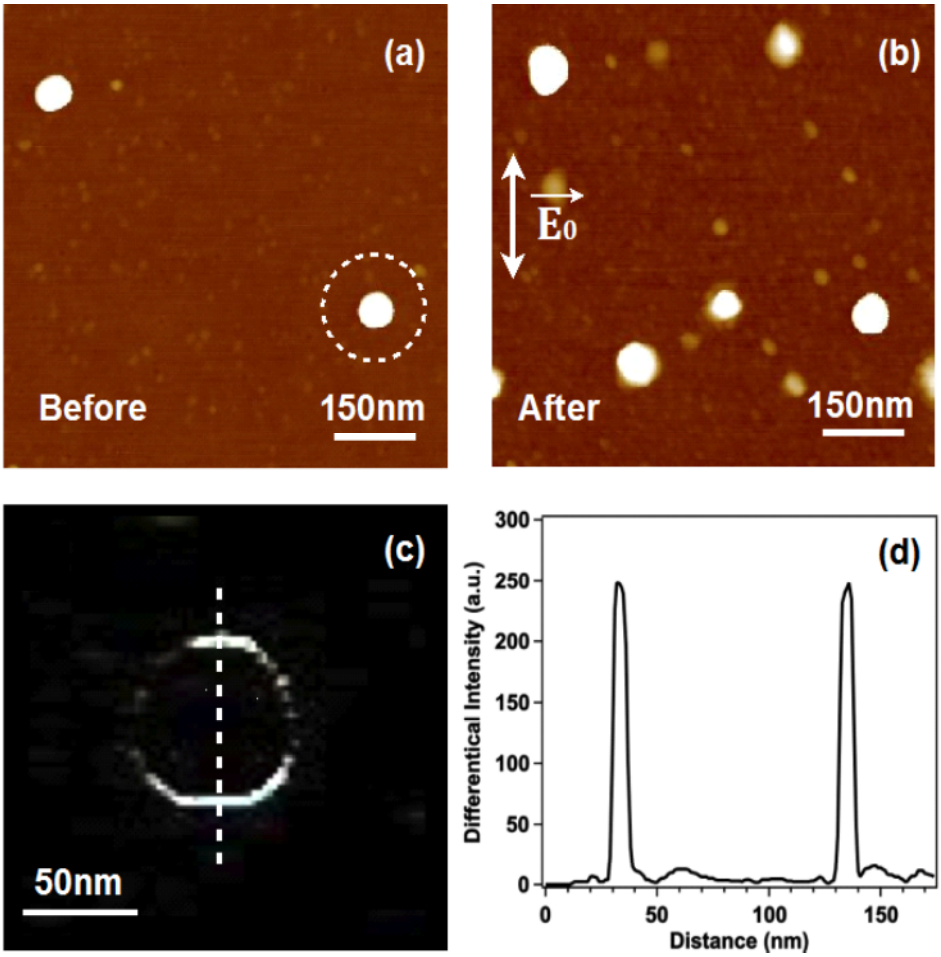


*Figure 5.6: Mesure du champ proche d'une nanosphère unique ($d = 70nm$). Image AFM (a) avant et (b) après la procédure photopolymérisation. Le plasmon de surface de la particule indiquée en panneau (a) est caractérisé par (c) l'image différentielle « avant – après » et (d) le profil de cette particule le long de la ligne en pointillé en panneau (c).*

Après avoir caractérisé par l'AFM (Figure 5.6 (a)), l'échantillon de nanosphère a été revêtue d'une goutte de la solution photopolymérisable. Un laser $\lambda = 532$nm avec une dose incidente de $D_0 = 75\%D_{th}$ a été utilisée pour l'exposition. Figure 5.6 (b) montre l'image AFM après la procédure. Pour une nanosphère individuelle, marquée avec le cercle en pointillés dans la Figure 5.6 (a) par exemple, on calcule l'image différentielle (Figure 5.6 (c)) et le profil de la section transversale (Figure 5.6 (d)) pour imprimer et mesurer quantitativement le champ proche. Les parties brillantes dans l'image différentielle et les deux pics du profil correspondent aux nanostructures du polymère et le plasmon de surface de cette particule. La taille de chaque lobe polymère obtenue est environ 13nm.

La Figure 5.6 montre un exemple d'une nanosphère de $d = 70$nm. On a effectué les mêmes procédures pour plusieurs nanoparticules de tous les diamètres de 12nm à 80nm. La taille moyenne des polymères est représentée dans la Figure 5.7 (a) en fonction du diamètre de la nanoparticule d'or. La dimension de polymère s'accroît en augmentant le diamètre du nanosphère de $d = 12$ à $d = 50$nm. On obtient un polymère maximum de 20nm au diamètre de 50nm. Après $d = 50$nm, la dimension du polymère diminue. La Figure 5.7 (b) représente les résultats simulés par la méthode DDA. La dimension du polymère calculée est du même ordre de grandeur que l'expérience et un maximum se trouve aussi au diamètre de 50nm.

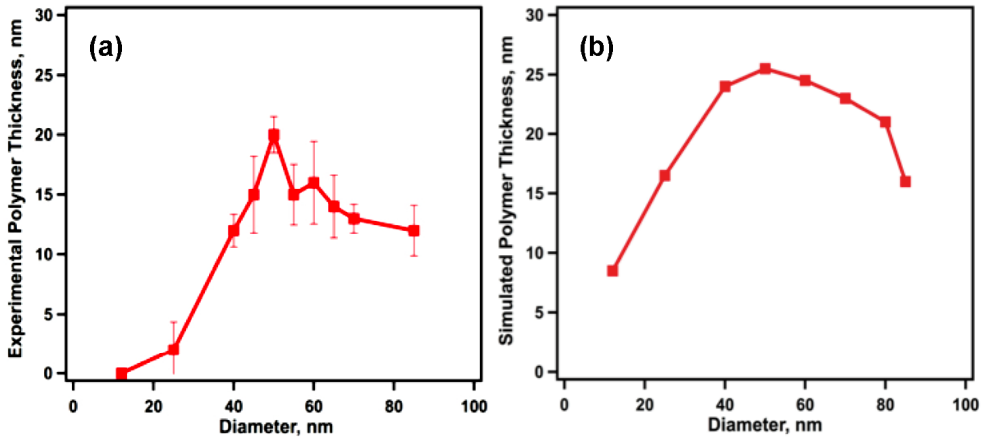


*Figure 5.7: La taille du nanopolymère (a) mesurée et (b) simulée en fonction du diamètre du nanosphère d'or.*

Pour savoir la raison de la dépendance de la taille polymère à la dimension particulaire, on a calculé le facteur d'exaltation de l'intensité du champ proche en fonction du diamètre de nanosphère. Dans la situation de l'approximation quasi-statique, le facteur d'exaltation $F_{nf}$ est exprimé par

$$F_{nf} = \frac{|E_{nf}|^2}{|E_0|^2} = |1 - \xi|^2 \tag{5.1}$$

où $E_{nf}$ et $E_0$ sont le champ proche et le champ incident, respectivement. Le coefficient $\xi$ correspond à la polarisabilité $\alpha$ par

$$\xi = \frac{\alpha}{R^3} = \frac{\varepsilon_m - \varepsilon_d}{\varepsilon_m + 2\varepsilon_d} \tag{5.2}$$

avec $R$ le rayon de la sphere, $\varepsilon_m = \varepsilon_r + i\varepsilon_i$ la fonction diélectrique du métal, et $\varepsilon_d$ la permittivité du diélectrique. Le facteur d'exaltation ne présente aucune dépendance à la taille de nanosphère (Figure 5.8 (a)).

Mais l'approximation quasi-statique est limitée par les effets de taille finie, précisément, l'amortissement radiatif et non radiatif, et la dépolarisation dynamique. L'amortissement radiatif induit une modification du facteur d'exaltation par

$$\xi' = \frac{\xi}{1 - k^2 R^2 \xi - i\frac{2}{3} k^3 R^3 \xi} \tag{5.3}$$

et l'amortissement non-radiatif est modifié *via* la fonction diélectrique du métal

$$\varepsilon_m(\omega) = \varepsilon_\infty - \frac{\omega_p^2}{\omega^2 + i\omega\gamma} \tag{5.4}$$

avec $k$ et $\omega$ le vecteur d'onde et la fréquence, respectivement, du laser incident, $\varepsilon_\infty$ la constante diélectrique à haute fréquence, $\omega_\mathrm{p}$ la fréquence de plasmon de volume du métal massif, et $\gamma$ le taux d'amortissement non-radiatif donné par

$$\gamma = \gamma_{bulk} + \frac{A v_f}{R} \tag{5.5}$$

où $\gamma_{bulk}$ est le taux de collision dans le matériau massif, $v_f$ est la vitesse des électrons au niveau de Fermi et A est un coefficient dépend de la géométrie de la nanoparticule. On obtient en panneaux (b) et (c) de Figure 5.8 la facteur d'exaltation influencé par les amortissements radiatif et non-radiatif, respectivement. Pour des nanoparticules petites ($d < 50$nm), l'amortissement non-radiatif domine. Alors que l'amortissement radiatif domine pour les nanoparticules grandes ($d > 50$nm). La dépolarisation dynamique contribue au dénominateur de $\xi'$ dans l'équation 5.3 par

$$3\varepsilon_d k^2 R^2 + i\varepsilon_i (1 - k^2 R^2) \tag{5.6}$$

La partie réelle (la diffusion) et la partie imaginaire (l'absorption) de ce facteur rencontrent à 58nm, comme représenté dans la Figure 5.8 (d). Le facteur d'exaltation calculé dans la Figure 5.8 (e) ne considère que la dépolarisation dynamique.

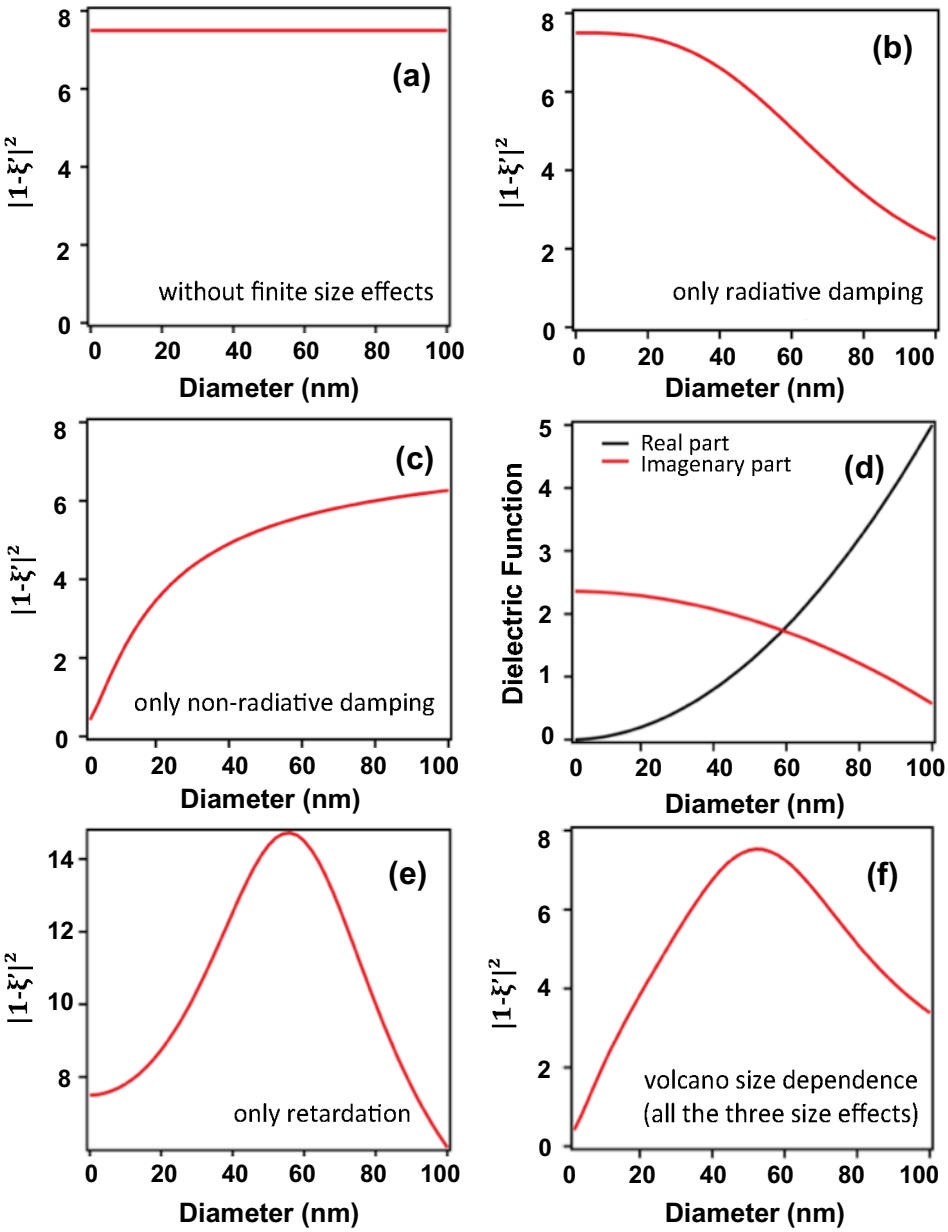


*Figure 5.8: Calcul du facteur d'exaltation de l'intensité du champ proche en considérant (a) sans aucun effet de la taille, (b) amorcement radiatif uniquement, (c) amorcement non-radiatif uniquement, (e) dépolarisation dynamique uniquement f) les trois effets simultanément. Panneau (d) est la partie réelle et la partie imaginaire de la fonction diélectrique dans l'expression 5.5.*

En considérant les trois effets de la taille des nanoparticules d'or, le facteur d'exaltation de l'intensité du champ proche est illustré en panneau (f). On trouve un diamètre de nanosphère optimum de 52nm, ce qui est en accord avec notre résultat expérimental.

### 5.3.2 Nanorods d'or : excitation hors-résonance

L'excitation hors la résonance de plasmons de surface n'est étudiée que très rarement parce que le champ proche est extrêmement faible dans ce cas. Notre technique a réussi à le mesurer. On donne un exemple de nanorods d'or dans cette section pour caractériser quantitativement le plasmon de surface qui a excité hors la résonance plasmonique des nanoparticules.

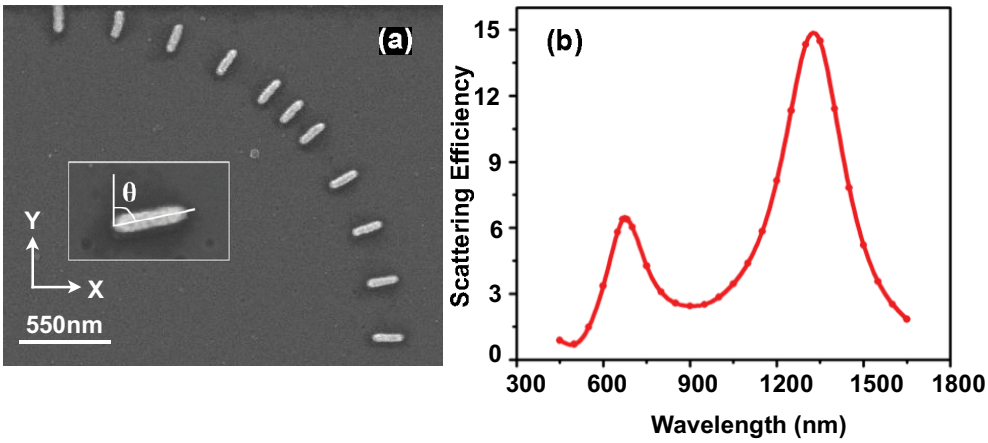


*Figure 5.9: (a) Image MEB des nanorods d'or. (b) Spectre de diffusion calculé d'un nanorod dans une medium d'indexe réfractive* $n = 1.485$.

Les nanorods avec des orientations différentes ont été fabriqués par EBL sur une lame de verre (Figure 5.9 (a)). On définie θ comme l'orientation du nanorod. Le spectre de diffusion a été calculé dans la Figure 5.9 (b) pour un nanorod unique. Les deux modes à 662nm et 1313nm correspondent respectivement au petit axe et au grand axe. Un laser $\lambda = 532\text{nm}$ d'une dose de $D_0 = 65\%D_{th}$ a été utilisé pour la photopolymérisation. Pour trois rods typiques (θ=$0°$, $22.5°$, et $90°$), la Figure 5.10 montre les images AFM collectées avant et après la procédure de photopolymérisation, ainsi que les images différentielles, et les images simulées par FDTD.

On a obtenu des élongations maximales de polymère aux points où le vecteur unitaire normale est parallèle à la polarisation incidente ($\boldsymbol{n} \parallel \boldsymbol{E_0}$). C'est le cas de l'extrémité du rod $\theta = 0°$, aux arrêtes du $\theta = 90°$, et aux points indiqués par les deux flèches solides du $\theta = 22.5°$. Aucune structure polymère a été fabriquée où $\boldsymbol{n} \perp \boldsymbol{E_0}$. Par exemple, aux arrêtes du rod $\theta = 0°$, aux bouts du $\theta = 90°$, et aux points indiqués par les deux flèches pointillées du $= 22.5°$ . La distribution du champ électromagnétique simulé de ces nanoparticules est en bon accord avec les images différentielles et on a obtenu un facteur d'exaltation maximum de 3.

Pour expliquer ce phénomène, on propose que la distribution du photopolymère résulte de la densité de charge de polarisation photo-induite à la limite de métal/diélectrique. Sur la base du Théorème de Gauss, on peut déduire finalement dans l'expression 5.7 le facteur normal du champ électrique:

$$E_{m,n} - E_{d,n} = \frac{\rho_{pol}}{\varepsilon_0} = \chi \boldsymbol{n} \cdot \boldsymbol{E_0} \tag{5.7}$$

où $E_{m,n}$ et $E_{d,n}$ sont les facteurs normaux du champ électrique dans le métal et dans l'électrique, respectivement. $\rho_{pol}$ est le densité de la charge de polarisation, $\varepsilon_0$ est le permittivité du vide, $\chi$ est le susceptibilité électrique du métal, $\boldsymbol{n}$ est le vecteur unité normal de surface, et $\boldsymbol{E_0}$ est le champ électrique incident.

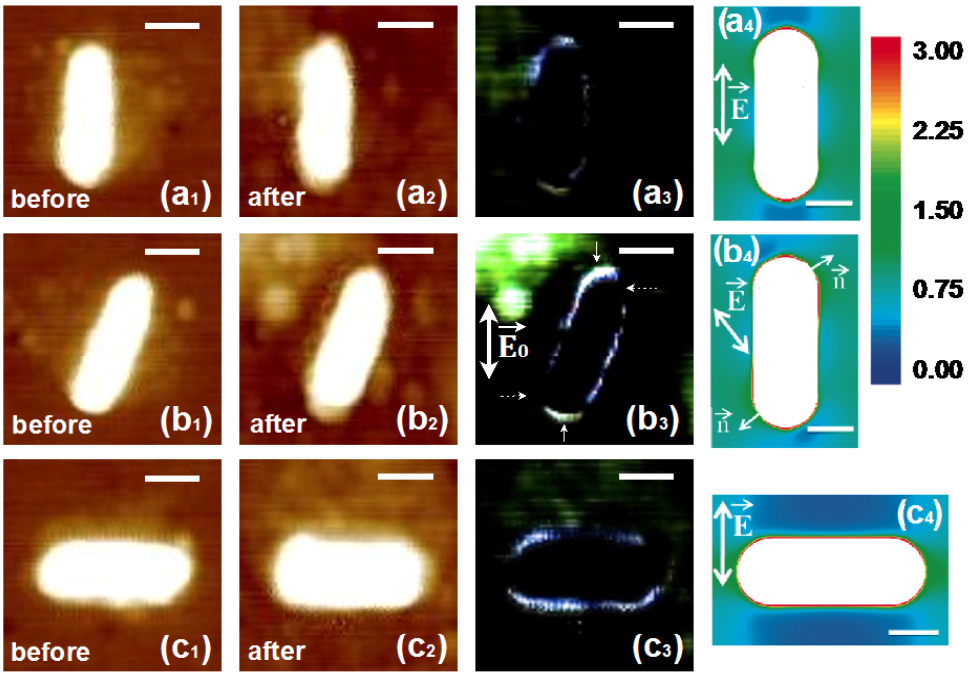


*Figure 5.10 : Images AFM collectées avant (colonne 1) et après (colonne 2) la photopolymérisation, les images différentielles (colonne 3), et les images calculées par FDTD (colonne 4). Les orientations des trois rods sont (a) $\theta = 0°$, (b) $\theta = 22.5°$, et (c) $\theta = 90°$.*

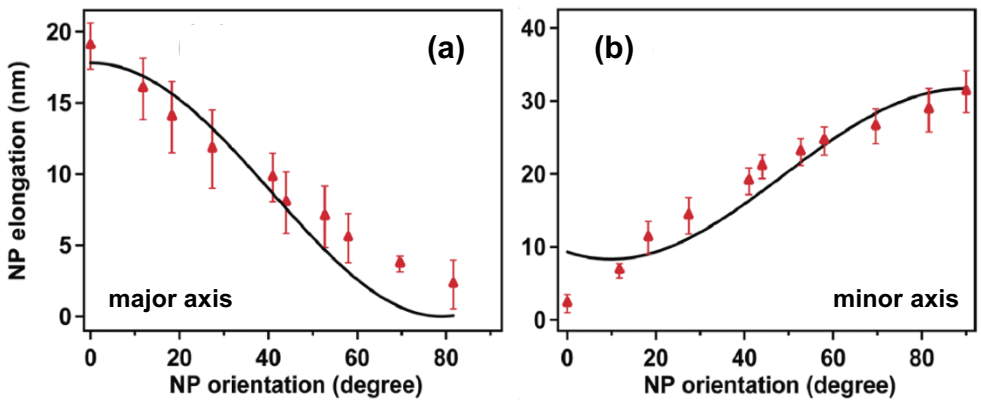


*Figure 5.11 : Élongation du polymère le long du (a) grand axe et (b) petit axe à mesure qu'on augmente l'orientation du nanorod. Les courbes en noirs sont des résultats numériques pour les datas mesurés (triangle en rouge).*

L'effet de l'orientation du nanorod sur l'élongation du photopolymère est montré dans la Figure 5.11. L'élongation du grand axe décroît à mesure que $\theta$ augmente du 0° à 90°. En comparaison, l'élongation du petit axe s'accroît avec une orientation du nanorod qui augmente. Dès que la dose locale dépasse le seuil, l'extension du polymère $l$ soit proportionnelle à l'intensité du champ électromagnétique à la surface de la nanoparticule $I_{surf}$:

$$l = \alpha I_{surf} \tag{5.8}$$

où $\alpha$ est une coefficient correspondante à la propriété photo-physique du polymère. $I_{surf}$ est défini par

$$I_{surf} = (\boldsymbol{E_0} + \chi \boldsymbol{n} \cdot \boldsymbol{E_0})^2 \tag{5.9}$$

On peut déduire des expressions 5.8 et 5.9 les élongations polymères le long du grand axe $l_M$ et du petit axe $l_m$ du rod :

$$l_M = l_0(1 + \chi^2 \cos^2\theta + 2\chi \cos\theta) \tag{5.10}$$

$$l_m = l_0(1 + \chi^2 \sin^2\theta + 2\chi \sin\theta) \tag{5.11}$$

où $l_0 = \alpha I_0$ correspond à l'extension minimal peut être détecté. Les courbes noires en Figure 5.11 représentent les élongations du polymère le long du grand axe exprimant par l'équation 5.10 et le long du petit axe en ajoutant un décalage dans l'équation 5.11 :

$$l_m = l_0(1 + \chi^2 \sin^2\theta + 2\chi \sin\theta) + l_1 \tag{5.12}$$

Nous avons obtenu une susceptibilité électrique de $\chi = -5.2 \pm 0.1$ pour le grand axe et en même temps $\chi = -5.8 \pm 0.3$ et $l_1 = 8.3$nm pour le petit axe. La valeur moyenne de la susceptibilité électrique est $\chi = -5.4$, qui est en bon accord avec la valeur rapportée dans la littérature.[129-130]

### 5.3.3 Nanocubes d'or : distribution du champ proche en fonction de l'orientation du nanocube

La solution colloïdale de nanocubes d'or de taille 60nm a été fabriquée par S. Marguet (CEA Saclay) dans une méthode de croissance chimique de grains. La Figure 5.12 (a) montre une image AFM de $2\mu m \times 2\mu m$ des nanocubes d'or sur une lame d'ITO. Le spectre d'extinction mesuré est représenté en panneau (b) en rouge. Un plafond se trouve à 562nm, qui est en bon accord avec la valeur calculée (570nm).

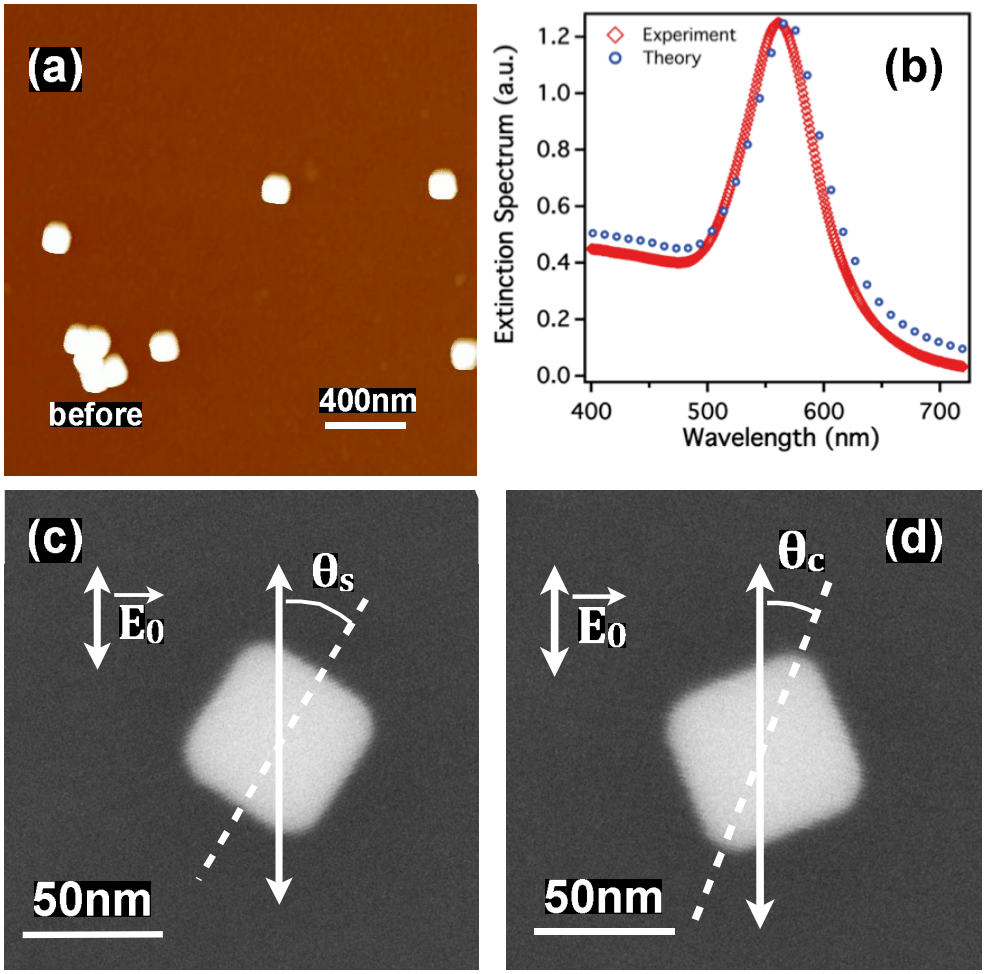


*Figure 5.12: (a) Image AFM des nanocubes d'or. (b) Spectres d'extinction mesuré (en rouge) et calculé (en bleu) des nanocubes dans l'eau. Les définitions de (c) l'orientation d'arête et (d) l'orientation de coin des nanocubes.*

Dans cette étude, on a mesuré le champ proche en fonction de l'orientation des nanocubes. Pour faciliter les discussions, on définit l'orientation d'arête $\theta_s$ en Figure 5.12 (c) et l'orientation de coin $\theta_c$ en Figure 5.12 (d). La polarisation incidente est montrée par $E_0$ en verticale. Les nanostructures polymères sont mesurées le long des lignes pointillées et sont dénotées comme l'élongation d'arête et l'élongation de coin en panneaux (c) et (d), respectivement.

Les nanoparticules sont caractérisées par AFM avant et après la procédure de photopolymérisation. Un laser $\lambda_0 = 532\text{nm}$ a été utilisé avec une dose incidente variant de 5% à 75% de la dose seuil. Les images différentielles des deux nanocubes typiques sont montrées dans Figure 5.13 (a) et (c). Les panneaux (b) et (d) sont les résultats simulés avec la méthode DDA de la distribution du champ électromagnétique pour les deux cubes en panneaux (a) et (c), respectivement.

On obtient une élongation du polymère maximale aux coins en haut et en bas du nanocube de $\theta_c = 0°$ (Figure 5.13 (a)) et aux arêtes en haut et en bas du nanocube de $\theta_s = 0°$ (Figure 5.13 (b)). À ces points, le vecteur unitaire normal de

surface $\boldsymbol{n}$ est parallèle à la polarisation incidente (la direction de $\boldsymbol{E_0}$). Les résultats simulés sont en bon accord avec les images différentielles. Nous traçons une ligne blanche d'iso-intensité pour marquer la frontière de la nanostructure photopolymère. Aux endroits où le vecteur n est perpendiculaire à $\boldsymbol{E_0}$, la taille du photopolymère est minimale (le coin gauche et le coin droite du nanocube dans de $\theta_c = 0°$ et l'arête gauche et droite dans le cas du nanocube de $\theta_s = 0°$).

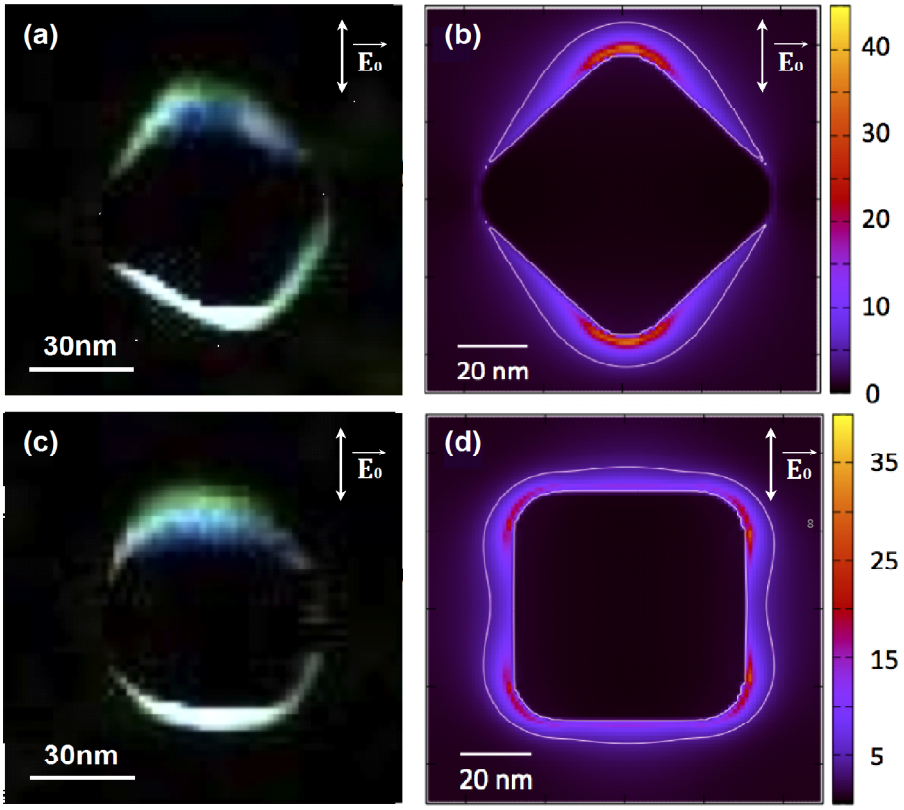


*Figure 5.13 : Images AFM différentielles des nanocubes (a) $\theta_c = 0°$ et (c) $\theta_c = 45°$. Les distributions du champ électromagnétique simulées sont montrées en panneaux (b) et (d).*

Les élongations polymères ont été mesurées, aux coins et aux arêtes, pour les nanocubes avec orientations différentes. Cette étude a été effectuée pour toutes les doses incidentes utilisées. La Figure 5.14 compare les data de $D_0 = 25\% D_{th}$ obtenues par expérience (panneau (a)) et calculassions (panneau (b)). Dans les deux cas des coins et les arêtes, la taille du polymère diminue à mesure qu'on augmente $\theta$ ($\theta = \theta_c$ pour l'élongation du coin et $\theta = \theta_s$ pour l'élongation de l'arête). Par ailleurs, l'élongation du coin est plus sensible que celle de l'arête au petit angle $\theta$ en raison de l'effet de pointe.

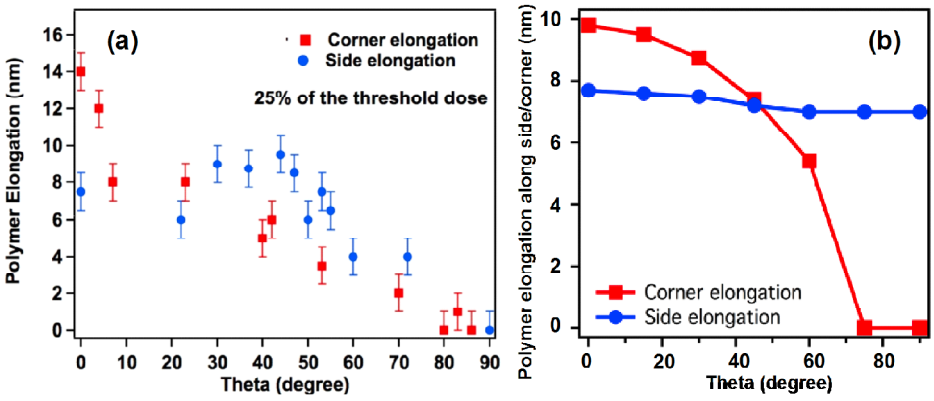


*Figure 5.14 : Élongations polymères (a) mesurées et (b) calculées au coin (carrés rouges) et à l'arête (points bleu). La dose incidente est* $D_0 = 25\%D_{th}$

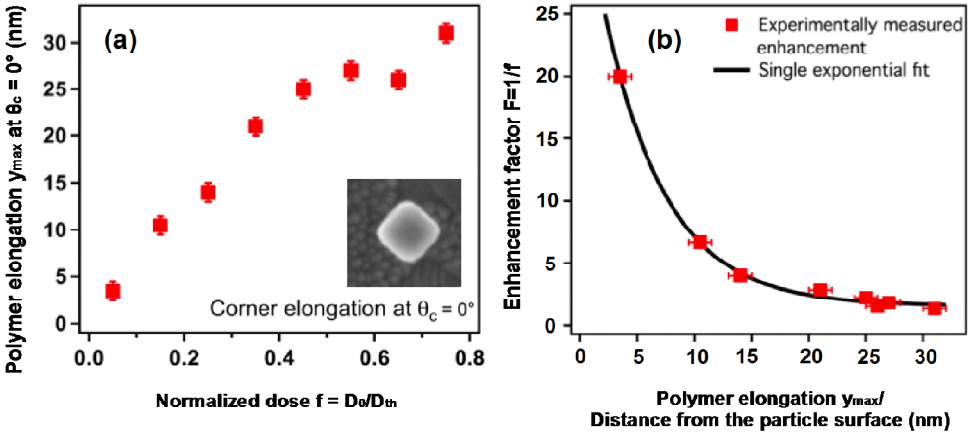


*Figure 5.15: (a) Élongation du polymère au coin des nanocubes* $\theta_c = 0°$ *en fonction de la dose normalisée. (b) Décroissance exponentielle du plasmon de surface reproduit par la photopolymérisation. La courbe noire est le fit du data mesurée (carrés rouge) par* $F = F_{max}e^{-\alpha y_{max}}$.

L'élongation du coin des nanocubes $\theta_c = 0°$ est montréd sur la Figure 5.15 (a) en fonction de la dose normalisée ($f = D_0 D_{th}$). Pour créer le polymère, un facteur d'exaltation minimal de $1/f$ est necessaire. C'est le facteur d'exaltation à la frontière du polymère, où la distance à la surface du nanocube est mesuré par l'élongation du coin $y_{max}$. Nous pouvons donc reproduire, comme ce qui est représentée dans la Figure 5.15 (b), la décroissance exponentielle du plasmon de surface par traçant $1/f$ en fonction de l'élongation du polymère.

La dose locale $D_{loc}$ décroît exponentiellement en fonction de la distance de la surface de nanoparticule $y$:[50]

$$D_{loc} = F_{max} D_0 e^{-\alpha y} \tag{5.13}$$

avec $F_{max}$ le facteur d'exaltation à la surface de nanoparticule. Par conséquent, aux frontières du polymère ($y = y_{max}$), le facteur d'exaltation est donné par

$$F = F_{max} e^{-\alpha y_{max}} \tag{5.14}$$

Cette équation est révélée Figure 5.15 (b) par la courbe noire avec un facteur d'exaltation à la surface de particule de $F_{max} = 35$ et une longueur de décroissance de $\alpha^{-1} = 5$ nm. Cela est en bon accord avec les mesures.

## 5.4 Plasmon hybride actif: NE anisotrope

La technique de nano-photo polymérisation nous permettre de caractériser le plasmon de surface avec une très haute résolution sub-5nm. Des molécules de colorant sont piégées dans les nanostructures polymères. Cela nous permet de développer la structure hybride de nanoparticule d'or/photopolymère comme un NE. Par rapport aux travaux publiés, la distribution de nos nanostructures hybrides est anisotrope au niveau de la géométrie. Dans nos études, les NEs anisotropes sont caractérisés soit par spectroscopie de fluorescence, soit via un spectre Raman.

### 5.4.1 Fluorescence du NE hybride de nanosphère d'or/photopolymère

Afin de souligner l'anisotropie de la configuration de nos NEs, on a choisi la nanosphère d'or de $d = 70$ nm, un nano-objet symétrique, pour supporter les plasmons de surface. Le colorant dans la solution photopolymérisable était EY. Un laser de $\lambda = 532$nm avec une dose incidente de $D_0 = 70\% D_{th}$ a été utilisé pour la photopolymérisation. Les profils topographiques d'une nanostructure hybride sont montrés dans la Figure 5.16. Avec une polarisation incidente le long de l'axe-Y, on a obtenu une nanostructure de 15nm en chaque côté le long de cet axe au voisinage de la nano sphère d'or.

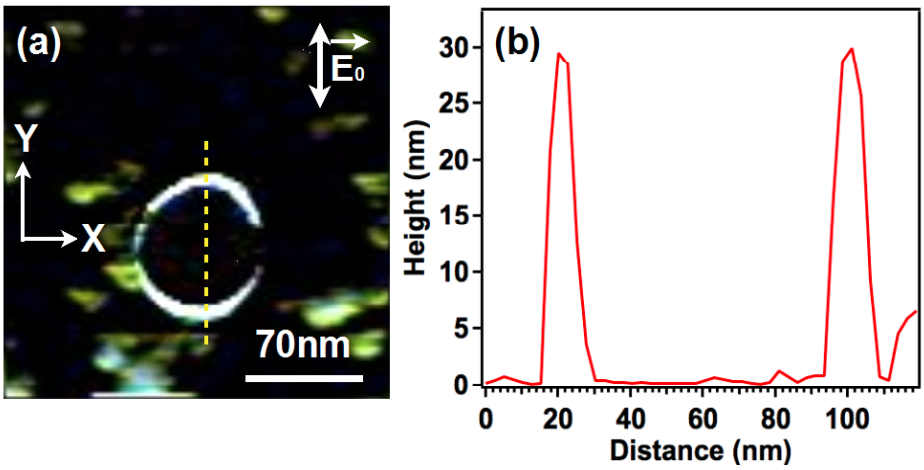


*Figure 5.16: (a) Image AFM différentielle d'un NE et (b) son profil de transversal le long de la ligne pointillée sur le panneau (a).*

La fluorescence d'EY dans le NE a été détectée avec deux polarisations incidentes différentes :

•**Sx** : le signal de fluorescence collecté avec une polarisation incidente qui est parallèle à l'axe-X et perpendiculaire aux structures de photopolymère (Figure 5.17 (a)). La fluorescence des molécules aux positions 2 et 3 est renforcée par le champ proche.

•**Sy** : le signal de fluorescence collecté avec une polarisation qui est parallèle à l'axe-Y et le long des structures de photopolymère (Figure 5.17 (b)). La fluorescence des molécules aux positions 3 et 4 est renforcée par le champ proche.

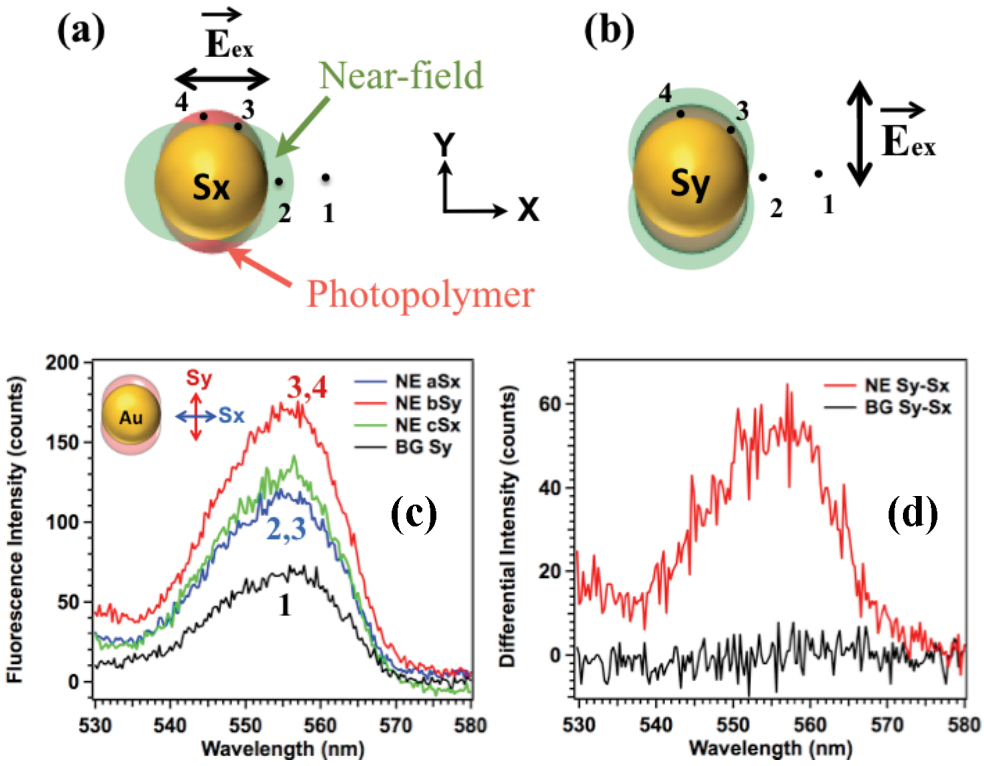


*Figure 5.17: Schéma des deux modes d'émissions: (a) Sx, avec et (b) Sy. (c) Spectres Sx et Sy du NE et signal de fluorescence sur le lame de verre. (d) Spectres différentiels Sy-Sx du NE et du BG.*

La Figure 5.17 (c) montre les spectres Sx et Sy du NE et la fluorescence de background (BG) sur la lame de verre (sans aucune nanoparticule dans la zone de détection). Les spectres ont été collectés l'une après l'autre dans un ordre chronologique a-b-c, correspondant à une variation X-Y-X de la direction de polarisation incidente. Le signal d'EY du BG (en noir) nous indique que le substrat n'était pas parfaitement nettoyé par le rinçage. En comparant les Sx du BG et du NE, on peut voir une modification de l'émission d'EY par la nanoparticule d'or. L'intensité de fluorescence a été augmentée pat 1.7 fois de 68 à 115 coups. Par ailleurs, on a obtenu une intensité du bSy (170) plus haute que aSx (115) sur le NE. L'anisotropie du NE hybride peut être décrite par les intensités de fluorescence corrigées: $(Sy - BG)/(Sx - BG) \approx 2.2$. Ce *ratio* résulte de l'augmentation du nombre de molécules qui sont excitées par le champ proche lorsque la direction de la

polarisation incidente est parallèle aux structures polymères. En comparant les spectres différentiels Sy – Sx sur le NE et sur la BG (Figure 5.17 (b)), on peut voir clairement l'anisotropie de la NE. La fluorescence de BG ne montre aucune dépendance à la polarisation incidente. Par contre, un résultat positif sur NE indique la sensibilité de l'émission à la polarisation.

En raison de la configuration complexe de notre NE, on n'a pas réussi, pour le moment, à décrire théoriquement la NE. Toutefois, comme la première étape, nous avons calculé le taux d'émission normalisé γemγem0 pour une seule molécule, avec $\gamma_{em}^{0}$ et $\gamma_{em}$ le taux d'émission dans l'espace libre et proche d'un nanoparticule, respectivement. En d'autres termes, on a calculé la modification de fluorescence en déplaçant une molécule de la position 1 à la position 2 dans la Figure 5.17 (a). L'orientation moléculaire est un facteur non-contrôlable dans notre expérience, mais il influence le taux d'émission par l'efficacité quantique Q et le taux d'excitation $\gamma_{ex}$:

$$\gamma_{em} = Q\gamma_{ex} \tag{5.15}$$

Ces deux facteurs sont sensibles à l'orientation moléculaire et à la distance molécule-nanoparticle. Dans notre expérience, ce sont des paramètres qui ne peuvent pas être contrôlés. En utilisant une moyenne orientation moléculaire moyenné, on a calculé la distribution spatiale du taux d'émission normalisé dans le milieu isotrope de $n = 1.48$. La Figure 5.18 montre les sections transversales (a) dans le plan XOZ et (b) le plan XOY passant par le centre de la particule. Le laser d'excitation de $\lambda_{ex}$=514nm se propage le long de l'axe-Z et polarisé selon l'axe-X.

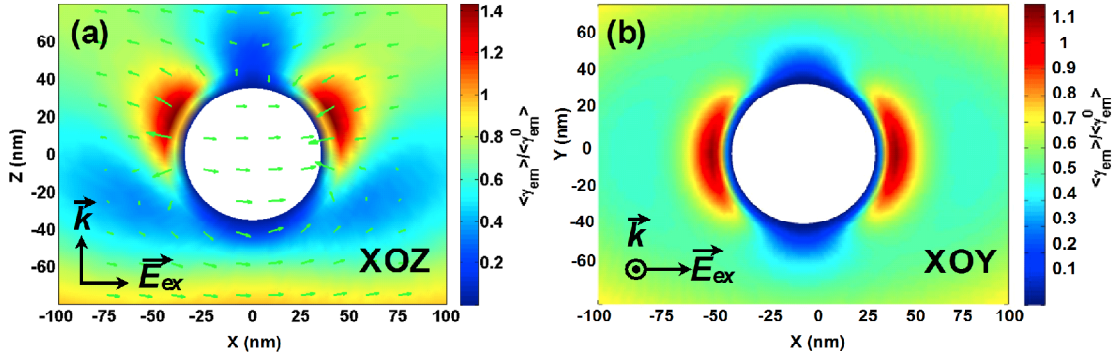


*Figure 5.18: Dépendance spatiale du taux d'émission normalisé $\gamma em\gamma em0$ d'une seule molécule EY près d'un nanosphère d'or de $d = 70nm$. Le calcul a été effectué dan un milieu isotrope de $n = 1.48$, avec une longueur d'onde d'excitation de $\lambda_{ex} = 514nm$ et une longueur d'onde d'émission de $\lambda_{em} = 555nm$. La lumière incidente se propage dans l'axe-Z et polarisé dans l'axe-X. Les flèches vertes représentent les orientations de champs électromagnétiques.*

On trouve dans la Figure 5.18 (a) que les pôles d'émission maximale sont inclinés vers l'axe-Z parce que les modes plasmons quadripolaire sont probablement légèrement excités. La section dans le plan XOY (Figure 5.18 (b)) montre que les pôles d'émission maximale sont orientés le long de la polarisation incidente. Une valeur maximale du taux d'émission normalisé de 1.45 est trouvée, ce qui

correspond à la "$NE\,Sx\,/\,BG\,=\,1.7$" obtenue par l'expérience. La différence entre théorie et expérience résulte de i) l'anisotropie de la géométrie du milieu, ce qui n'était pas inclus dans le modèle, et de ii) la concentration de molécules d'EY excités en champ proche qui est plus haut en position 3 qu'en position 2. Cela confirme aussi l'anisotropie de notre NE hybride.

### 5.4.2 SERS sur dimère d'or/photopolymère dopé par MB

Le SERS est une autre technique que l'on a utilisée pour caractériser le NE. Le nano-objet choisi était le dimère de nanodisques avec un diamètre de $d = 100$nm et un écart variant de $g = 0$ à $g = 55$nm entre les deux monomères. Nous avons cette fois utilisé le bleu deMéthylène (région d'absorption [550-700] nm avec un maximum à 660nm dans PETIA) comme le colorant incorporé dans la solution photopolymérisable. La dose incidente du laser $\lambda = 647$ nm pour la photo polymérisation était $D_0 = 70\%D_{th}$. La polarisation incidente était le long de l'axe-X dans la Figure 5.19.

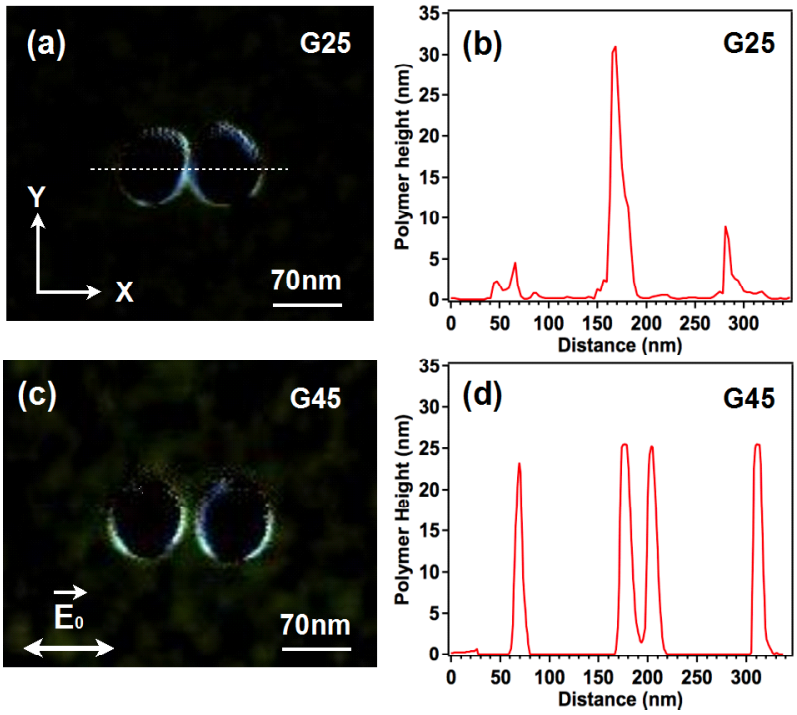


*Figure 5.19: (a) Image AFM différentielle d'un dimère de $g = 25nm$ (G25) et (b) son profile de section transversale le long de la ligne pointille en panneau (a). (c) Image différentielle et (d) le profile d'un dimère de $g = 45nm$ (G45).*

La Figure 5.19 montre les images AFM différentielles et les profils correspondants de deux NEs typiques. Le gap du dimère $g = 25$nm (Figure 5.19 (a) et (b)) est rempli par le photopolymère en raison d'un couplage plasmonique de ses deux monomères. La distribution de photopolymère du dimère $g = 45$nm (Figure

5.19 (c) et (d)) démontre quant à elle qu'il n'y a pas de couplage plasmonique dans son gap.

Nous avons mesuré les spectres de diffusion pour tous les dimères hybrides de $g = 0$ à $55$nm. La Figure 5.20 (a) montre les spectres qu'on a détectés avec une polarisation incidente le long du grand axe. La résonance de plasmon es décalée vers le rouge en diminuant le gap de $g = 30$nm à $10$nm. À partir de $g = 30$nm, le spectre de diffusion ne varie plus (625nm). Dans le cas $g = 0$, le mode quadripolaire du plasmon de surface a été excité. Cela explique la résonance plasmonique à 590nm, qui est décalée vers le bleu en comparaison avec les autres spectres. Le spectre de diffusion du dimère à $g = 5$nm est très intense à nos connaissances. Le pic de ce dimère est décalé vers le rouge par rapport à $g = 10$nm en raison du couplage plasmonique. La résolution (environ 10nm) de EBL utilisé pour fabriquer cet échantillon peut être responsable du décalage vers le bleu. En d'autres termes, l'écart de ce dimère est en fait beaucoup plus petit (moins de 0.5 nm comme dans les littératures[136-138]). Le maximum de diffusion du petit axe est constant (Figure 5.20 (b)).

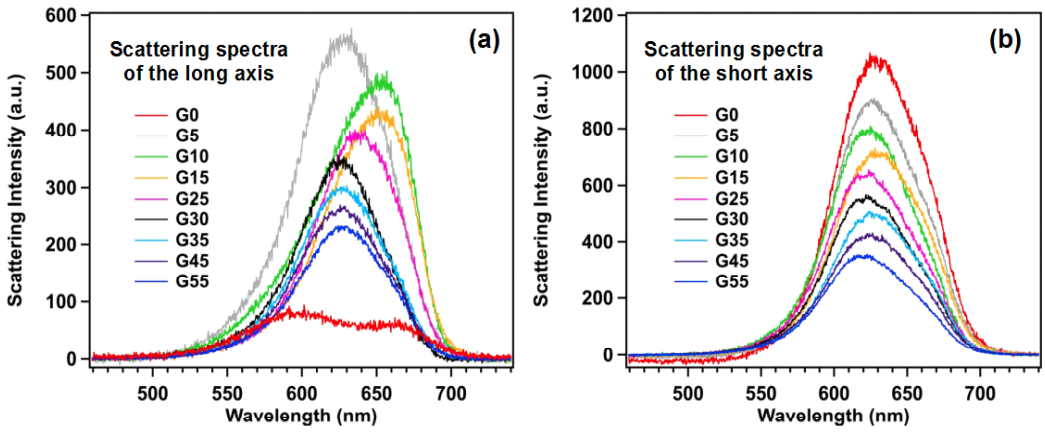


*Figure 5.20: Spectres de diffusion le long du (a) grand axe et du (b) petit axe des dimères de $g = 0$ à $g = 55nm$.*

Les signaux SERS ont été collectés avec un laser $\lambda = 633$ nm à deux polarisations différentes: le long du grand axe (Sx) et du petit axe (Sy). La Figure 5.21 montre deux exemples typiques de dimères à petit écart ($g = 10$nm sur le panneau (a) et à grand écart de $g = 55$nm sur le panneau (b). Les spectres ont été collectés dans un ordre chronologique a-b-c-d. Evidemment, l'intensité du Sx est plus haute que Sy, surtout le mode de 1620cm$^{-1}$. Par ailleurs, on peut voir un effet de photo-blanchement en comparant aSy et cSy, ou bSx et dSx. Le petit écart fournie une grande augmentation d'exaltation.

Autre que le renforcement électromagnétique, le nombre de molécules qui est plus important le long du grand axe a contribué aussi à l'anisotropie du signal SERS. La contribution du nombre de molécules est illustrée par le dimère $g = 55$nm dans Figure 5.21 (b). Nous avons montré dans la Figure 5.20 (a) que le couplage

plasmonique entre les deux nanodisques du dimère a disparu à partir de l'écart de $g = 30$ nm. La Figure 5.21 (b) illustre des spectres de deux monomères de nanodisques individuels. La différence des intensités de Sy et Sx a diminué, mais on peut voir quand même clairement une augmentation de Sx pour le mode 1620cm$^{-1}$.

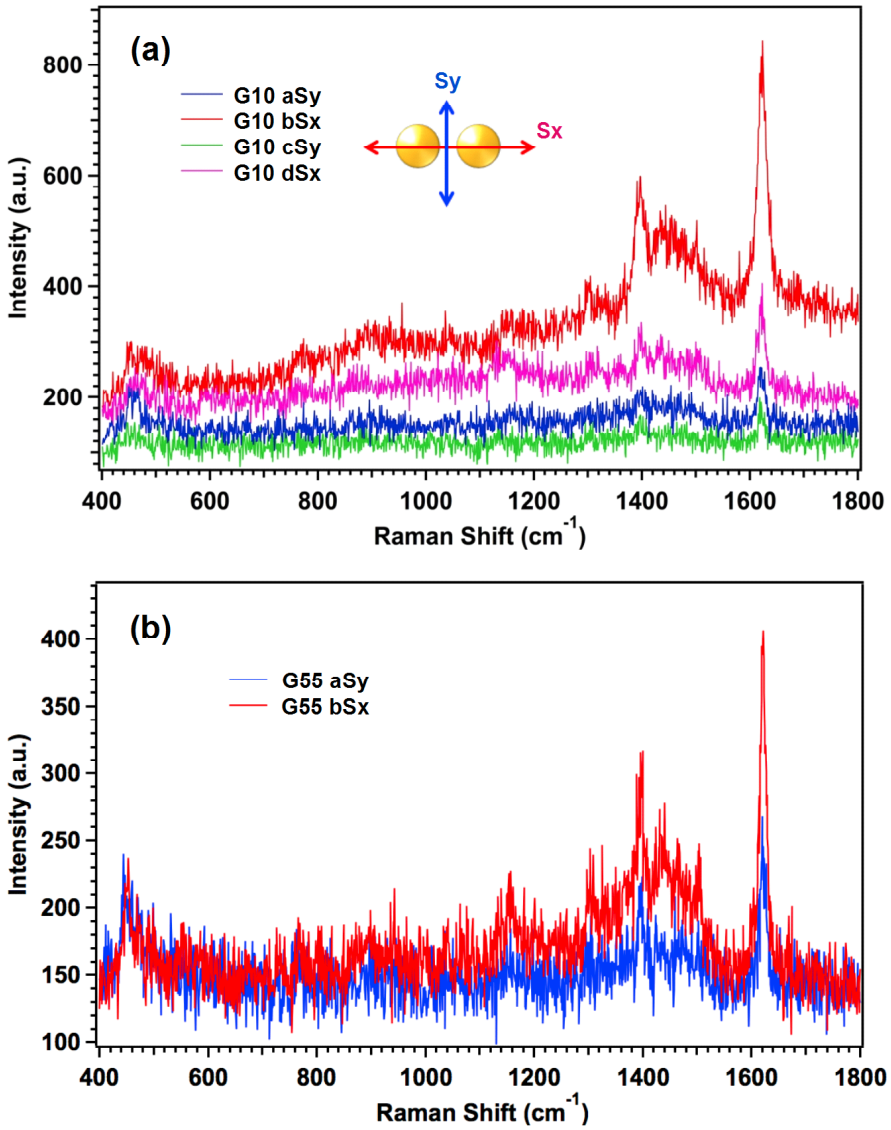


*Figure 5.21: Spectres du SERS sur le dimère (a) $g = 10nm$ et (b) $g = 55nm$. Les spectres ont été collectés dans un ordre chronologique de a-b-c-d. Le signal Sx est plus grand que Sy.*

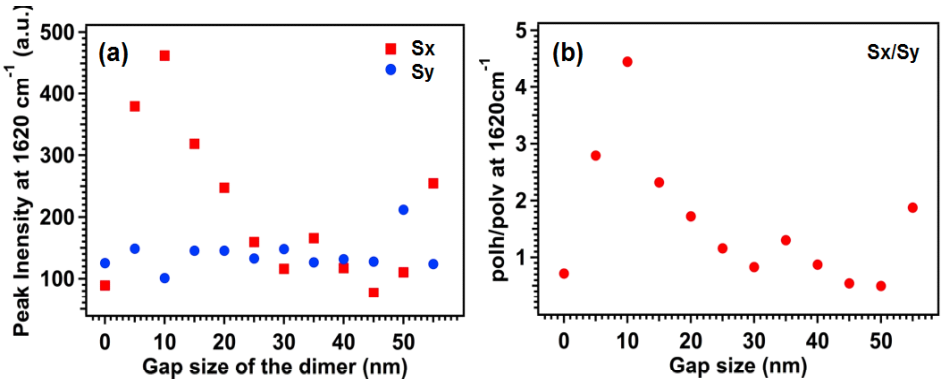


*Figure 5.22: (a) Intensités du mode 1620cm$^{-1}$ (baseline corrigé) pour tous les dimères. (b) ratio Sx/Sy du mode 1620cm$^{-1}$.*

Nous avons mesuré les intensités du mode 1620cm$^{-1}$ (baseline corrigé) pour tous les dimères (Figure 5.22 (a)). Le signal du Sy présente une faible variation. Par conte, le Sx est dépendant de la taille du gap $g$. La Figure 5.22 (b) illustre le ratio Sx/Sy de l'intensité du mode 1620 cm$^{-1}$. On peut voir un maximal Sx/Sy de 4.6 au dimère $g = 10$nm. Il est décroissant en général lorsque le gap augmente. Pour quelque dimères, de $g = 30$nm à $g = 50$nm, plus précisément, le ratio fluctue autour de 1. Le fait qu'un couplage plasmonique existe entre les deux monomères de nanodisque et l'effet du photo-blanchiment peuvent être responsables de ce résultat.

## 5.5 Conclusions et perspectives

Nous avons présenté une nanostructure plasmonique hybride qui a été développée pour caractériser le champ proche optique, et qui a été appliqué dans cette thèse pour étudier quantitativement plusieurs effets optiques à l'échelle nanométrique et pour fabriquer des nanoémetteurs optiques anisotropes.

La fabrication de la nanostructure hybride est basée sur la photopolymérisation nanométrique. Les photopolymères sont crée uniquement aux endroits où l'énergie du champ local excède le seuil pour photopolymérisation, et la dose du champ local est contrôlée par les plasmons de surface supportés par les nanoparticules métalliques. En imprimant la distribution des plasmons de surface via le nanopolymère fabriqué, la nanostructure hybride métal/polymère nous fournit le profil détaillé du champ proche d'une nanoparticule individuelle. La taille de la structure polymère est une mesure de la profondeur de décroissance de plasmon.

Le plasmonique passive hybride contribue à la caractérisation quantitative du champ proche. Nous avons étudié dans cette thèse la distribution du champ proche de nanosphères d'or qui présentent une dépendance spécifique du diamètre de la sphère, avec une taille optimisée de $d = 50$ nm. Ceci est en raison des effets de taille finie: amortissement radiatif, amortissement non radiatif et dépolarisation. En outre, nous avons réussi à imaginer et mesurer le champ proche de nanorods et de nanocubes d'or avec des orientations différentes. Il s'agit d'une observation directe de la distribution spatiale des charges de polarisation photoinduites à l'interface

métal/diélectrique. Nous avons montré à la fois la possibilité de détecter un champ proche faible qui est excité hors-résonance, et la capacité de cette technique à reproduire la décroissance exponentielle des plasmons de surface. Ces études ont démontré une résolution spatiale sub-5nm.

En bénéficiant des molécules de colorant piégées dans la nanostructure polymère, nous avons développé des NEs. A l'aide du plasmon dipolaire, les nanostructures hybrides émettent un champ dont l'intensité dépend de la polarisation incidente.. Ceci a été confirmé par la détection des signaux de fluorescence sur un NE hybride de nanosphère d'or/polymère. Nous avons obtenu un maximum intensité de fluorescence avec une polarisation incidente le long des structures de photopolymère. En outre, les signaux SERS sensibles à la polarisation incidente ont été collectés sur des NEs hybrides dimères d'or/photopolymère. En profitant de l'augmentation électromagnétique du champ local et des densités de molécules plus élévées dans les gaps, un signal SERS optimum a été obtenu pour un gap de 10nm.

Bien que beaucoup de résultats aient été obtenus dans cette thèse, il reste encore des points/effets à améliorer/contrôler: contrôle de la distribution et l'orientation des molécules de colorant, photo-blanchissement des molécules colorant, processus du rinçage,... Nous doperons la solution par des boîtes quantiques en raison d'une durée de vie plus longue et d'une meilleure stabilité optique. De plus, une coquille de silicium peut être fabriquée pour contrôler la distance de nanoparticule-molécule. En outre, le plasma d'oxygène sera utilisé pour mieux nettoyer les échantillons après la photo polymérisation.

# APPENDIX

As has been presented in Chapter 1, numerical simulations play very important roles in near-field studies. In this dissertation, the simulated results have helped us in better understanding our experimental data in providing images of field distributions, values of field intensity enhancement factors, plasmon resonance of nanoparticles, and the fluorescence intensity of dyes. Three methods for numerical simulations have been involved: the finite-difference time-domain (FDTD), the discrete dipole approximation (DDA), and the Mie theory calculations. We will briefly introduce the basics of each method in the appendix.

## I Mie calculation applied to nano-emitter

Mie calculation is a method based on Mie theory, which provides exact solution for electromagnetic problems in the case of spherical particles. The general divergence-less $(\nabla \cdot \boldsymbol{E} = 0)$ solution of Helmholtz equation $\nabla^2 \boldsymbol{E} + k^2 \boldsymbol{E} = 0$ can be written in spherical coordinates as[58]

$$\boldsymbol{E}(\boldsymbol{r}) = E_0 \sum_{n=0}^{\infty} \sum_{m=-n}^{m=n} a_{nm} M_{nm}^{(i)}(k, \boldsymbol{r}) + b_{nm} N_{nm}^{(i)}(k, \boldsymbol{r}) \quad (1)$$

where $k = \sqrt{\varepsilon}\,\omega/c$ is the wave vector, $E_0$ is the electric field amplitude, $a_{nm}$ and $b_{nm}$ are expansion coefficients, $M_{nm}^{(i)}(k, \boldsymbol{r})$ and $N_{nm}^{(i)}(k, \boldsymbol{r})$ are the vector spherical harmonics. They correspond to the electric field of magnetic ($M_{nm}^{(i)}$) and electric ($N_{nm}^{(i)}$) dipoles ($n = 1$) or multipoles ($n > 1$). The index $i = 1,2,3,4$ correspond to four types of spherical Bessel function $z_n$ (singular/infinite field or not, plane wave or ingoing/outgoing waves). The vector spherical harmonics are defined as[58]

$$M_{nm}(k, \boldsymbol{r}) = \nabla \times z_n(kr)\boldsymbol{r} \sqrt{\frac{2n+1}{4\pi n(n+1)} \frac{(n-m)!}{(n+m)!}} P_n^m(\cos\theta) e^{im\phi} \quad (2)$$

$$N_{nm}(k, \boldsymbol{r}) = \frac{1}{k} \nabla \times M_{nm}(k, \boldsymbol{r}) \quad (3)$$

where $P_n^m(\cos\theta)$ is the associated Legendre functions.

For a MNP with radius $R$ (dielectric function $\varepsilon_2$) that is surrounded by a dielectric medium (permittivity $\varepsilon_1$), its local electric field $\boldsymbol{E}_{loc}$ is the sum of incident field $\boldsymbol{E}_{inc}$ and the scattered field $\boldsymbol{E}_{sca}$:

$$\boldsymbol{E}_{loc}(\boldsymbol{r}) = \boldsymbol{E}_{inc}(\boldsymbol{r}) + \boldsymbol{E}_{sca}(\boldsymbol{r}) \quad (4)$$

with the incident field and scattering field expressed as[58]

$$\boldsymbol{E}_{inc}(\boldsymbol{r}) = E_0 \sum_{n,m} a_{nm} M_{nm}^{(1)}(k,\boldsymbol{r}) + b_{nm} N_{nm}^{(1)}(k,\boldsymbol{r}) \tag{5a}$$

$$\boldsymbol{E}_{sca}(\boldsymbol{r}) = E_0 \sum_{n,m} \mathrm{A}_n a_{nm} M_{nm}^{(3)}(k,\boldsymbol{r}) + \mathrm{B}_n b_{nm} N_{nm}^{(3)}(k,\boldsymbol{r}) \tag{5b}$$

$\mathrm{A}_n$ and $\mathrm{B}_n$ are the Mie coefficients defined as[58,133]

$$A_n = \frac{j_n(\rho_1)\psi_n'(\rho_2) - j_n(\rho_2)\psi_n'(\rho_1)}{j_n(\rho_2)\zeta_n'(\rho_1) - h_n^{(1)}(\rho_1)\psi_n'(\rho_2)} \tag{6a}$$

$$B_n = \frac{\varepsilon_1 j_n(\rho_1)\psi_n'(\rho_2) - \varepsilon_2 j_n(\rho_2)\psi_n'(\rho_1)}{\varepsilon_2 j_n(\rho_2)\zeta_n'(\rho_1) - \varepsilon_1 h_n^{(1)}(\rho_1)\psi_n'(\rho_2)} \tag{6b}$$

where $\rho_1 = k_1 R$, $\rho_2 = k_2 R$, $k_1 = \sqrt{\varepsilon_1}\,\omega/c$, $k_2 = \sqrt{\varepsilon_2}\,\omega/c$. $j_n$ is the spherical Bessel function, $h_n^{(1)}$ is the Hankel function, $\psi_n(x) = x j_n(x)$, and $\zeta_n(x) = x h_n^{(1)}(x)$.

Now let us consider a randomly oriented quantum emitter (i.e., dye, QDs…) that is located at $(d,0,0)$ near a metallic sphere centered at the original. The normalized total decay rate $\gamma/\gamma_0$ of this emitter can be calculated as[134]

$$\frac{\gamma}{\gamma_0} = \frac{1}{3}\frac{\gamma_\perp}{\gamma_0} + \frac{2}{3}\frac{\gamma_\parallel}{\gamma_0} \tag{I.7}$$

with the subscript $\perp$ and $\parallel$ associated with a dipole perpendicular and parallel, respectively, to the surface of the MNP. $\gamma_0$ is the total decay rate of the quantum emitter in free space. $\gamma = \gamma^{Rad} + \gamma^{NR}$ is the nanoparticle-modified total decay rate, $\gamma^{Rad}$ is the modified radiative decay rate, and $\gamma^{NR}$ is the modified non-radiative decay rate. For a vertical dipole[133]

$$\frac{\gamma_\perp}{\gamma_0} = 1 + \frac{3}{2} Re \sum_{n=1}^{\infty} (2n+1) n(n+1) B_n \left[\frac{h_n^{(1)}(u)}{u}\right]^2 \tag{8a}$$

$$\frac{\gamma_\perp^{Rad}}{\gamma_0} = \frac{3}{2}\sum_{n=1}^{\infty} (2n+1) n(n+1) \left|\frac{j_n(y_1) + B_n h_n^{(1)}(u)}{u}\right|^2 \tag{8b}$$

For a horizontal dipole [133]

$$\frac{\gamma_\parallel}{\gamma_0} = 1 + \frac{3}{2} Re \sum_{n=1}^{\infty} \left(n + \frac{1}{2}\right) \left\{ B_n \left[\frac{\zeta_n'(u)}{u}\right]^2 + A_n [h_n^{(1)}(u)]^2 \right\} \tag{9a}$$

$$\frac{\gamma_\parallel^{Rad}}{\gamma_0} = \frac{3}{4}\sum_{n=1}^{\infty} (2n+1) \left[ \left| j_n(u) + A_n h_n^{(1)}(u) \right|^2 + \left| \frac{\psi_n'(y_1) + B_n \zeta_n'(u)}{u} \right|^2 \right] \tag{9b}$$

where $u = k_1 d$. The modified quantum yield and emission rate of this quantum emitter can be calculated based on equations 7 to 9.

Mie theory works perfectly with spheres. The applications are now expanded to multilayer shells, multispheres, etc. However, for an arbitrary shaped nanoparticle (cube for example), it is no more applicable. In this context, simulation methods such as FDTD and DDA are wise choices for solving the electromagnetic problems.

## II FDTD

The main idea of FDTD method is to divide both space and time into segments, and then find solutions to Maxwell's equations at a given position and time-step. The smallest unit of the space unit is a Yee cell[140] (Figure 1) with a size of $(\Delta x, \Delta y, \Delta z)$, while the smallest unit of time-step $\Delta t$ represents the required time that electromagnetic wave propagates from one Yee cell to the next. The time-step should be selected to meet the requirement of stable limit:[141]

$$\Delta t < \frac{1}{c\sqrt{\frac{1}{(\Delta x)^2}+\frac{1}{(\Delta y)^2}+\frac{1}{(\Delta z)^2}}} \tag{10}$$

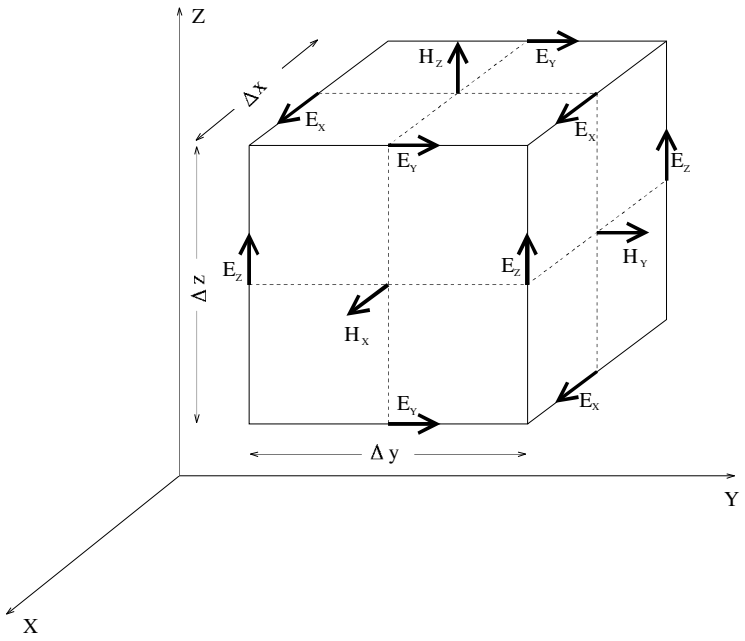


*Figure 1: Yee unit cell.*[140]

In three dimensions, the time-dependent Maxwell's equations in differential form is written as

$$\frac{\partial \boldsymbol{B}}{\partial t} = -\nabla \times \boldsymbol{E} - \boldsymbol{M} \tag{11a}$$

$$\frac{\partial \boldsymbol{D}}{\partial t} = -\nabla \times \boldsymbol{H} - \boldsymbol{J} \tag{11b}$$

$$\nabla \cdot \boldsymbol{D} = 0 \tag{11c}$$

$$\nabla \cdot \boldsymbol{B} = 0 \tag{11d}$$

with $\boldsymbol{E}$ the electric field, $\boldsymbol{D}$ the electric flux density, $\boldsymbol{H}$ the magnetic field, $\boldsymbol{B}$ the magnetic flux, $\boldsymbol{M}$ the equivalent magnetic current density, and $\boldsymbol{J}$ the electric current density. In a linear, isotropic, nondipersive materials,

$$\boldsymbol{D} = \varepsilon \boldsymbol{E} = \varepsilon_r \varepsilon_0 \boldsymbol{E} \tag{12a}$$

$$\boldsymbol{B} = \mu \boldsymbol{H} = \mu_r \mu_0 \boldsymbol{H} \tag{12b}$$

where $\varepsilon$, $\varepsilon_r$, and $\varepsilon_0$ are the electrical permittivity, relative permittivity, and free-space permittivity, respectively; $\mu$, $\mu_r$, $\mu_0$ are the magnetic permeability, relative permeability, and free-space permeability, respectively. By considering $\boldsymbol{J}$ and $\boldsymbol{M}$ as independent sources and energy loss in the material, one can deduce[141]

$$\boldsymbol{J} = \boldsymbol{J}_{source} + \sigma \boldsymbol{E} \tag{13a}$$

$$\boldsymbol{M} = \boldsymbol{M}_{source} + \sigma_m \boldsymbol{H} \tag{13b}$$

where $\sigma$ is the electric conductivity, $\sigma_m$ is the equivalent magnetic loss, $\boldsymbol{J}_{source}$ and $\boldsymbol{M}_{source}$ are sources of E and H fields, respectively. As a consequence, the Maxwell's curl equations can be expressed as

$$\frac{\partial \boldsymbol{H}}{\partial t} = \frac{1}{\mu}\left[-\nabla \times \boldsymbol{E} - \left(\boldsymbol{M}_{source} + \sigma_m \boldsymbol{H}\right)\right] \tag{14a}$$

$$\frac{\partial \boldsymbol{E}}{\partial t} = \frac{1}{\varepsilon}\left[-\nabla \times \boldsymbol{H} - \left(\boldsymbol{J}_{source} + \sigma \boldsymbol{E}\right)\right] \tag{14b}$$

In $(x, y, z)$ coordinates, equations 14a and 14b are written as

$$\frac{\partial H_x}{\partial t} = \frac{1}{\mu}\left[\frac{\partial E_y}{\partial z} - \frac{\partial E_Z}{\partial y} - \left(M_{source,x} + \sigma_m H_x\right)\right] \tag{15a}$$

$$\frac{\partial H_y}{\partial t} = \frac{1}{\mu}\left[\frac{\partial E_z}{\partial x} - \frac{\partial E_x}{\partial z} - \left(M_{source,y} + \sigma_m H_y\right)\right] \tag{15b}$$

$$\frac{\partial H_z}{\partial t} = \frac{1}{\mu}\left[\frac{\partial E_x}{\partial y} - \frac{\partial E_y}{\partial x} - \left(M_{source,z} + \sigma_m H_z\right)\right] \tag{15c}$$

$$\frac{\partial E_x}{\partial t} = \frac{1}{\varepsilon}\left[\frac{\partial H_z}{\partial y} - \frac{\partial E_y}{\partial z} - \left(J_{source,x} + \sigma E_x\right)\right] \tag{15d}$$

$$\frac{\partial E_y}{\partial t} = \frac{1}{\varepsilon}\left[\frac{\partial H_x}{\partial z} - \frac{\partial E_z}{\partial x} - \left(J_{source,y} + \sigma E_y\right)\right] \tag{15e}$$

$$\frac{\partial E_z}{\partial t} = \frac{1}{\varepsilon}\left[\frac{\partial H_y}{\partial x} - \frac{\partial E_x}{\partial y} - \left(J_{source,z} + \sigma E_z\right)\right] \tag{15f}$$

Equations 15a to 15f are the basics of three-dimension FDTD algorithm. It can be reduced to two dimensions and or dimension if necessary. Details can be found in reference [141].

For a given point $(i,j,k)$ in the space and with time of $t_n = n\Delta t$ ($i,j,k,n$ are integers), a function $u$ of space and time can be found in the coordinate system via

$$u(i\Delta x, j\Delta y, k\Delta z, n\Delta t) = u_{i,j,k}^{n} \tag{16}$$

Both space and time can be expressed using finite-difference approximations, which is second-order accurate:[141]

$$\frac{\partial u}{\partial x}(i\Delta x, j\Delta y, k\Delta z, n\Delta t) \approx \frac{u_{i+1/2,j,k}^{n} - u_{i-1/2,j,k}^{n}}{\Delta x} \tag{17a}$$

$$\frac{\partial u}{\partial y}(i\Delta x, j\Delta y, k\Delta z, n\Delta t) \approx \frac{u_{i,j+1/2,k}^{n} - u_{i,j-1/2,k}^{n}}{\Delta y} \tag{17b}$$

$$\frac{\partial u}{\partial z}(i\Delta x, j\Delta y, k\Delta z, n\Delta t) \approx \frac{u_{i,j+1/2,k}^{n} - u_{i,j,k-1/2}^{n}}{\Delta z} \tag{17c}$$

$$\frac{\partial u}{\partial t}(i\Delta x, j\Delta y, k\Delta z, n\Delta t) \approx \frac{u_{i,j,k}^{n+1/2} - u_{i,j,k}^{n-1/2}}{\Delta t} \tag{17d}$$

Based on equations 17a to 17d, one can deduce the electromagnetic field components. The accuracy of simulated results is associated with the size of Yee cell. Generally, the smaller the Yee cell, the better the result. The computational resource is another factor that has to be cogitated in practice.

# III DDA

As a common method for simulating the light scattering and the absorption on arbitrary shaped particles, DDA divides the target particle (volume $V$) into an array of N discrete point dipoles. Each dipole has a size $d$ satisfying $d^3 = V/N$. Figure 2 shows an example of the discrete dipole arrays for a sphere.[142]

The polarization of the a dipole at position $\boldsymbol{r}_i$, which is resulted from the interaction of dipole with the local field $\boldsymbol{E}_{loc,i}$, is written as[143-144]

$$\boldsymbol{P}_i = \boldsymbol{\alpha}_i \cdot \boldsymbol{E}_{loc,i} \tag{18}$$

with $\boldsymbol{\alpha}_i$ the polarizability tensor given by[144]

$$\boldsymbol{\alpha}_i = \frac{3d^3}{4\pi}\frac{\varepsilon_i - 1}{\varepsilon_i + 2} \tag{19}$$

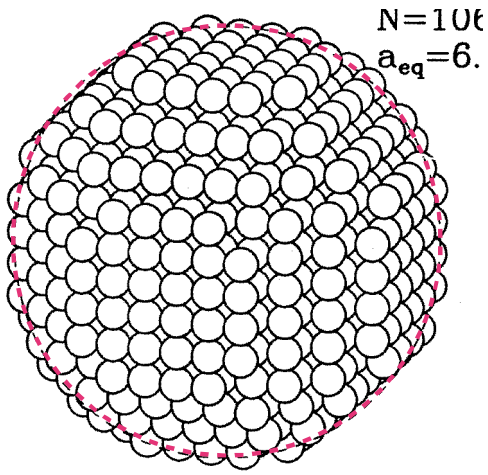


*Figure 2: Discrete dipole arrays with $N = 1064$ for a sphere.*[142]

where $\varepsilon_i$ is the dielectric function at $\boldsymbol{r}_i$. The local field is constituted by both incident field and the field caused by other dipoles at this position $\boldsymbol{E}_{dip,i}$[143-145]

$$\boldsymbol{E}_{loc,i} = \boldsymbol{E}_{inc,i} + \boldsymbol{E}_{dip,i} \tag{20}$$

The incident field at $\boldsymbol{r}_i$ is expressed as

$$\boldsymbol{E}_{inc,i} = \boldsymbol{E}_0 e^{i\boldsymbol{k}\cdot\boldsymbol{r}_i} \tag{21}$$

with $\boldsymbol{E}_0$ and $\boldsymbol{k}$ the amplitude and free space wave vector, respectively, of the incident field. The additional field at position $\boldsymbol{r}_i$ caused by other dipoles is given by[143]

$$\boldsymbol{E}_{dip,i} = -\sum_{i\neq j} \boldsymbol{A}_{ij} \cdot \boldsymbol{P}_j \tag{22}$$

where $\boldsymbol{A}_{ij}$ is the matrix that describes the interaction between dipole at $\boldsymbol{r}_i$ and any other dipole $\boldsymbol{r}_j$ ($i \neq j$). Consequently, $\boldsymbol{A}_{ij} \cdot \boldsymbol{P}_j$ can be expressed as[143-144]

$$\boldsymbol{A}_{ij} \cdot \boldsymbol{P}_j = \frac{1}{r_{ij}^3} e^{ikr_{ij}} \left\{ k^2 \boldsymbol{r}_{ij} \times (\boldsymbol{r}_{ij} \times \boldsymbol{P}_j) + \frac{1 - ikr_{ij}}{r_{ij}^2} \times \left[ r_{ij}^2 \boldsymbol{P}_j - 3\boldsymbol{r}_{ij} (\boldsymbol{r}_{ij} \cdot \boldsymbol{P}_j) \right] \right\} \tag{23}$$

where $\boldsymbol{r}_{ij} = \boldsymbol{r}_i - \boldsymbol{r}_j$.

# REFERENCES


[1] A. G. Curto, G. Volpe, T. H. Taminiau, M. P. Kreuzer, R. Quidant, N. F. van Hulst. Unidirectional emission of a quantum dot coupled to a nanoantenna. Science, 2010, 329, 930-933.

[2] O. Kulakovich, N. Strekal, A. Yaroshevich, S. Maskevich, S. Gaponenko, I. Nabiev, U. Woggon, and M. Artemyev. Enhanced luminescence of CdSe quantum dots on gold colloids. Nano Lett, 2002, 2 (12), 1449-1452.

[3] J. Kim, G. Dantelle, A. Revaux, M. Bérard, A. Huignard, T. Gacoin, and J-P. Boilot. Plasmon-induced modification of fluorescent thin film emission nearby gold nanoparticle monolayers. Langmuir, 2010, 26 (11), 8842-8849.

[4] T. Sen and A. Patra. Recent advances in energy transfer processes in gold-nanoparticle-based assemblies. J. Phys. Chem. C, 2012, 116 (33), 17307-17317.

[5] A. Kinkhabwala, Z. Yu, S. Fan, Y. Avlasevich, K. Müllen, and W. E. Moerner. Large single-molecule fluorescence enhancements produced by a bowtie nanoantenna. Nature Photonics, 2009, 3, 654-657.

[6] A. Furube, L. Du, K. Hara, R. Katoh, and M. Tachiya. Ultrafast plasmon-induced electron transfer from gold nanodots into TiO2 nanoparticles. J. Am. Chem. Soc., 2007, 129 (48), 14852-14853.

[7] H. Cong, R. Toftegaard, J. Arnbjerg, and P. R. Ogilby. Silica-coated gold nanorods with a gold overcoat: controlling optical properties by controlling the dimensions of a gola-silica-gold lyered nanoparticle. Langmuir, 2010, 26 (6), 4188-4195.

[8] W. Paige Hall, S. NI. Ngatia, and R. P. Van Duyne. LSPR biosensor signal enhancement using nanoparticle-antibody conjugates. J. Phys. Chem. C, 2011, 115 (5), 1410-1414.

[9] S. Roy, C. K. Dixit, R. Woolley, R. O'Kennedy, and C. McDonagh. Synthesis and characterization of a noble metal enhanced optical nanohybrid (NEON): a high brightness detection platform based on a dye-doped silica nanoparticle. Langmuir, 2012, 28 (21), 8244-8250.

[10] K. Leong, M. T. Zin, H. Ma, M. Sarikaya, F. Huang, and A. K-Y. Jen. Surface plasmon enhanced fluorescence of cationic conjugated polymer on periodic nanoarrays. ACS Appl. Mater. Interfaces, 2010, 2 (11) 3153-3159.

[11] C. F. Bohren and D. R. Huffman. Absorption and scattering of light by small particles. Wiley: New York, 1983.

[12] J. A. Lock and G. Gouesbet. Generalized Lorenz-Mie theory and applications. Journal of Quantitative spectroscopy and Radiative Transfer, 2009, 110 (11), 800-807.

[13] G. Gonella and H. L. Dai. Determination of adsorption geometry on spherical particles from nonlinear Mie theory analysis of surface second harmonic generation. Phys. Rev. B, 2011, 84, 121402.

[14] P. Das, T. K. Chini, and J. Pond. Probing higher order surface plasmon modes on individual truncated tetrahedral gold nanoparticle using cathodoluminescence imaging and spectroscopy combined with FDTD simulations. J. Phys. Chem. C, 2012, 116, 15610-15619.

[15] A. Brioude, X. C. Jiang, and M. P. Pileni. Optical properties of gold nanorods: DDA simulations supported by experiments. J. Phys. Chem. B, 2005, 109, 13138-13142.

[16] E. Moreno, D. Erni, C. Hafner, and R. Vahldieck. Multiple multipole method with automatic multipole setting applied to the simulation of surface plasmons in metallic nanostructures. J. Opt. Soc. Am. A, 2002, 19 (1), 101-111.

[17] L. Zhao, K. L. Kelley, and G. C. Schatz. The extinction spectra of silver nanoparticle arrays: influence of array structure on plasmon resonance wavelength and width. J. Phys. Chem. B, 2003, 10, 7343-7350.

[18] D. Sarid and W. Challener. Mordern introduction to surface plasmons: theory, mathematical modeling, and applications. Cambridge university press: Cambridge, 2010. ISBN 9780521767170.

[19] C. Sönnichsen, T. Franzl, T. Wilk, G. von Plessen, and J. Feldmann. Drastic reduction of plasmon damping in gold nanorods. Phys. Rev. Lett., 2002, 88, 077402.

[20] T. V. Teperik, V. V. Popov, F. Garcia de Abajo. Radiative decay of plasmons in metallic nanoshell. J. Phys. Rev. B, 2004, 69, 155402.

[21] C. Dahmen, B. Schmidt, G. von Plessen. Radiation damping in metal nanoparticle pairs. Nano Lett., 2007, 7, 318-322.

[22] K. L. Kelly, E. Coronado, L. L. Zhao, and G. C. Schatz. The optical properties of metal nanoparticles: the influence of size, shape, and dielectric environment. J. Phys. Chem. B, 2003, 107, 668-677.

[23] J. Lermé, H. Baida, C. Bonnet, M. Broyer, E. Cottancin, A. Crut, P. Maioli, N. Del Fatti, F. Vallée, and M. Pellarin. Size dependence of the surface plasmon

resonance damping in metal nanospheres. J. Phys. Chem. Lett., 2010, 1, 2922-2928.

[24] M. M. Alvarez, J. T. Khoury, T. G. Schaaff, M. N. Shafigullin, I. Vezmar, and R. L. Whetten. Optical absorption spectra of nanocrystal gold molecules. J. Phys. Chem. B, 1997, 101, 3706-3712.

[25] M. Meier and A. Wokaun. Enhanced fields on large metal particles: dynamic depolarization. Opt. Lett., 1983, 8 (11), 581-583.

[26] C. J. F. Böttcher. Theory of electric polarization. 2nd ed. Elservier: Amsterdam, 1973. vol1.

[27] M. Navarro-Cia and S. A. Maier. Broad-band near-infrared plasmonic nanoantennas for higher harmonic generation. ACS Nano, 2012, 6 (4), 3537-3544.

[28] D. P. Lyvers, J-M. Moon, A. V. Killdishev, V. M. Shalaev, and A. Wei. Gold nanorod arrays as plasmonic cavity resonators. ACS Nano, 2008, 2 (12) 2569-2576.

[29] A. Mazzucco, N. Geuquet, J. Ye, O. Stéphan, W. Van Roy, P. Van Drope, L. Henrard, and M. Kociak. Ultralocal modification of surface plasmons properties in silver nanocubes. Nano Lett., 2012, 12 (3), 1288-1294.

[30] L. J. Sherry, S-H. Chang, G. C. Schatz, and R. P. Van Duyne. Localized surface plasmon resonance spectroscopy of single silver nanocubes. Nano Lett., 2005, 5 (10), 2034-2038.

[31] K. A. Stoerzinger, W. Hasan, J. Y. Lin, A. Robles and T. W. Odom. Screening nanopyramid assemblies to optimize surface enhanced Raman scattering. J. Phys. Chem. Lett., 2010, 1 (7), 1046-1050.

[32] M. Jin, V. Pully, C. Otto, A. van den Berg, E. T. Carlen. High-density periodic arrays of self-aligned subwavelength nanopyramids for surface-enhanced Raman spectroscopy. J. Phys. Chem. C, 2010, 114, 21953-21959.

[33] F. Tam, G. P. Goodrich, B. R. Johnson, and N. J. Halas. Plasmonic enhancement of molecular fluorescence. Nano Lett., 2007, 7 (2), 496-501.

[34] N. T. Fofang, N. K. Grady, Z. Fan, A. O. Govorov, and N. J. Halas. Plexciton dynamics: exciton-plasmon coupling in a J-aggregate-Au nanoshell complex provides a mechanism for nonlinearity. Nano Lett., 2011, 11 (4), 1556-1560.

[35] C. Tabor, D. Van Haute and M. A. El-Sayed. Effect of orientation on plasmoinc coupling between gold nanorods. ACS Nano, 2009, 3 (11), 3670-3678.

[36] L. S. Slaughter, Y. Wu, B. A. Willingham, P. Nordlander and S. Link. Effects of symmetry breaking and conductive contact on the plasmon coupling in gold nanorod dimers. ACS Nano, 2010, 4 (8), 4657-4666.

[37] D. P. Fromm, A. Sundaramurthy, P. J. Schuck, G. Kino, and W. E. Moerner. Gap-dependent optical coupling of single “bowtie” nanoantennas resonant in the visible. Nano Lett. 2004, 4 (5), 957-961.

[38] D.-S. Kim, J. Heo, S-H. Ahn, S. W. Han, W. S. Yun, and Z. H. Kim. Real-space mapping of the strongly coupled plasmons of nanoparticle dimers. Nano Lett., 2009, 9 (10), 3619-3625.

[39] L. Wang, Y. Nishijima, K. Ueno, H. Misawa, and N. Tamai. Effect of dipole coupling on near-IR LSPR and coherent phonon vibration of periodic gold pair nanobuboids. J. Phys. Chem. C, 2012, 116 (33), 17838-17846.

[40] S. Hudlet, S. Aubert, A. Bruyant, R. Bachelot, P. M. Adam, J. L. Bijon, G. Lérondel, P. Royer, and A. A. Stashkevich. Apertureless near field optical microscopy: a contribution to the understanding of the signal detected in the presence of a background field. Opt. Comm., 2004, 230, 245-251.

[41] P. Anger, P. Bharadwaj, and L. Novotny. Enhancement and quenching of single-molecule fluorescence. Phys. Rev. Lett., 2006, 96, 113002.

[42] T. Kalkbrenner, M. Ramstein, J. Mlynek, and V. Sandoghdar. A single gold particle as a probe for apertureless scanning near-field optical microscopy. Journal of Microscopy, 2001, 202 (1), 72-76.

[43] T. Klar, M. Perner, S. Grosse, G. von Plessen, W. Spirkl, and J. Feldmann. Surface-plasmon resonances in single metallic nanoparticles. Phys. Rev. Lett. 1998, 80, 4249-4252.

[44] H. Heinzelmann, D. W. Pohl. Scanning near-field optical microscopy. Appl. Phys. A, 1994, 59, 89-101.

[45] A. Hartschuh, E. J. Sanchez, X. S. Xie, and L. Novotny. High-resolution near-field Raman microscopy of single-walled carbon nanotubes. Phys. Rev. Lett. 2003, 90, 095503.

[46] J. Nelayah, M. Kociak, O. Stéphan, F. J. G. de Abajo, M. Tencé, L. Henrard, D. Taverna, I. Pastoriza-Santos, L. M. Liz-Marzan, and C. Colliex. Mapping surface plasmons on a single metallic nanoparticle. Nature Physics, 2007, 3, 348-353.

[47] L. Douillard, F. Charra, Z. Korczak, R. Bachelot, S. Kostcheev, G. Lérondel, P. M. Adam, and P. Royer. Short range plasmon resonances probed by photoemission electron microscopy. Nano Lett., 2008, 8, 935-940.

[48] C. Hubert, A. Rumyantseva, G. Lérondel, J. Grand, S. Kostcheev, L. Billot, A. Vial, R. Bachelot, P. Royer, S. Chang, S. K. Gray, G. P. Wiederrecht, and G. C. Schatz. Near-field photochemical imaging of noble metal nanostructures. Nano Lett., 2005, 5 (4), 615-619.

[49] H. Ibn El Ahrach, R. Bachelot, A. Vial, G. Lérondel, J. Plain, and P. Royer, Spectra degeneracy breaking of the plasmon resonance of single metal nanoparticles by nanoscale near-field photopolymerization. Phys. Rev. Lett., 2007, 98, 107402.

[50] C. Deeb, R. Bachelot, J. Plain. A-L. Baudrion, S. Jradi, A. Bouhelier, O. Soppera, P. K. Jain, L. Huang, C. Ecoffet, L. Balan, and P. Royer. Quantitative analysis of localized surface plasmons based on molecular probing. ACS Nano, 2010, 4 (8), 4579-4586.

[51] C. Deeb, C. Ecoffet, R. Bachelot, J. Plain, A. Bouhelier, and O. Soppera. Plasmon-based free-radical photopolymerization: effect of diffusion on nanolithography process. J. Am. Chem. Soc., 2011, 133, 10535-10542.

[52] E. Fermi. Nuclear Physics: course notes complied by J. Orear, A. H. Rosenfeld, and R. A. Schluter. The University of Chicago Press: London. 1974. ISBN 0226243656.

[53] E. Dulkeith, A. C. Morteani, T. Niedereichholz, T. A. Klar, and J. Feldmann. Fluorescence quenching of dye molecules near gold nanoparticles: radiative and nonradiative effects. Phys. Rev. Lett., 2002, 89, 203002.

[54] C. D. Geddes and J. R. Lakowicz. Metal-enhanced fluorescence. Journal of Fluorescence, 2002, 12 (2), 121-129.

[55] R. Bardhan, N. K. Grady, J. R. Cole, A. Joshi, and N. J. Halas. Fluorescence enhancement by Au nanostructures: nanoshells and nanorods. ACS Nano, 2009, 3 (3) 744- 752.

[56] T. Härtling, P. Reichenbach, and L. M. Eng. Near-field coupling of a single fluorescent molecule and a spherical gold nanoparticle. Optics Express, 2007, 15 (20), 12806-12817.

[57] P. Johansson, H. Xu, and M. Käll. Surface-enhanced Raman scattering and fluorescence near metal nanoparticles. Phys. Rev. B, 2005, 72, 035427.

[58] E. C. Le Ru and P. G. Etchegoin. Principles of surface-enhanced Raman spectroscopy and related plasmonic effects. Elsevier: Oxford. 2009. ISBN 9780444527790.

[59] L. Novotny and B. Hecht. Principles of nano-optics. Cambridge: New York. 2012. ISBN 9781107005464.

[60] L. Zhao, T. Ming, L. Shao, H. Chen, and J. Wang. Plasmon-controlled Förster resonance energy transfer. J. Phys. Chem. C, 2012, 116 (14), 8287-8296.

[61] J. R. Lakowicz. Topics in fluorescence spectroscopy: volum 4 probe design and chemical sensing. Plenum: New York. 1994. ISBN 0306447843.

[62] L. Song, E. J. Hennink, I. T. Young, H. J. Tanke. Photobleaching kinetics of fluorescein in quantitative fluorescence microscopy. Biophysical Journal, 1995, 68, 2588-2600.

[63] J. R. Lakowichz. Topics in fluorescence spectroscopy: volum 1 techniques. Kluwer academic publishers: New York. 2002. ISBN 0306438748.

[64] S. M. Ramasamy, V. P. Senthilnathan, and R. J. Hurtubise. Determination of room-temperature fluorescence and phosphorescence quantum yields for compounds adsorbed on solid surfaces. Anal. Chem. 1986, 58 (3), 612-616.

[65] M. Fleischmann, P. J. Hendra, and A. J. McQuillan. Raman spectra of pyridine adsorbed at a silver electrode. Chem. Phys. Lett., 1974, 26 (2), 163-166.

[66] D. L. Jeanmaire and R. P. Van Duyne. Surface Raman spectroelectrochemistry: part I. heterocyclic, aromatic, and aliphatic amines adsorbed on the anodized silver electrode. J. Electroanalytical Chemistry and Interfacial Electrochemistry, 1977, 84 (1) 1-20.

[67] M. G. Albrecht, J. A. Creighton. Anomalously intense Raman spectra of pyridine at a silver electrode. J. Am. Chem. Soc. 1977, 99 (15), 5215-5217.

[68] Y. Huang, Y. Fang, and M. Sun. Remote excitation of surface-enhanced Raman scattering on single Au nanowire with quasi-spherical termini. J. Phys. Chem. C, 2011, 115, 3558-3561.

[69] Y. Fang, H. Wei, F. Hao, P. Nordlander and H. Xu. Remote-excitation surface-enhanced Raman scattering using propagating Ag nanowire plasmons. Nano Lett., 2009, 9 (5), 2049-2053.

[70] S. Ayas, H. Güner, B. Türker, O. Ö. Ekizm, F. Dirisaglik, A. K. Okyay, and A. Dâna. Raman enhancement on a broadband meta-surface. ACS Nano, 2012, 6 (8), 6852-6861.

[71] P. Nagpal, N. C. Lindquist, S-H. Oh, D. J. Norris. Ultrasmooth patterned metals for plasmonics and metamaterials. Science, 2009, 325, 594- 597.

[72] W. E. Doering and S. Nie. Spectroscopic tags using dye-embedded nanoparticles and surface-enhanced Raman scattering. Anal. Chem., 2003, 75, 6171-6176.

[73] X. Huang, I. H. El-Sayed, W. Qian, and M. A. El-Sayed. Cancer cells assemble and align gold nanorods conjugated to antibodies to produce highly enhanced, sharp, and polarized surface Raman spectra: A potential cancer diagnostic marker. Nano Lett., 2007, 7 (6), 1591-1597.

[74] V. Schwikhard, A. Grubisic, T. A. Baker, I. Thomann, and D. J. Nesbitt. Polarization-dependent scanning photoionization microscopy: ultrafast plasmon-mediated electron ejection dynamics in single Au nanorods. ACS Nano, 2011, 5 (5), 3734-3735.

[75] J. M. McLellan, Z-Y. Li, A. R. Siekkinen, and Y. Xia. The SERS activity of supported Ag nanocubes strongly depends on its orientation relative to laser polarization. Nano Lett., 2007, 7 (4), 1013-1017.

[76] L.-L. Tay, J. Hulse, D. Kennedy, and J. P. Pezacki. Surface-enhanced Raman and resonant Rayleigh scatterings from adsorbate saturated nanoparticles. J. Phys. Chem. C, 2010, 114, 7356-7363.

[77] K. D. Alexander, K. Skinner, S. Zhang, H. Wei, and R. Lopez. Tunable SERS in gold nanorod dimers through strain control on an elastomeric substrate. Nano Lett., 2010, 10, 4488-4493.

[78] T. Dadosh, J. Sperling, G. W. Bryant, R. Breslow, T. Shegai, M. Dyshel, G. Haran, and I. Bar-Joseph. Plasmonic control of the shape of the Raman spectrum of a single molecule in silver nanoparticle dimer. ACS Nano, 2009,

[79] N. A. Hatab, C-H. Hsueh, A. L. Gaddis, S. T. Retterer. J-H. Li, G. Eres, Z. Zhang, and B. Gu. Free-standing optical gold bowtie nanoantenna with variable gap size for enhanced Raman spectroscopy. Nano Lett., 2010, 10, 4952-4955.

[80] B. Pettinger, B. Ren, G. Picardi, R. Schuster, and G. Ertl. Nanoscale probing of adsorbed species by tip-enhanced Raman spectroscopy. Phys. Rev. Lett., 2004, 92 (9), 096101.

[81] W. Zhang, B. S. Yeo, T. Schmid, and E. Zenobi. Single molecule tip-enhanced Raman spectroscopy with silver tips. J. Phys. Chem. C, 2007, 111, 1733-1738.

[82] K. Kneipp, Y. Wang, R. R. Dasari, and M. S. Feld. Approach to single mode detection using surface-enhanced resonance Raman scattering: a study using rhodamine 6G on colloidal silver. Applied Spectroscopy, 1995, 49 (6), 780-784.

[83] D. H. Murgida and P. Hildebrandt. Electron-transfer processes of cytochrome c at interfaces. New Insights by surface-enhanced resonance Raman spectroscopy. Acc. Chem. Res., 2004, 37, 854-861.

[84] K. Kneipp, Y. Wang, H. Kneipp, L. T. Perelman, I. Itzkan. Single molecule detection using surface-enhanced Raman scattering. Phys. Rev. Lett., 1997, 78 (9), 1667-1670.

[85] S. Nie and S. R. Emory. Probing single molecules and single nanoparticles by surface-enhanced Raman scattering. Science, 1997, 275, 1102-1106.

[86] K. D. Alexander, M. J. Hampton, S. Zhang, A. Dhawan, H. Xu, and R. Lopez. A high-throughput method for controlled hot-spot fabrication in SERS-active gold nanoparticle dimer arrays. Journal of Raman Spectroscopy, 2009, 40, 2171-2175.

[87] C. E. Talley, J. B. Jackson, C. Oubre, N. K. Grady, C. W. Hollars, S. M. Lane, T. R. Huster, P. Nordlander, and N. J. Halas. Surface-enhanced Raman scattering from individual Au nanoparticles and nanoparticle dimer substrates. Nano Lett., 2005, 5 (8), 1569-1574.

[88] G. C. Schatz. Theoretical studies of surface enhanced Raman scattering. Acc. Chem. Res., 1984, 17, 370-376.

[89] T. Vo-Dinh. Surface-enhanced Raman spectroscopy using metallic nanostructures. Trends in analytical chemistry, 1998, 17, 557-582.

[90] A. Campion and P. Kambhampati. Surface-enhanced Raman scattering. Chemical Society Reviews, 1998, 27, 241-250.

[91] E. Smith and G. Dent. Modern Raman spectroscopy: a practical approach. Wiley: UK. 2005. ISBN 0471497940.

[92] H. Xu, J. Aizpurua, M. Käll, and P. Apell. Electromagnetic contributions to single-molecule sensitivity in surface-enhanced Raman scattering. Phys. Rev. E, 2000, 63 (3), 4318-4324.

[93] E. C. Le Ru, J. Grand, N. Félidj, J. Aubard, G. Lévi, A. Hohenau, J. R. Krenn, E. Blackie, and P. G. Etchegoin. Experimental verification of the SERS electromagnetic model beyond the E4 approximation: polarization effects. J. Phys. Chem. C, 2008, 112 (22), 8117-8121.

[94] W. E. Doering and S. Nie. Single-molecule and single-nanoparticle SERS: examining the roles of surface active sites and chemical enhancement. J. Phys. Chem. B, 2002, 106, 311-317.

[95] S. M. Morton and L. Jensen. Understanding the molecule-surface chemical coupling in SERS. J. Am. Chem. Soc., 2009, 131, 4090-4098.

[96] B. N. J. Persson, K. Zhao, and Z. Zhang. Chemical contribution to surface-enhanced Raman scattering. Phy. Rev. Lett., 2006, 96, 207401.

[97] L. Qin, S. Zou, C. Xue, A. Atkinson, G. C. Schatz, and C. A. Mirkin. Designing, fabricating, and imaging Raman hot spots. PNAS, 2006, 36, 13300-13303.

[98] Y. Leroux, E. Eang, C. Fave, G. Trippe, J. C. Lacroix. Conducting polymer/gold nanoparticle hybrid materials: a step toward electroactive plasmonic devices. Electrochemistry Communications, 2007, 9, 1258-1262.

[99] Y. Chen, K. Munechika, I. J-L. Plante, A. M. Munro, S. E. Skrabalak, Y. Xia, and D. S. Ginger. Excitation enhancement of CdSe quantum dots by single metal nanoparticles. App. Phys. Lett., 2008, 93, 053106.

[100] O. Kulakovich, N. Strekal, A. Yaroshevich, S. Maskevich, S. Gaponenko, I. Nabiev, U. Woggon, and M. Artemyev. Enhanced Luminescence of CdSe quantum dots on gold colloids. Nano Lett., 2002, 2 (12), 1449-1452.

[101] E. Dulkeith, M. Ringler, T. A. Klar, and J. Feldmann. Gold nanoparticles quench fluorescence by phase induced radiative rate suppression. Nano Lett., 2005, 5 (4) 585-589.

[102] Z. Gueroui and A. Libchaber. Single-molecule measurements of gold-quenched quantum dots. Phys. Rev. Lett. 2004, 93 (16), 166108.

[103] W. P. Hall, S. N. Ngatia, and R. P. Van Duyne. LSPR biosensor signal enhancement using nanoparticle-antibody conjugates. J. Phys. Chem. C, 2011, 115, 1410-1414.

[104] N. P. Ivleva, M. Wagner, A. Szkola, H. Horn, R. Niessner, and C. Haisch. Label-free in situ SERS imaging of biofilms. J. Phys. Chem. B, 2010, 114, 10184-10194.

[105] A. Barhoumi and N. J. Halas. Label-free detection of DNA hybridization using surface enhanced Raman spectroscopy. J. Am. Chem. Soc. 2010, 132, 12792-12793.

[106] M. A. Noginov, G. Zhu, A. M. Belgrave, R. Bakker, V. M. Shalaev. E. E. Narimanov, S. Stout, E. Herz, T. Suteewong and U. Wiesner. Demonstration of a spaser-based nanolaser. Nature, 2009, 460, 1110-1112

[107] J. Li S. K. Cushing, J. Bright, F. Meng, T. R. Senty, P. Zheng, A. D. Bristow, and N. Wu. Ag@Cu2O core-shell nanoparticles as visible-light plasmonic photocatalysts. ACS Catal. 2013, 3, 47-51.

[108] C. Wu and Q-H. Xu. Stable and functionable mesoporous silica-coated gold nanorods as sensitive localized surface plasmon resonance (LSPR) nanosensors. Langmuir, 2009, 25 (16), 9441-9446.

[109] H. Wang, D. W. Brandl, F. Le, P. Nordlander, and N. J. Halas. Nanorice: a hybrid plasmonic nanostructure. Nano Lett., 2006, 6 (4) 827-832.

[110] O. Soppera, S. Jradi, D. J. Lougnot. Photopolymerization with microscale resolution: influence of physic-chemical and photonic parameters. Journal of Polymer Science: Part A: Polymer Chemistry. 2008, 46, 3783-3794.

[111] A. Espanet, G. D. Santos, C. Ecoffet, D. J. Lougnot. Photopolymerization by evanescent waves: characterization of photopolymerizable formulation or photolithography with nanometric resolution. Applied Surfeace Science,1999, 138-139, 87-92.

[112] G. Wurtz, D. Burget. C. Carre. Photopolymerization-induced materialization of the dipolar response from isolated metallic nanoparticles. SPIE, 2004, 5458.

[113] N. R. Jana, L. Gearheart, and C. J. Murphy. Evidence for seed-mediated nucleation in the chemical reduction of gold salts to gold nanoparticles. Chem. Mater. 2001, 13, 2313-2322.

[114] Y. Yu, Q. Zhang, X. Lu, and J. Y. Lee. Seed-mediated synthesis of monodisperse concave trisoctahedral gold nanocrystals with controllable sizes. J. Phys. Chem. C 2010, 114, 11119−11126.

[115] T. K. Sau, C. J. Murphy. Room temperature, high-yield synthesis of multiple shapes of gold nanoparticles in aqueous solution. J. Am. Chem. Soc. 2004, 126, 8648− 8649.

[116] G.-N. Xiao, S.-Q. Man. Surface-enhanced Raman scattering of methylene blue adsorbed on cap-shaped silver nanoparticle. Chem. Phys. Lett. 2007, 447, 305-309.

[117] C. Ruan, W. Wang, B. Gu. Single-molecule detection of thionine on aggregated gold nanoparticles by surface enhanced Raman scattering. Journal of Raman Spectroscopy. 2007, 38, 5, 568-573.

[118] E. Hao, G. C. Schatz. Electromagnetic fields around silver nanoparticles and dimers. J. Chem. Phys. 2004, 120, 357-336.

[119] C. J. Orendorff, A. Gole, T. K. Sau, C. Murphy. Surface-enhanced Raman spectroscopy of self-assembled monolayers: sandwich architecture and nanoparticle shape dependence. J. Anal. Chem. 2005, 77, 10, 3261-3266.

[120] J.-H. Klein-Wiele, P. Simon, H.-G. Rubahn. Size-dependent plasmon lifetimes and electron-phonon coupling time constants for surface bound Na clusters. Phys. Rev. Lett. 1998, 80, 45-48.

[121] C. Sönnichsen, T. Franzl, T. Wilk, G. Von Plessen, J. Feldmann, O. Wilson, P. Mulvaney. Drastic reduction of plasmon damping in gold nanorods. Phys. Rev. Lett. 2002, 88, 077402.

[122] P. B. Johnson, R. W. Christy. Optical constants of the nooble metals. Phys. Rev. B, 1972, 6, 4370-4379.

[123] M. Yi, D. Zhang, P. Wang, X. Jiao, S. Blair, X. Wen, Q. Fu, Y. Lu, H. Ming. Plasmonic interaction between silver nano-cubes and a silver ground plane studied by surface-enhanced Raman scattering. Plasmonics. 2011, 6, 3, 515-519.

[124] Y. H. Lee, Y. Yan, L. Polavarapu, Q-H. Xu. Nonlinear optical switching behavior of Au nanocubes and nano-octahedra investigated by femtosecond Z-scan measurements. Appl. Phys. Lett, 2009, 95, 023105.

[125] J. M. McMahon, Y. Wang, L. J. Sherry, R. P. Van Duyne, L. D. Marks, S. K. Gray, and G. Schatz. Correlating the structure, optical spectra, and electrodynamics of single silver nanocubes. J. Phys. Chem. C, 2009, 113, 2731-2735.

[126] R. Bachelot, F. H'dhili, D. Barchiesi, G. Lerondel, R. Fikri, P. Royer, N. Landraud, J. Peretti, F. Chaput, G. Lampel, et al. Apertureless near-field optical microscopy: a study of the local tip field enhancement using photosensitive azobenzen-containing films. J. Appl. Phys. 2003, 94, 2060-2073.

[127] J. Van Bladel. Singular electromagnetic fields and sources. Wiley-IEEE Press: New York, 2002.

[128] S. J. Orfanidis. Electromagnetic waves and antennas. Book online 2008. http://eceweb1.rutgers.edu/~orfanidi/ewa

[129] C. Corti, R. Holliday. Gold: science and applications CRC Press: Boca Raton. 2010. ISBN: 9781420065237.

[130] J. H. Weaver and H. P. R. Frederikse. "Optical properties of selected elements" in CRC Handbook of Chemistry and Physics. D. R. Lide (ed.). CRC Press: Boca Raton, 2001.

[131] Achim Hartschuh. Tip-enhanced near-field optical microscopy. Angew. Chem. Int. Ed. 2008, 47, 8178-8191.

[132] T. Ming, L. Zhao, Z. Yang, H. Chen, L. Sun, J. Wang, and C. Yan. Strong polarization dependence of plasmon-enhanced fluorescence on single gold nanorods. Nano. Lett. 2009, 9, 11, 3896-3903.

[133] Y. S. Kim, P. T. Leung and T. F. George. Classical decay rates for molecules in the presence of a spherical surface: a complete treatment. Surface Science. 1988, 195, 1-14.

[134] S. Derom, R. Vincent, A. Bouhelier and G. Colas des Francs. Resonance quality, radiative/ohmic loss and modal volume of mie plasmons. EPL, 2012, 98, 47008.

[135] J. Sancho-Parramon. Near-field coupling of metal nanoparticles under tightly focused illumination. Opt. Lett. 2011, 36, 17, 3527- 3529.

[136] T. Atay, J.-H.Song, and A. V. Nurmikko. Strongly interacting plasmon nanoparticle pairs: from dipole-dipole interaction to conductively coupled regime. Nano Lett. 2004. 4, 9, 1627-1631.

[137] J. Zuloaga, E. Prodan, and P. Nordlander. Quantum description of the plasmon resonances of a nanoparticle dimer. Nano Lett. 2009. 9, 2, 887-891.

[138] J. B. Lassiter, J. Aizpurua, L. I. Hernandez, D. W. Brandl, I. Romero, S. Lal, J. H. Hafner, P. Nordlander, and N. J. Halas. Close encounters between two nanoshells. Nano Lett. 2008. 8, 4, 1212-1218.

[139] R. C. Maher, L. F. Cohen, P. Etchegoin. Single molecule photo-bleaching observed by surface enhanced resonant Raman scattering (SERRS). Chem. Phys. Lett. 2002. 352, 378-384.

[140] K. S. Yee. Numerical solution of initial boundary value problems involving Maxwell's equations in isotropic media. Antennas and Propagation. 1966, 14, 3, 302-307.

[141] A. Taflove, S. C. Hagness. Computational electrodynamics: the finite-difference time-domain method. Second edition. Artech House Publishers: Norwood. 2000. ISBN 1580530761.

[142] B. T. Draine. The discrete-dipole approximation and its application to interstellar graphite grains. The Astrophysical Journal. 1988, 333, 848-872.

[143] W.-H. Yang, G. C. Schatz, and R. P. Van Duyne. Discrete dipole approximation for calculating extinction and Raman intensities for small particles with arbitrary shapes. J. Chem. Phys. 1995, 103, 3, 869-875.

[144] B. R. Draine, P. J. Flatau. Discrete-dipole approximation for scattering calculations. Opt. Soc. Am. A. 1994, 11, 4, 1491-1499.

[145] M. A. Yurkin and A. G. Hoekstra. The discrete dipole approximation: an overview and recent developments. J. Quant. Spectrosc. Radiat. Transf. 2007, 106, 558-589.

# Xuan ZHOU

## Doctorat : Optique et Nanotechnologies

Année 2013


## Nouvelles avancées en nano-plasmonique hybride : intégration de fonctions passives et actives


La plasmonique hybride est un sujet d'actualité qui exploite des interactions physiques entre nano-objets métalliques et d'autres nanomatériaux. En bénéficiant des propriétés de chacun de leurs constituants, les nanostructures hybrides sont utilisées dans de nombreuses applications comme la détection d'espèces bio-chimiques. Dans cette thèse, nous présentons une nouvelle nanostructure hybride polymère/métal qui est non seulement utilisée comme nano-émetteur anisotrope qui s'avère aussi être un outil puissant de caractérisation du champ proche optique.

La fabrication de cette nouvelle nanostructure est basée sur une approche de par photopolymérisation à l'échelle nanométrique. Cette technique, en comparaison aux méthodes traditionnelles de caractérisation, ne fournit pas seulement l'image de la distribution du champ, mais permet aussi des mesures quantitatives des plasmons de surface avec une résolution sub -5nm, incluant une description fine de la décroissance exponentielle des ondes évanescentes impliquées.

A l'aide du mode plasmon dipolaire, une distribution anisotrope de matériau organique est intégrée dans le voisinage de la nanoparticule métallique. Avec une haute concentration de molécules de colorant dans le polymère, l'intensité des signaux de fluorescence et Raman du nano-émetteur hybride dépend de la polarisation incidente. À notre connaissance, il s'agit de la première réalisation d'un nano-émetteur dont le milieu à gain présente une distribution spatiale complexe le rendant sensible à la polarisation.



Mots clés : optique en champ proche – plasmons - spectroscopie de fluorescence - Raman, effet augmenté en surface - matériaux nanostructurés - polymérisation.


## Advances in Hybrid Plasmonics: From Passive to Active Functions


Hybrid plasmonics has given rise to increasing interest in the context of the interaction between metal nano-objects and other materials. By benefiting from each of its constituents, hybrid nanostructures are commonly adopted in studies and optimization of biological and chemical sensors, nanoparticle with high plasmon resonance tunability, and nano-emitters. This PhD thesis presents a hybrid nanostructure of photopolymer/metal nanoparticle that is used as a near-field characterizing tool and as an anisotropic nano-emitter.

The fabrication of this hybrid nanostructure is a near-field imprinting process based on nanoscale photopolymerization. This technique, compared with traditional near-field characterization methods, provides not only the image of the field distribution, but also enables quantification of the surface plasmon properties with sub-5nm resolution and reproduction of the exponential decay of the near-field.

Under dipolar mode plasmon, the photopolymer was created anisotropically in the vicinity of the metal nanoparticle. With high concentration of dye molecules trapped in the polymer, the hybrid nano-emitter displays surface enhanced fluorescence and Raman signal that is dependent on the incident polarization. To our knowledge, this is the first achievement of the anisotropic nano-emitter based on the inhomogeneous distribution of the active molecule.



Keywords: near-field optics - plasmons (physics) - fluorescence spectroscopy - Raman effect, surface enhanced - nanostructured materials – polymerization.


**Thèse réalisée en partenariat entre :**


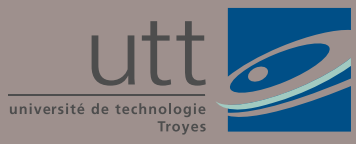


**Ecole Doctorale** "Sciences et Technologies"